Author:
Prasse, Philipp

Title:
Development of seismic anisotropy in deforming salt bodies

Development of seismic anisotropy in deforming salt bodies

By

PHILIPP PRASSE

Supervisors: James Wookey and J.-Michael Kendall

School of Earth Sciences
UNIVERSITY OF BRISTOL

A dissertation submitted to the University of Bristol in accordance with the requirements of the degree of DOCTOR OF PHILOSOPHY in the Faculty of Sciences.

JULY 2019

Abstract

Physical properties of salt, such as its low permeability, density and viscosity make it an important component in various industrial applications, e.g., natural salt deposits can form hydrocarbon traps in the subsurface. Many polycrystals develop a texture (lattice preferred orientation, LPO) and become seismically anisotropic when subject to plastic deformation. The potential of deformed rock salt to generate such anisotropy, the impact on seismic waveforms and seismic images is investigated, by using both, seismic data and sophisticated elasticity modelling. A vertical seismic profile (VSP) dataset from the Mahogany salt body (located in the Northern Gulf of Mexico) is investigated using shear-wave splitting analysis. The results show that shear wave phases, converted at the top of the salt body show significantly higher splitting than those, converted at the base of the salt body. The observations are clear signs of seismic anisotropy within the salt. Various scenarios are tested to explain the anisotropy by creating simple forward models. We conclude that LPO of halite is the most likely explanation of the splitting observed, although others causes, such as the presence of aligned water inclusions can not be disregarded. Motivated by the results, we use texture plasticity modelling to predict LPOs in halite polycrystalline aggregates and associated seismic anisotropy. First, rock salt texture deformed in simple deformation regimes (simple shear and uniaxial compression) is simulated and we analyse the ability to use texture modelling to predict anisotropy in naturally deformed rock salt. Seismic anisotropy predicted is around 10% for S-waves and 6% for P-wave. We develop a work-flow, based on calculating strain history of deformed salt formations, to estimate salt anisotropy due to deformation plasticity in more complex deformation scenarios, and demonstrate its adequacy on a salt diapir deformation model. The results show that the anisotropy pattern is complex, with higher anisotropy in regions which experienced larger deformation. The predicted anisotropy is significant and would falsify seismic images, if not accounted for properly. Then, the workflow is applied to a realistic Mahogany salt deformation model. A synthetic VSP-dataset is created, based on the calculated elasticity of the deformed salt. Synthetic shear-wave splitting results are consistent with the VSP field-data set results from Mahogany. This is strong evidence that the splitting observed is due to LPO of constituent rock salt crystals. Salt formation experience large deformation and can show, consequently, seismic anisotropy. Usually, salt anisotropy is not accounted for is seismic data, and therefore this study has potentially large impact on traditional seismic imaging in rock salt settings, which experienced strong deformation. This study places the common assumption of salt isotropy on unsafe ground.

Acknowledgements

Firstly, I want to thank the persons who contributed most to this thesis: My both supervisors, James Wookey and Michael Kendall. I honestly could not have wished for better supervisors. Your support and enthusiasm throughout my PhD was superb. I am very thankful for all the opportunities and conferences you encouraged me to attend.

My PhD project was part of the Marie Curie Innovative Training Network. I want to thank Andrea Tommasi, who coordinated the project, and also gave me fruitful comments on my work. The training, conferences and opportunities I could attend were a great privilege. I thank Christopher Spiers, his comments, insights and discussions were very helpful. This study was done in collaboration with Rockfield Global. Special thanks to Martin Dutko, who made the cooperation possible and Daniel Roberts, who gave me excellent guidance during my stay at Rockfield.

I also want to thank all my friend and lovely people who made this PhD, and my time here in Bristol, to such a wonderful experience. The everyday friendly and stimulating environment, the geophysics group here in Bristol, and my office mates made it possible that I could get up happy (almost) every morning.

I thank you, Maryory, for your love, support, encouragement and warm words. You always had faith in me. Your optimism and your happy nature are an everyday blessing – I can't thank you enough.

Above all I thank my family. My brother, you always had an open ear during my time here in Bristol. Its wonderful to know that I have such an amazing support in my family. Mom and dad – without you I could never be where I am. You are the most important persons in my life.

Ich danke euch, dass Ihr mich zu dem Menschen gemacht habt, der ich heute bin. Eure ständige Unterstüng, euer Vertrauen, eure Liebe und euer Rückhalt hat diese Arbeit erst möglich gemacht. Ich danke euch von ganzem Herzen. Ihr seid großartige Eltern.

Author's declaration

I declare that the work in this dissertation was carried out in accordance with the requirements of the University's Regulations and Code of Practice for Research Degree Programmes and that it has not been submitted for any other academic award. Except where indicated by specific reference in the text, the work is the candidate's own research. Work done in collaboration with, or with the assistance of, others, is indicated as such. Any views expressed in the dissertation are those of the author.

Philipp Prasse

Table of Contents

List of Tables

List of Figures

CHAPTER 1

INTRODUCTION

Naturally-occurring deposits of rock salt are important in a range of industrially-significant settings. For example, large salt deposits are present in many sedimentary environments associated with significant hydrocarbon reserves. Many large evaporite basins, such as the Luan Salt basin in the Gulf of Mexico, the Hormouz Evaporites in the Persian Gulf, the Permian Zechstein Basin in the North Sea or the Santos Basin, located in Brazil, are associated with significant oil and gas discoveries (e.g., *Dribus et al.*, 2008; *Hudec et al.*, 2013; *Jackson and Hudec*, 2017b). Understanding salt processes and dynamics affecting hydrocarbon reservoir production is important for their exploration and efficient exploitation. Furthermore, the unique sealing properties of salt makes it a candidate lithology for hazardous waste disposal or storage(*Langer*, 1993; *Chapman and Hooper*, 2012). Salt caverns or salt mines are used for gas-, oil-, and carbon dioxide sequestration. Also related to this is the storage potential of energy in the form of compressed air in salt caverns (compressed energy air storage, CAES). The air can be released at peak times, when energy is needed most (*Crotogino et al.*, 2001).

Salt has a low viscosity and low density, and is nearly impermeable. It flows under tectonic forces (on geological time scales) if the deviatoric stresses are high enough; salt is often the most deformable part of the sedimentary environment, and has the ability to flow rather than to fracture. Its low density and high viscosity make it relatively more buoyant than surrounding sediments. The flow of the salt can deform caprock layers, forming structural barriers for fluids, concentrating them spatially and preventing further migration (e.g., hydrocarbon traps). The impermeability of rocksalt acts as a seal that can impede the flow of oil and gas, making it crucial in forming these hydrocarbon traps.

The crystalline nature of salt – and its tendency to be highly deformed – means that it has

the potential to manifest significant seismic anisotropy, resulting from the alignment of its constituent crystals. Fundamentally, seismic anisotropy is the variation of wave speed with propagation direction. Many crystalline materials develop texture (lattice preferred orientation of crystal lattices: LPO) and become seismically anisotropic when being deformed. As rock salt is a common polycrystalline solid, which is highly deformed in geological environments, it is reasonable to investigate its potential to manifest seismic anisotropy due to crystal alignment. Halite, the main constituent of natural rock salt, has a cubic crystal structure and displays a significant elastic seismic anisotropy on single crystal scale (e.g, *Vargas-Meleza et al.* (2015); *Zong et al.* (2014); *Raymer et al.* (2000b,a)). When subject to an overall alignment by crystal plastic deformation, salt may exhibit anisotropy at a scale relevant to seismic waves. Accurate imaging of subsalt structures is an important in many reservoir settings. The assumption of an isotropic subsurface, which is in fact anisotropic will lead to distorted seismic images and erroneous interpretation. In case of exploration seismology, this might result in, for example, costly drilling errors.

Despite recent advances in salt imaging and studies showing evidence of seismic anisotropy in rock salt, it is still a common assumption to treat salt as being seismically isotropic (*Jones and Davison*, 2014). This study investigates the possibility of rock salt to manifest significant seismic anisotropy and the consequences of such for seismic imaging. The goal of this work is to better understand seismic anisotropy of rock salt and the effects in exploration seismology. The main objectives are:

- Examine seismic anisotropy in rock salt due to lattice preferred orientation and other effects.
- Obtain measurements of salt anisotropy from field data sets and compare the results with model predictions.
- Investigate the effects of salt anisotropy on seismic wave propagation.
- Develop techniques to assess seismic anisotropy and its importance in seismic processing.

This introduction chapter provides general background of properties of rock salt, its origin and development, and the structures formed in natural environments. Deformation and its relation to lattice preferred orientation are described. I present the fundamental principles of seismic anisotropy, and review studies showing evidence of seismic anisotropy in rock salt. Finally, an outlook of the thesis and each chapter is given.

1.1 Salt

Evaporite deposits are typically found in arid and semi-arid areas, where salt water evaporates faster than it can be replaced by rainfall, surface- or sub-surface water inflow (*Jenyon*, 1986).

Evaporite basins usually evolve due to a lack of access to open sea water, which restricts the influx of fresh salt water, resulting in an effective loss of water by evaporation. The salt water influx is sufficient to replace the water lost by evaporation, which allows continuous deposition of evaporites over geological time scales (*Warren*, 1989). Examples where such conditions are met are the Mediterranean, where the Messian basin was formed or the Gulf of Mexico with the Louann Salt Basin.

Evaporite deposits contain various minerals. The term "rock salt" usually refers to halite (NaCl), which is the most common mineral in most evaporite deposits (*Borchert and Muir*, 1964). Salt bodies are formed by evaporation: the salt content in the isolated water body becomes enriched and precipitates the solid when the content in the water exceeds saturation. The less soluble a mineral is, the earlier it precipitates out of the solution. The first to precipitate are usually calcite ($CaCO_3$) and dolomite ($CaMg(CO_3)_2$), followed by gypsum ($CaSO_4 \cdot 2H_2O$) and anhydrite ($CaSO_4$), after which halite precipitates. The last to precipitate are potassium and magnesium salts (sylvite (KCl), bischofite ($MgCl_2 \cdot 6H_2O$), carnalite ($MgCl_2 \cdot KCl \cdot 6H_2O$)) (*Warren*, 2006). The relative contribution of the minerals to evaporite deposits vary from region to region. While rock salt in the Gulf Coast typically contains mainly halite (~95% or more (*Jenyon*, 1986; *Zong et al.*, 2015)) and is considered to be very pure, other areas can contain higher amount of anhydrite or gypsum (*Borchert and Muir*, 1964; *Jenyon*, 1986). Also salt structures with halite/anhydrite layering are observed (*Wardlaw and Schwerdtner*, 1966). Table 1.1 contains an overview of the most common evaporite deposit minerals, together with its crystal structure and density.

Mineral	Composition	Density [kgm^{-3}]	Crystal symmetry
Calcite	$CaCO_3$	2710	trigonal
Dolomite	$CaMg(CO_3)_2$	2840	trigonal
Gypsum	$CaSO^4$ $2H_2O$	2300	monoclinic
Anhydrite	$CaSO^4$	2970	orthorhombic
Halite	NaCl	2160	cubic
Sylvite	KCl	1990	cubic
Carnallite	$MgCl_2$ Kcl $6H_2O$	1600	orthorhombic
Bischofite	$MgCl_2$ $6H_2O$	1560	monoclinic

TABLE 1.1. Most common evaporite minerals, their chemical composition and crystal symmetry. Halite is the main mineral in most evaporite deposits, though the exact mineral fraction varies from region to region.

Halite is the main mineral in most evaporite basins. It has a cubic crystal structure, with a face centred unit cell with additional lattice points at the centre of each face and four lattice points per unit cell (e.g., *Gebrande*, 1982). Its crystal structure is schematically displayed in Figure 1.1. Halite has a density of around 2160 kgm^{-3} and in dry conditions a viscosity of around $\mu = 10^{18}$ PaS (*Warren*, 2016), which can be a magnitude higher when the salt is wet. Typically, natural rock

salts deform under wet conditions (*Heege et al.*, 2005).

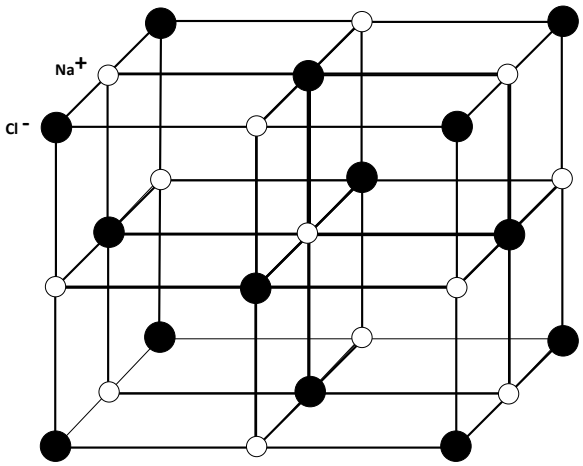

FIGURE 1.1. Halite crystallographic structure. Its chemical composition is NaCl. halite has a cubic face-centred crystal structure. Halite is the main constituent mineral of rock salt and the focus of this study.

1.2 Deformation and texture development

Rock salt is a common polycrystalline solid, which is highly deformed in geological environments. Polycrystals are solids that are composed of various crystals of different size and orientation of each crystal lattice. When subject of plastic deformation, the grain shape of the polycrystals change and the grain boundary area increases. Deformation leads to generation of dislocations, which tends to increase the grain boundary area. Dislocations are defects, such as voids, within the crystallographic structure. The generation of dislocations leads to an internal structure within the grains. Besides, the grain orientations change depending on the applied stress. This process leads to a non-random lattice orientation of constituent crystals. Generally, higher strain leads to stronger texture. This mechanism is observed in most solid materials, including evaporites, such as halite. Numerical and experimental evidence show that halite can exhibit significant texture when being deformed (*Carter and Hansen*, 1983; *Carter et al.*, 1993; *Lebensohn and Tomé*, 1993; *Wenk et al.*, 2009; *Wenk and Van Houtte*, 2004; *Lebensohn et al.*, 2003).

1.2.1 Deformation mechanisms of halite

Polycrystalline aggregates deform by different mechanisms and processes, depending on the properties of the aggregate, the temperature, and pressure under which the deformation happens. The main mechanisms observed in halite include dislocation glide/climb, dynamic recrystallisation,

and pressure solution creep (Figure 1.2) (*Urai*, 1987; *Drury and Urai*, 1990; *Passchier and Trouw*, 2005; *Ter Heege et al.*, 2005; *Urai and Spiers*, 2007). We shortly describe each mechanism below.

Dislocation glide/climb

Dislocation glide describes the movement of dislocations along a slip plane, propagating shear strain. The movement in dislocation glide is accommodated by switching crystal bonds between neighbouring atoms, but does not involve the transport of matter. Dislocation glide causes plastic deformation of individual crystals and to the material. During dislocation glide, the crystal lattice rotate, depending on the applied stress. Consequently, the orientation of the crystal changes during deformation, leading to texture. Dislocation climb differs from dislocation glide in a way that it allows dislocations to move out of its slip plane, perpendicular to it. It does not lead to lattice preferred orientation, as crystal orientation does not change in the process.

Pressure solution

Pressure solution is a process that happens at the grain boundaries. Grains dissolve at grain boundaries into aqueous pore fluid around highly stressed areas. The high stress at grain to grain contacts makes the material there more soluble. After diffusion of the material through the grain boundary fluid, the material crystallises at areas of relative low stress (*Urai and Spiers*, 2007). Pressure solution is an example of diffusive mass transfer (*Passchier and Trouw*, 2005). Pressure solution happens at moderate temperatures and relatively low strain rates and is more common in bedded salt structures (*Schléder et al.*, 2008).

Dynamic recrystallisation

Recrystallisation describes the process in which grains of a polycrystal evolve in a new structure or new grain shape. Deformed grains are replaced by new grains that nucleate and grow until the old grain is entirely consumed. The main processes involved in dynamic recrystallisation are the migration of grain boundaries (grain boundary migration) and the formation of new high angle grain boundaries. In grain boundary migration low energy grains grow at the expense of high energy grains. When grains are being consumed, dislocation-energy is decreased. This can be seen in a stress drop in the strain/stress curve, measured in the laboratory in halite deformation experiments under wet conditions (*Ter Heege et al.*, 2005; *Urai et al.*, 1986a; *Heege et al.*, 2005).

Recrystallisation is commonly observed in halite and even small amount of water (about 25ppm is enough) can lead to grain boundary migration recrystallisation (*Heege et al.*, 2005). In dry halite sub grain rotation recrystallisation is observed; no, or very little, grain boundary migration recrystallisation can be seen in dry halite samples. Grain boundary migration tends to weaken LPO and texture in halite (*Trimby et al.*, 2000).

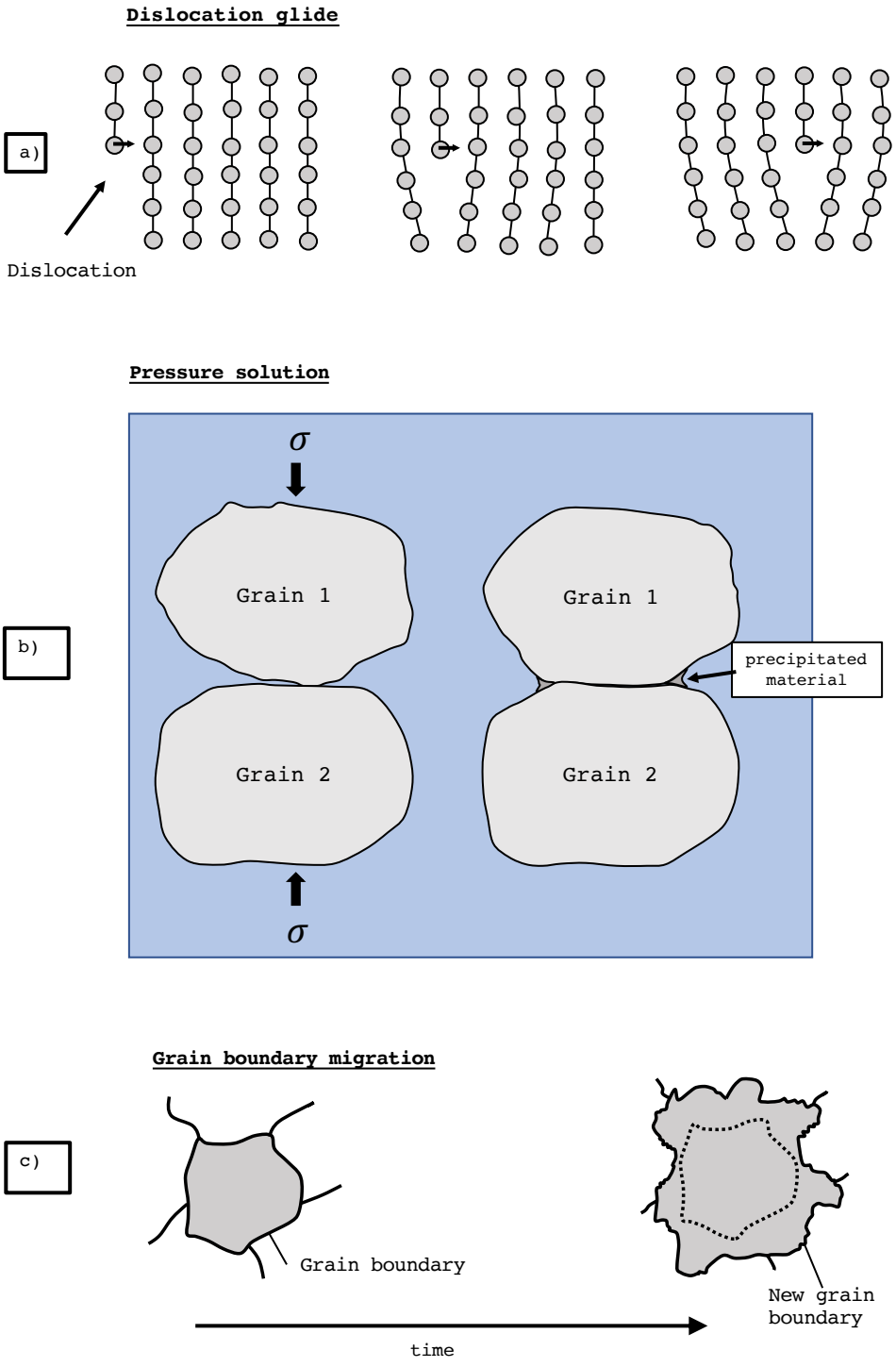

FIGURE 1.2. Schematic description of the main deformation mechanisms observed in halite. (a) Dislocation glide describes the process where a dislocation is gliding along a slip plane. It causes plastic deformation and lattice orientation. (b) In pressure solution material at highly stresses grain to grain boundaries dissolve into pore fluids. (c) In grain boundary migration grains with a low dislocation energy are growing at the expense of high energy grains.

1.2.2 Evidence of texture in rocksalt

Texture evolution of synthetic and natural rock salt has been investigated in previous studies, demonstrating that halite can exhibit significant crystal preferred orientation. Early studies investigated the evolution of LPO of rock salt deformed in the laboratory. *Skrotzki and Welch* (1983) performed extrusion experiments on rock salt for different temperature conditions. The samples showed strong texture at high strains. At high strains recrystallisation accompanied the deformation. *Franssen and Spiers* (1990) deformed dry polycrystalline salt in uniaxial compression and shear in temperature conditions from 250°C to 350°C. The observed microstructure was characterised by strongly deformed grains. In the experiments, rock salt was shown to be weaker in simple shear than in uniaxial compression. Franssen (1994) investigated crystallographic preferred orientation in compression experiments of synthetic rock salt for different temperature regimes (250°C to 780°C). The microstructure in all temperature ranges is characterised by the {110} pole rotating towards the compression direction. *Wenk et al.* (2009) observed strong texture in high strain torsion experiments of polycrystalline halite. The samples were prepared in a way that grain boundary migration was avoided, to focus on deformation by dislocation glide. The study suggest a complex texture evolution with continuously rotating crystal orientation, with increasing shear strain.

Although rarely investigated, rock salt texture of naturally deformed samples can display significant texture. Distinct LPO was observed in halite dominated rock salt specimens from the Winnefield salt dome in Louisiana (*Schwerdtner*, 1968) and the Grand Saline salt dome in Texas (*Muehlberger and Clabaugh*, 1968). Rock salt samples from the Asse Anticline in Germany (*Kern and Richter*, 1985) or rock salt fabrics from a shear zone in the South-Pyrenees (*Miralles et al.*, 2001) also show significant lattice orientation. Texture of pole figures shown in *Miralles et al.* (2001) are displayed in Figure 1.3.

Although halite is the main constituent mineral of rock salt, preferred orientation of other evaporites minerals may also contribute to the effective seismic anisotropy. For example, *Hildyard et al.* (2009a) reported strong crystallographic alignment in a gypsum sample from the Umbria-Marche Apennines of Central Italy. *Vargas-Meleza et al.* (2015) investigated 20 natural evaporite samples from a single diapir province in Nova Scotia considering their mineralogy, microstructure and the related seismic anisotropy, assessed by using ultrasonic velocity measurements. Anhydrite and gypsum dominated samples showed a strong LPO.

In contrast, some natural halite fabrics also show weak lattice orientation (e.g., *Vargas-Meleza et al.*, 2015; *Thiemeyer et al.*, 2016). In such cases the investigated rock salt fabrics perhaps either did not experience strong deformation or, as the authors argue, recrystallisation processes were active in a way that the microstructure was almost completely reset.

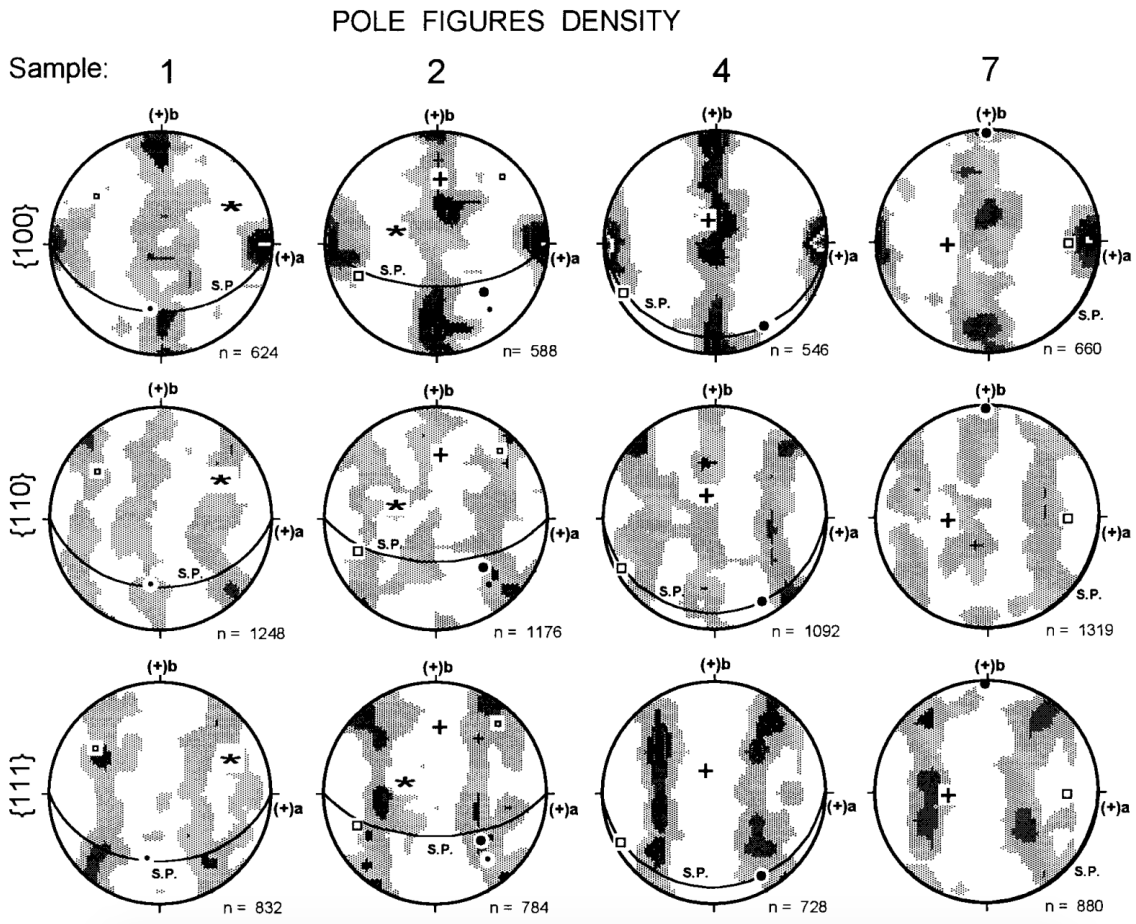

FIGURE 1.3. Figure from *Miralles et al.* (2001). Shown is the texture of four investigated halite dominated rock salt samples from a shear zone in the South-Pyrenees. Projection planes are {100}, {110} and {111}. Data is plotted in lower-hemisphere equal area projection. The shear plane, indicated as S.P., is plotted as a great circle. "The textures show a main maximum quasi parallel to the fold axis and a girdle along the bc plane and perpendicular to the a axis" (*Miralles et al.*, 2001).

1.3 Seismic anisotropy

A common consequence of LPO in minerals is the manifestation of seismic anisotropy. Seismic anisotropy is defined as the directional dependency of the velocity of a seismic wave.

1.3.1 Definition

Seismic wave velocity depends on the elasticity and density of a material. Density is a scalar quantity. The elasticity tensor relates applied stresses and resulting strain in the generalised

Hookes law:

$$\sigma_{ij} = c_{ijkl}\epsilon_{kl}, \tag{1.1}$$

where σ_{ij} is the 3×3 stress tensor, ϵ_{ij} is the 3×3 strain tensor and c_{ijkl} is the fourth rank $3 \times 3 \times 3 \times 3$ elasticity tensor, relating stress and strain. The subscripts $i, j, k, l = 1, 2, 3$ describe Cartesian axes.

The elasticity tensor is not does not only relate stress and strain, it also contains information about elastic waves travelling through material. This is given by the Christoffel equation (*Babuska and Cara*, 1991):

$$\left[M_{ik} - \rho V^2 \delta_{ik}\right] U_k = 0, \tag{1.2}$$

where ρ is the density of the material, V is phase velocity and $\mathbf{U}$ is the displacement vector of a plane wave. δ is the Kronecker delta, and M_{ik}, defined as (*Babuska and Cara*, 1991):

$$M_{ik} = c_{ijkl}\, n_j n_l, \tag{1.3}$$

for a plane wave, where $\mathbf{n}$ is a unit vector in the slowness direction (inverse of the wave velocity) and c_{ijkl} is the stiffness tensor.

Stress-, and strain tensor are symmetric, which reduces the number of independent coefficient of the elasticity tensor to 36. These can be represented conveniently in the Voigt notation as a 6×6 matrix C_{ij}, where

$$ij \rightarrow i,\ kl \rightarrow j, \tag{1.4}$$

and

$$11 \rightarrow 1,\ 22 \rightarrow 2,\ 33 \rightarrow 3,\ 32 = 23 \rightarrow 4,\ 31 = 13 \rightarrow 5,\ 12 = 21 \rightarrow 6. \tag{1.5}$$

The 6×6 C_{ij} is symmetric itself (*Hudson*, 1980; *Babuska and Cara*, 1991), which further reduces the number of independent constants from 36 to 21. Often the symmetry can be reduced further, depending on the properties of the material. Halite has a cubic crystal symmetry and is anisotropic on single crystal scale. Cubic symmetry is given by the elasticity tensor:

$$c_{\mathrm{cubic}} = \begin{pmatrix} C_{11} & C_{12} & C_{12} & 0 & 0 & 0 \\ C_{12} & C_{11} & C_{12} & 0 & 0 & 0 \\ C_{12} & C_{12} & C_{11} & 0 & 0 & 0 \\ 0 & 0 & 0 & C_{44} & 0 & 0 \\ 0 & 0 & 0 & 0 & C_{44} & 0 \\ 0 & 0 & 0 & 0 & 0 & C_{44} \end{pmatrix} \tag{1.6}$$

A common assumed symmetry in analysing seismic wave propagation is transverse isotropy (TI), where the seismic velocity is symmetric about an axis normal to a symmetry plane. Within the plane the seismic velocity is the same and changes with declination from the axis. A special case of TI is VTI (vertical transverse isotropy) and the rotated equivalent HTI (horizontal transverse isotropy). The VTI case is often associated with horizontal layering of rocks, where compression by gravity is the dominant stress field (*Backus*, 1962). A common cause for HTI symmetry in shallow reservoirs is due to preferred alignment of vertical fractures. Seismic velocity is higher parallel to the fractures then perpendicular to them (*Hudson*, 1980). Seismic anisotropy can be caused not only by layering and fracturing, but also by preferred aligned of crystals inside a polycrystal, where each single crystal is seismically anisotropic. A preferred orientation inside the polycrystal would lead to effective seismic anisotropy (*Mainprice et al.*, 2000).

TI is a case of hexagonal symmetry, which has 5 independent elastic constants, describing this style of anisotropy. A formulation of these coefficients are the three Thomsen-parameters δ, ε and γ which are used, along with the vertical S- and P-wave velocities, to describe this form elastic anisotropy (*Thomsen*, 1986). If x_3 is the symmetry axis and the x_1-x_2 is the symmetry plane, then the Thomsen-parameters are defined in the following way:

$$\delta = \frac{1}{2}\frac{(C_{13}+C_{44})^2-(C_{33}+C_{44})^2}{C_{33}(C_{33}-C_{44})},$$

$$\varepsilon = \frac{C_{11}-C_{33}}{2C_{33}}, \tag{1.7}$$

$$\gamma = \frac{C_{66}-C_{44}}{2C_{44}}.$$

The parameters ε and γ describe the fractional difference between the horizontal P- and SH-velocities. δ is not that easy to interpret, as it affects the P- and SV-velocities away from the vertical direction.

1.3.2 Accounting for seismic anisotropy

Seismic anisotropy is observed at various scales, from large scale anisotropy, investigated by global seismology to much smaller scale, which can be measured at samples in laboratories. For a long time, seismic anisotropy was not accounted for in seismic data.

One of the first investigation of seismic anisotropy in the upper mantle, due to the alignment of olivine crystals in the northern Pacific was done by *Hess* (1964) and shows an example of intrinsic anisotropy. Intrinsic anisotropy describes anisotropy due to the internal structure or fabric of rocks. Lattice preferred orientation of crystals is a famous example of such type of anisotropy.

Seismic anisotropy can also arise due to layering of originally isotropic material. *Backus* (1962) showed that a stack of homogeneous, isotropic material can be modelled as a thick anisotropic material.

The interest in seismic anisotropy increased with new exploration concepts, realising that three component shear waves give information about the of rock they traverse, such as possible fracture directions *Crampin* (1985). With these new concepts, together with better acquisition and measurement geometries (for example wide azimuth 3D seismic data), seismic anisotropy began to impact exploration seismology. Today, many seismic processing methods utilise seismic anisotropy, which improved seismic imaging.

Following up on Thomsen's work on anisotropy notation (*Thomsen*, 1986), the discovery of the parameter η, greatly improved characterisation of anisotropy in exploration seismology. η describes the anellipticity of the P-wave phase slowness in VTI media:

$$\eta = \frac{\varepsilon - \delta}{1 + 2\delta}, \tag{1.8}$$

where ε and δ are the described Thomsen parameter. The normal moveout (NMO) describes the effect of distance between a source and a receiver on the resulting arrival time of a seismic reflection. Offset traces must be corrected by this effect. The relationship between the increasing offset and arrival time is, in the isotropic case, hyperbolic. In the presence of anisotropy, the η-parameter describes the effect of non-hyperbolic moveout on the traveltime-offset relationship (*Alkhalifah*, 1997):

$$t^2(x) = t_0 + \frac{x^2}{V_{NMO}^2} - \frac{2\eta x^4}{t_0^2 V_{NMO}^4}, \tag{1.9}$$

where t is the total traveltime, t_0 is the two-way travel time at zero offset and x is the offset. V_{NMO} is the normal moveout velocity. This equation describes the traveltime for a reflections from horizontal interfaces in homogeneous VTI media. The first two term describe the hyperbolic, thus isotropic, part of the normal moveout. The third term describes the influence of anisotropy, which is zero when $\eta = 0$ (*Alkhalifah*, 1997). Thus, η can be determined in seismic reflection traveltime curves.

Another application of seismic anisotropy in exploration seismology is the characterisation of fracture in the subsurface. If the fractures are vertically aligned, they will produce azimuthal anisotropy, where the the amplitude versus offset (AVO) is azimuthally dependent. The concept of AVO can be expanded in AVOA analysis, investigating amplitude variation with offset and azimuth (*Hall et al.*, 2002).

1.3.3 Field scale evidence of seismic anisotropy in evaporites

Although halite is optically isotropic, it is elastically anisotropic at the single crystal level. In this study the maximum shear wave splitting is calculated for the propagation direction that gives the largest difference between the fast- and the slow shear wave. The P-wave anisotropy is defined by the difference between the highest and lowest P-wave velocity, considering all propagation directions. The maximum P-wave anisotropy in percent and the maximum shear wave splitting in percent, respectively are defined by:

$$A_P[\%] = 200 * \frac{V_{P,max} - V_{P,min}}{V_{P,max} + V_{P,min}}, \tag{1.10}$$

$$A_S[\%] = 200 * \frac{V_{S1,max} - V_{S2,min}}{V_{S1,max} + V_{S2,min}}. \tag{1.11}$$

Calculations, based on elastic constants of rock salt give a P-wave anisotropy of 7% and S-wave anisotropy of 14% (*Gebrande*, 1982; *Raymer et al.*, 2000b,a; *Vargas-Meleza et al.*, 2015; *Zong et al.*, 2015). Generally, salt is treated as being seismically isotropic in seismic processing (*Jones and Davison*, 2014). Anisotropy is only incorporated into velocity building of surrounding rock strata (*Yan et al.*, 2016).

A range of studies investigated seismic anisotropy in rock salt. Some of the main studies are summarised in the following. *Raymer et al.* (2000a) investigated seismic anisotropy in a salt body in the Gulf of Mexico using ocean bottom seismic reflection data. Reflection data showed non-hyperbolic moveout, an indication of seismic anisotropy. The anisotropy was described using the Thomsen-parameter δ, which describes the relation between the zero-offset velocity and the normal-moveout velocity (which is the velocity to flatten CMP seismic gathers). The data suggest a significant amount of anisotropy (δ = -0.13).

Planchart (2014) analysed salt anisotropy using a vertical profile dataset (VSP) from the Mansiyah salt formation, located in Saudi Arabia. The dataset consisted of a walk around, walk away and zero offset VSP. The salt body showed azimuthal anisotropy. By comparing seismic velocities at different offsets, the δ-parameter was estimated to be δ = -0.2.

Direct seismic velocity measurements were performed on rocksalt samples from Sifto‚Äôs Goderich Mine, Canada (*Zong et al.*, 2014). The rock salt samples were very pure, mainly consisting of halite (less than 2 % impurities). Ultrasonic measurements show a range in P-wave velocity from 4.44kms^{-1} to 4.76kms^{-1}, with orientation - a P-anisotropy of 6.9%. They explained the velocity change with cubic elastic anisotropy of the halite samples. These studies strongly suggest that despite the general assumption of isotropy, rocksalt can display significant seismic anisotropy.

Despite the described weak LPO in the halite dominated samples analysed in *Vargas-Meleza et al.* (2015), compressional seismic velocities measured in two coarse-grained halite samples show consistently larger values when measured normal to the foliation-plane, explained by long grains aligned preferentially on the foliation plane. Contrary, shear wave velocities showed lower values perpendicular to this fabric. The P-wave anisotropies were 5.82% and 7.28% and S-wave anisotropies were 9.09% and 8.36% in the two measured samples, respectively. Seismic velocities were obtained with the ultrasonic pulse transmission.

1.4 Effect of anisotropy on seismic imaging

Seismic anisotropy can affect seismic processing and accordingly the final depth image. Recent progress made it possible to account for seismic anisotropy in depth imaging, where incorporating anisotropy is limited to VTI, HTI or tilted TTI (*Sena and Toksöz*, 1993; *Anderson et al.*, 1996; *Alkhalifah*, 1997; *Tsvankin et al.*, 2010). Higher symmetry is not regularly used in seismic processing. Anisotropy is incorporated into sediment velocities, and little attempt has been made to build anisotropy into velocity models of the rock salt structure.

Depth imaging with P-wave reflections have been greatly influenced by the parametrisation work of *Thomsen* (1986), especially the P-wave time-processing parameter η (*Alkhalifah and Tsvankin*, 1995). Anisotropic migration gives typically better focus and positioning of seismic reflectors. examples are shown in Figures 1.4 and 1.5 (both taken from *Tsvankin et al.* (2010)).

Figure 1.4 shows the result of anisotropic time processing of a 2D seismic line from offshore West-Africa, where TI anisotropy caused imaging problems. The figure shows the difference between isotropic- and VTI time imaging. The processing sequence included NMO- and DMO (Dip-move out) and poststack migration. When accounting for the non-hyperbolic moveout η, the seismic reflectors are better imaged. η interval values were between $\eta = 0$ and $\eta = 0.2$. The main differences between the isotropic and anisotropic migration are highlighted by the arrows. For example, fault planes could be clearer imaged when using anisotropy.

Figure 1.5 is a comparison between VTI time and depth imaging, both incorporating seismic anisotropy. In prestack depth migration images are even more influenced by anisotropy, because the results of prestack imaging are very sensitive to the velocity model. The depth image was generated by VTI velocity analysis and Kirchhoff prestack depth migration. The depth image helps in interpreting deeper parts of the image, removing false dips. Faults are better focused, and reflectors are better positioned. This example, and also other previous work on anisotropy effects on seismic imaging, as for example (*Alkhalifah et al.*, 1996), suggest that applying isotropic

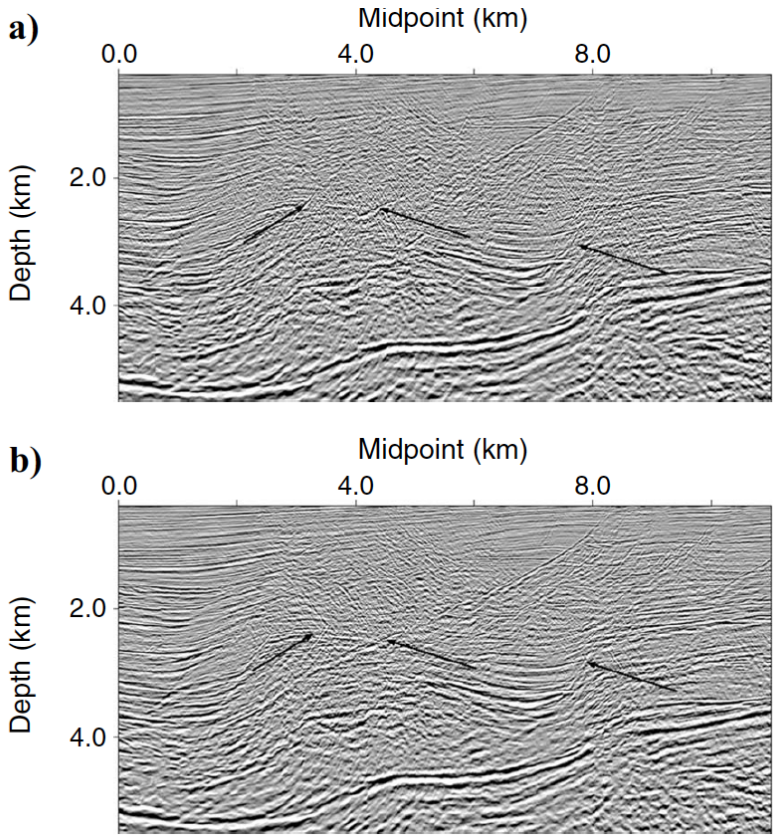

FIGURE 1.4. Comparison between isotropic (a) and anisotropic (b) VTI time imaging of a 2D seismic line in offshore West-Africa, after (*Tsvankin et al.*, 2010). Both sections are stretched to depth. The arrows show the main improvements in the anisotropic time processed image. For example, anisotropic processing could image the fault plane at 7.5km Midpoint and depth of 3km (right arrow). Also, the fault plane from Midpoint 2km to 8km (highlighted by the centre arrow) is better imaged in the anisotropic processed image.

imaging methods is not justified in the presence of anisotropy. The question, how much anisotropy is needed to significantly distort seismic images cannot be answered fall all cases. However, the pictures showed that η ranging from 0 to 0.2 was enough to have a large impact on the seismic image.

1.5 Previous work and aim of this study

This study is motivated by *Raymer et al.* (2000b) who first investigated seismic anisotropy in deforming rock salt. They simulated halite LPO and seismic anisotropy under low temperature conditions for simple deformation regimes (simple shear and axial extension) by the use of dislocation plasticity models. The results show considerable amount of seismic anisotropy (up

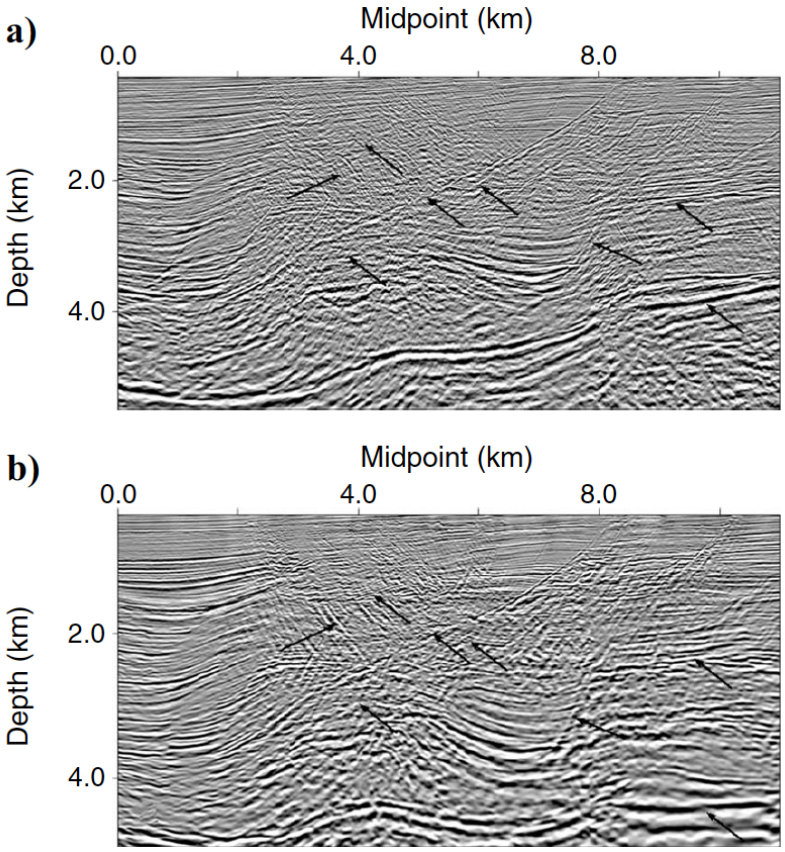

FIGURE 1.5. Comparison between VTI time (a) and depth imaging (b). The seismic line is the same as in Figure 1.5(a) is the image after anisotropic time processing (same as Figure 1.4(b)) and 1.5(b) is the image with anisotropic velocity analysis and prestack depth migration. The arrows point to the main differences in the two sections.

to 4% P-wave anisotropy). However, the deformation regimes as well as the amount of strain were partly arbitrary and no comparison to a seismic dataset were made. This study takes a next step and analyses salt anisotropy by deformation both numerically, and with a seismic VSP dataset. We establish methodology to estimate anisotropy in any deformed salt body, with the use of texture modelling, this work-flow is summarised graphically Figure 1.6.

This thesis is presented in four main chapters, which are structured as followed. First, we motivate the topic further by presenting evidence of salt-anisotropy from a VSP-dataset from the Mahogany salt body (Chapter 2). We simulate halite texture in various deformation regimes and texture modelling input parameters (Chapter 3). After that we develop a work-flow which predicts LPO induced seismic anisotropy in any deformed rock salt body (Chapter 4), which is one of the main outcomes from this thesis. The work-flow is applied to a geomechanical salt deformation model of the Mahogany salt sheet, developed by us, showing that it predicts anisotropy

parameters observed in a VSP-dataset from the same region (Chapter 5).

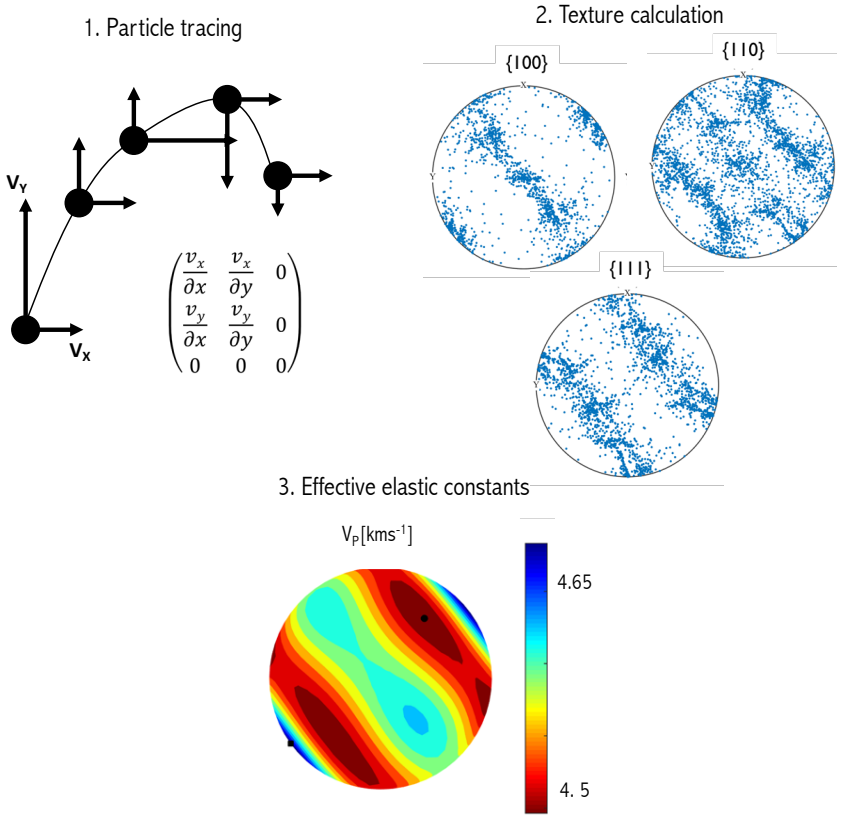

FIGURE 1.6. Workflow summary connecting salt deformation and seismic anisotropy. We track particles through a deformation model and calculate the deformation history of the each particle. Then, LPO is calculated with the use of plasticity models, which uses the deformation history of the salt body. LPO is used in the last step to calculate the elasticities and anisotropy values.

1.6 Thesis outline

This study investigates the possibility of seismic anisotropy in rock salt and how its affecting seismic traveltime, -images and seismic processing. We show that seismic anisotropy in rock salt must be taken into account when treating in seismic data. This thesis has potential high impact on traditional seismic imaging in and around salt bodies. It is presented in four main chapters.

- In chapter two we present evidence that the Mahogany salt body, located in the Northern Gulf of Mexico is seismically anisotropic. Shear-wave splitting data from a vertical seismic profile (VSP) dataset is analysed. The compressional wave, converted to a shear wave at the top of the salt showed clear seismic anisotropy, while the phase converted at the base of

the salt does not show clear splitting results. Different simple seismic models are evaluated to investigate the cause of the seismic anisotropy is caused. These are based on crystal alignment of anhydrite or halite, layering and seismic anisotropy due to water inclusions in the rock salt. Although it is not entirely possible to exclude certain scenarios, we conclude that alignment of halite crystals and water inclusions are the most likely scenarios.

- Chapter three: Motivated by the shear wave splitting observations, and the possibility of aligned halite LPO, we numerically predicts lattice preferred orientation (and the associated seismic anisotropy) of halite polycrystalline aggregates in simple shear and compression, using VPSC (visco-plastic self-consistent modelling approach) modelling. Natural salt deformation is affected by various conditions (e.g., temperature, finite strain, deformation mechanisms and others). We use texture modelling factors to investigate under which conditions seismic anisotropy may arise and which factors control the strength and style of seismic anisotropy. Various critically resolved shear stresses (representing different temperature conditions) and various stress exponent are used to calculate seismic anisotropy and Thomsen-parameters with ongoing strain in simple shear and compression. The results show that generally seismic anisotropy increases under lower temperature conditions and with higher stress exponent. Depending on deformation conditions, the P-wave anisotropy reaches values up 6% and S-wave anisotropy up to 8%. The results show that salt anisotropy is well approximated by VTI-symmetry. Finally, we use seismic raytracing and estimate the impact of seismic anisotropy on imaging. Travel times of an isotropic- and anisotropic salt model are compared. Aligned halite would have significant effect on, for example, depth estimation from seismic sections.

- In chapter four we further investigate the hypothesis of polycrystalline halite aligning due to deformation and generating seismic anisotropy. A numerical work-flow is developed to link salt deformation and associated seismic anisotropy to a geomechanical deformation model. The work flow is adapted from mantle deformation studies, investigating LPO evolution of, e.g., olivine. Passive tracer particles are followed through the model in time, where each particle represents polycrystalline packet of halite which is individually deformed. VPSC is used to simulate deformation-induced seismic anisotropy inside the entire salt body. We demonstrate the work-flow using a simple salt diapir deformation model in 2d. The result show that highly deformed areas show higher seismic anisotropy. We use full-wave form modelling techniques to estimate how much the seismic anisotropy impacts the seismic wavefields in the particular case of the deformed salt diapir. We create a seismic model with a water layer on top and a salt diapir surrounded by isotropic sediments. A synthetic seismic gather is created. The traveltimes of an isotropic and anisotropic salt diapir are compared. Both, The traveltimes and amplitudes of phases interacting with salt show significant difference between the isotropic- and anisotropic model.

- In chapter five we develop a full geomechanical deformation model of the Mahogany salt body (located in the Gulf of Mexico). The Mahogany salt body is deformed effectively as an extruding salt sheet, rafting along the surface. The model is parametrised with typical Gulf of Mexico properties, including the rheology of the salt. The workflow, developed in chapter 4 is applied to the Mahogany deformation model, predicting LPO and the associated seismic anisotropy inside the salt body. The full-wave form modelling software Specfem2d is used to generate a synthetic vertical seismic profile VSP dataset. The synthetic VSP-dataset is processed and analysed in the same way as the real VSP-field data set to calculate shear-wave splitting. Shear wave delay times are compared to field data described in chapter 2. The results show that the synthetic shear wave splitting results match the observed VSP-field data well. Therefore, we can explain the observed shear wave splitting results with alignment of polycrystalline halite.
- In the last chapter I summarise the thesis and the discussions and main conclusions from each chapter. Also, I give a outlook for possible future directions of the work.

All results and interpretations are my own research in cooperation with my supervisors. Comments on chapter three were made by Christopher Spiers and Andrea Tommasi. The deformation models in chapter four and chapter five were built with the help from Rockfield Global and in particular Martin Dutko and Daniel Roberts, who helped during my stay at Rockfield.

CHAPTER 2

SEISMIC ANISOTROPY IN THE MAHOGANY SALT BODY

In this chapter we present evidence that the Mahogany salt body, located in the Northern part of the Gulf of Mexico, is seismically anisotropic. Evidence of anisotropy comes from shear-wave splitting data obtained from a vertical seismic profile dataset. The dataset consists of 48 vertically aligned receivers in a borehole, drilled through the salt body. Shear wave splitting analysis is performed on shear wave phases which are converted from compressional waves at the top- and bottom of the salt body, respectively. The phase converted at the top of the salt layer shows clear sign of seismic anisotropy, while the P- to S converted phase at the base of the salt layer shows less clear evidence of seismic anisotropy. We discuss different proposals to explain the observed seismic anisotropy. For that, simple seismic models are created. We investigate seismic anisotropy due to different scenarios: The presence of anhydrite, layering of halite and shale, water inclusions in the rock salt or preferred alignment of halite crystals. By reflecting all possibilities, we come to the conclusion that seismic anisotropy of the Mahogany salt body due to lattice preferred orientation of the constitutive halite polycrystals is the most likely scenario. However, other possible explanations can not be disregarded entirely but are less convincing. This supports the hypothesis that deformation of salt structures can lead to significant seismic anisotropy and confronts the common assumptions of seismically isotropic salt bodies. This study is valuable not only for the Gulf of Mexico and Mahogany, but also for other areas, where salt is highly deformed.

2.1 Introduction

The Gulf of Mexico is a marginal sea of the Atlantic Ocean, located between the Northern and Southern American continent. It is between the US Gulf Coast states (Texas, Louisiana, Mississippi, Alabama, Florida) in the north and Cuba and Mexico to the south and southwest, respectively. The overall area of the Gulf of Mexico is about 1.6 million km^2.

The Gulf of Mexico hosts a range of industrial applications, most importantly, hydrocarbon production and exploration. It is one of the most productive petroleum basins in the world and the site of major offshore oil production for the United States. In 2018, annual oil production reached a record of 10.96 million barrels oil per day (17% higher than in 2017). United States crude oil production has increased significantly over last the decade and, according to the EIA (US energy information administration), is expected to continue growing in 2019 and 2020, averaging 12.3 million barrels per day and 13.0 million barrels per day, respectively (*US Energy Information Administration*, 2016, 2019). The Gulf of Mexico is characterised by extensive and thick evaporite structures, which have been deposited over millions of years. In some areas the salt layers have a thickness of up to 6 km (*Close et al.*, 2008). Rock salt is an important mineral in creating structural traps for hydrocarbons. Its low viscosity and density mean that it is easily deformable, and it flows under tectonic forces. This leads to the formation of structural traps in the subsurface, where rock salt seals hydrocarbons over geological time scales, as it is impermeable to fluid incursions. Rock salt is responsible for the accumulation of oil and gas in many areas in the world (*Jenyon*, 1986), including the Gulf of Mexico. Figure 2.1 shows the distribution of shallow salt structures across the Northern Gulf of Mexico together with known major faults.

The extensive hydrocarbon industry in the Gulf of Mexico means that it has been intensively studied with geophysics, especially marine reflection seismology. Salt structures in the Gulf of Mexico pose significant technical challenges to hydrocarbon extraction, due to various drilling hazards around, and inside of the salt structure related to stress changes, or pore pressure variations (*Jackson and Hudec*, 2017a). Furthermore, these bodies pose issues for seismic imaging. The complicated 3D geometry of the salt structures, such as steeply dipping salt flanks, requires special effort and computationally expensive techniques in seismic processing (such as pre-stack depth migration) and acquisition (such as wide-, and multi azimuth acquisition (*Jones and Davison*, 2014)). Also, the velocity contrast between the (high velocity) salt and the (low velocity) surrounding sediments complicates the scenario, as most of the seismic energy is not entering the salt structure. The Gulf of Mexico has been subject of several studies to improve seismic imaging in sub-salt settings, including new seismic migration techniques (e.g., reversed time migration, (*Jones and Davison*, 2014)), advanced seismic acquisition and the use of converted phases (e.g., *Kendall et al.*, 1998).

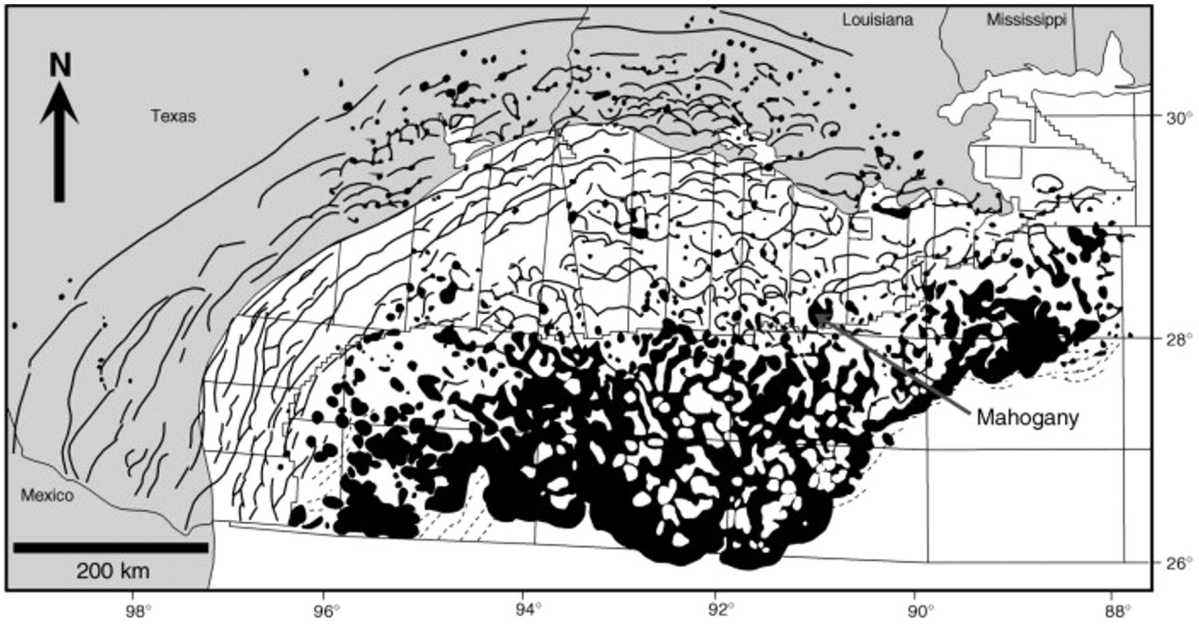

FIGURE 2.1. Map of salt distribution of the Northern Gulf of Mexico. The figure is taken from (*Rowan et al.*, 2001) and has been modified after (*Diegel et al.*, 1995). Shallow salt distribution is shown in black. Faults are shown as black lines. The location of the Mahogany salt body in the North-East is shown and marked inside the figure with the grey arrow.

However, despite recent advances it is still a common assumption to treat rock salt as being seismically isotropic when building velocity models (*Jones and Davison*, 2014). So far, little attempt has been made to consider salt anisotropy, and, therefore, this is a potential study area for future improvement in seismic imaging. Seismic anisotropy describes the dependence of seismic wave velocity on its propagation and polarisation direction. Despite laboratory- and field-scale evidence of seismic anisotropy in rock salt (e.g., *Raymer et al.*, 2000b; *Planchart*, 2014; *Zong et al.*, 2015), it is conventionally treated as being isotropic. In particular the Gulf of Mexico salt is often very pure, with little anhydrite or gypsum inside (e.g., *Fredrich et al.*, 2007; *Zong et al.*, 2017) and is therefore assumed to not show seismic anisotropy (e.g., *Yan et al.*, 2014).

Here, we provide evidence that seismic anisotropy can develop in Gulf of Mexico salt bodies. We present results from a vertical seismic profile (VSP) dataset from the Mahogany salt body, located in the northeast part of the Gulf of Mexico (Figure 2.1). We measure shear wave splitting (e.g., *Crampin*, 1985; *Silver and Chan*, 1991) in downgoing converted (P-S) wave phases from the top and base of the salt. We compare these to infer anisotropic contribution of the rock salt, and conclude that it exhibits significant anisotropy. We test the potential for several mechanisms to be the cause of this anisotropy, and conclude that texturing in halite – the main constitutive

mineral of the salt body – is the most likely explanation.

2.2 Geologic evolution of the Gulf of Mexico

The Gulf of Mexico is known for its large salt deposits and its associated industrial use. It is an exemplary area, which went through extensive tectonic deformation, leading to the formation of various salt sheets and salt diapirs. The tectonics and sedimentation history of the Gulf of Mexico is related to the present hydrocarbon system. Geologic evolution of the area was documented in several studies (*Wilhelm and Ewing*, 1972; *Salvador*, 1991; *Diegel et al.*, 1995; *Hall*, 2001; *Pindell and Kennan*, 2009; *Hudec et al.*, 2013).

Prior Jurassic (before 200 Myrs ago)

The main tectonic events prior to the Jurassic which effect the region were extensional deformation due to the break-up of the super continent Pangaea. The North- and South American plate were drifting apart and during that process, deep rifts begin to form (*Rowan et al.*, 2001). This period lead to stretching of the continental crust (*Dribus et al.*, 2008), and to the creation of grabens, which were filled with volcanic deposits and terrestrial red beds (*Diegel et al.*, 1995). Red beds are reddish coloured sedimentary rocks, such as sandstone, siltstone or shale. Oxidising conditions are commonly observed in dry and hot areas, such as the Gulf of Mexico (*Dribus et al.*, 2008). The Eagle Mills formation in the Northern Gulf of Mexico consists mainly of red beds, dikes and sills. The Eagle Mills formation is a famous geological formation, containing fossils which provide some of the earliest record of the rifting process in the Gulf of Mexico (*Dribus et al.*, 2008).

Jurassic (~ 200 Myrs - 150 Myrs ago)

During the early to mid-Jurassic the Yucatan block began to rotate and separated the South and North American continent (*Dribus et al.*, 2008). The Yucatan block is a major tectonic plate, located in between the North American plate and the Caribbean plate. Changes in sea level combined with thermal activity from ongoing rifting lead to a shallow sea basin. The water influx from the Atlantic Ocean was limited, which lead to high evaporation and increased salinity in the sea water (*Hall*, 2001; *Dribus et al.*, 2008). Thick salt layers were deposited in the shallow margin of the basin. The Louann salt body in the Northern Gulf of Mexico was formed out of the evaporite sediments around that time (*Peel et al.*, 1995; *Hudec et al.*, 2013). The Louann salt is particularly important as it is relevant for petroleum and hydrocarbon systems in the Northern Gulf of Mexico (*Peel et al.*, 1995). The Mahogany salt body was formed from Luan salt deposits. The age of the Louann salt itself is poorly known, as it does not contain any fossils to constrain the date of its formation. The salt age is estimated from the sedimentary strata above and below the salt. The dikes, sills and red beds have been dated as young as 180 Myrs

and overlying formation were deposited in the late Jurassic to early Cretaceous, aged no younger than 156 Myrs (*Salvador*, 1991). Thus, the age of the Louann salt is estimated to about 160 Myrs (*Salvador*, 1991; *Dribus et al.*, 2008).

Cretaceous to Quaternary (~ 150 Myrs ago to present)

After the Jurassic the Yucatan plate continued to drift southwards (*Pindell and Kennan*, 2009). During the early Cretaceous (~100 Myrs ago) the drifting stopped and formed a dormant rift zone, which characterises the Gulf of Mexico today (*Dribus et al.*, 2008). Cretaceous sediments are clastics and carbonates deposited by rivers influx. Most of the source-rocks responsible for the hydrocarbon accumulation were deposited around the late Jurassic/early Cretaceous (*Kennicutt Ii et al.*, 1992). The carbonates were rich in organic material and with heat and pressure associated with burying kerogens and later hydrocarbons were formed. The sedimentation during the Quaternary (2.6 Myrs ago to date) was dominated by terrigeous sediments. Sand and clay erosion have led to thick depositions along the basin (*Salvador*, 1991).

2.2.1 Mahogany salt body

The Mahogany oilfield is located in the North-East of the Gulf of Mexico, in the southern Ship Hoal area (block 349 and 359). Its associated salt body is allochthonous: it originated at a distance from its current location, indicating it underwent intensive deformation. The Mahogany salt body now extends about 30 km in North-South direction and about 15 km in East-West direction. The location and the geometry are shown in Figure 2.2. A cross section of the Mahogany salt body is shown in Figure 2.3.

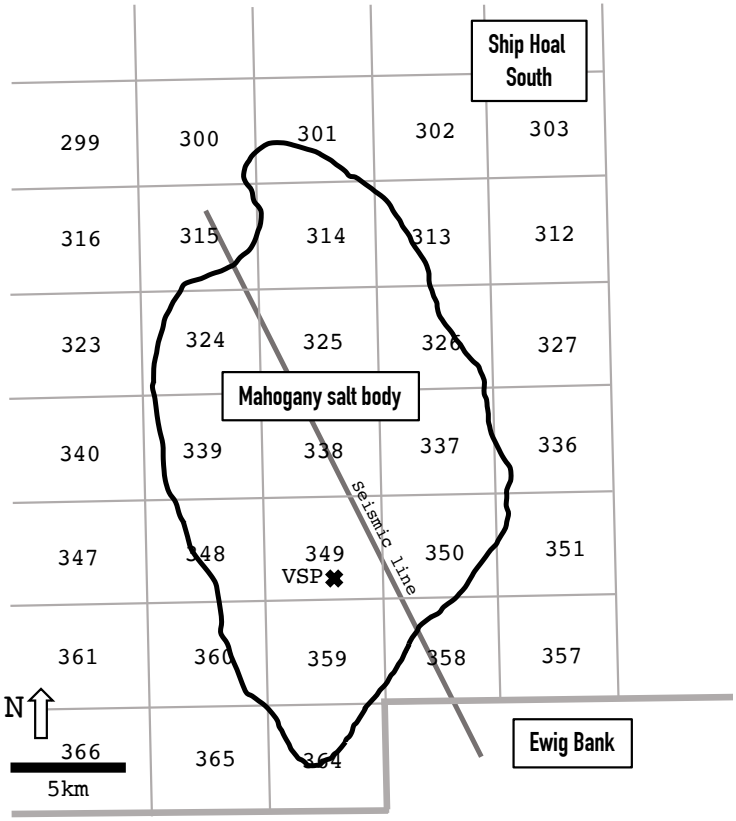

FIGURE 2.2. Location and dimension of the Mahogany salt body is shown. The figure is modified from *Rowan et al.* (2001). The Mahogany salt body is located in the South Ship Hoal area. The VSP well is at the South of Ship Hoal block 349. The seismic data from this VSP is presented in this chapter. The Mahogany salt body have a dimension of about 15 km in East-West direction and about 30 km in North-South direction. The seismic line was used for seismic restoration, performed by *Rowan et al.* (2001). A cross section along this line is shown in Figure 2.3.

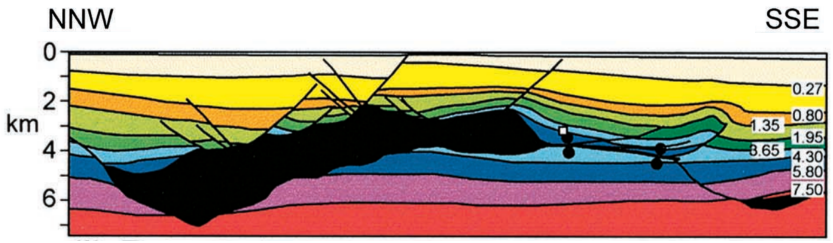

FIGURE 2.3. 2D Cross section of the Mahogany salt body. The cross section was generated by seismic restoration along the seismic line shown in Figure 2.2. Left-hand side is north-northwest, the right-hand side south-southeast of the seismic line. Salt is shown in black. Sequential restoration of the 0.27 Myrs, 0.8 Myrs 1.35 Myrs, 1.95 Myrs, 3.36 Myrs, 4.3 Myrs, 5.8 Myrs and 7.5 Myrs interpreted horizons are shown. The picture is modified from *Rowan et al.* (2001).

Mahogany was discovered 1993 by the companies Phillips, Anadarko and Amoco (*Weimer et al.*, 1998; *Rowan et al.*, 2001; *Harrison et al.*, 2010). After more investigations and three years later in 1996, Mahogany became the first commercially employed sub-salt oil production of the Gulf of Mexico (*Dribus et al.*, 2008). The field is a faulted anticline, forming a stratigraphic structural trap overlain by allochthonous salt (*Camp*, 1998; *Harrison et al.*, 2010).

The Mahogany salt body was deformed as a salt sheet, formed from the Louan salt evaporite sediments deposited during the Jurassic. The sub-salt reservoir is a highly pressured oil-saturated sand with high permeability and porosity, which dated around the upper Miocene (20 Mrys to 5 Myrs) (*Rowan et al.*, 2001). The reservoir is below the large Mahogany salt sheet that converges with other salt sheets neighbouring the salt body. Gross thickness of the oil-paying reservoir strata ranges from 30 m to 107 m, below an approximately 1160 m thick salt layer (*Camp*, 1998). The large salt sheets pose significant challenges for seismic imaging required to exploit the oil- and gas discoveries. The salt has moved and is being deformed over geological time scales. Understanding the complex geology in this area is important for the exploration, as the geology has direct influence on the hydrocarbon system.

2.3 VSP data set

2.3.1 Geometry

The seismic data presented in this chapter is obtained from a vertical seismic profile (VSP) dataset located in the Mahogany oil field, in the South of Ship Hoal block 349, close to the South end of the associated salt body. The location of the VSP inside Mahogany is shown in a 2D map view in Figure 2.2. The Mahogany oilfield has multiple subsalt wells, but here we focus on the seismic data from a single sub salt bore-well.

The 3-component receivers of the VSP are aligned inside the subsalt well. The source is a single far-offset source. It is located in North-East direction from the borehole. The VSP consist of 48 receivers, with a spacing of 15 m between each receiver, so a total receiver layout of 720 m is covered. The receivers are 3-component receivers. The borehole is drilled vertically down through the entire salt body. The upper 10 receivers are in the salt and the lower 38 receivers are located in the shale beneath the rock salt layer. The first receiver is at a depth of about 3536 m, the last receiver about 720 m beneath. Figure 2.4 shows a schematic picture of the geometry and setup of the VSP. Because of the far-offset source, strong wave conversions are seen from the top and from the base of the salt. This is a good geometry for studying anisotropy in the salt body: the far-offset VSP provides long travel paths through the salt (providing the opportunity to accrue anisotropic effects) while the one-way nature of the propagation reduces possible attenuation problems. The traveltimes should also not be strongly affected by invaded zones due to drilling processes near the borehole. We measure shear wave splitting in P-S conversions at both the top and base of the salt. This allows us to study seismic anisotropy in the salt body itself, without being contaminated by anisotropy in either the over- or underlying sediments.

2.3.2 Data preparation

The data discussed here was originally presented, processed and analysed by *Kendall and Raymer* (1999). The data was processed to isolate (as best as possible) downgoing shear wave energy. The up- and downgoing P- and S-wave arrivals were identified in the data, and the wavefields were separated using a fk-filter (e.g., *Christie et al.*, 1983; *Sheriff and Geldart*, 1995). In the fk-domain, the various down- and upgoing wave modes are easier to separate. Extraneous arrivals were then removed by the use of the fk-filter. Finally, the data were then restored to its original position (*Kendall and Raymer*, 1999). This is the format we received the data in, no access was possible to the original raw data. Although the data looked promising, it showed contradictory results with very high delay times (*Kendall and Raymer*, 1999). Furthermore, the methodology uses to obtain the results was not documented. Here, we revisit these data, and use up to date, robust analysis methods for measuring seismic anisotropy and shear wave splitting (*Wuestefeld et al.*, 2010).

The final, filtered VSP-data is shown in Figure 2.5. The X- (transverse) and Y-components (radial) are shown in red and blue, respectively. Both PS-phases, on which the shear wave splitting measurements are performed, are highlighted. The phases were picked by hand. Our aim is to analyse seismic anisotropy in the salt: The PS top-salt conversion will show shear wave splitting associated with both the rock salt and layers below. The PS base-salt conversion should only be affected by anisotropy beneath the salt. Thus, the difference should constrain the splitting associated with the salt body.

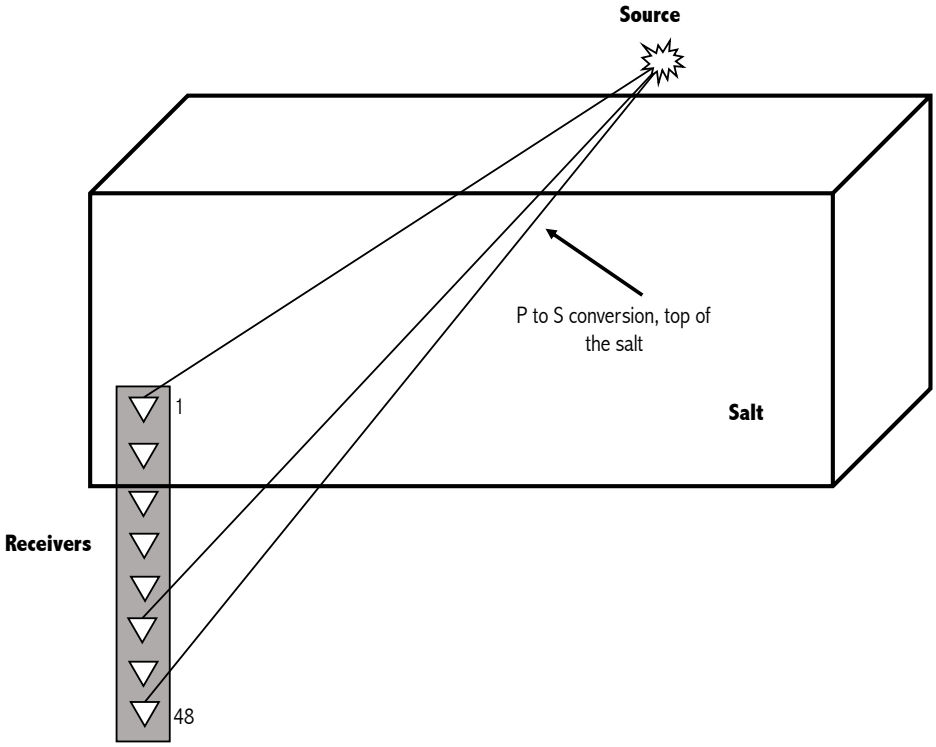

FIGURE 2.4. Schematic overview of the VSP measurement geometry. The source is located northeast from the borehole, where 48 receivers are vertically aligned, with a receiver spacing of 15 m. We use the P- to S converted phases at the top of the salt to investigate for seismic anisotropy arising from the salt layer. Receiver 1 is at the top of the borehole and receiver 48 is the last receiver at the bottom of the well. Receiver number 1 to 10 are in the salt, while 11 to 48 are beneath the Mahogany salt body.

The deeper the receiver, the longer is the travel time. The salt/sediment boundary is located around receiver 10-11. The phases arrive with a larger time delay between each other at receivers 11-48, indicating a lower velocity. Receivers 1-10 are located within the high-velocity salt. We use shear wave splitting (e.g., *Silver and Chan*, 1991) as a technique to validate seismic anisotropy in the investigated salt body.

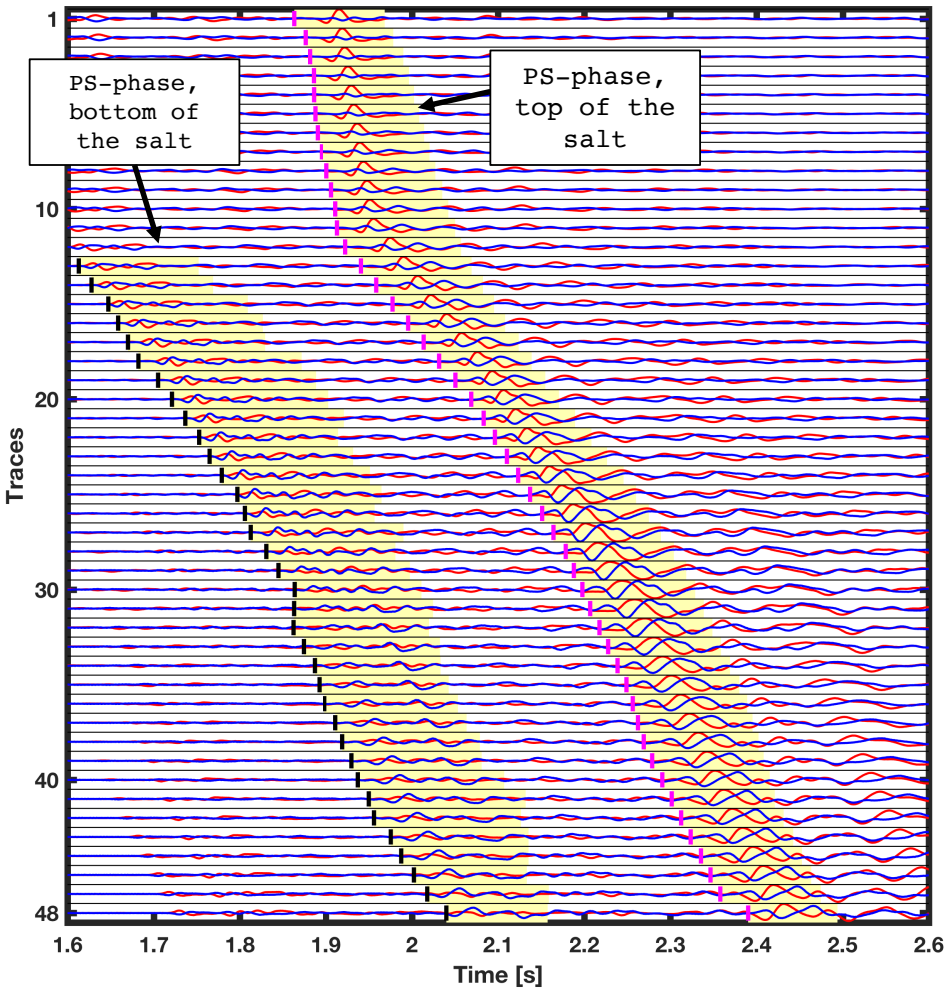

FIGURE 2.5. Displayed is the filtered VSP data for all 48 receivers, where receiver 1 is at the top and receiver 48 is at the bottom. The X- (radial) and Y-component (transverse) are shown in red and blue, respectively, for each receiver. The receivers, which are within the salt (traces 1-10) show higher velocities than the receivers outside of the salt (traces 11-48). The picked PS-phases, converted at the top of the salt and bottom of the salt are highlighted for each receiver.

2.3.3 Shear wave splitting measurements

We estimate splitting parameters (time delay dt and fast shear wave polarisation Φ) for the VSP field data set on all traces. The angle of fast shear wave polarisation is measured in degrees is the clockwise angle from the direction of the radial component when looking along the downgoing vertical (Z-component) towards the origin (Figure 2.6). This measurement has a 180^o ambiguity. We perform shear wave splitting analysis on two phases: The P- to S converted wave at the top of

the salt body and the P- to S converted wave at the base of the Mahogany salt body. Thus, we can identify seismic anisotropy originating from the rock salt.

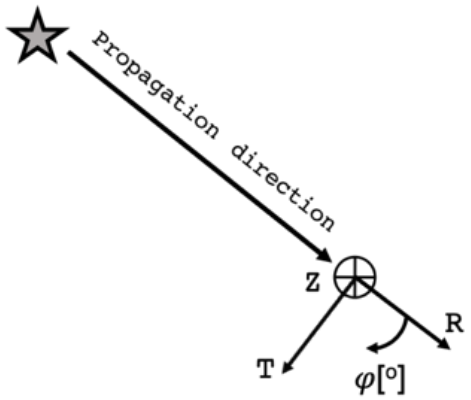

FIGURE 2.6. Radial- and Transverse direction and the angle of the fast shear wave direction. It is measured clockwise in degrees from Radial component, when looking along the downgoing Z-direction.

We perform shear wave splitting measurements with the splitting software SHEBA (*Wuestefeld et al.*, 2010), which is built on the seismic analysis code (SAC) platform (*Helffrich et al.*, 2013). The traces are initially in the transverse and radial component reference frame. Rotation into ray frame was performed, by assuming the incidence angles. The incidence angles are estimated using Snells law according to Figure 2.7 for an incoming wave front separated by a time difference Δt and a receiver spacing Δs (*Shearer*, 2019). The incidence angle θ is then in this case:

$$sin(\theta) = \frac{\Delta s}{\Delta x} = \frac{\Delta s}{V_S \cdot \Delta t}, \tag{2.1}$$

where we assume a salt velocity $V_S = 3.0 kms^{-1}$. The gradient $\frac{\Delta s}{\Delta t}$ was determined over all salt and shale incoming waves. The arrival times and the approximate gradient is shown in Fig. 2.8. However, the estimation of incidence angle is only approximate and therefore the traces will be in approximately ray frame.

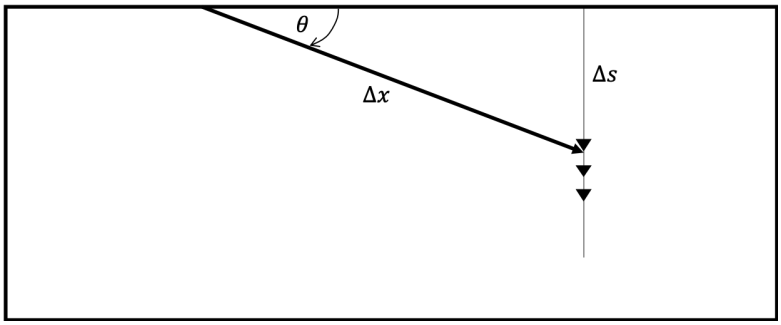

FIGURE 2.7. Estimation of the incidence angle from an incoming wavefront using Snells law. The picture is modified after *Shearer* (2019) for a VSP setup. Using Snells law (Equation 2.1), we can estimate incidence angle.

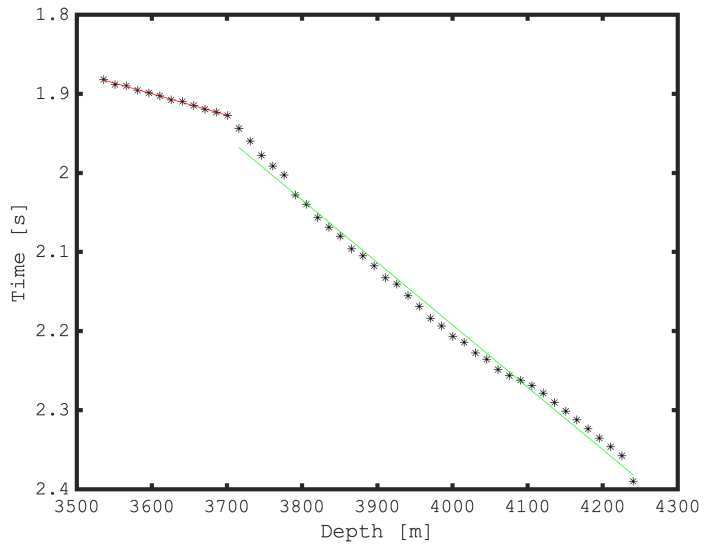

FIGURE 2.8. Picked arrival times and associated gradient for the shale (red) and salt (green). The incidence angle is then estimated according to Equation 2.1.

The receivers show the P-SV energy on the radial component and the SH energy on the transverse component, respectively. The shear wave splitting window is picked around the PS-phase on both analysed phases. The splitting parameters are found by rotating the components into fast- and slow-direction, using the eigenvalue- and cross correlation method (e.g., *Wuestefeld and Bokelmann*, 2007). For each measurement, the best splitting results are found from 100 candidate windows. Splitting parameters are estimated for all the 48 receivers on the P- to S converted phase at both boundaries. We also estimate Q, the shear-wave splitting quality (*Teanby et al.*, 2004; *Wuestefeld and Bokelmann*, 2007)). This allows us to assess the robustness of the result.

2.4 Results

Example shear wave splitting measurements are shown in Figure 2.9 and Figure 2.10. They show the shear wave splitting results from the PS-converted phase at the top of the salt (Figure 2.9) and bottom of the salt (Figure 2.10) recorded at receiver 37 (beneath the salt). The splitting results from the top-converted PS-phase shows a clear result with a high degree of confidence in the estimated splitting parameters. The bottom converted PS-phase shows a smaller delay time than the top converted phase, and generally a less convincing quality in the estimated splitting parameter ($Q = 0.85$ compared to $Q = 0.0$).

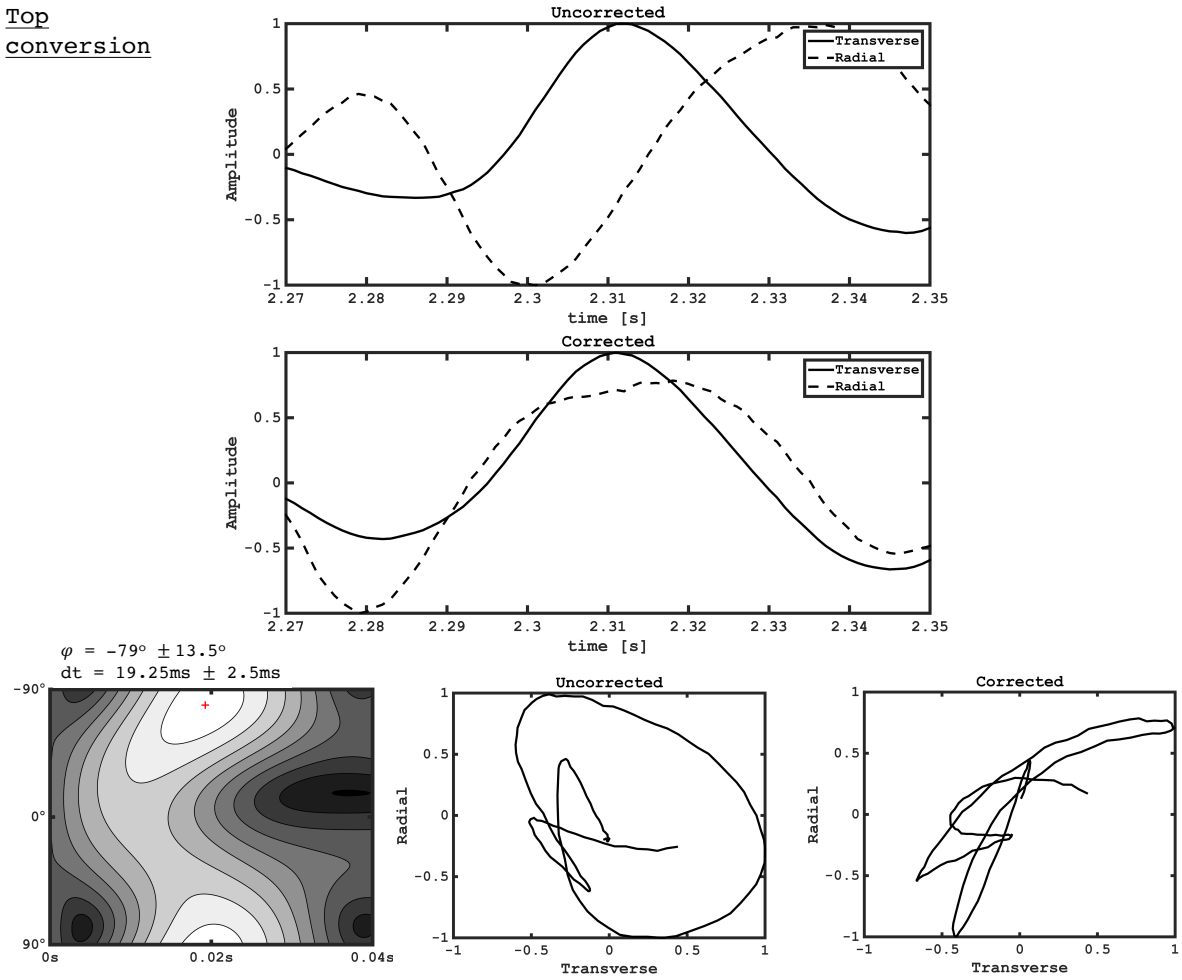

FIGURE 2.9. Sample shear wave splitting results from receiver 37 from the PS-top converted wave. Shown are the uncorrected and the corrected traces and the related particle motion. In the uncorrected case, the traces are separated by a time delay dt and the particle motion is elliptic. In the corrected case, the traces do not show a time delay and the particle motion is linear, because the splitting is removed, and energy is only polarised in one direction. The error-surface of the eigenvalue-method is shown.

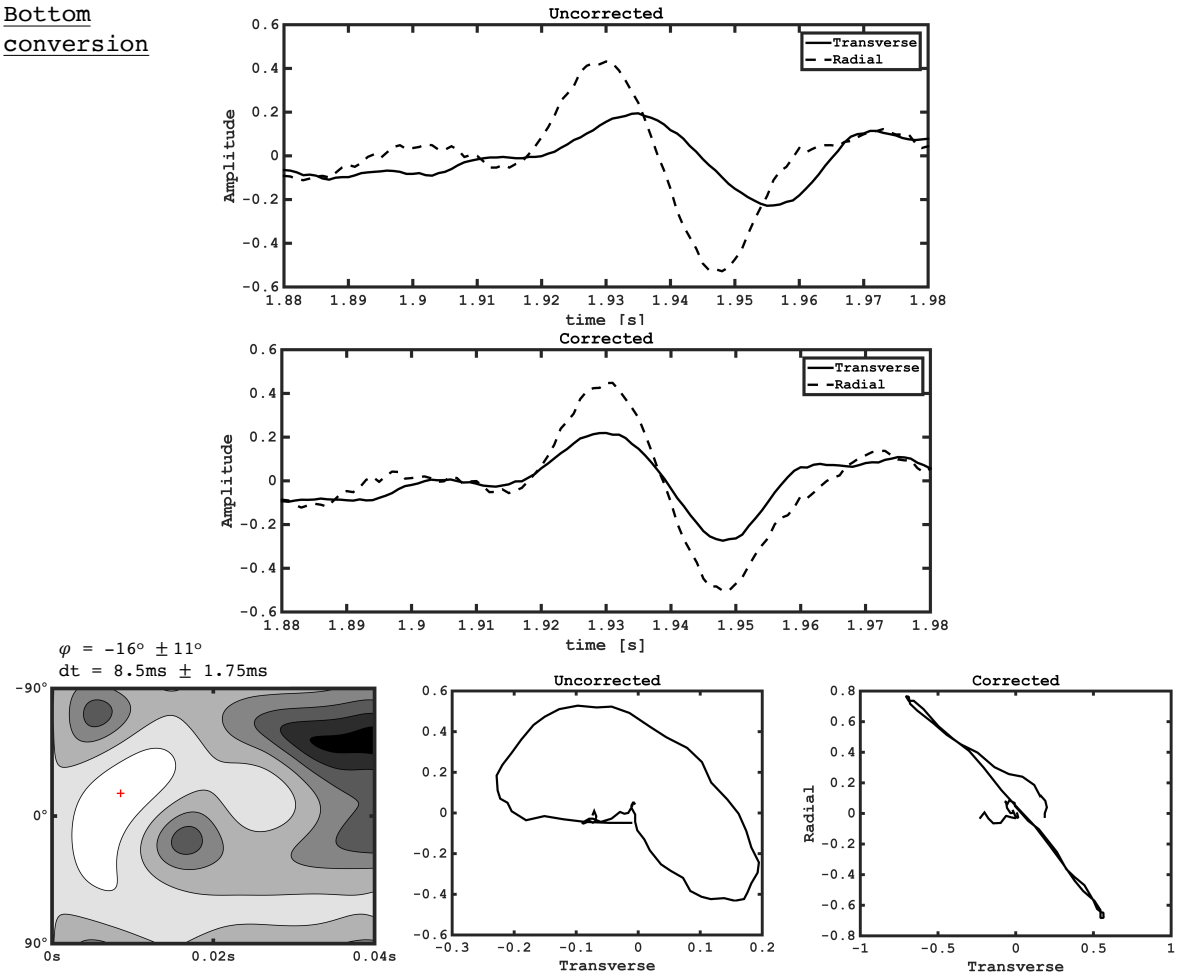

FIGURE 2.10. Sample shear wave splitting results from receiver 37 from the PS-bottom converted wave (same receiver as in Figure 2.9). Shown are the uncorrected and the corrected traces and the related particle motion. In the uncorrected case, the traces are separated by a time delay dt and the particle motion is elliptic. In the corrected case, the traces do not show a time delay and the particle motion is linear, because the splitting is removed, and energy is only polarised in one direction. The error-surface of the eigenvalue is shown.

2.4.1 PS-conversion - top of the salt

Shear wave splitting results (time delay dt and the fast shear wave polarisation Φ) for the top-salt conversion are shown in Figure 2.11. The error bars indicate the 95% confidence level in each measurement. The quality-parameter (Q) is represented by the colour (blue to yellow), which ranges from -1 (clear null) over 0 (ambiguous) to +1 (clear splitting) (*Teanby et al.*, 2004; *Wuestefeld and Bokelmann*, 2007; *Wuestefeld et al.*, 2010).

The delay time shows a steady increase in delay time from receiver 1 to receiver 10. The delay times on those receivers are small (around 6 ms). After receiver 11, the delay times increase drastically to about 35 ms at receiver 13 to 16. At receiver 17 to 20 the delay decreases again to around 20 ms. The receivers 21 to 48 show stable delay times, with just slightly increasing delay times from receiver 25 (16 ms) to receiver 35 (20 ms).

Receiver 13-16 show very high delay times. As these receivers are just beneath the salt/underburden boundary they might be contaminated by other phases than the P to S-converted phase from the top of the salt. For example, we can expect a degree of S-P phase conversion at the base salt, which might not be entirely removed by the applied fk-filter. The delay times at these receivers around this depth range also have significantly higher errors and lower Q-values. These are indicated by the red region in Figure 2.11.

If we discount these results the delay time generally increases with depth within the salt and remains approximately stable at around 20 ms below. The best constrained results are from the receivers which are outside of the salt (Receiver 32-48). These have a constantly high quality, low error and give similar and consistent delay times.

Fast shear wave polarisations range between ~ 60^o to 130^o, indicating an approximately SH-polarised fast shear wave. This is displayed in Figure 2.12 as a rose plot from -90^o to +90^o, taking into account the ambiguity of the shear wave splitting measurements. This would correspond in the simplest case to a VTI-medium, though we cannot constrain this with a single data azimuth. Constraint in the polarisations follow a pattern similar to the delay times, with the best results being from the receivers 19 and below.

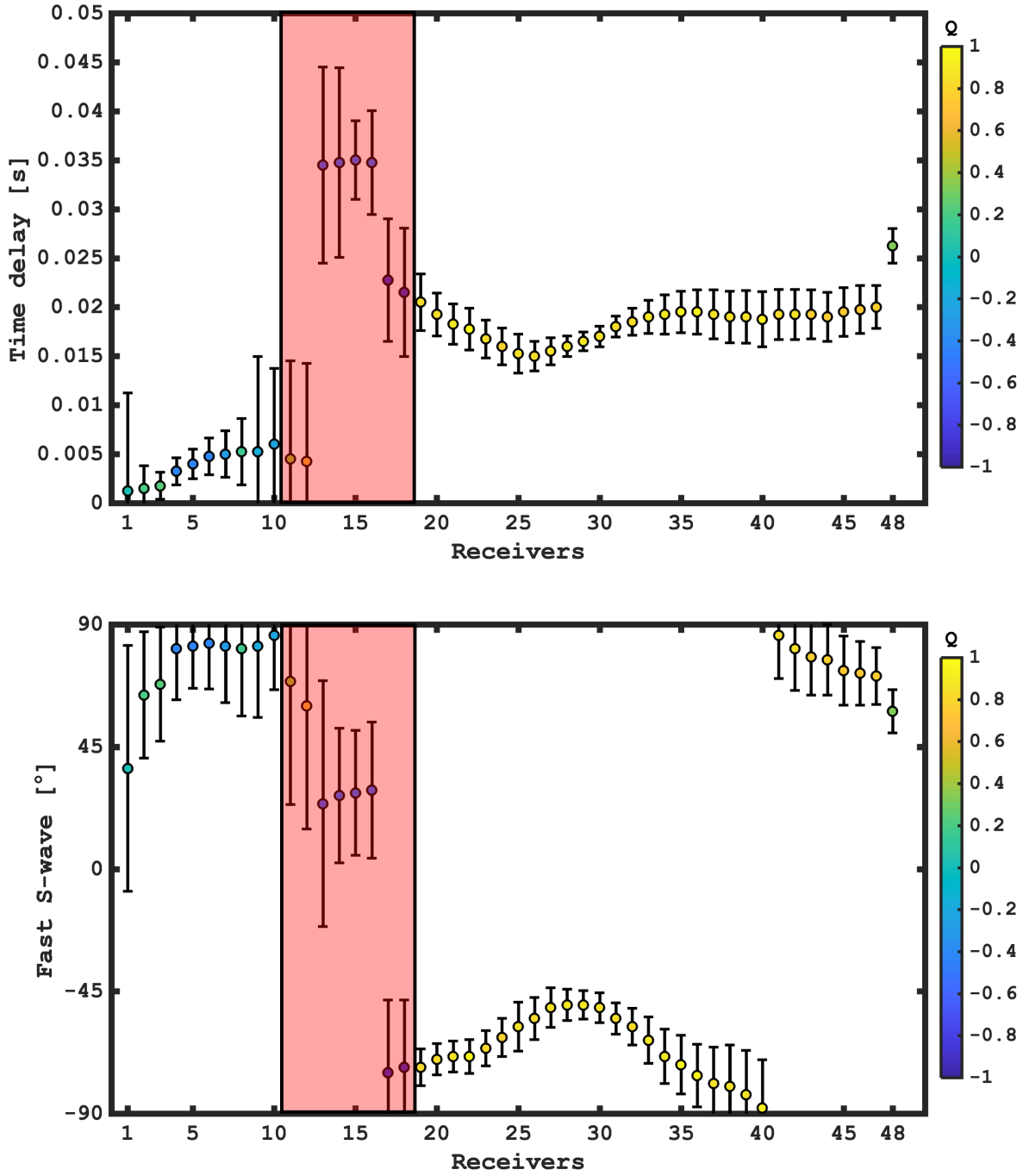

FIGURE 2.11. Shear wave splitting results from the VSP data set from the PS-top converted phase. Time delay (top) and fast shear wave polarisation direction (bottom) measured at all receiver signals, together with the 95% confidence interval error bar. The best results are found for receivers below the salt, with distance to the salt/sediment boundary. The colour represents the quality-value and therefore the credibility of the results. Receiver 11 to 19 show high errors and are marked with a red box.

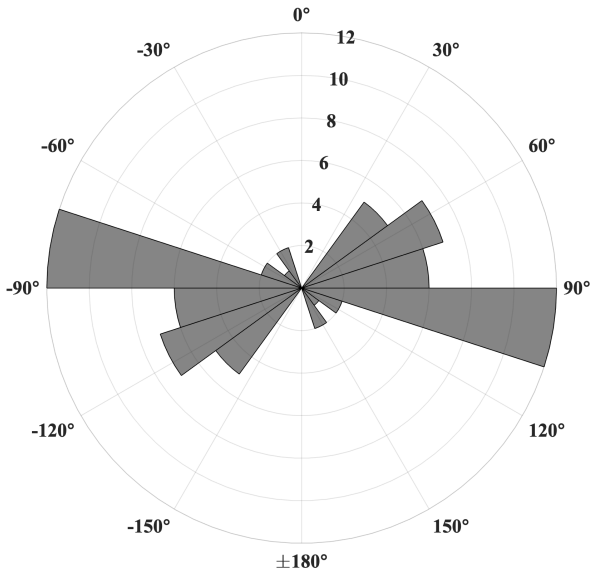

FIGURE 2.12. Rose diagram of the fast shear wave polarisation for the top-salt conversion at all receivers. The majority of results are around ±90°, indicating that SH polarised shear waves travel predominantly faster than SV polarised waves. In the simplest case this would correspond to a simple VTI medium.

2.4.2 PS-conversion - bottom of the salt

The P-wave converted to a S-wave at the bottom of the salt layer can also be identified in the data. This phase should be insensitive to seismic anisotropy within the salt body. We analyse this phase from receiver 15 onwards (Figure 2.4). The bottom converted phase arrives before the top converted phase. An example shear wave splitting analysis for this phase at receiver 37 is shown in Figure 2.10.

Shear wave splitting results for receiver 15-48 are shown in Figure 2.9. The time delays from receiver 15-29 show clear splitting results, although the time delay is small (~4-8 ms). Receivers 30-48 show poorly constrained measurements, with predominantly negative Q values. The fast shear wave polarisation is relatively stable, around 0°. That indicates that the fast shear wave is polarised in the vertical-radial (SV) plane, approximately perpendicular to the splitting in the top-salt conversion. A vertical fast shear wave polarisation can be associated with, for example, vertical fracturing (*Crampin*, 1985; *Baird et al.*, 2017).

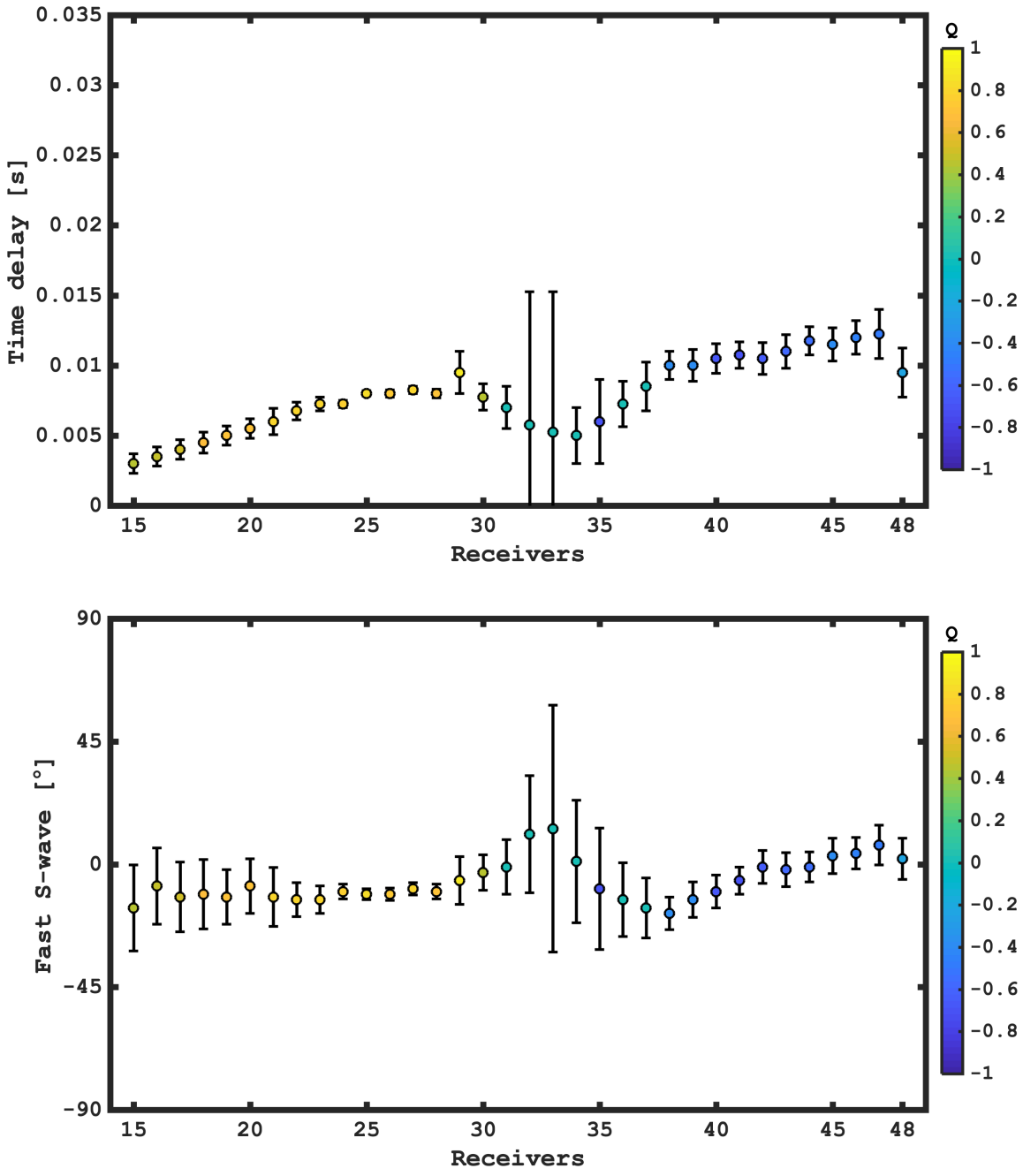

FIGURE 2.13. Shear wave splitting results from the PS-bottom converted phase. Time delay (top) and fast shear wave polarisation direction (bottom) measured at receiver 14-48 for the PS-converted phase at the bottom of the salt. The colour represents the Q-value (-1: no splitting, +1:splitting). The data shows lower delay times and less clear evidence for seismic anisotropy outside of the salt layer, compared to the PS-top converted phase.

2.5 Discussion

As shown above, both top- and base-salt PS-conversions recorded for the Mahogany VSP dataset show splitting. The top-salt conversion shows considerably more splitting than the base-salt at all depths. Figure 2.14 shows the splitting delay time of the top- and base PS conversions for all receivers. These results make it clear that there is significant seismic anisotropy within the Mahogany salt body. The delay time results suggest that the salt layer is seismically anisotropic. Furthermore, for the top-salt conversion, the increasing delay time with receiver depth, and stable results for receivers beneath the salt indicate that the anisotropy is higher near the bottom of the salt body. This is consistent with deformation-induced seismic anisotropy, as we would expect stronger anisotropy at the bottom of the salt sheet, as they are often rafting along the surface with higher expected strain at the bottom of the salt sheet (*Jackson and Hudec*, 2017b).

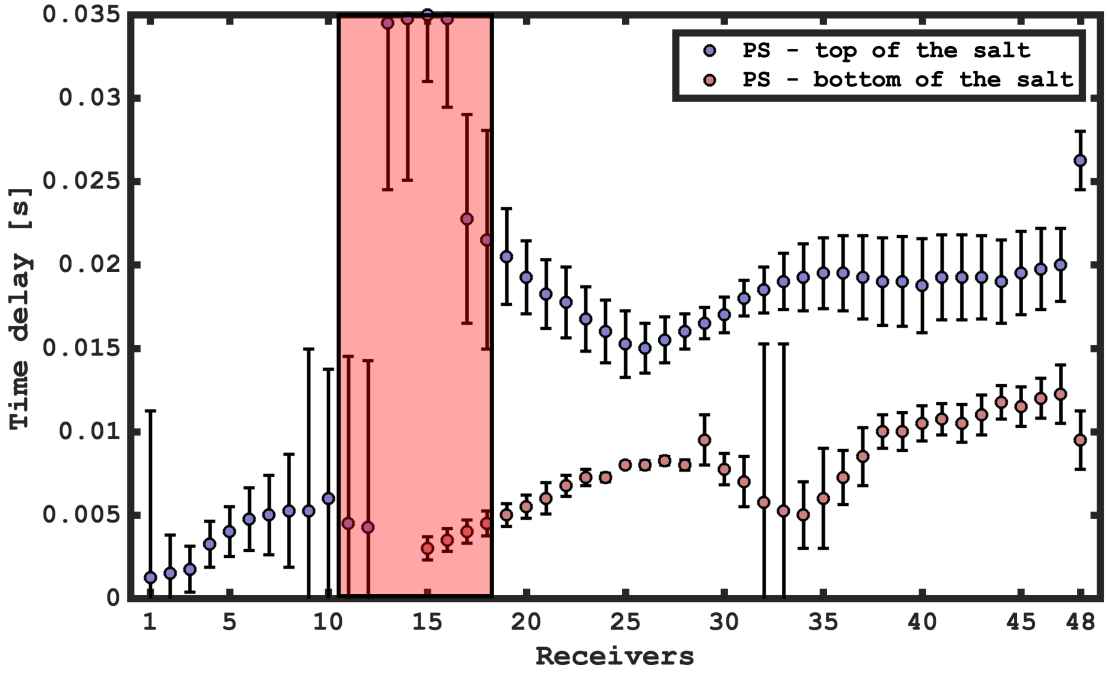

FIGURE 2.14. Comparison of the delay times from the P- to S-converted phase at the top of the salt layer (shown in blue) and the bottom of the salt layer (shown in red). The top converted phase shows significantly higher delay times than the bottom converted phase. This indicates clear seismic anisotropy in the salt layer.

There are several mechanisms by which this seismic anisotropy could arise. The first class is due to the lattice-preferred orientation of the constituent minerals of the salt body, including anhydrite or halite. The second is a shape-preferred orientation of larger inhomogeneities such as layers or water inclusions which have different elastic properties to the host rock. We explore

these possibilities further below. In following we focus on the measured time delay dt. The fast shear wave polarisation does not discriminate between the proposed models, as mainly all models would predict a horizontal fast shear wave polarisation, agreeing with measured fast orientation in the splitting data. Therefore, we focus on the time delay to discriminate which scenario is best explaining the splitting results.

A simple raytracing model is created, to distinguish better if the change in delay time results from the change in traveltime or change of incidence angle. The model is a 3-layered model, as shown in figure 2.15. It is a highly simplified version of the VSP field data setup, where isotropic velocities were assumed. We trace P-S phases, converted at the top of the salt. For raytracing we used the Matlab toolbox ATRAK. The receiver depths are the same as in the VSP dataset, also the thickness of the salt. The rays are traced to the very top and very bottom receiver and their raypath and incidence angles through salt of the two rays are compared. The bottom receiver shows a salt path length of 2130 m and an incidence angle of 45° (measured clockwise from horizontal to the raypath). The top receiver has a travelpath of 2088 m through the salt and a incidence angle of 39°. The travelpath through the salt is very similar for both receivers. Even though the incidence angle is also close to each other, its change is more likely to explain the splitting results. The path effect is a less likely candidate for the change of delay time with receiver depth. However, both, change in incidence angle and change in travelpath will act together. Also, the model, and the assumed parameters, will be different from what we see in the real Mahogany salt sheet. Therefore, this simple numerical model suggest that the change in incidence is the cause of the delay time change with receiver depth.

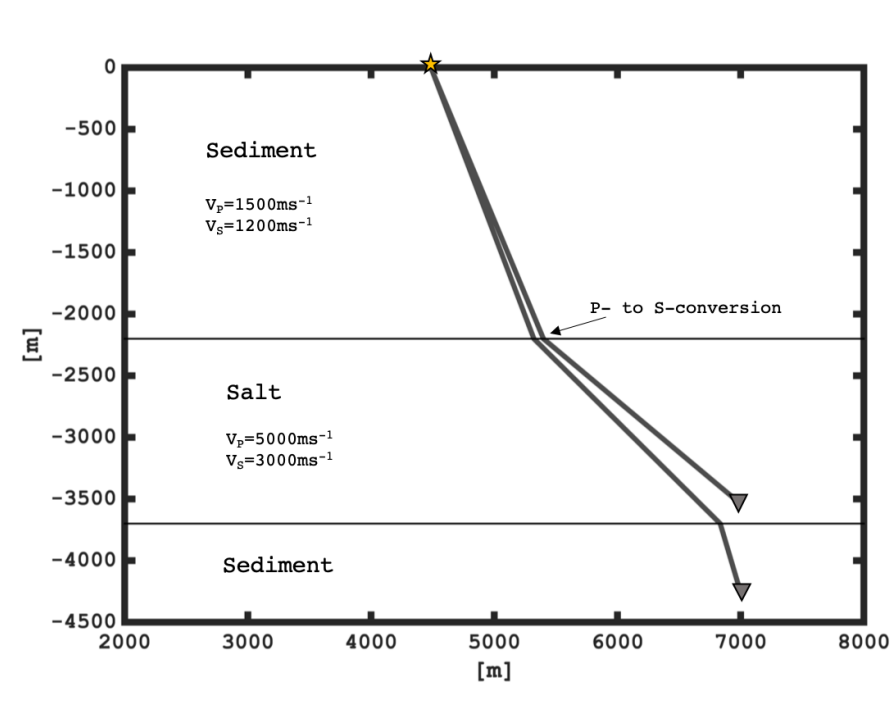

FIGURE 2.15. Simple 3-layed raytracing model, representing the VSP data setup (receiver depths, layer thickness and velocities). Rays are traced to the very top receiver and the very bottom receiver, the take off angle are chosen match approximately match the observed traveltimes. The difference in incidence angle of the ray travelling through the salt change more significantly between the two receivers then the travelpath through the salt. This simple model suggest that the incidence angle is more likely to be the reason to the change of delay time with receiver depth.

2.5.1 Alignment of halite polycrystals

Halite – the main constituent mineral of rocksalt – has a cubic crystal structure and is seismically anisotropic on single crystal scale (e.g., *Wenk et al.*, 1989). Thus, if the constituent halite crystals of a rock salt layer are aligned due to deformation a salt layer will manifest seismic anisotropy. If we assume that all halite crystals are perfectly aligned, and the salt layer consistent solely of halite, the seismic velocities of the salt would correspond to the velocities displayed from a single halite crystal. The single elastic properties of halite are well constrained (*Gebrande*, 1982), with a maximum S-wave anisotropy of 14% (Figure 2.16). This occurs at 45^o angle of incidence and azimuth (parallel to {111}); along the {100}, {010} and {001} axes the S-wave anisotropy is zero.

We calculate the delay time between the fast and slow shear wave, travelling through a single crystal halite layer with 1 km travelpath, as a function of the incidence angle, defined as the angle in degrees clockwise from horizontal to the ray direction. The measured delay time from the VSP

data set (with an inferred incidence angle of 30^o-40^o) can comfortably be explained with crystal alignment of halite polycrystals. The single crystal model over predicts the seismic anisotropy (about 40 ms compared to 20 ms), however in nature complete crystal alignment is not expected. Further evaluating whether a halite texture could be responsible for the splitting requires both a plausible model of strain in the Mahogany salt body, and more sophisticated modelling of the development of a polycrystalline fabric. However, this simple model setup does predict delay times similar to those observed in the VSP data set from the Mahogany salt body.

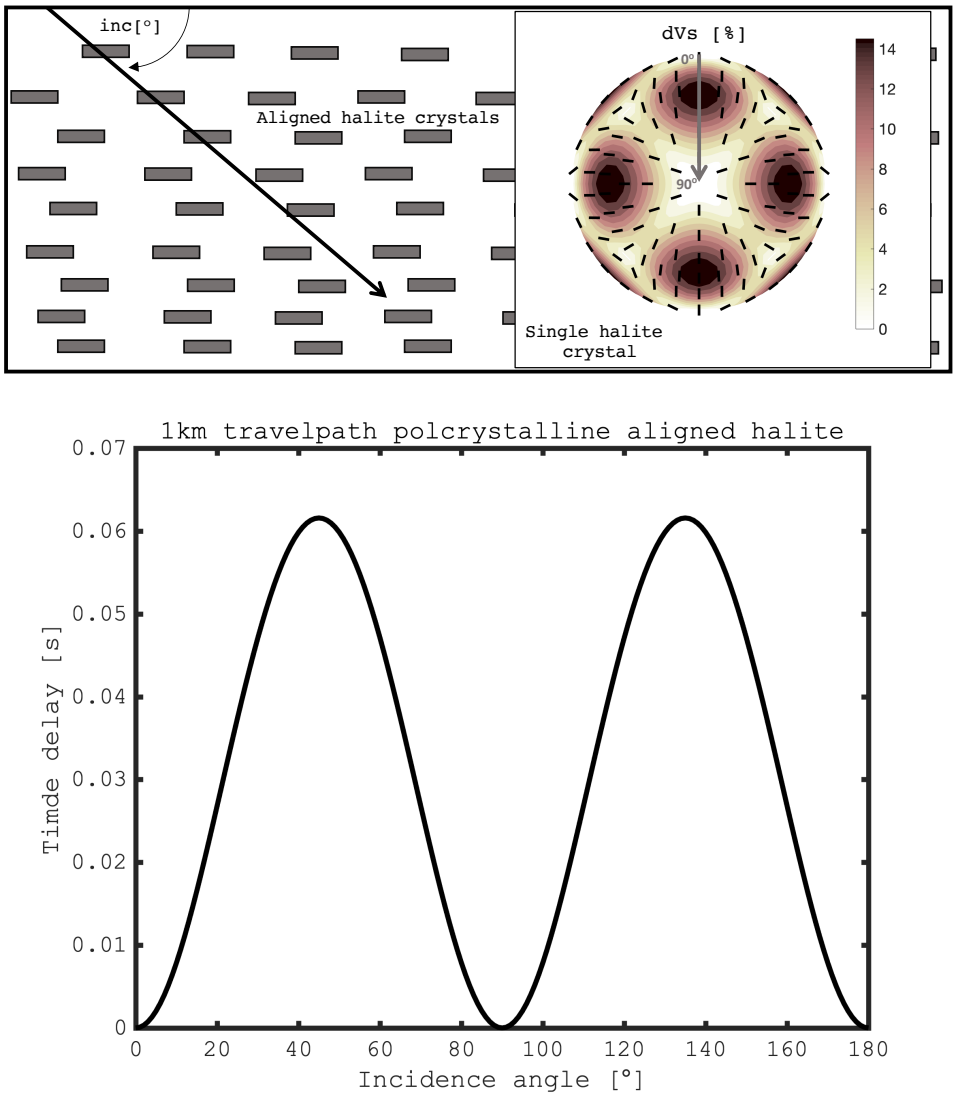

FIGURE 2.16. Schematic model of a salt layer consisting solely of halite with crystals aligned all parallel. This generates effective seismic anisotropy, as halite is seismically anisotropic on single crystal scale. The single elastic properties used are from (*Gebrande*, 1982). The shear wave splitting surface of the model is shown, displayed as an equal area projection pole figure. The black bars represent the fast shear wave polarisation. Results for a vertically propagating shear wave would be in the centre (inc = 90°); splitting predictions for horizontally propagating waves are on the perimeter (inc = 0°). The cubic crystal structure is clearly visible. Zero delay time would arise for an incidence angle of 0° and 90°, respectively and the highest delay would arise for 45°. The resulting delay time between fast and slow shear wave travelling through the model is shown as a function of the incidence angle, measured from the raypath clockwise to the vertical direction. A travelpath of 1 km is assumed. Polycrystalline alignment of halite can explain the observed delay time.

2.5.2 Anhydrite

Anhydrite usually makes about 1-3% of the rock salt content, though it is not generally uniformly distributed. Anhydrite has an orthorhombic crystal symmetry with the a-axis being the shortest axis (6.245Å) and the b- and c-axis having almost similar length (6.995Åand 6.993Å, respectively) (Anthony, 1997). It is seismically very anisotropic at the single crystal scale, with S-wave anisotropy up to 61% (*Vargas-Meleza et al.*, 2015). Several studies on anhydrite deformation exist, observing lattice orientation in naturally as well as in experimentally deformed samples (*Müller et al.*, 1981; *Heidelbach et al.*, 2001; *Hildyard et al.*, 2009b). It has been established that one of the major slip systems is translation glide on {001}. For example, *Vargas-Meleza et al.* (2015) investigated naturally deformed polycrystalline anhydrite samples and observed strong crystal alignment, such that poles to {100} are aligned with the foliation plane and poles to {001} are aligned oblique to the foliation plane. The shear wave splitting surface and the P-wave velocity surface calculated for the elasticity tensor of single crystalline anhydrite is shown in Figure 2.17, using elastic parameters from *Bass* (1995). Aligned anhydrite is, therefore, a possible explanation for the observed anisotropy.

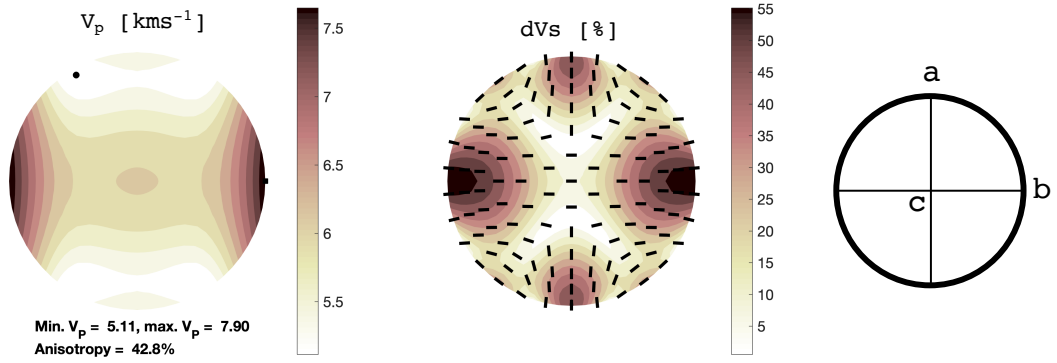

FIGURE 2.17. Stereographic projections of the P-wave velocity surface and S-wave splitting surface of single crystalline anhydrite. The displayed velocities are observed for a crystal orientation shown on the right side, where the a-axis is vertically up, b-axis is horizontal and the c-axis into the plane. The plots are equal area pole figures. The S-wave anisotropy is displayed as shear wave splitting in percent for each polarisation direction. The black bars represent the fast shear wave polarisation. Results for a vertically propagating shear wave would be in the centre; splitting predictions for horizontally propagating waves are on the perimeter. Anhydrite is highly anisotropic on single crystal scale, with P-wave anisotropy up to 42.8% S-wave anisotropy up to 60%. The single elastic properties were obtained from *Bass* (1995).

However, anhydrite is usually left as a cap at the top of an evaporite deposit sequence (Walker,

1976), whereas the observed seismic anisotropy by the field data VSP is highest at the bottom at the salt body. If an upper anhydrite layer is the primary cause of the observed seismic anisotropy, we would expect to see similar delay times on all receivers. Moreover, Gulf of Mexico rock salts have generally low anhydrite content (e.g., *Fredrich et al.*, 2007; *Zong et al.*, 2017). Overall, we consider the anhydrite crystals is an unlikely candidate for the anisotropy we observe.

2.5.3 Layering

The fine-scale layering of isotropic materials can lead to effective seismic anisotropy (*Backus*, 1962; *Folstad and Schoenberg*, 1992; *Stovas et al.*, 2006). When the seismic wavelengths are significantly larger than the thickness of individual layers, the layered medium can be modelled as a homogeneous seismically anisotropic medium (*Backus*, 1962). Fine-scale layering might result from intrusions of sediment into the salt body during deposition; these would naturally be spread out by horizontal shearing during salt body flow. A plausible candidate for this is shale, one of the main deposited sediment in the Northern Gulf of Mexico (*Dribus et al.*, 2008). We therefore model a seismic anisotropy associated with a layered isotropic salt/shale medium. We assume velocity and density for the isotropic sediments and salt as shown in Table 2.1, from *Bourbié et al.* (1987). We calculate the effective medium with the MSAT MATLAB toolbox (*Walker and Wookey*, 2012), based on the method of *Backus* (1962). This predicts a VTI medium, which would be consistent with the horizontal fast shear wave observed in the data.

To compare delay times, we assume a travel path of 1 km through the salt/shale layered medium at an incidence angle of 35°, defined in degrees from horizontal to the raypath, approximately equivalent to the geometry of the VSP, and calculate the resulting difference between the fast and slow shear wave arrival times. The calculations are performed for a range of gross salt/shale ratios. A schematic picture of the model together with the calculated delay times is displayed in Figure 2.18. To reproduce the splitting observed in the data – around 20 ms – requires a shale content of about 40%, This is very high – uncommon for any salt structure – but in particular in the Gulf of Mexico, which is known for very pure rock salt (e.g., *Zong et al.*, 2015). However, we modelled clay as an isotropic medium. Shale can show significant anisotropy which would change the results (*Baird et al.*, 2017). Our calculations are approximate, and do not conclusively rule out layering as a possible explanation for the measured anisotropy.

$\mathbf{VP_{Shale}}$	$\mathbf{VS_{Shale}}$	$\rho_{\mathbf{Shale}}$	$\mathbf{VP_{Salt}}$	$\mathbf{VS_{Salt}}$	$\rho_{\mathbf{Salt}}$
$2.5\,\mathrm{kms^{-1}}$	$1.2\,\mathrm{kms^{-1}}$	$2200\,\mathrm{kgm^{-3}}$	$4.575\,\mathrm{kms^{-1}}$	$2.6\ \mathrm{kms^{-1}}$	$2160\,\mathrm{kgm^{-3}}$

TABLE 2.1. Isotropic velocities and densities of the salt and shale

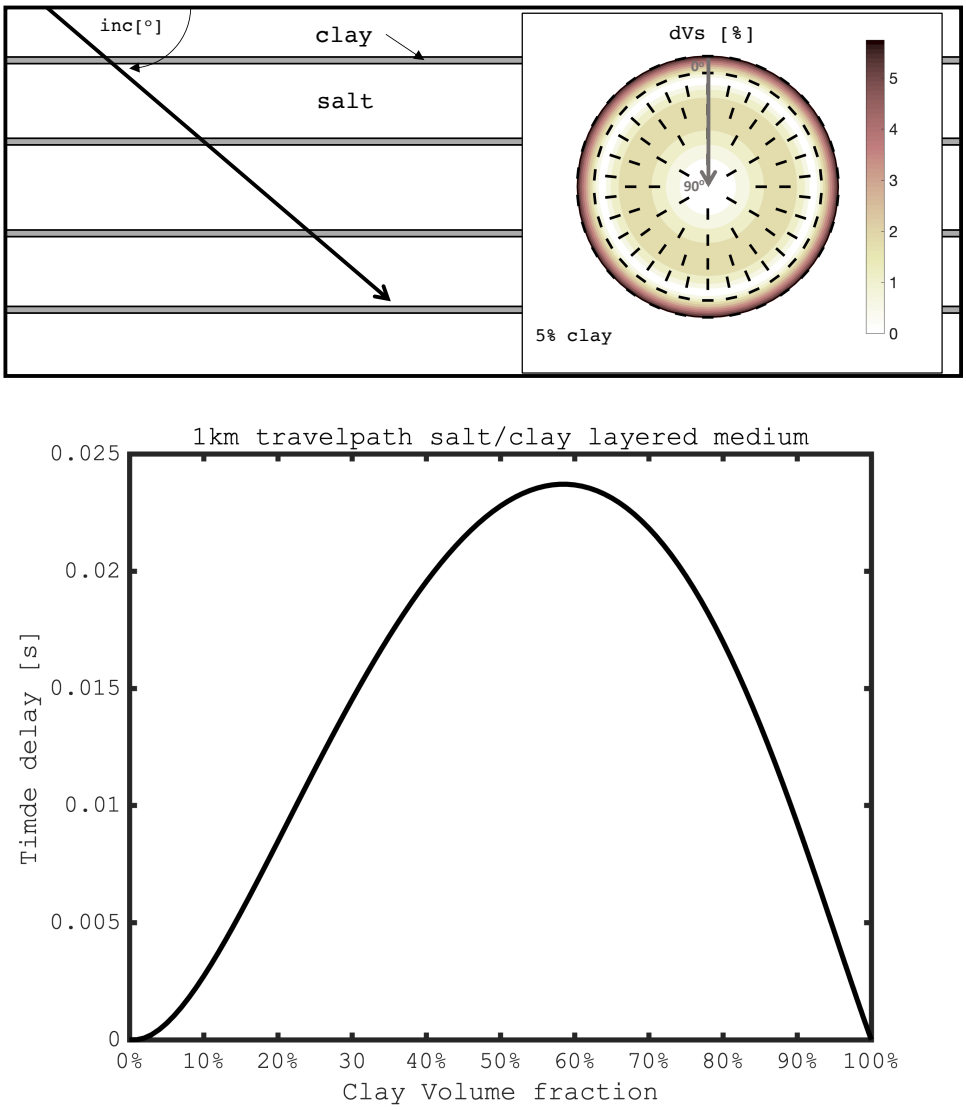

FIGURE 2.18. Schematic model description for a salt/shale layered medium (top picture). A layered medium can be modelled as an effective anisotropic medium (*Backus*, 1962). The assigned isotropic velocities are found in Table 2.1. The incidence angle is defined clockwise from horizontal to the seismic ray direction. The S-wave splitting surface for a shale volume fraction of 5% is displayed (equal area projection). The black bars represent the fast shear wave polarisation. Results for a vertically propagating shear wave would be in the centre (inc = 90°); splitting predictions for horizontally propagating waves are on the perimeter (inc = 0°). The resulting delay for this model acquisition as a function of the shale volume fraction is displayed. We assume a travelpath of 1 km trough the effectively anisotropic medium and an incidence angle of 35° for the incoming shear wave. For the assumed acquisition and model properties a shale volume fraction of 40% would be necessary to explain the delay time observed in the VSP field data.

2.5.4 Water inclusions

The second class of shape-preferred orientation mechanism we test is the presence of water inclusions. Inclusion of materials with different elastic properties alter the effective seismic parameters of the medium. If there is a preferred alignment of non-spherical inclusions they can manifest as an effective seismic anisotropy (e.g., *Hudson*, 1981; *Tandon and Weng*, 1984). Fluid inclusions are particularly effective at generating seismic anisotropy as they have zero shear-modulus. Inclusions of fluid (including water and melt) have been invoked as explanations of seismic anisotropy in scenarios including glaciers, divergent margins, and the lowermost mantle (*Kendall and Silver*, 1996; *Holtzman and Kendall*, 2010; *Smith et al.*, 2017). Rock salt usually contain large amount of small fluid inclusions (*Isherwood*, 1979; *Roedder*, 1984; *Urai et al.*, 1986a). Water content in rock salt ranges from about 0.1% to 1% (*Roedder*, 1984). Fluid inclusions range in size from less than 1 μm in the longest dimension to several millimetres.

To test this possibility, we model the effective elasticity tensor for oblate-spheroid shaped water (brine) inclusions in an isotropic halite host medium and compare shear shear-wave splitting with our observations from the VSP data. The effective elasticity tensor is calculated with the MSAT MATLAB toolbox (*Walker and Wookey*, 2012), based on *Tandon and Weng* (1984). Here, we assume a volume fraction of 0.5% for all the calculations. A higher volume fraction would lead to higher seismic anisotropy. A schematic picture of the model is displayed in Figure 2.14. As in the previous model, we assume a travel path of 1 km. The fluid inclusions are assumed to have a compressional velocity of $V_{PWater} = 1500\,ms^{-1}$ and a density of $\rho = 1000\,kgm^{-3}$. The salt seismic velocities and density are the same as in the previous model (Table 2.1). In Figure 2.19 we model the delay time due to fluid inclusions as a function of angle of the incoming seismic ray and inclusion shape (axis ratios between the short and long oblate spheroid inclusions tested are 1:10, 1:5, 1:3.3 and 1:2.5).

The estimated incidence angle observed in the VSP data is about 30° - 40°, measured clockwise in degrees from horizontal to the ray direction. An aspect ratio of 1:5 does give the best agreement with the delay times measured from the field VSP data (~20 ms). Water inclusions in rock salt are most often cubic in shape, not necessarily aligned in a specific direction (e.g., *Isherwood*, 1979; *Roedder*, 1984). Spherical water inclusions without a specific elongation direction are not able to generate seismic anisotropy. However, it is reasonably to assume that in highly deformed areas water inclusions would align in deformation direction. Therefore we conclude that brine/water inclusions parallel elongated uni directional might be an explanation for the observed seismic anisotropy. Nevertheless, we are not aware of studies which observed such unidirectional water inclusions in naturally deformed rock salt.

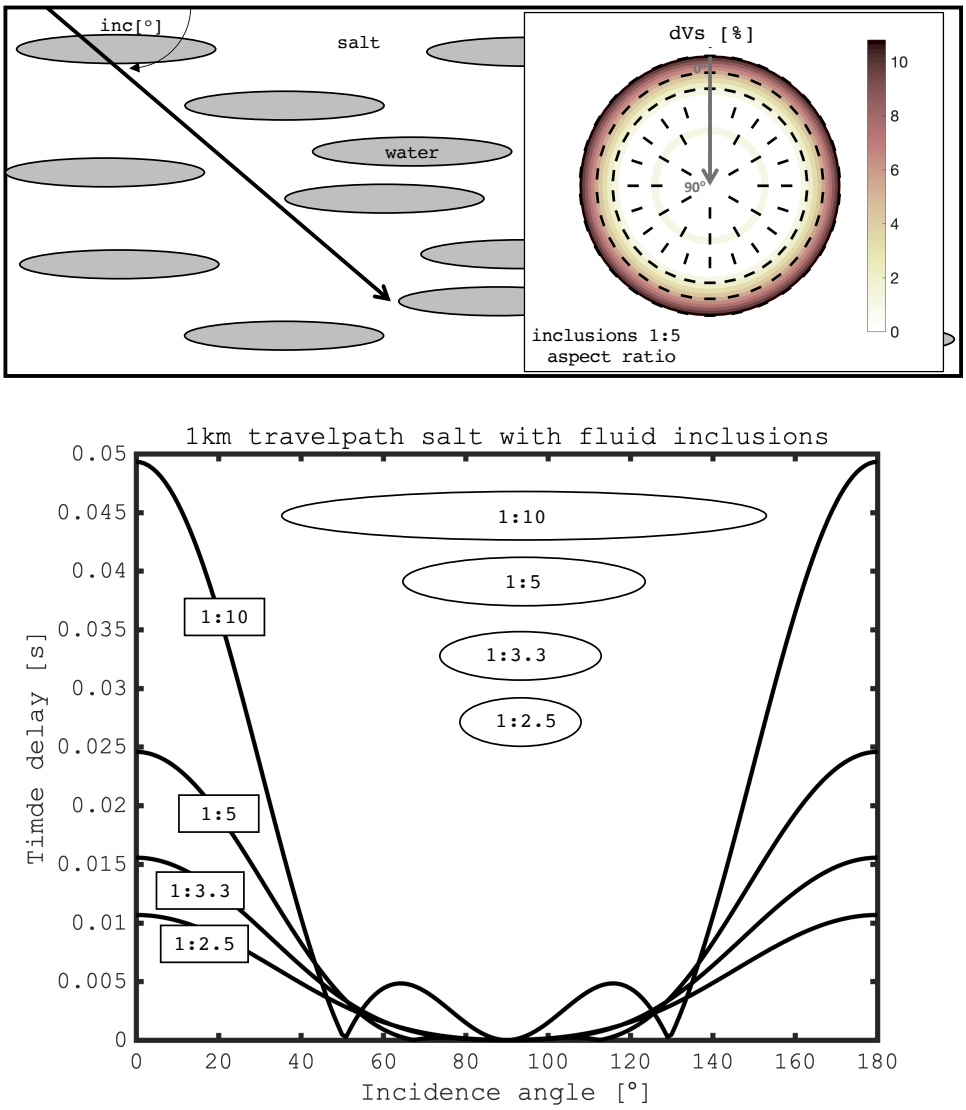

FIGURE 2.19. Schematic model description, consisting of isotropic halite with spheroid brine inclusions. Isotropic media with inclusions can be modelled as an effective anisotropic medium (*Tandon and Weng*, 1984). We assume a water volume fraction of 0.5%. We model the shear wave delay times due to seismic anisotropy expected from this model setup for a travelpath of 1 km through the model. The water inclusions are modelled as oblate spheroids with an axis ratio between the short and long axis of 1:10, 1:5, 1:3.3 and 1:2.5. The shear wave splitting surface for an axis ratio of 1:5 is displayed as an equal area projection. The delay times are calculated as a function of the incidence angle, defined as shown in the figure (angle from horizontal to the raypath). The black bars represent the fast shear wave polarisation. Results for a vertically propagating shear wave would be in the centre (inc = 90^o); splitting predictions for horizontally propagating waves is on the perimeter (inc = 0^o). The model with fluid inclusions having an axis ratio of 1:5 could explain the observed delay times of the VSP field data.

2.5.5 Anisotropy in the Mahogany salt body

All of the mechanisms explored above could potentially explain the shear-wave splitting we observe in the Mahogany salt body. In this thesis we choose LPO of halite to focus on, as it s the dominant component of the salt body, and has been shown to form anisotropic fabric under deformation (*Wenk et al.*, 1989; *Raymer et al.*, 2000a; *Lebensohn et al.*, 2003; *Wenk et al.*, 2009). In our view anisotropy associated with halite should prioritised to be explored further to see if it can explain our results under more realistic conditions.

2.6 Conclusion

In this chapter we provide strong evidence that the Mahogany salt body, for the given location, acquisition and geometry, is seismically anisotropic. We calculate and analyse shear wave splitting, obtained from a vertical seismic profile data set. The data set consists of an airgun shot recorded at an array of 48 3-component receivers deployed every 15 m in vertical well which passes through the salt body. Velocity filtering was used to extract the downgoing shear wave energy on the transverse and radial component. The shear wave splitting analysis is performed on two phases: The P- to S-converted waves at the top and base of the salt layer. The top-salt conversion shows clear shear-wave splitting with delay times of about 20 ms and a nearly horizontal fast shear wave polarisation, whereas the base-salt conversion shows a much smaller time delay (~6-8 ms). Comparing the splitting in the two phases allows us to exclude seismic anisotropy outside of the salt layer as the major reason for the observed splitting on the top-salt conversion. We observe that horizontally polarised waves are faster than vertically polarised shear waves. This gives us confidence that we are measuring anisotropy associated with the salt body itself.

We discuss possible explanations for this observed seismic anisotropy. We create simple seismic models of crystal alignment of anhydrite and halite, and a shape-preferred orientation thin sediment layers or aligned water inclusions. While we cannot conclusively exclude any of these mechanisms, LPO of halite or SPO of water inclusions fit the observations best. A lack of previous evidence for highly deformed inclusions of water in rock salt bodies – and the fact that halite is its major constituent mineral – lead us to favour the LPO explanation. It remains to be established, however, whether more realistic models of salt deformation and the resulting texture development still predict shear-wave splitting which is consistent with that observed.

However, setting aside the causative mechanism, the anisotropy we measure is sufficient to have a significant effect on, for example, seismic reflection image processing. The study substantiates the view that seismic anisotropy in rock salt might need to be accounted for when seismic accurate rock salt images are necessary.

CHAPTER 3

USING VISCO-PLASTIC SELF-CONSISTENT TEXTURE MODELLING TO PREDICT SEISMIC ANISOTROPY

This chapter numerically predicts LPO evolution in halite polycrystalline aggregates and relates the calculated quantities to seismic velocities. Seismic anisotropy associated with crystal alignment in simple shear and uniaxial compression is simulated, using the texture plasticity simulation VPSC (visco-plastic self-consistent approach). We simulate deformation conditions up to Von-Mises strains of 5 and 2 for shear- and compression geometries, respectively, and show that significant seismic anisotropy is predicted. We investigate lattice preferred evolution of rock salt and associated seismic anisotropy by dislocation plasticity, neglecting the effect of recrystallisation. Treatment of anisotropy in seismic data usually requires the assumption of simpler symmetry, and we show that salt anisotropy is well-approximated by a vertically-transverse isotropic medium. Our models predict Thomsen-, and η-parameters for VTI media of δ_{Shear} = -0.096, $\varepsilon_{\text{Shear}}$ = -0.0134 , γ_{Shear} = 0.0435 and η_{Shear} = 0.1022 for shear, and δ_{Comp} = -0.085, $\varepsilon_{\text{Comp}}$ = -0.0177 , γ_{Comp} = 0.0375 and η_{Comp} = 0.0822 for compression. Seismic raytracing is used to predict the potential effect of salt anisotropy on seismic traveltimes in a simple layered model. We show that the predicted travel time of the base salt reflection differs significantly from isotropic estimates, especially at long offsets. The predicted VTI medium implies an ~10% change in the estimated thickness of the salt layer if the anisotropy is ignored. This study strongly suggests that seismic anisotropy should be considered in the treatment of seismic data in settings where salt deformation has occurred.

3.1 Introduction

Most major oil and gas discoveries are connected to rock salt. Examples are the Gulf of Mexico, the Santos basin or the Persian Gulf, which are characterised by large evaporite deposits and significant oil- and gas discoveries. Also, rock salt is used to store waste or carbon dioxide in the sub surface. This is, because the salt brings excellent properties, which can be exploited for industrial use. Salt is nearly impermeable and flows, rather than to fracture, on geological time scales. It is high in viscosity and low in density. It relatively more buoyant than surrounding strata. Salt resist tectonic forces and flows, forming various striking salt structures in subsurface, which can form structural traps for hydrocarbons. The impermeability of the salt seals hydrocarbons and prevent further migration.

Although rock salt has the ability to behave like a fluid on geological time scales, it is a crystalline solid. Most polycrystalline solids exhibit a lattice preferred orientation, or texture, when being deformed. It has been observed that halite – the main constituent mineral in evaporite deposits – develop texture when being deformed, both in the laboratory (*Skrotzki and Welch*, 1983; *Spiers et al.*, 1990; *Wenk et al.*, 2009) and under natural deformation (*Muehlberger and Clabaugh*, 1968; *Schwerdtner*, 1968; *Kern and Richter*, 1985; *Miralles et al.*, 2001). Halite has a cubic crystal structure and is seismically anisotropic (*Gebrande*, 1982). As rock salt experiences large deformation, it is plausible to investigate its potential to develop seismic anisotropic due to lattice preferred orientation. Seismic anisotropy describes the dependency of a seismic wave velocity on its propagation and polarisation direction. Exploration seismology and other industrial uses of rock salt rely on accurate seismic images of rock salt in the subsurface. Seismic anisotropy might alter and blur seismic images if not accounted for. Despite laboratory (*Zong et al.*, 2014) and field scale evidence of seismic anisotropy in rock salt (*Raymer et al.*, 2000a; *Planchart*, 2014), it is often neglected, when treating seismic data in salt environments (*Jones and Davison*, 2014).

We limit this study to halite, as it is the most common mineral in evaporite deposits. In this study we investigate the potential for seismic anisotropy in rock salt due to lattice preferred orientation. We use numerical texture plasticity models, simulating crystal orientations caused by deformation. The resulting textures, combined with single crystal elastic properties of halite, are used to calculate seismic velocity for all polarisation direction and thus, seismic anisotropy. Finally, we estimate the impact of such anisotropy on seismic imaging.

3.1.1 Plasticity modelling studies on halite

Numerical simulations are often used to interpret preferred orientation in halite by comparing predictions with laboratory experimental results. Texture simulations numerically predict the lattice orientation of polycrystals when being deformed. A number of previous texture plasticity

modelling studies have used halite as a mineral to test different texture simulation codes and approaches, as it has a strongly anisotropic single crystal yield surface (*Carter and Heard*, 1970; *Skrotzki and Haasen*, 1981; *Wenk et al.*, 1989).

In an early study, *Wenk et al.* (1989) applied the visco-plastic self consistent texture modelling approach (*Molinari et al.*, 1987) to deformation of polycrystalline halite and compared the results with those predicted by the Taylor theory (*Taylor*, 1938). They found significant differences between the two theories in predicting texture and active slip systems. Both model predictions were compared with laboratory experiments, where halite was deformed in axial extension, simple shear and compression. The visco-plastic self consistent model showed better agreement with the laboratory measurements of deformation texture.

Raymer et al. (2000b) used plasticity models to simulate texture of deformed halite and relate those textures to seismic velocities. Deformation was simulated for simple shear and axial extension in low temperature conditions (input parameters were taken from *Wenk et al.* (1989)), up to 600% strain in simple shear and 200% strain in axial extension. They showed that under such deformation conditions, high seismic anisotropy can develop (e.g., P-wave anisotropy of 4.7%).

Lebensohn et al. (2003) compared three different modelling approaches for texture development in halite: a Taylor modelling approach, a self-consistent approach and a finite-element methodology (FEM). They calculated textures in extension to a maximum finite strain of 30% at two temperatures (20°C and 100°C). The results were then compared to laboratory deformation, where pure halite samples were extended in a triaxial multi anvil apparatus. Neither numerical formulations perfectly reproduced the resulting texture, but the FEM and self-consistent method gave good predictions of the microstructural evolution. The Taylor model overpredicted the texture.

To help to interpret the lab torsion-deformation experiment of *Wenk et al.* (2009), texture simulations were performed, reproducing the lab deformation with polycrystalline plasticity models. At high strains, grain size reduction due to subgrain rotation recrystallisation was observed, though with no effect on the texture. Dislocation is still the most active mechanism, so plasticity models give reasonably accurate solutions to the evolving lattice orientation.

These studies showed that texture simulation can be used to predict crystallographic orientations of halite during plastic deformation. However, most of these studies did not consider the seismic consequences of crystal lattice orientation in rock salt. In seismic exploration, halite is often assumed to be homogeneous and isotropic, and is treated as such in building velocity models during seismic data processing.

3.1.2 Aim of this chapter

In nature, salt deforms under a range of complex deformation conditions, varying with temperature, water content or finite strain. Previous studies of texture modelling of polycrystalline halite often calibrated input parameters to match the specific (usually laboratory-derived) deformation conditions, stress/strain curves and measured crystal orientations. However, salt deforms naturally under different deformation conditions. Our study follows the approach of *Raymer et al.* (2000b,a), predicting lattice preferred orientation of polycrystalline halite and the associated seismic anisotropy with texture simulations, while taking a next step and analysing seismic anisotropy with increasing strain in multiple deformation regimes. Those deformation conditions are represented by different critical resolved shear stresses (CRSS), different stress exponents and applied deformation (simple shear and compression). Furthermore, we investigate the capability of texture simulations to predict LPO in naturally deformed rock salt and we suggest texture modelling parameters, which might be best to reproduce natural deformation conditions. We also estimate the potential impact of the calculated seismic anisotropy on reflection seismic processing, by using a simple seismic model consisting of a salt layer with isotropic sediments. Raytracing is used to calculate traveltimes of reflected P-waves for an isotropic and an anisotropic salt layer, demonstrating the impact of salt anisotropy on seismic imaging.

3.2 Numerical texture modelling

Polycrystal texture simulations numerically predict and simulate mineral texture development (or LPO), under imposed deformation. In this study, texture simulations are run for various critically resolved shear stresses (CRSS, the stress required to activate slip on a given plane) and various stress exponents (inverse of strain rate sensitivity) for all slip systems. This helps to understand, firstly, how well texture simulations can be used to predict rock salt fabrics in nature and secondly, under which conditions deformation-induced seismic anisotropy might be observed in rock salt. We perform texture simulations with the visco-plastic self consistent texture modelling approach (VPSC, *Lebensohn and Tomé* (1993)).

3.2.1 Visco-plastic self consistent - VPSC

The VPSC approach can model a range of conditions, from the homogeneous deformation assumption (Taylor model) to the stress equilibrium assumption (Sachs model) (e.g., *Wenk et al.*, 2009). The averaged stress predicted by VPSC is placed somewhere between the predictions by the upper-bound Taylor model and lower-bound Sachs model. A detailed description can be found in *Tomé et al.* (1991) and *Lebensohn and Tomé* (1993); here we briefly summarise the approach and its main principles. The shear rate $\dot{\gamma}^s$ of a slip system s in an individual grain is assumed to

be related to the resolved shear stress τ_r^s in the following way:

$$\dot{\gamma^s} = \left(\frac{\tau_r^s}{\tau_0^s}\right)^n \dot{\gamma_0}, \tag{3.1}$$

Where $\dot{\gamma_0}$ and τ_0^s are the reference shear rate and the reference CRSS, respectively. The grain's shear rate $\dot{\epsilon}$ is then given by the sum of shear rates over all slip systems. The stress exponent is n, which is the inverse of the strain rate sensitivity. For a given set of reference shear stresses and stress exponents for all active slip systems, initial lattice orientations and the imposed deformation, VPSC calculates the microscopic stresses and strain rates for each grain $(\sigma, \dot{\epsilon})$. This is done under the assumption that the grain's volume average of grain scale stress $\langle\sigma_{ij}\rangle$ and strain $\langle\dot{\epsilon}_{ij}\rangle$ is equal to the polycrystal's overall stress and strain $(\Gamma_{ij}, \dot{E}_{ij})$ (*Tommasi et al.*, 2000),

$$\langle\sigma_{ij}\rangle = \Gamma_{ij}, \tag{3.2}$$

$$\langle\dot{\epsilon}_{ij}\rangle = \dot{E}_{ij}.$$

VSPC represents the interaction between grains by embedding each grain in a homogeneous effective medium (HEM). Its properties are the averaged properties of all modelled single crystal grains. The tangent VPSC method uses a more general model description (*Lebensohn and Tomé*, 1993), which incorporates a formulation for a plastically anisotropic HEM. The interaction problem is solved using the inclusion formalism, described by *Eshelby* (1957). The local variables (stress σ_{ij} and strain ϵ_{ij}) on a grain scale are related to the same variables on the global scale (Γ_{ij}, E_{ij}) with the interaction tensor M, which depends on the shape and the rheological properties of grains. For the visco-plastic inclusion problem, the Eshelby solution is (e.g., *Walker et al.*, 2011):

$$\dot{\epsilon_{ij}} - \dot{E_{ij}} = -\alpha M_{ijkl}(\sigma_{kl} - \Gamma_{kl}), \tag{3.3}$$

where α is a parameter controlling the interaction between the grains and the HEM, e.g., to impose more or less strict kinematic conditions on grains (*Tommasi et al.*, 2000). For $\alpha = 0$ the Taylor assumption is imposed $\left(\dot{\epsilon}_{ij} = \dot{E}_{ij}\right)$. The Sachs assumption would correspond to a very high value of α, where each crystal is oriented individually. The tangent VPSC scheme applied in this work assumes $\alpha = 1$. The lattice rotation rate for each grain ω is determined by:

$$\dot{\omega}_{ij} = \dot{\Omega}_{ij} - \dot{\omega^p}_{ij} + \dot{\tilde{\omega}_{ij}}, \tag{3.4}$$

where Ω is the anti-symmetric component of the imposed deformation (given by the velocity gradient tensor L_{ij}), ω_{ij}^p is the plastic rotation rate tensor and $\tilde{\omega}_{ij}$ describes the reorientation rate of the associated ellipsoidal inclusion. The reorientation rate depends on the difference between the grain and polycrystal strain rate, increasing with increasing deformation. The velocity gradient L_{ij} describes the change of deformation velocity in space. The VPSC model

calculates the crystallographic texture, the activity of the slip systems and the stress/strain response of the polycrystal during the deformation. Required inputs are the initial grain shape and orientation, slip systems and their critical resolved shear stresses, single crystal properties (density and the elasticity tensor), the applied deformation and numerical parameters controlling the convergence and precision of each simulation. The grain shapes are treated as ellipsoidal inclusions and their shapes are defined by the ellipsoidal axis ratios. The slip systems (from *Carter and Hansen* (1983)) used in this study are shown in Tab. 3.1.

Slip system	Number of slip modes	slip plane	Slip direction
{110}⟨110⟩	6	1 1 0	1 –1 0
		–1 1 0	1 1 0
		1 0 1	1 0 –1
		1 0 -1	1 0 1
		0 1 1	0 1 -1
		0 1 -1	0 1 1
{100}⟨110⟩	6	1 0 0	0 1 1
		1 0 0	0 1 –1
		0 1 0	1 0 –1
		0 1 0	–1 0 1
		0 0 1	1 –1 0
		0 0 1	–1 1 0
{111}⟨110⟩	12	1 1 1	1 –1 0
		1 1 1	1 0 –1
		1 1 1	0 1 –1
		–1 1 1	0 1 –1
		–1 1 1	1 0 1
		–1 1 1	1 1 0
		1 –1 1	0 1 1
		1 –1 1	1 0 –1
		1 –1 1	1 1 0
		–1 –1 1	0 1 1
		–1 –1 1	1 0 1
		–1 –1 1	1 –1 0

TABLE 3.1. Slip systems and slip modes being active in halite: {110}⟨110⟩ is the weakest slip system; {100}⟨110⟩ and {111}⟨110⟩ are more difficult to activate. Different CRSS-ratios (section 4.1) and different stress exponent (section 4.2) for each slip system are investigated. From *Carter and Hansen* (1983).

3.2.2 VPSC limitations

Halite deforms by different mechanism and processes. The main processes altering the texture observed in halite include dislocation glide, grain boundary migration, and pressure solution creep (*Urai et al.*, 1986b; *Urai*, 1987; *Drury and Urai*, 1990; *Spiers et al.*, 1990; *Ter Heege et al.*, 2005; *Urai and Spiers*, 2007). VPSC only accounts for plastic dislocation deformation, it does not account for boundary migration or pressure solution. Grain boundary migration is commonly observed in wet halite and will affect the texture (*Heege et al.*, 2005). Grain boundary migration tends to weaken the LPO in rock salt (*Trimby et al.*, 2000). However, few studies investigate quantitatively the influence of recrystallisation on lattice preferred orientation of polycrystalline halite. We recognise this as a limitation, but further studies are needed to infer recrystallisation mechanisms from LPO textures. Moreover, halite can develop LPO under plastic deformation and under natural conditions (*Muehlberger and Clabaugh*, 1968; *Schwerdtner*, 1968; *Kern and Richter*, 1985; *Raymer et al.*, 2000b; *Miralles et al.*, 2001). We limit this study to investigate the effect of dislocation plasticity on salt texture and the associated seismic anisotropy.

3.3 Performed simulations

We analyse the effect of different deformation conditions and regimes on LPO and link it to seismic anisotropy. We simulate compression and simple shear textures for various CRSS ratios (1:1:1, 1:2:2, 1:3:3 and 1:5:5) and stress exponents (n = 2, n = 4, n = 6 and n = 10). To summarise, the main main modelling parameters chosen to be varied are the CRSS and the stress exponents.

In the modelling the CRSS are relative values, normalised by the strength of the weakest slip system. A CRSS ratio of, e.g., 1:5:5 means that {110}<110> has a CRSS 5 times lower than {100}<110> and {111}<110>. To test the influence of the CRSS-ratio, the stress exponent is constrained at n = 6. When varying the stress exponent, the CRSS-ratio is constrained at 1:5:5. Each simulation is done until a Von-Mises shear strain of 5 in simple shear and 2 in compression is reached, respectively. The strain ranges chosen are partly arbitrary, however it is known that at the edges of diapir stems and salt sheets high strains are observed, with higher expected shear- than compressional strain (*Talbot and Jackson*, 1987).

The numerical texture simulations are preformed with VPSC in compression and simple shear, which are the most relevant deformation mechanisms of naturally deformed salt. The deformation is imposed by applying a macroscopic deformation velocity gradient tensor for each time step of the simulation. The imposed deformation velocity tensors are constant. Compression is applied in the x-direction, while the shear plane is the xz-plane. The velocity gradients for compression

and simple shear are given by:

$$L_{comp} = \begin{pmatrix} -1 & 0 & 0 \\ 0 & \frac{1}{2} & 0 \\ 0 & 0 & \frac{1}{2} \end{pmatrix}, \quad L_{shear} = \begin{pmatrix} 0 & 1 & 0 \\ 0 & 0 & 0 \\ 0 & 0 & 0 \end{pmatrix}. \tag{3.5}$$

In this work we use the Von-Mises stress Γ^{VM} and Von-Mises strain rate $\dot{E}^{VM}$ to quantify the deformation (described in *Hosford* (2010)). The Von-Mises strain is a function of the macroscopic stress and strain rate tensors (Γ_{ij} and $\dot{E}_{ij}$, respectively), representing the global stress and strain state in the following way:

$$\Gamma^{VM} = \sqrt{\frac{3}{2}\Gamma'_{ij}\Gamma'_{ij}}, \tag{3.6}$$

$$\dot{E}^{VM} = \sqrt{\frac{2}{3}\dot{E}_{ij}\dot{E}_{ij}}.$$

The different input parameters represent different modelling conditions and deformation regimes. The strength of the slip systems depends primarily on the temperature at which the polycrystal is being deformed. Natural rock salt deforms under various conditions and temperatures. Salt flow occurs at temperature ranges from 20°C to 200°C (*Urai et al.*, 2008). High temperatures lead to more easy activated slip systems and therefore lower critical revolved shear stresses (*Wenk et al.*, 1989). At room temperature the soft slip system ({110}<110>) has a CRSS about 5-6 times lower than the hard slip systems ({100}<110> and {111}<110>). With increasing temperature the relative strength of the slip systems decreases. At about 250°C the CRSS have a comparable strength (*Carter and Heard*, 1970; *Carter and Hansen*, 1983; *Wenk et al.*, 1989). The stress exponent is the inverse of the strain rate sensitivity (see Equation 1). The stress exponent depends on which deformation mechanisms are active. In regimes where deformation occurs largely by slip, the stress exponent is high (8-10). When climb is active, the stress exponent is slightly lower (7-8) (*Carter and Heard*, 1970; *Wenk et al.*, 1989). This applies to dry halite. In wet halite, the stress exponent is low (1-4) (*Skrotzki and Welch*, 1983). That indicates that other mechanism are active, such as diffusion creep or pressure solution (*Wenk et al.*, 1989; *Urai and Spiers*, 2007).

The temperature gradient in the crust is about 20°Ckm^{-1} to 30°Ckm^{-1}, the deformation temperature of naturally deformed rock salt differs from 20°C to 200°C (*Urai and Spiers*, 2007). In many numerical, and schematic models of salt diapirism, the salt diapir reaches the surface and extruded at the surface as a salt sheet (e.g., *Van Keken et al.*, 1993; *Rowan et al.*, 2001; *Hudec and Jackson*, 2007). Near surface, low temperature deformation conditions would imply a critical resolved shear stress ratio of 1:4:4 to 1:6:6 (*Wenk et al.*, 1989; *Picard et al.*, 2018). Stress exponents used in flow laws for natural rock salt vary between 4-6 (*Heege et al.*, 2005). Therefore,

we suggest that a input parameter set of 1:5:5 for the CRSS-ratio and a stress exponent of n = 6 are best to represent natural deformation conditions.

3.3.1 Seismic anisotropy in deformed halite

Each aggregate consists of an initial set of 500 randomly oriented grains. Due to its random orientation the polycrystal shows no seismic anisotropy before it is being deformed. Grains are treated as ellipsoidal inclusion. In their initial undeformed stage, each has a spherical axis aspect ratio of 1:1:1. Each crystal has the properties of a halite single crystal. Elastic properties of halite has been analysed in various studies; we take the single crystal stiffness tensor and the density from *Gebrande* (1982), which are $C_{12} = 14\,\text{GPa}$, $C_{11} = 49.1\,\text{GPa}$, $C_{44} = 12.7\,\text{GPa}$ and a density of $\rho = 2160\,\text{kgm}^{-3}$.

The orientation of each deformed crystal can be described by the Euler angles (ϕ, ψ, θ) of each grain. The three Euler angles define the difference in orientation between the crystal axes and a fixed coordinate system. Before the deformation, each aggregate consists of an initial set of 500 randomly oriented grains. After deformation, effective elastic constants of each polycrystal are calculated, which can be seen as an average across all stiffness tensors. The stiffness- or elasticity tensor is a $3 \times 3 \times 3 \times 3$ tensor which has 21 independent elastic constants. It is a material property and generalises Hooke's law in three dimensions, relating strain and stress in the elastic deformation regime. Due to its symmetry the fourth order elasticity tensor can be rewritten in the Voigt notation as a 6×6 tensor C_{ij}) (see Chapter 1). The inverse of the stiffness tensor is called the compliance tensor (in Voigt notation), $S_{ij} = C_{ij}^{-1}$.

The Euler angles of each crystal can be converted into a rotation matrix, which is applied to the stiffness tensor for single crystal halite. The average of all rotated stiffness tensors is known as the Voigt-average C_{ij}^V. Accordingly, the average of all similarly rotated compliance tensors is called Reuss-average S_{ij}^R. The Voigt- and Reuss averages represent the upper and lower bound, respectively, on the elastic properties of the polycrystalline aggregate. Assuming equal volume of each grain, C_{ij}^V and S_{ij}^R are

$$C_{ij}^V = \sum_{n=1}^{500} C_{ij}^n \frac{1}{500}, \tag{3.7}$$

$$S_{ij}^R = \sum_{n=1}^{500} S_{ij}^n \frac{1}{500}.$$

The Voigt-Reuss-Hill (VRH) average (*Hill*, 1952) is the intermediate value between C_{ij}^V and the inverted compliance tensor,

$$C_{ij}^R = \left(S_{ij}^R\right)^{-1}. \tag{3.8}$$

The VRH average thus provides a way to estimate the elastic constants of a textured polycrystal:

$$C_{ij}^{VRH} = \frac{1}{2}\left(C_{ij}^{V} + C_{ij}^{R}\right), \tag{3.9}$$

The elastic constants describe, together with the density, the velocity surface of the entire polycrystal and hence the seismic anisotropy (*Kendall and Thomson*, 1989).

3.4 Results

We present texture simulations results for simple shear and axial compression. We investigate evolving seismic anisotropy for different temperature conditions (represented by the CRSS) in section 4.1 and various stress exponents in section 4.2. We calculate texture and the accompanied seismic anisotropy with increasing Von-Mises strain and in case of simple shear, increasing shear strain γ.
In section 4.3 we choose a set of input parameters, which might be the best approximation, based on literature, to estimate texture in naturally deformed rock salt. We examine how seismic anisotropy and the specific texture develops for that set of input parameters and present LPO pole figures for compression and shear deformation.

3.4.1 CRSS - Temperature dependent deformation

We show simulations for CRSS ratios of 1:1:1, 1:2:2, 1:3:3 and 1:5:5. We constrain the stress exponent to n = 6 for all simulations. Fig. 3.1 shows the P-wave anisotropy with ongoing strain for compression and simple shear simulations. We only show the P-wave seismic anisotropy, as P-waves are more commonly used for seismic imaging. Seismic anisotropy is dependent on the CRSS, where higher CRSS ratio lead to higher seismic anisotropy, regardless the deformation style.

3.4.2 Stress exponent

We analyse the resulting seismic anisotropy for different stress exponents, ranging from 2-10 by performing texture simulations. The critical resolved shear stress ratio is set at 1:5:5. The results are shown in Fig. 3.2, where the P-wave anisotropy with increasing strain is shown for a stress exponent of n = 2, 4, 6 and 10. A higher stress exponent lead to higher seismic anisotropy. Generally, seismic anisotropy depends significantly on the chosen CRSS and stress exponent.

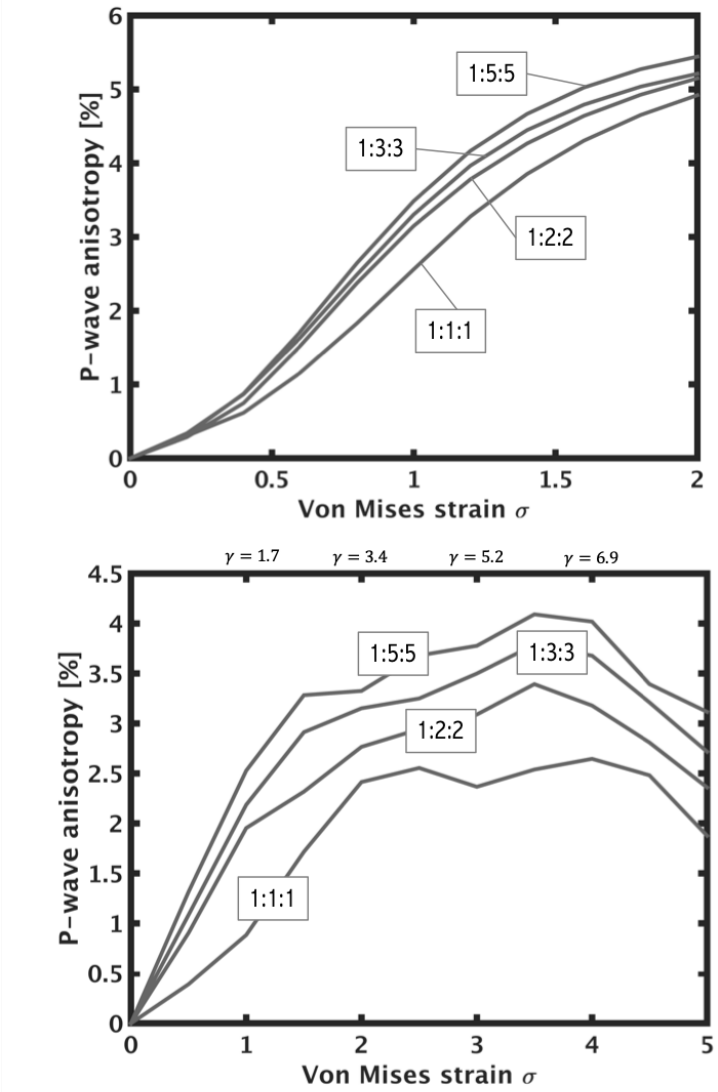

FIGURE 3.1. P-wave anisotropy versus strain for compression (top) and shear (bottom) for various CRSS ratios. Deformation of halite polycrystals are simulated for different critical resolved shear stress ratios. A stress exponent of 6 is used in all calculations. Seismic P-wave anisotropy is calculated from effective elastic constants of each deformed polycrystal. The maximum P-wave anisotropy (considering all propagation directions) is shown as a function of the Von-Mises strain. The lines represent different CRSS ratios of the soft 110<110> slip system to the two hard slip systems {100}<110> and {111}<110>. Most rocksalt is naturally deformed at moderate temperature (not higher than 100°C) would correspond to values of about 1:3:3 to 1:5:5 (*Picard et al.*, 2018; *Wenk et al.*, 1989).

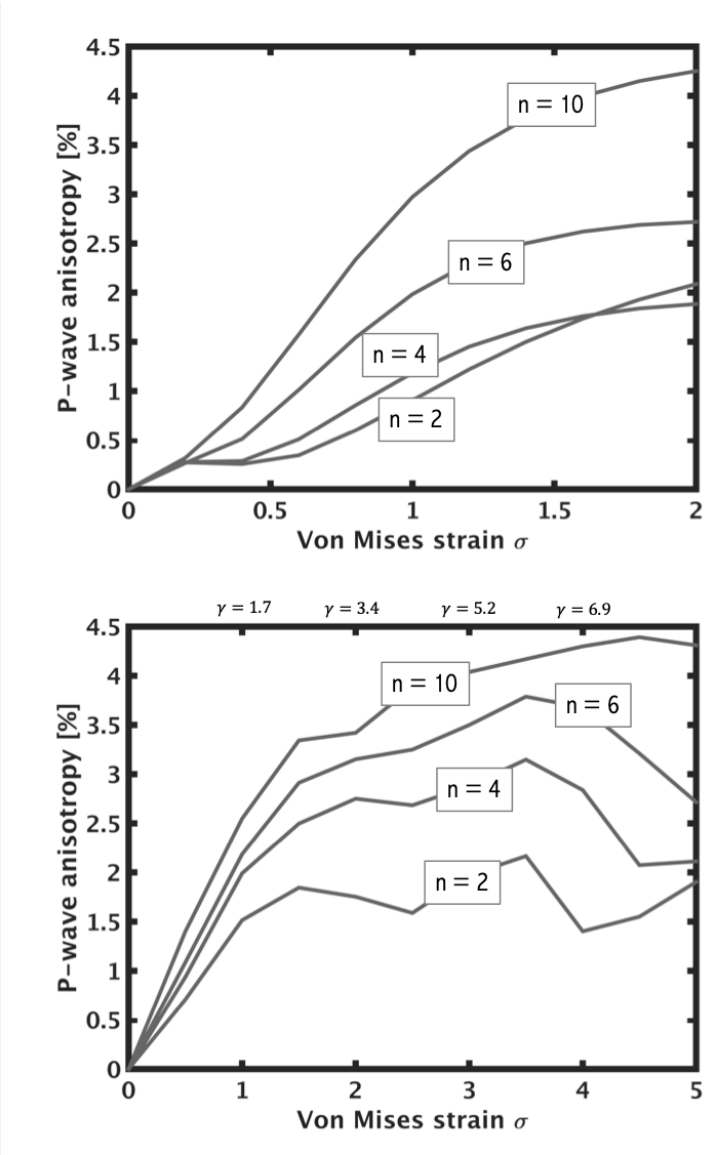

FIGURE 3.2. P-wave anisotropy versus strain for compression (top) and simple shear (bottom) for various stress exponents, n. Deformation of halite polycrystals are simulated for different stress exponents (at a fixed CRSS ratio of 1:5:5). Seismic P-wave anisotropy is calculated with effective elastic constants of each deformed polycrystal. The maximum P-wave anisotropy (considering all propagation directions) is shown as a function of the Von-Mises strain. Stress exponents in flow laws describing natural rock salt deformation are in the range of 4-6 (*Urai*, 1987; *Urai and Spiers*, 2007).

3.4.3 Texture and seismic anisotropy

The calculations performed above show that significant texture (and associate seismic anisotropy) develops in a range of models, including those we suggest are most appropriate to the relevant

naturally occurring rock salt formations. Fig. 3.3 and Fig. 3.4 show the development of texture for such a model which assumes a slip system CRSS ratio of (1:5:5) and a stress exponent of n = 6. The models are deformed by compression (Fig. 3.3) and by simple shear (Fig. 3.4), up to a Von-Mises strain of 5 and 2, respectively.

A texture simulation for a non-random initial texture is shown in Fig. 3.5. Simulated is a compression in Y-direction (left), X-direction (right) and a combined compression, where first compression in X- and then a compression Y-direction was simulated. The pole figures contains features for both deformation styles. Therefore, it is important to consider the whole deformation history of a polycrystal, when calculating the tetxure.

The figures show how the texture evolves with ongoing deformation and strain. Texture plots are shown for four different deformation steps in time. In compression, grains are preferentially aligned along <100>, which is the compression direction. The texture gets stronger with ongoing deformation. A slight maximum is observed along the y-direction, normal to the compression direction. The strongest texture can be seen on the (100) plane; the (110) and (111) planes show comparably weak texture. In simple shear a clear four-fold symmetry can be observed, with strongest textures normal to shear plane (x-z plane as indicated in the figures). In general, compression generates a stronger texture (MRD up to 10) than simple shear (MRD up to 4). The textures observed agree qualitatively with previous texture simulation experiments in compression (*Wenk et al.*, 1989) and simple shear (*Wenk et al.*, 2009).

At the end of each texture simulation, seismic anisotropy is calculated. The results are shown in Fig. 3.6; P-wave velocities and shear wave splitting magnitudes for all propagation directions are shown for simple shear and compression. The compression- or shear direction is indicated. The P-wave anisotropy in percent is calculated based on the maximum and minimum P-wave velocity respecting all orientation directions (equation 11). Maximum P-wave anisotropies of 5.5% in compression and 2.8% for simple shear are reached. The maximum shear wave splitting is 9.44% and 5.35% in compression and simple shear, respectively. The results are compared to a VTI (vertical transverse isotropy) fit of the P-wave velocity surface and S-wave splitting surface calculated for a single halite crystal, showing that salt anisotropy is well approximated by a VTI symmetry.

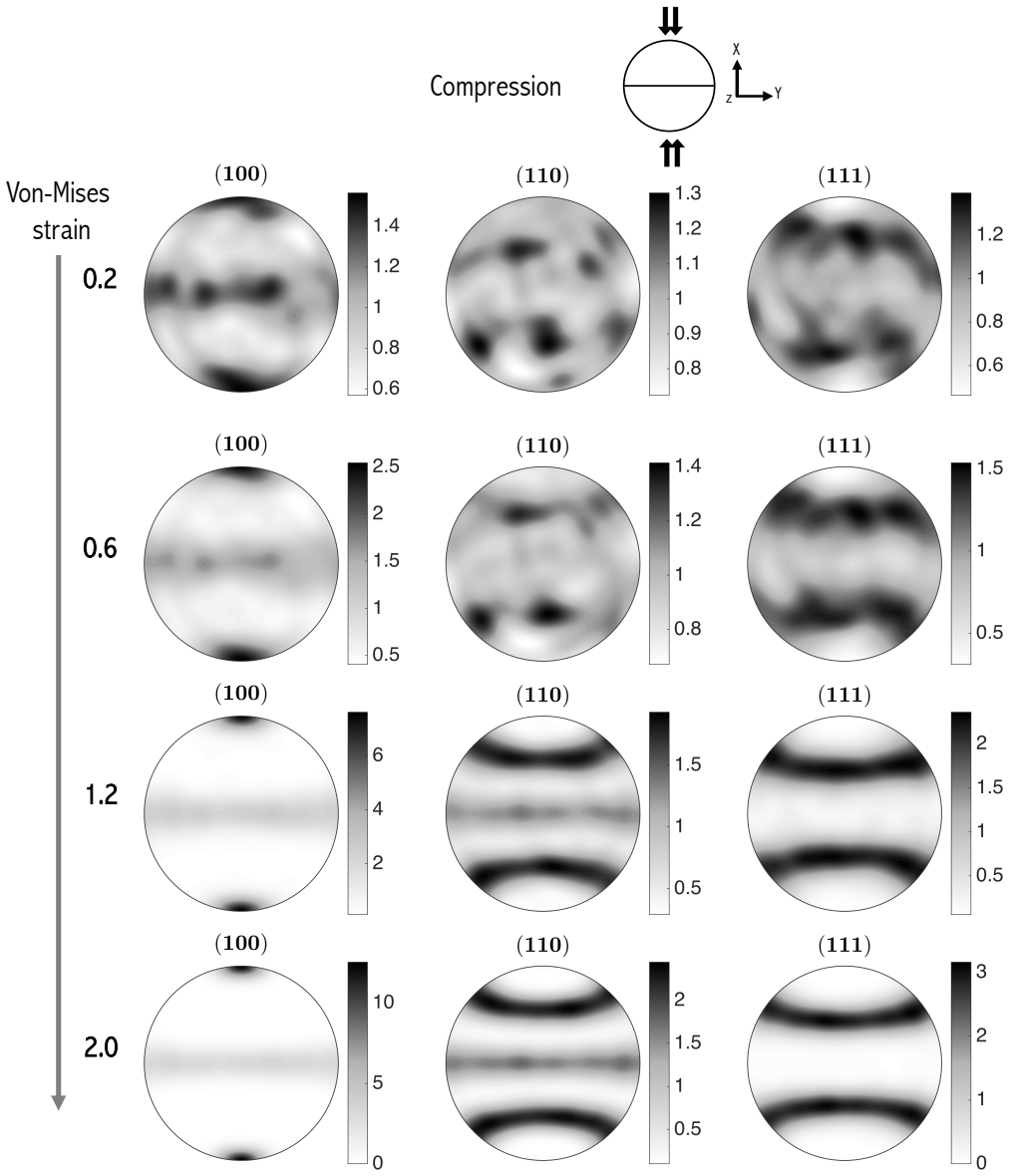

FIGURE 3.3. Sample textures for compression simulations, presented in equal area pole figures (upper hemispheric projection). Colourscale denotes the strength of alignment of individual crystals, measured in units of multiples of a random distribution along the three crystal planes {100}, {110} and {111}. With ongoing deformation the texture strength increases. The {110} slip system has been set to be five times weaker than the stronger slip systems (1:5:5) and a stress exponent of 6 has been chosen. Those conditions are in the range expected for natural rock salt deformation. This demonstrates that a strong fabric develops under such conditions.

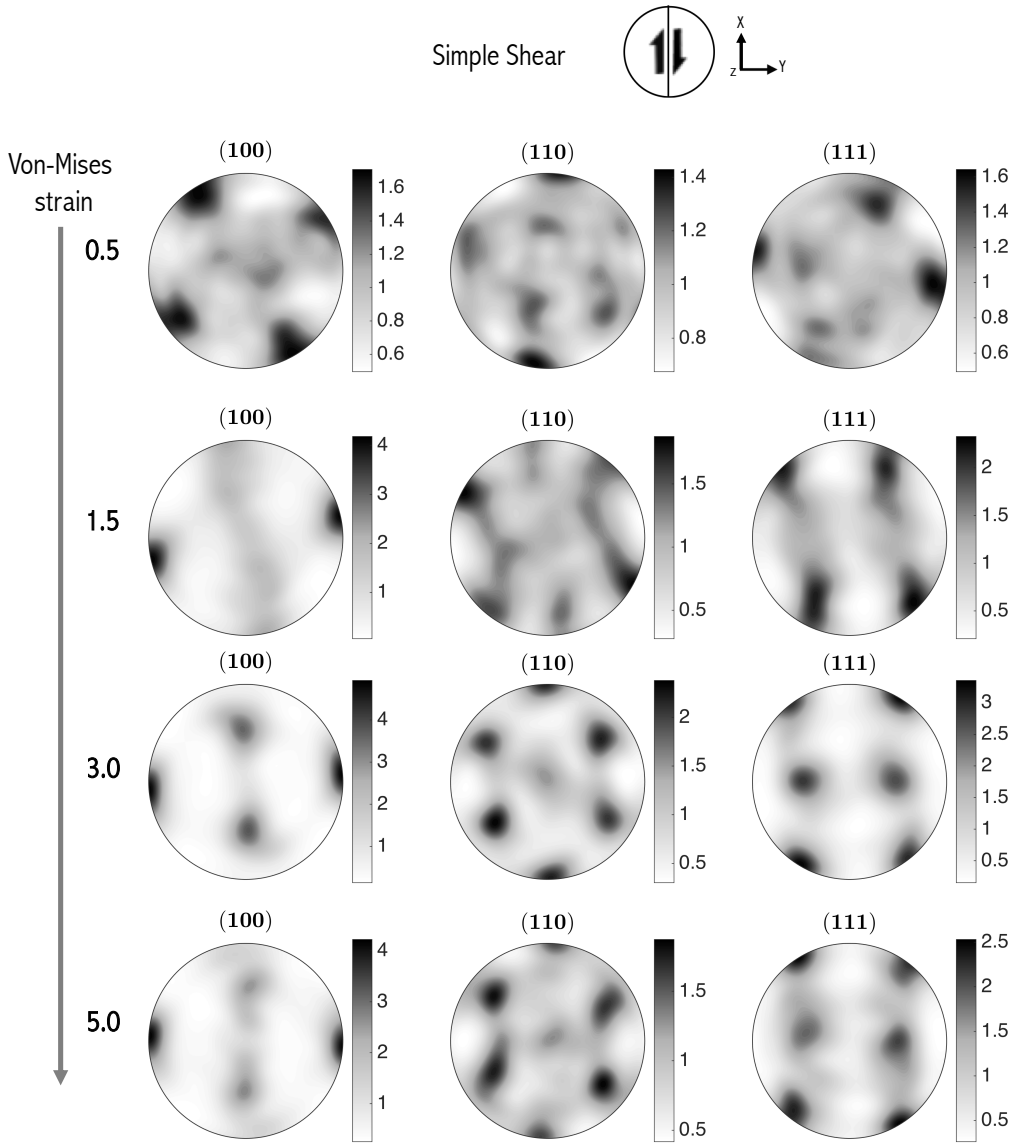

FIGURE 3.4. Sample textures calculated for simple shear deformation, presented in equal area pole figures (upper hemispheric projection). Colourscale denotes the strength of alignment of individual crystals, measured in units of multiples of a random distribution along the three crystal planes {100}, {110} and {111}. Similarly, to the compression case (Fig. 3.3), deformation conditions thought to best simulate natural conditions are chosen. However, unlike the compression case, a change in symmetry can be seen as the material is continuously deformed. This has implications for the evolution of the texture.

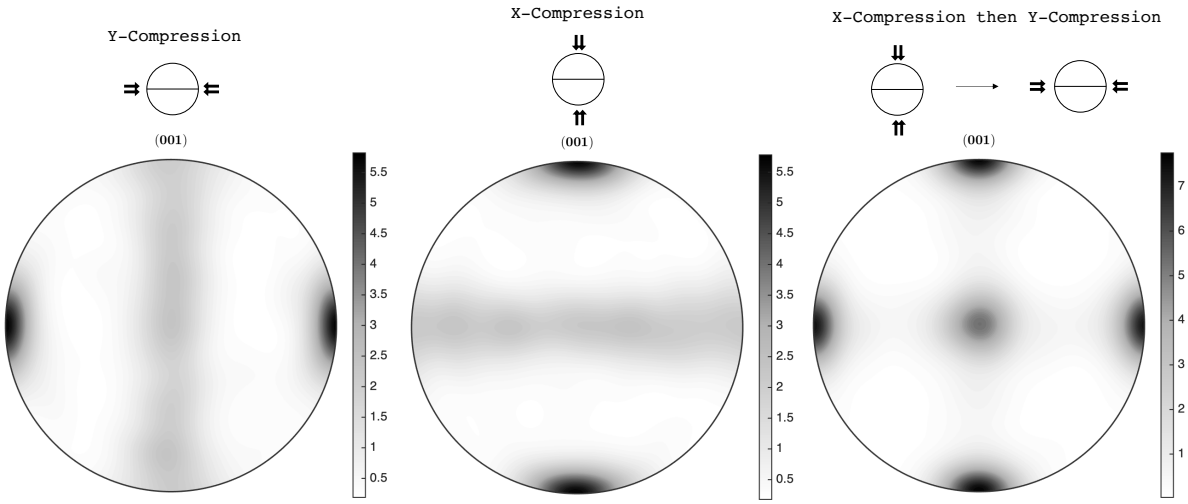

FIGURE 3.5. Representing texture evolution for a non-random initial texture simulation. Shown are equal area pole figures after compression in the Y-direction (left), X-direction (centre) and after both first compression in Y-direction and the compression in X-direction (right). Deformation is after a Von-mises strain of 1 for the Y- and X-compression. For the combined compression first a Von-mises strain of 1 in Y-direction and then a Von-mises strain of 1 in X-direction is applied. The texture for the combined compression contains features of both compression directions.

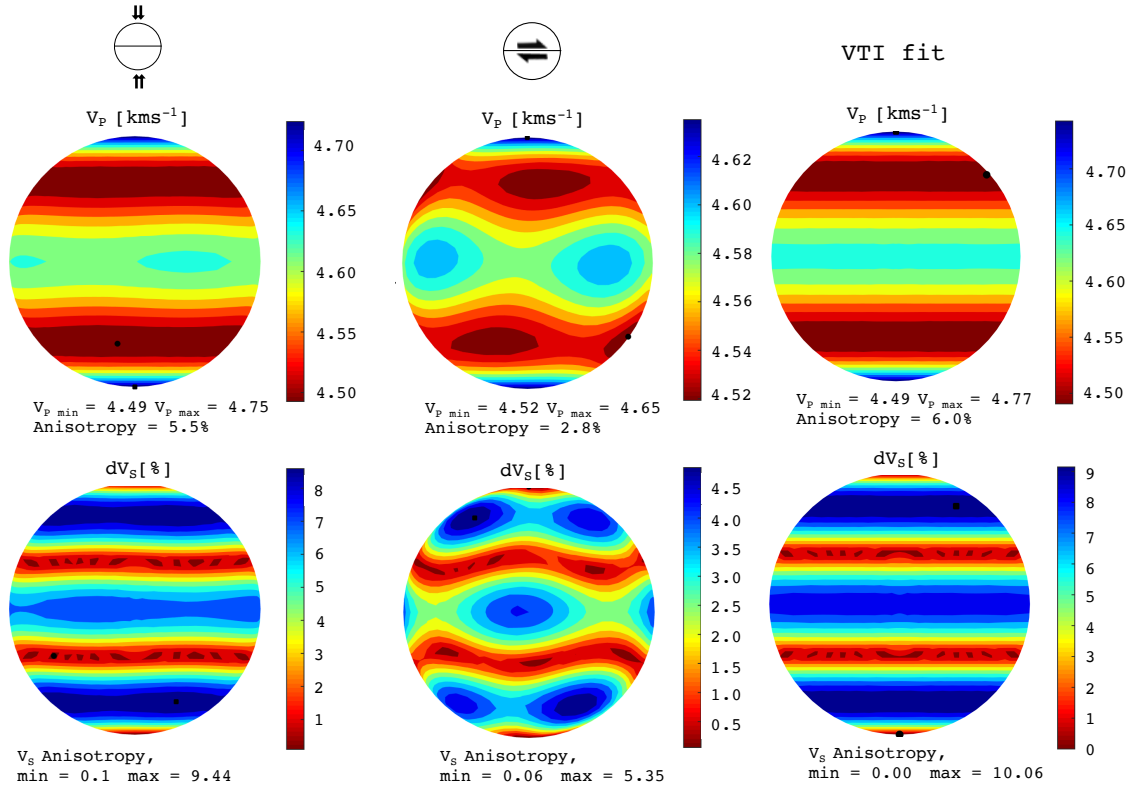

FIGURE 3.6. Predicted seismic anisotropy for halite deformed under compression and simple shear compared to the VTI fit of the elasticity tensor of a single halite crystal. The VTI fit was calculated from the elasticity tensor of halite, by decomposing the tensor into isotopic, hexagonal and lower symmetry parts. This is accomplished with the use of MSAT (*Walker and Wookey*, 2012), which uses the decomposition methodology described in *Browaeys and Chevrot* (2004). The velocities were calculated after a shear strain of 5 for simple shear and 2 for compression, from effective elastic constants of the simulated deformed halite polycrystals. The deformation conditions are the same as used in the texture simulation displayed in Fig. 3.3 and Fig. 3.4 (n = 6, CRSS 1:5:5). The pole figures are shown as upper hemispheric projections. The upper panel shows variation in P-wave velocity for all propagation directions, while the lower shows the equivalent shear wave splitting.

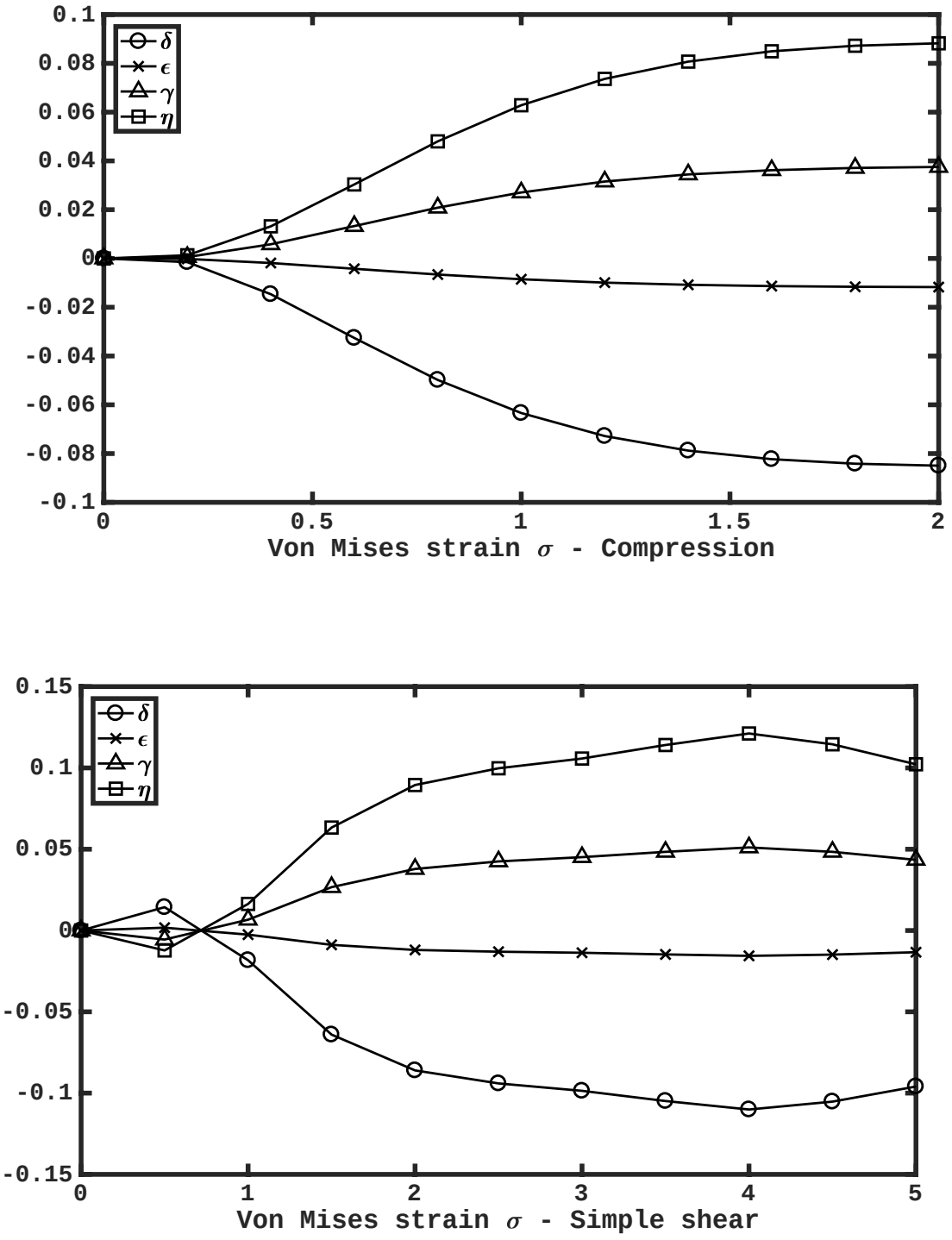

FIGURE 3.7. The evolution of the Thomsen parameters with increasing Von-Mises strain for compression (upper picture) and simple shear (lower picture). Simulation conditions are n = 6 and a CRSS ratio of 1:5:5 (those we suggest are appropriate to natural deformation conditions). Simulations are performed until a Von-Mises shear strain of up to 5 and up to 2 for simple shear and compression, respectively. In both cases anisotropy rapidly reaches a significant level.

3.5 Seismic implications

We investigate potential impact of the seismic anisotropy in salt on seismic traveltime and therefore on seismic processing. Seismic anisotropy is described by the elasticity (or stiffness) tensor C_{ijkl}. An often assumed symmetry, when analysing seismic wave propagation, is VTI (vertical transverse isotropy) and the rotated equivalent HTI (horizontal transverse isotropy), described by 5 independent coefficients. A formulation of these coefficients are the three Thomsen-parameters δ, ε and γ which are used, along with the vertical S- and P-wave velocities, to describe this form elastic anisotropy (*Thomsen*, 1986).

To estimate the impact on seismic processing we calculate the Thomsen-parameters (δ, ε, γ) and the η-parameter (*Thomsen*, 1986; *Alkhalifah and Tsvankin*, 1995). In reflection seismic processing they are essential parameters to quantify and to correct for the seismic anisotropy affecting seismic gathers. Thomsen-parameters are defined in the following way (see also Chapter 1):

- δ describes the relationship the NMO-velocity and the vertical (zero-offset) velocity. It is commonly used, because of its easy measurement.

$$\delta = \frac{1}{2}\frac{(C_{13}+C_{44})^2-(C_{33}+C_{44})^2}{C_{33}(C_{33}-C_{44})} = \frac{1}{2}\left(\frac{V_{PNMO}^2}{V_{P0}^2}-1\right) \tag{3.10}$$

- ε is the fractional difference between the vertical and horizontal P-wave velocity (*Thomsen*, 1986).

$$\epsilon = \frac{C_{11}-C_{33}}{2C_{33}} = \frac{V_{P90}^2-V_{P0}^2}{2V_{P0}^2} \tag{3.11}$$

- γ describes the shear-wave anisotropy. It is defined similarly to the ε-parameter but is formulated for horizontal S-waves. It gives a relationship between the SH-wave velocity in horizontal and vertical direction.

$$\gamma = \frac{C_{66}-C_{44}}{2C_{44}} = \frac{V_{SH90}^2-V_{SH0}^2}{2V_{SH0}^2} \tag{3.12}$$

- η measures the anellipticity of the P-wave phase slowness surface. It is dependent on δ and ε.

$$\eta = \frac{\epsilon-\delta}{1+2\delta} \tag{3.13}$$

We calculate the Thomsen-parameters for a Von-Mises shear strain of up 5 in simple shear and of up to 2 in compression, using a stress exponent of n = 6 and a CRSS ratio of 1:5:5. We calculate the best fitting set of VTI-parameter for each effective elasticity tensor using the MSAT toolbox (*Walker and Wookey*, 2012).

Once texture is established, the δ- and ε-parameters are always negative and the γ- and η-parameter are always positive, regardless the style of deformation. The parameters at the final finite strain at 2 and 5 for compression and simple shear are shown in Tab. 3.2. In both, simple shear and compression, the δ-parameter is the most negative, followed by ε, γ and η for both deformation scenarios. Generally, the Thomsen-parameters have high magnitudes and represent large seismic anisotropy. Simple shear deformation show slightly higher magnitudes than compression, but both deformation mechanisms show similar values.

δ_{Comp}	$\varepsilon_{\text{Comp}}$	γ_{Comp}	η_{Comp}
-0.085	-0.0117	0.0375	0.0882
δ_{Shear}	$\varepsilon_{\text{Shear}}$	γ_{Shear}	η_{Shear}
-0.0960	-0.0134	0.0435	0.1022

TABLE 3.2. Parameters at final finite strain for compression and simple shear

We demonstrate the impact of this seismic anisotropy on travel times by generating a simple seismic model. Seismic raytracing software package ATRAK (*Kendall and Thomson*, 1989) is used, as it supports fully-anisotropic media to predict seismic traveltimes. The model setup is shown in Fig. 3.8. A 2D-model, with a salt sill surrounded by isotropic shale/sediments is considered. The salt layer has a thickness of 3500 m. The model has dimensions of 4500m × 15000m. We use raytracing to predict the travel times of the P-wave phase being reflected from the base of the salt. The travel times for different offsets have been determined for an isotropic and an anisotropic salt layer, the latter is assigned with Thomsen-parameters for a compressed halite polycrystal (Tab. 3.2). The difference in travel time for the isotropic and for the anisotropic case is calculated for an offset ranging from up to 12000 m. The results show significant differences in travel time, and the effect of seismic anisotropy increases with longer offset. At an offset of 12000 m, the model predicts a travel time difference of 75 ms.

Using the δ parameter, we can also estimate the error in the measurement of reflector depth from a zero-offset stacked section, if seismic anisotropy would be neglected. The zero offset traveltime t_0 is given by the two way traveltime with the zero offset P-wave velocity V_{P0}:

$$t_0 = 2 \cdot \frac{z_{true}}{V_{P0}}, \tag{3.14}$$

where z_{true} is the correct salt layer thickness. When we (falsely, in the case of seismic anisotropy) assume that the normal-moveout velocity V_{PNMO} is the same as zero offset velocity, then we can substitute for the traveltime t_0, as the traveltime would be the same in both cases. This leads to:

$$\frac{z_{true}}{V_{P0}} = \frac{z_{dist}}{V_{PNMO}}, \tag{3.15}$$

where z_{dist} is the distorted reflector depth, due to seismic anisotropy. The relation between the normal-moveout velocity V_{PNMO} and the zero-offset velocity V_{P0} is (*Alkhalifah and Tsvankin*, 1995):

$$V_{PNMO} = V_{P0} \cdot \sqrt{1+2\delta}. \tag{3.16}$$

Replacing V_{PNMO} in equation 3.15 yields:

$$z_{dist} = z_{true} \cdot \sqrt{1+2\delta}, \tag{3.17}$$

where δ = -0.085. The model shown in Fig. 3.8 suggests a difference of 311 m between the true and distorted reflector depth. That corresponds to a difference of 8.9% between the true and the distorted reflector depth, which is a significant.

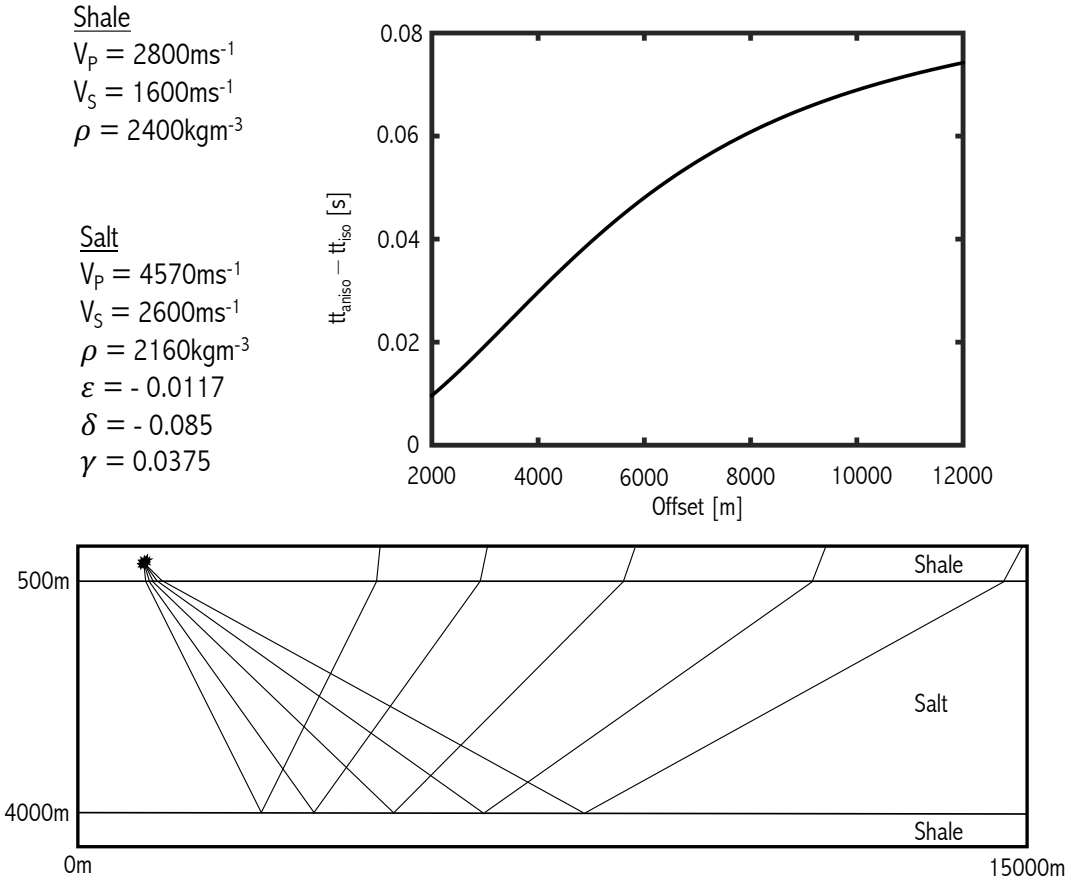

FIGURE 3.8. The effects of the calculated seismic anisotropy on seismic travel times. The model used consists of a salt layer with isotropic shale above and below the salt. We investigate P-wave phases being reflected at the bottom of the salt layer using an isotropic and an anisotropic salt layer; the latter with anisotropy implemented through the Thomsen-parameters estimated from the compression simulation, shown in Fig. 3.7. The velocities, densities and the Thomsen-parameters assigned to the shale and salt layer are shown. The travel time difference between the isotropic and anisotropic case is shown in the upper panel.

3.6 Discussion

3.6.1 Anisotropy for various deformation conditions

We have investigated and simulated halite deformation under a range of possible conditions and calculated the texture-associated elastic seismic anisotropy. We analysed how different stress exponents and strength of slip systems influence the texture/anisotropy in both compression and shear deformation. In general, increasing strain leads to increasing anisotropy.

Higher stress exponent leads to higher seismic anisotropy. A high stress exponent applies to regimes where deformation arises mainly due to slip, a low stress exponent indicates that other mechanisms are active (*Wenk et al.*, 1989, 2009). Anisotropy magnitudes for compression are progressing towards a maximum for each stress exponent, while for shear no stable maximum is reached, as the texture continues to evolve.

In simple shear all CRSS ratios predict significant seismic anisotropy. Seismic anisotropy is most pronounced for highly different CRSS and the weakest values are observed when the slip systems have similar strength. Also, in contrast to compression, a maximum in seismic anisotropy is not reached, at maximum shear strain applied. This can be explained by observing the texture during the compression and shear simulations, as shown in Fig. 3.3 and Fig. 3.4. Under shear (Fig.3.3), texture is continuously evolving, as the lattices continue to rotate. No final lattice orientation is reached. The change in texture is more rapid for lower stress exponents, as the material is weaker and rotations are easier. This effect is quickly shown in Figure 3.9, where we calculated the P-wave anisotropy for a CRSS of 1:5:5 and a stress exponent of n=6. Compression is more efficient than simple shear in developing texture and seismic anisotropy.

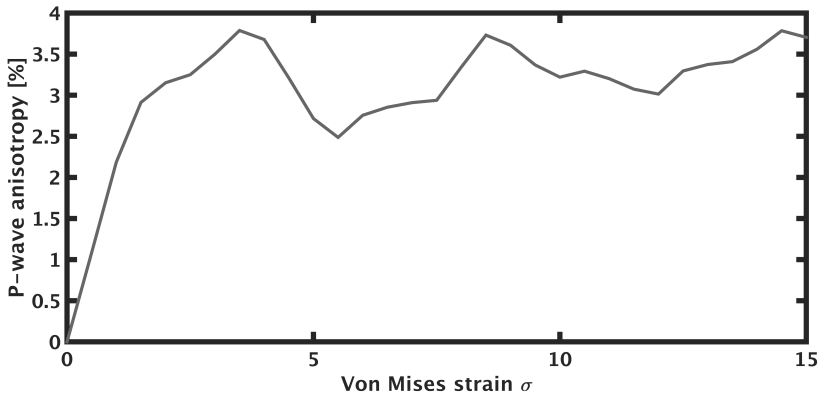

FIGURE 3.9. P-wave anisotropy calculations for large shear strains, demonstrating that the texture and therefore the anisotropy values continues to evolve for large strain. The calculations are done for a CRSS of 1:5:5 and a stress exponent of n=6.

It is clear that textures and seismic anisotropy vary significantly under different deformation conditions. For most of the simulations shown here a significant seismic anisotropy is observed. In the simulation which we suggest gives the best approximation, based on the literature, to natural deformed rocksalt (CRSS 1:5:5, n = 6), a maximum P-wave anisotropy of 5.5% in compression and 2.8% in simple shear is observed (Fig.3.6). However, as demonstrated the seismic anisotropy is sensitive for the tested input parameters (CRSS and stress exponent). The velocity surfaces are well approximated by a VTI symmetry.

3.6.2 Implications for reflection seismic processing

We demonstrated the potential impact on seismic processing by calculating Thomsen- and η-parameters and test the effect of such anisotropy on seismic traveltimes using a simple 2D model. We estimated the possible misfit in depth inferred to a reflector based on the parameters measured at finite strain (δ_{Comp} = -0.085 and δ_{Shear} = -0.96). Using these parameters, the base salt reflection, would have a depth misfit of nearly 10%. For a significant salt body such a misfit could implies depth estimates erring by tens of metres. This could have a serious impact on the accuracy of horizontal drilling, and consequentially on the associated risks and costs. We show that VTI is a good approximation for salt anisotropy, which is important when treating such anisotropy in seismic data.

Few studies have considered the seismic anisotropy of natural rock salt formations, despite their importance for a range of industries. This study highlights the need for further investigations of the seismic anisotropy of rock salt in the field, to test and refine the predictions of these models. We have also only made simple estimates of the effect of salt anisotropy on seismic data. Future avenues include extending modelling to S-waves (including measurement of shear-waving splitting) and for other types of seismic data (for example VSP surveys, or the passive monitoring of microseismicity).

3.6.3 Limitations of texture modelling

In modelling fabric crystal orientation, VPSC has limitations; most importantly, it only accounts for plastic deformation by dislocation. Other texture developing mechanisms are neglected, for example, dynamic recrystallisation. Recrystallisation can have a significant effect on the resulting texture. New plasticity models need to be developed to include other physical deformation mechanisms. Subgrain-rotation recrystallisation would likely not alter the lattice orientation significantly, as shown in *Gomez-Rivas et al.* (2017) or *Wenk et al.* (2009). On the other hand, grain boundary migration recrystallisation can lead to texture change. More studies are needed to infer recrystallisation mechanisms from LPO textures and quantify the effect of grain boundary migration on the LPO of rock salt. One approach to approximately capture this using VPSC, is to use a lower stress exponent. This does not capture the physics, but might provide a better

estimate of the rock salt deformation in nature.

We predict thus far only seismic anisotropy due to crystal alignment of halite crystals. Other mechanisms are not considered, such as layering or alignment of other evaporite minerals. Anhydrite and gypsum are seismically anisotropic (*Vargas-Meleza et al.*, 2015). In case of alignment of these minerals, we would expect an even larger effect. Also, seismic anisotropy of the overburden or the surrounding rocks might complicate the situation further.

3.6.4 Naturally deformed rock salt

Natural deformation conditions of salt deformation vary significantly from region to region (e.g., temperature, water content, strain-rate and strain-history...). A possible future direction would be to estimate seismic anisotropy in realistic deformation regimes, which are more complex than isolated compression or shear. In many real scenarios the deformation history of salt is highly complicated as evidenced by the often complex morphology of natural salt bodies. Such deformation history can be modelled using this approach, and future work will consider such scenarios.

Usually, salt deforms at low temperature conditions (up 100°C), but that can vary with deformation depth. Also, multiple deformation mechanisms are active. Natural rock salt and stress exponents used in creep deformation models of rock salt are in the range of 4-6. Using texture simulation, we would therefore suggest using CRSS of about 1:5:5 and a stress exponent in the range of n = 4-6.

Previous studies on texture in rock salt showed that LPO can be observed (*Schwerdtner*, 1968; *Muehlberger and Clabaugh*, 1968; *Carter and Hansen*, 1983; *Miralles et al.*, 2001), but is not seen in all observed specimens (*Vargas-Meleza et al.*, 2015; *Thiemeyer et al.*, 2016). A possible explanation is that LPO fabrics can result when rock salt is actively deforming, so that dislocation plasticity is the main mechanisms determining the texture.

This study demonstrates the effect of dislocation plasticity on salt textures and that the resulting seismic anisotropy is sufficient to significantly distort seismic images. This potentially has high impact on exploration seismology in salt tectonic regimes and challenges the common assumption of salt isotropy.

CHAPTER 4

NUMERICAL WORK FLOW ESTIMATING LATTICE ORIENTATION AND SEISMIC ANISOTROPY FROM A SALT FLOW MODEL

We present a numerical work flow combining rock salt deformation with seismic anisotropy, investigating the possibility of plastic deformation of rock salt generating seismic anisotropy. The work-flow is based on calculating strain rate evolution along multiple stream lines through a geomechanical salt deformation model in time, together with texture plasticity modelling, which simulates the change of polycrystalline lattice orientation during deformation. For demonstration purposes, we apply the work flow to an example model of a typical evolution of a salt diapir in an extensional- and compressive deformation regime with intermittent sedimentation in 2D. The results show that the deformed rock salt develops a significant amount of lattice preferred orientation and seismic anisotropy. Highly deformed areas show a universal anisotropy index (*Ranganathan and Ostoja-Starzewski*, 2008a) of uA=0.06 and a δ-parameter (*Thomsen*, 1986) of δ=-0.12. We create a synthetic seismic gather, based on the velocity and anisotropy structure, calculated by the work flow. The seismic gather mimics a typical offshore seismic measurement. We show traveltimes through an anisotropic salt model, differ significantly to an equivalent isotropic model. The amount of seismic anisotropy we predict would be enough to distort seismic images, if not properly accounted for. We numerically asess seismic anisotropy by dislocation plasticity in salt tectonic environments, which has potentially high importance for seismic imaging and processing.

4.1 Introduction

Naturally deformed rock salt is known to undergo very complex deformation. Some salt evaporite sediments are found kilo-metres away from where they were deposited originally. If rock salt deforms plastically and the crystals align in the direction of flow than this will manifest in effective seismic anisotropy. However, in traditional seismic processing, it is a common assumption to treat salt as being seismically isotropic; little attempt is made to incorporate seismic anisotropy in seismic velocity model in rock salt environments (*Jones and Davison*, 2014; *Zong et al.*, 2014).

In previous chapters we have presented observations of seismic anisotropy of the Mahogany salt body in the Gulf of Mexico, showing that rock salt can exhibit significant seismic anisotropy. We have also analysed the development of seismic anisotropy of polycrystalline halite under simple shear and compression using plasticity modelling. In this chapter we extent the work into development of anisotropy in more complex deformation regimes than just simple shear and compression. We propose a numerical work flow adapted from studies, which predict crystal alignment and lattice orientation of olivine in mantle flow and subduction settings (e.g., *Blackman et al.*, 2002a,b; *Di Leo et al.*, 2014). The evolution of texture along stream lines in salt deformation models is simulated. For this we calculate the strain rate development along specified tracer particles through the model in time. In this study, we use the word strain rate as the temporal strain derivative. Each particle represents a package of polycrystalline halite individually deformed by its path, representing the deformation history. We use the strain rate development as an input for the texture plasticity model VPSC (visco-plastic self-consistent), predicting the LPO of the entire salt body. The seismic velocities and seismic anisotropy is determined, based on each polycrystalline lattice orientation (*Kendall and Thomson*, 1989).

We apply the work flow to a model simulating the development of a typical salt diapir. In the initial geometry, a salt layer is covered by an upper sedimentary layer. The model is a 2D model and consists of two phases (salt and sediment). The salt diapir develops in an extensional and compressive tectonic regime, together with deposition of new material. The model does not resemble a specific salt diapir, but has value for different areas around the world, as it includes typical salt diapirism features, such as salt welding and the formation of a salt canopy. Salt diapirs are commonly observed in various areas, as for example in the Gulf of Mexico or the North Sea (*Hudec et al.*, 2013) (see Chapter 1).

The application shows that a significant amount of seismic anisotropy develops due to lattice orientation of the constituent halite crystals. We assume that rock salt consists entirely of halite, which simplifies the texture modelling. Furthermore, we investigate possible seismic implication due to the resulting seismic anisotropy. We create a simple 2D seismic model, consisting of a water layer at the top and sediments surrounding a salt canopy, with a geometry based on the

salt diapiric model. The model mimics a typical offshore seismic reflection experiment. By using full wave form simulations, a synthetic seismic shot-gather is created. We compare travel times in two models, where in the first model the salt diapir is implemented as being isotropic and in the second model it is considered to be anisotropic. The travel time difference arising due to lattice orientation and the associated seismic anisotropy is clearly enough to have strong influence on seismic images in rock salt settings.

4.2 Work flow

We present a numerical work flow to estimate LPO and the associated seismic anisotropy in a deformed salt body. The deformation of the salt body is described by a geomechanical deformation model. Strain along multiple path lines is calculated through the model in time. These strain paths are used to define the applied deformation for texture simulation, calculating rock salt LPO by dislocation plasticity inside the deformation model, following Chapter 3. The resulting predicted lattice orientations are taken to calculate effective elasticity tensors and thus seismic velocities of the entire salt body.

The work flow follows a method originally used in studies investigating flow-induced seismic anisotropy in, for example the upper mantle (e.g., *Blackman et al.*, 2002a,b) or in subduction settings (e.g., *Di Leo et al.*, 2014). We apply and adjust it for the case of deformed rock salt. It can be summarised in the following steps:

- Particles are traced through a salt deformation model in time. Strain along each path-line is calculated, which defines the deformation history of each particle.
- Each particle is taken to represent a package of polycrystalline halite. Texture simulation is used to calculate the LPO evolution based on the individual deformation of each halite polycrystal (this study uses the visco-plastic self-consistent (VSPC) texture modelling approach).
- The texture of each halite polycrystal is used to calculate the effective elastic constants, representing the whole polycrystal, based on the lattice preferred orientation by using a Voigt-Reuss-Hill (VRH) average of a set of single crystal elastic constants for halite. The effective elastic constants are used to calculate seismic velocities and thus seismic anisotropy.

4.2.1 Step1: Modelling strain along path lines in a geodynamic model

To define the applied deformation, passive tracer particles are followed through a salt deformation model. The texture change of a polycrystal due to dislocation plasticity depends on the strain applied through the evolution of the model. To have a good representation throughout the salt

body, many passive tracer particles are necessary. At each time step, the deformation velocity gradient tensor L of each particle is calculated. It is defined as the change of the deformation velocity with direction and defines the applied deformation entirely. The components are described by the derivatives of the deformation velocities v_x, v_y, v_z to each space direction x, y, z:

$$L = \begin{pmatrix} \frac{\partial v_x}{\partial x} & \frac{\partial v_x}{\partial y} & \frac{\partial v_x}{\partial z} \\ \frac{\partial v_y}{\partial x} & \frac{\partial v_y}{\partial y} & \frac{\partial v_y}{\partial z} \\ \frac{\partial v_z}{\partial x} & \frac{\partial v_z}{\partial y} & \frac{\partial v_z}{\partial z} \end{pmatrix}. \tag{4.1}$$

Each path line is divided into equal time steps. In each time step the velocity gradient tensor (equation 4.1) is calculated. The velocity gradient contains information about both the strain- and rotation-rate and is used as an input for the texture plasticity modelling. The velocity gradient tensor is divided into a symmetric part and skew-symmetric part, which represents the strain-rate tensor $\dot{E}_{ij}$ and the rotation-rate tensor $\dot{W}_{ij}$ (e.g. *Munson et al.*, 2013):

$$L_{ij} = \dot{E}_{ij} + \dot{W}_{ij}, \tag{4.2}$$

where the strain rate and rotation rate tensors are defined as:

$$\dot{E}_{ij} = \frac{(L_{ij} + L_{ji})}{2}, \tag{4.3}$$

and

$$\dot{W}_{ij} = \frac{(L_{ij} - L_{ji})}{2}. \tag{4.4}$$

The velocity gradients are evaluated using finite differences. At a time t the particle position is $\vec{s} = (x, y, z)$. So, for example, the first component of the velocity gradient tensor $\frac{v_x}{\delta x}$ (at time t) can be the determined numerically:

$$\frac{v_x}{\delta x}(\vec{s}, t) = \frac{v_x(\vec{s} + \vec{dx}, t) - v_x(\vec{s} - \vec{dx}, t)}{2dx}, \tag{4.5}$$

where $\vec{dx} = (dx, 0, 0)$ is a finite displacement vector in x-direction. The other components would be calculated accordingly. Here we will only look at examples which are 2d deformation models. In this case $v_z = 0$ and $\frac{v_x}{\delta z} = \frac{v_y}{\delta z} = 0$. An example demonstration is shown in Figure 4.1. The blue dots represent one single particle being traced through a model in time. Each point represents the particle position at a specific time. We only consider 2D models; the velocity gradient tensor has only four non zero components in this case. In each time step the velocity gradients of each particle position are used as demonstrated to describe the deformation history experienced by each particle.

4.2.2 Step2: Texture simulation

Each particle represents a halite polycrystal. A polycrystal aggregate is composed of multiple crystals with varying lattice orientations. Polycrystalline texture models simulate and predict the

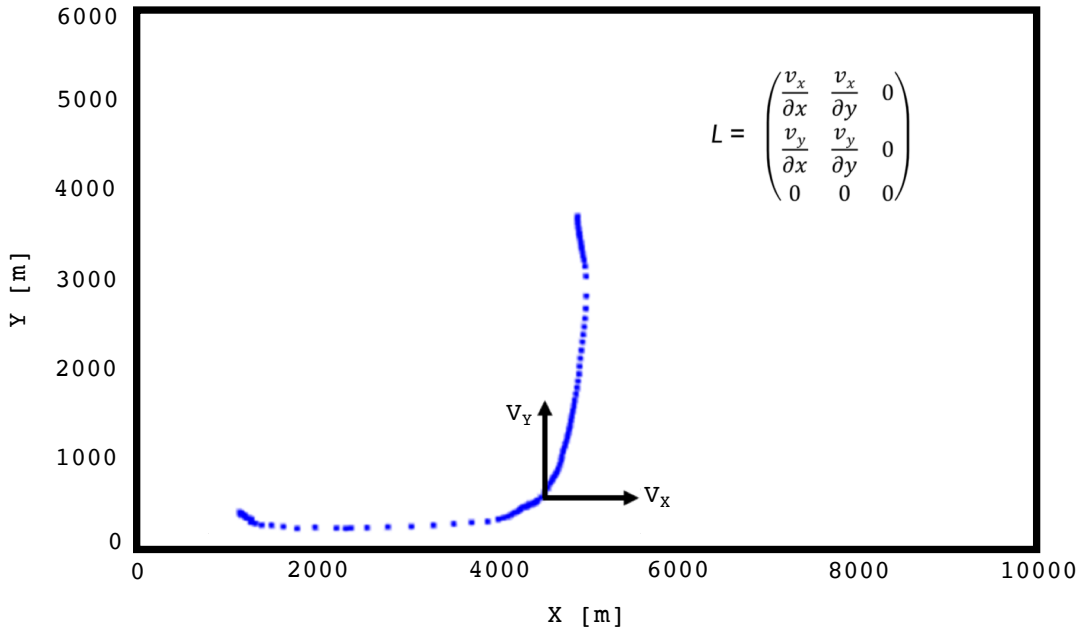

FIGURE 4.1. One particle being traced though a model in time. The blue dots represent the particle position at a specific time. The velocity gradient tensor L is calculated in each time step. This would be done for all particles being traced though the model.

evolution of lattice preferred orientation during deformation. This study uses the tangent visco-plastic self-consistent texture simulation approach (*Wenk et al.*, 1989; *Tomé and Lebensohn*, 2009). It assumes that crystals act as ellipsoidal inclusions in a visco-plastic homogeneous medium with averaged properties. The tangent VPSC method uses a more general model description, which incorporates a formulation for a plastically anisotropic visco-plastic medium (Chapter 3, or for, example *Tomé and Lebensohn* (2009) or *Lebensohn and Tomé* (1993) contain more detailed description of the plasticity code, together with underlying theory).

The input variables in VPSC are the applied deformation, single crystal properties and various numerical parameters, controlling the simulation. In VPSC, the velocity gradient tensor defines the applied deformation, which was calculated in the previous work-flow step. The single crystal properties is the elasticity and density of halite, the crystal structure, slip systems and their associated strengths.

We assume that the salt body consists entirely of halite. Modelling studies have shown that the texture of polycrystalline halite can be estimated by using texture modelling simulations (*Wenk et al.*, 1989; *Tomé et al.*, 1991; *Lebensohn et al.*, 2003; *Wenk et al.*, 2009), reproducing the textures

observed in laboratory studies.

The input parameter chosen are based on the results obtained from Chapter 3. The single elastic constants of halite are C_{12} = 14 GPa, C_{11} = 49.1 GPa, C_{44} = 12.7 GPa (cubic symmetry) and the density used for the calculation is $\rho = 2160\,\mathrm{kgm}^{-3}$ (*Gebrande*, 1982). The stress exponent used is $n = 6$ for all active slip systems and we assume a CRSS (critical resolved shear stress) ratio of 1:5:5 describing the strength of the easy ({110}<110>, CRSS = 1) and hard ({100}<110> and {111}<110>, CRSS = 5) to active slip systems. Those input parameters are best, as discussed in Chapter 3, to estimate LPO in natural deformed rock salt.

Each traced particle represents one polycrystal, consisting of 500 individual crystals. This is a high enough number to have a statistically good representation of the lattice preferred orientation and a low enough number to limit computational time. At the beginning of the simulation, crystals are randomly orientated, without any lattice preferred orientation. In this case, no effective seismic anisotropy would arise. Each polycrystal is deformed individually based on their velocity gradient tensor history (as discussed above). After each deformation step, the crystal orientation is updated. After the simulation, each polycrystal has a specific lattice preferred orientation, described by the Euler angles of each crystal lattice. The resulting lattice orientation for each polycrystal is dependent on the specific deformation it experiences.

4.2.3 Step3: Elasticities

After the deformation, each polycrystal has a distribution of directions for its composing crystals, dependent on the deformation is has experienced. The effective elasticity tensor of the polycrystal is then calculated. This is achieved by utilising the Voigt-Reuss-Hill (VRH) averaging technique (*Hill*, 1952). The VRH-average represents an average across all elasticity tensors, rotated by the Euler angles of each individual lattice orientation. In effective medium theory, the Voigt-representation is an upper bound approximation on the stiffness tensor, assuming the same strain across the polycrystal. The Reus-model is a lower bound-approximation, assuming that the state of stress is uniform everywhere. The VRH-average is then defined as the mean of the elastic stiffness between those two end-member models (*Hill*, 1952).

After the VRH-average is calculated, each polycrystal is represented by a single effective elasticity tensor. The seismic group velocity can be calculated for a given wave front and a set of elastic constants (*Kendall and Thomson*, 1989) with the Christoffel equation (see Chapter 1). Seismic velocities for all polarisation directions define the anisotropic velocity surface of each polycrystal. This process is repeated for all particles. The LPO and the associated seismic anisotropy inside the entire salt body is estimated. Halite is seismically anisotropic at the single crystal scale (7 % P-wave velocity and 16 % S-wave velocity, see Chapter 1). Those are the highest possible values

of deformation-induced seismic anisotropy of a halite polycrystal, as those would correspond to the case where all crystals are aligned in the same direction.

Once a model consisting of the elasticity tensors for salt has been calculated, the work flow is effectively finished and can be followed by further seismic analysis. The work flow can be applied to any salt deformation model. Using texture simulation, the LPO by dislocation plasticity and the associated seismic anisotropy can be assessed quickly.

4.2.4 Limitations of the workflow

The work flow, presented above is based on various assumptions. Halite texture changes and depends on various mechanisms and processes. Those processes include dislocation plasticity, dynamic recrystallisation and pressure solution creep (*Urai*, 1987; *Drury and Urai*, 1990; *Urai and Spiers*, 2007), which all may contribute to the texture. The texture model in use only considers plastic deformation by dislocation (as discussed in Chapter 3). We recognise this as a possible limitation, although several studies showed that naturally deformed salt can exhibit significant lattice preferred orientation (*Muehlberger and Clabaugh*, 1968; *Schwerdtner*, 1968; *Kern and Richter*, 1985; *Miralles et al.*, 2001). Grain boundary migration tend to weaken the occurring texture in rock salt (*Trimby et al.*, 2000). To date, no texture simulation which incorporates grain boundary migration has been applied to polycrystalline halite. It is clear that grain boundary migration will be active in naturally deformed rock salt. However, it is not clear how large the effect of grain boundary migration on lattice orientation in natural rock salt is and how to quantify the potential loss of LPO.

We also assume that the salt body consist entirely of halite. This assumption might be sensible for areas where the salt is very pure. However, rock salt might vary in content of, for example, anhydrite, which is also very seismically anisotropic on its own (*Vargas-Meleza et al.*, 2015). Other mechanisms, such as layering are not included as a cause of seismic anisotropy. We speculate that if other minerals contribute to the rock salt, higher seismic anisotropy would be predicted, as other evaporites are seismically more isotropic on single crystal scale than halite.

4.3 Example deformation model: a simple salt diapir

We demonstrate the work flow by applying it to an example deformation model, simulating a simple salt diapir. Its geometry and evolution is not based on a salt specific real diapir, but captures features which are observed typically in salt diapirism, as for example, welding and the development of a salt canopy. It is very suitable to test the work flow on, as generally salt diapirs are common salt structures and can be found in many areas (*Jenyon*, 1986; *Hudec et al.*, 2013), for example, salt canopy predicted by the deformation model is very similar to those found

along the Angola margin (*Fort et al.*, 2004). The model is a ready-built model by Rockfield Global, which was created to demonstrate their software Elfen's capacity to model strain-evolution in adjacent sediments around a typical salt diapir (*Rockfield Global*, 2014). We use the model to demonstrate the work-flow.

The model is a forward plane-strain finite-element model, simulating a high resolution salt diapir and the halokinetic sequence in an extensional and compressive tectonic regime in 2D. This model is built and run using the finite-element software package Elfen, provided by Rockfield Global. Elfen can be utilised to solve a range of different geomechanical and physical problems and is suitable to analyse geological simulations. Elfen has been previously applied to model deformation in salt deformation settings (*Heidari et al.*, 2016; *Thigpen et al.*, 2019). The Elfen geomechanical computational frame-work used in this work is summarised briefly below.

4.3.1 Finite element numerical modelling

A range of studies investigate salt tectonics with the use a finite-element frame work (*Ings et al.*, 2004; *Gemmer et al.*, 2004, 2005; *Allen and Beaumont*, 2012). This work uses the 2D-plane strain finite-element models developed and run using Elfen numerical codes from Rockfield Global. A complete description of the computational framework is found in *Perić and Crook* (2004); *Thornton and Crook* (2014). The governing equations are the equations of linear-momentum balance (*Thigpen et al.*, 2019):

$$\nabla \cdot \left(\sigma' + \alpha I p_f\right) + \rho_B(\phi) g = 0, \tag{4.6}$$

∇ is the gradient operator in space direction, σ' is the effective stress tensor and α is the Biot coefficient, p_f is the pore-pressure, I is the second order identity tensor and $\rho_B(\phi)$ is the bulk density and g is the gravitational constant. The bulk density is defined as

$$\rho_B = \left(1-\phi\right)\rho_s + \phi\rho_f, \tag{4.7}$$

where ϕ is the porosity, ρ_s is the rock density and ρ_f is the pore fluid density. It can be shown, that from a bulk volume strain perspective, the Biot coefficient may be defined as (*Thornton and Crook*, 2014):

$$\alpha = 1 - \frac{K'}{K_S}, \tag{4.8}$$

where K' is the bulk modulus of the rock and K_S is the grain stiffness. The deformation is assumed to be quasi-static and inertia-terms are omitted from equation 4.6 (*Rockfield Global*, 2013). The mechanical field is solved by central differences in time to advance the solution (*Rockfield Global*, 2013). The Langrangian formulation of the kinematic equation can result in distorted finite element meshes. An automatic adaptive remeshing algorithm is used to handle

mesh distortion. Elfen uses the advancing front technique, described in *Peraire et al.* (1987). In the advancing front technique, new mesh elements are progressively added, starting at the boundaries of the mesh to presence model preserve model resolution in region of large strain.

4.3.2 Model properties

The deformation model covers the following typical phases of salt diapir behaviour (*Rockfield Global*, 2014):

- Reactive intrusion of the overburden by salt during regional extension
- Active ascent driven by salt buoyancy, along with upward rotation of adjacent sediments during diapir breakthrough
- Passive syndepositional growth
- Thrust related squeezing during lateral compression
- Developing of a canopy and a weld

The evolution of the model in time is shown in Figure 4.2. The initial model dimensions are 10 000 m × 2200 m. The model consists of two phases, which are the salt and the sediments. The salt (800 m thick) is initially is buried by sediment (1400 m thick) covering the salt layer. The model consists of six tectonic sequences, including of compression, extension and sedimentation with different duration and compression- or extension rates.

Deposition is implemented in the model by an aggregation method, where sedimentary layers are deposited until a specified horizon is reached (*Rockfield Global*, 2013). The horizon is placed above the top of the domain in each sedimentation step.

During the deformation, sedimentary layers can be highly stretched which may lead to significant layer thinning. In this study two approaches are applied in combination to control layer thinning. These are pinch-out prevention, where the thickness of a layer can not fall below a specific value and geometric pinch-out, where layers are allowed to pinch out and break over the emerging salt (*Rockfield Global*, 2013).

Geostatic initialisation is used to establish current-day stresses before the domain is extended and then compressed in a series of stages, with quiescent periods interspersed by intermittent sedimentation (*Rockfield Global*, 2014). For the first 5.5 Myrs the model regime is extended, with applied external forces. During this process, the overburden is lengthened and thinned. The salt fills the resulting spaces and grows laterally. After 5.5 Myrs the model is compressed and the salt continues to flow upwards. The salt pierces the sediments and extrudes at the surface. The

compressional forces form eventually a salt canopy, visible at around 9 Myrs. A salt weld begins to form, connecting the canopy and the salt source layer beneath. With ongoing compression, the canopy is detached and reaches the final model state at 14 Myrs (Figure 4.2).

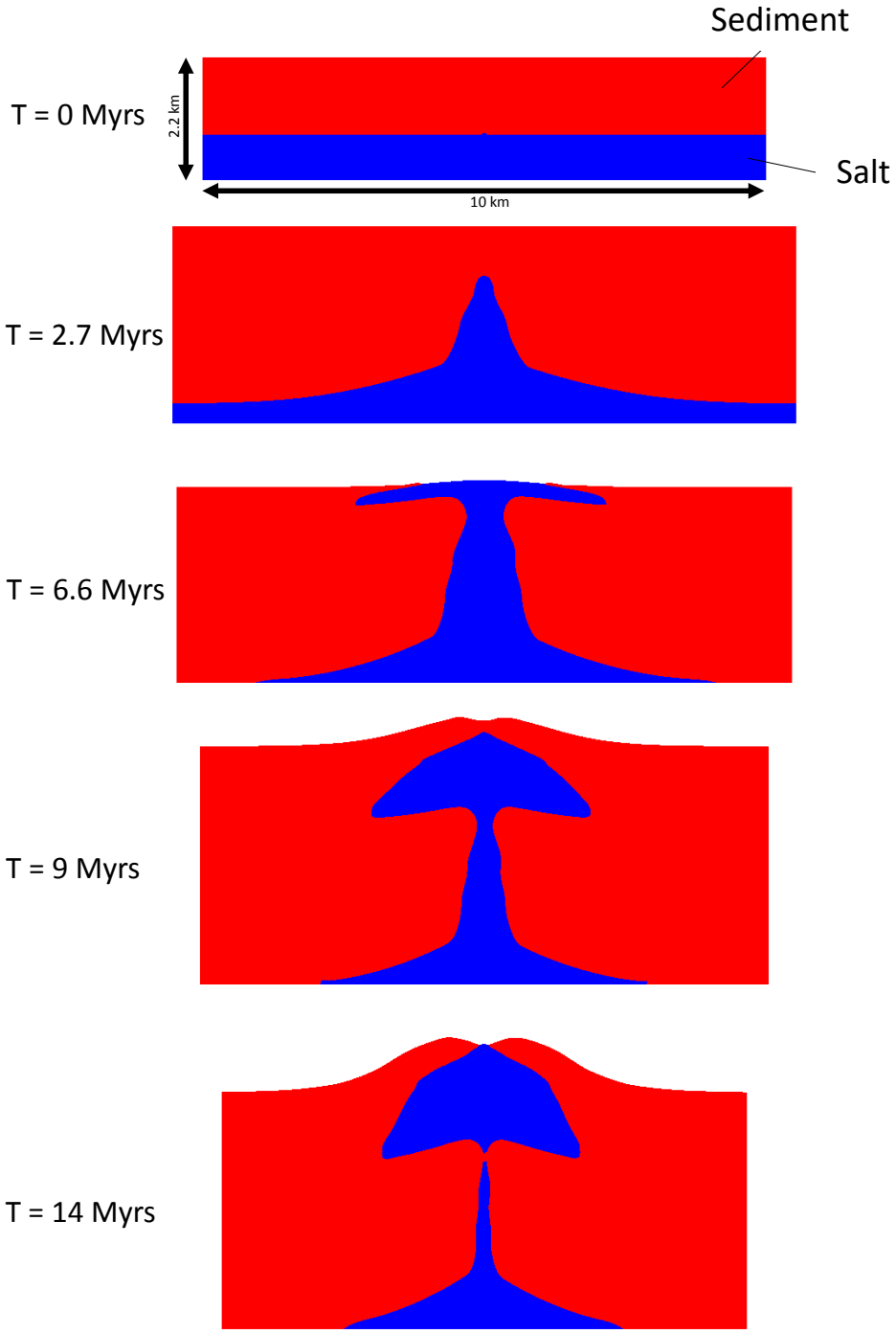

FIGURE 4.2. Evolutionary geomechanical 2D salt diapir model, created and run with the finite-element code Elfen from Rockfield Global (*Rockfield Global*, 2013). The model is initially 2.2 km × 10 km. The model domain experiences extension and compression in a series of stages accompanied sedimentation. Typical salt diapir behaviour is taken into account, such as salt welding and the formation of a canopy (*Jackson and Hudec*, 2017a). The salt has an assumed density of $\rho_{Salt} = 2.16 gcm^{-3}$ and is modelled as a Newtonian fluid with a viscosity of $\mu = 10^{19} Pas$.

4.3.3 Model rheology

In following the material rheology of the sediments and salt is described. The salt is modelled using a Newtonian fluid model and the sand deformation behaviour is approached by using a modified cam-clay model (*Drucker and Prager*, 1952). The model is a pre-built model by Rockfield Global, which was originally used to investigate sediment stress- and strain changes in salt diapir settings. Stress changes are an important safety issue, which must be considered when drilling in such environments. For that reason, the salt rheology is kept simple, and the sediment rheology is approached by a more sophisticated rheology model. However, the model is an adequate test case for the workflow to, which is independent of the deformation model and the applied material rheology.

Newtonian salt rheology

The rheology of the salt is modelled using a Newtonian fluid model, with a viscosity of $\mu=10^{19}$Pas and a density of ρ_{Salt} = 2.16gcm^{-3}. In a Newtonian fluid, the applied viscous stresses are proportional to the local strain rate:

$$\tau = \mu \frac{du}{dy}, \tag{4.9}$$

where τ is the shear stress, μ is the shear viscosity and $\frac{du}{dy}$ is the shear rate (*Munson et al.*, 2013). Although more sophisticated salt creep rheology models exist, it has been assumed in several studies that rock salt behaves like a Newtonian fluid on geological time scale (*Van Keken et al.*, 1993; *Koyi*, 1996).

SR3 model

The rheology of the sediments are modelled using the SR3 material model. The SR3 material model is a constitutive critical-state poroelastic-plastic material model, based on the "cam clay" material model concept (*Drucker and Prager*, 1952). It has been used to model strain in adjacent salt sediments (e.g. *Heidari et al.*, 2016). See Appendix E for a description of the model rheology, including the parameter used in this study.

Model limitations

The fact that the salt rheology model (viscous) is modelled differently than in the texture modelling (visco-plastic), is a limitation. However, the work-flow is only dependent on the deformation in time, specifically, the change of the deformation velocities in space directions. Also, while deformation proceeds, mechanical parameters of the material changes which could potentially be a feedback into a non-linear model parameterisation. This feature is not included in the current salt rheology, but can be subject of future work.

4.4 Results

We perform forward simulation, where the initial coordinates of the particles are defined, without knowing where the particles will end up after the deformation is complete. Strain along 882 particle paths are calculated. The accrued finite strain inside the salt canopy for each particle and a histogram displaying the distribution of finite strain is shown in Figure 4.3. Here, only the salt diapir head is considered. The salt diapir is highly deformed with final Von-Mises finite strains up to 50. The most deformed part is the base of the canopy, but generally, high deformation is observed. Throughout most of the salt, strain between 5-10 is reached (Figure 4.3).

The initial and final position of all traced particles is displayed in Figure 4.4, together with six example complete deformation paths. The deformation history shows that the particles experience complex deformation, and are all deformed individually. At each time step the velocity gradient tensor is calculated. Each particle undergoes individual and complex deformation. To better distinguish the deformation style, we separated the shear-components ($\dot{\varepsilon}_{xy}$ and $\dot{\varepsilon}_{yx}$) and the normal-strain components ($\dot{\varepsilon}_{xx}$ and $\dot{\varepsilon}_{yy}$) from the strain-rate tensor. The normal strain corresponds to compression or extension. Due to the symmetry of the strain rate tensor $\dot{\varepsilon}_{xy} = \dot{\varepsilon}_{yx}$. The evolution of shear- and normal strain for each particle is displayed in Figure 4.5. The particles undergo very complex deformation; each particle experiences an individual strain-path. Although the deformation is complex, shear strain is the dominant style of deformation. Nevertheless, it might be insufficient to approximate the deformation purely by simple shear or compression/extension.

Figure 4.6 shows the final lattice orientation of two halite polycrystals after deformation at finite strain and their calculated shear-wave velocity surfaces. Their location within the model is highlighted by two red points, P1 and P2. One polycrystal is taken from the the base of the canopy and experienced high deformation (P1). The other point is taken from the centre/top of the diapir head, an area which shows comparable weak deformation (P2). The texture is shown as an upper hemisphere, equal area projection pole figure for the (100), (110) and (111) crystal plane. The polycrystal at point P2 is not highly deformed. Therefore, the texture and consequently, the seismic anisotropy is lower. The texture is representative for other polycrystals from the centre part of the diapir head. On the other hand, the polycrystal at the point P1 is highly deformed. The base of the diapir head is heavily sheared and shows generally higher deformation and higher seismic anisotropy (Figure 4.7 displays seismic anisotropy inside the salt model). The texture is more pronounced than the texture seen for the polycrystal at point P2, and the associated anisotropy is also higher. In conclusion, the deformation behaviour and the development of fabric in this salt diapir is complex. A general relation between higher strain/deformation and higher seismic anisotropy can be seen. However, the anisotropy pattern remains complex.

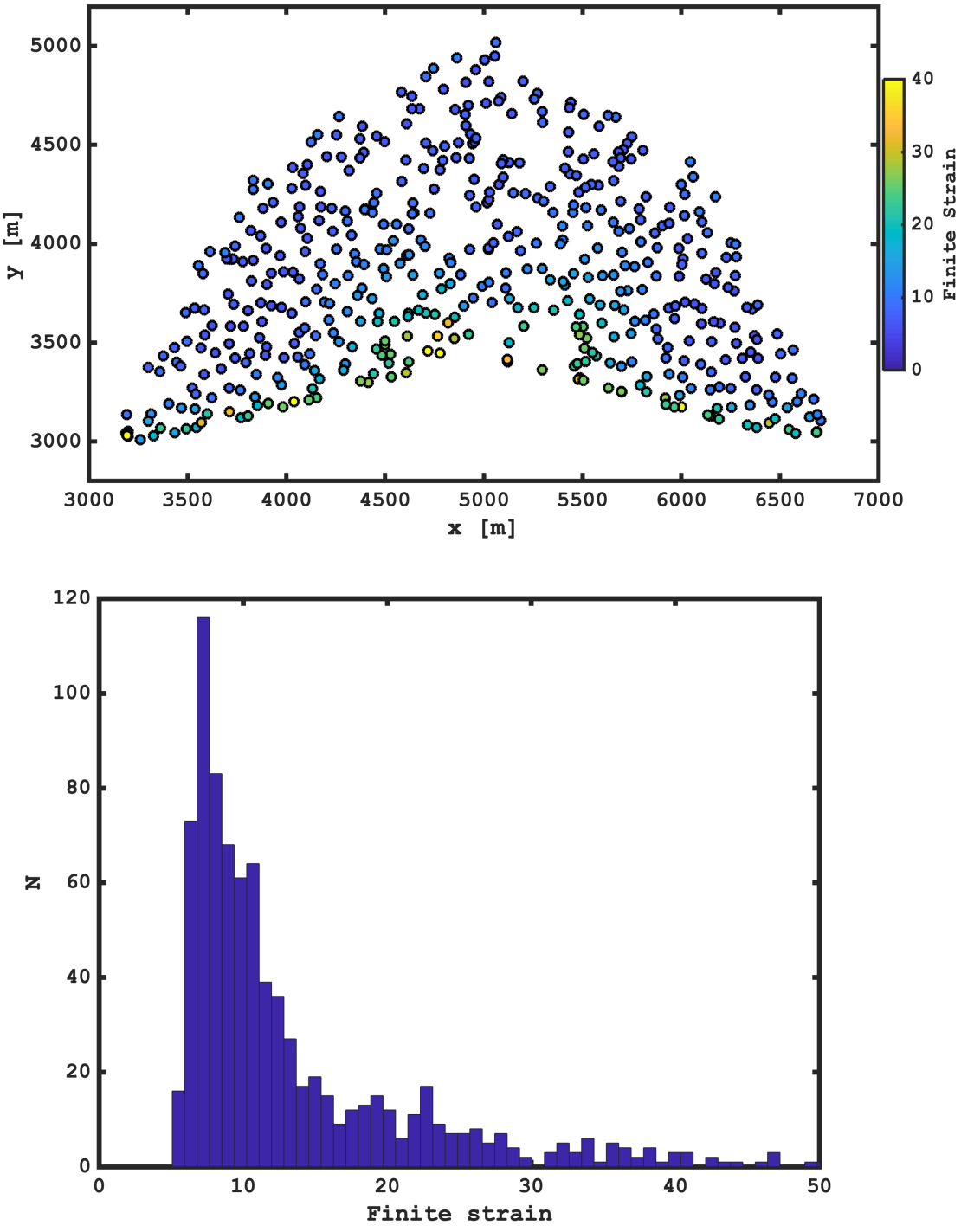

FIGURE 4.3. Final finite Von-Mises strain inside the salt diapir (upper panel). The diapir is highly deformed, with strains up to 50. The most deformed part is the base of the salt canopy. Strain histogram of all particles is shown (lower panel). Most of the particles experienced a deformation of a finite Von-Mises strain between 5-10 during model evolution.

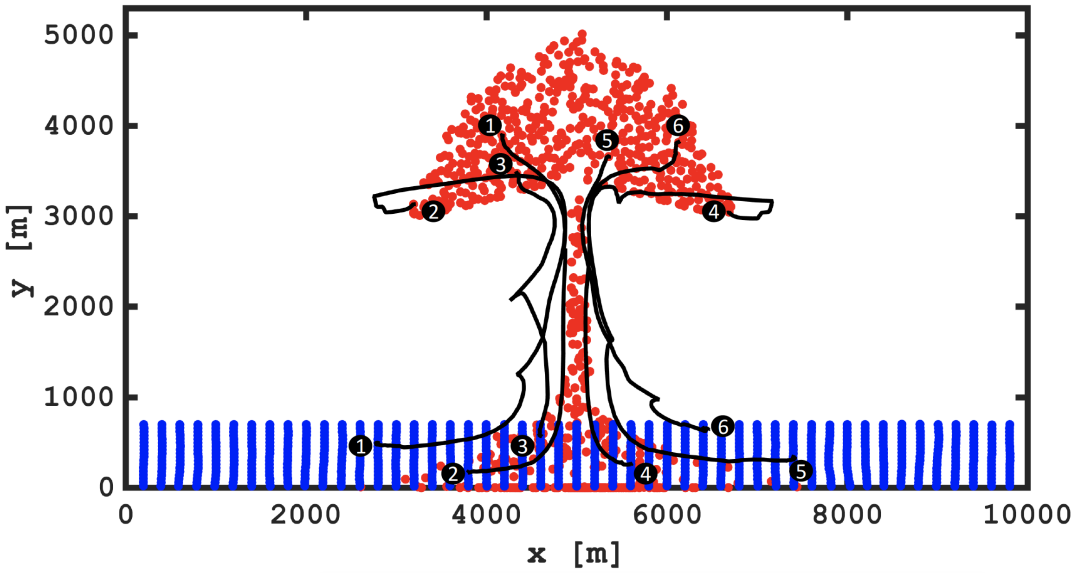

FIGURE 4.4. Starting (blue) and ending (red) points of all traced particles are shown. 882 particles are traced through the salt diapir deformation model in time. Six example deformation path are displayed, where the positions of the particles throughout model evolution are shown. This highlights the complexity of each individual deformation path.

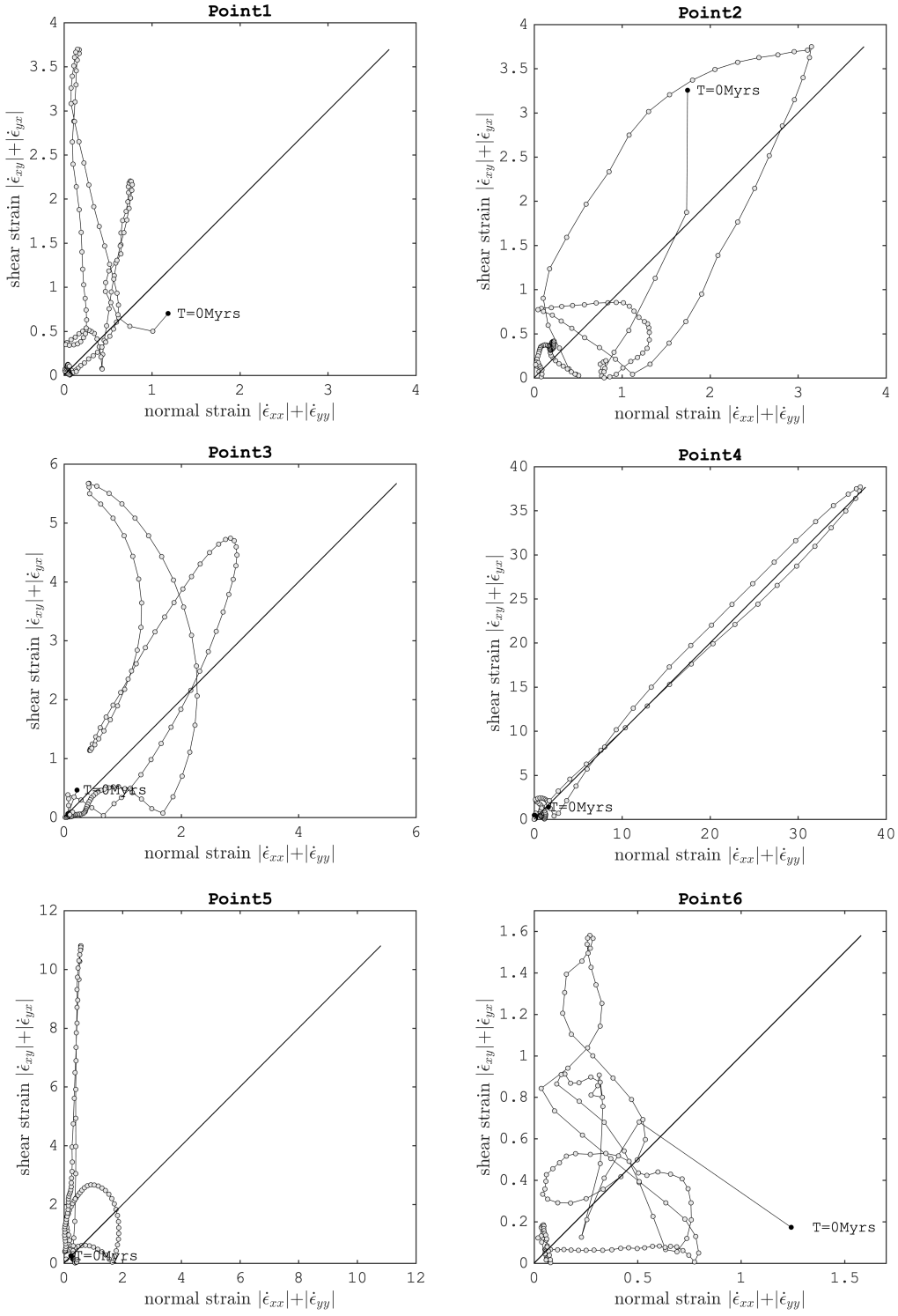

FIGURE 4.5. Shear-strain rates ($|\dot{\epsilon}_{xy}| + |\dot{\epsilon}_{yx}|$) and normal-strain rates ($|\dot{\epsilon}_{xx}| + |\dot{\epsilon}_{yy}|$) of the six particles shown in Figure 4.4 are shown in relationship to each other. Along the black line, shear- and normal shear rates are equal, referring to plain-strain. Shear-strain is the dominant deformation for the particles 1, 3 and 5, while for particles 2 and 4, plain-strain is observed. Particle 6 experiences generally lower deformation with low observed shear rates.

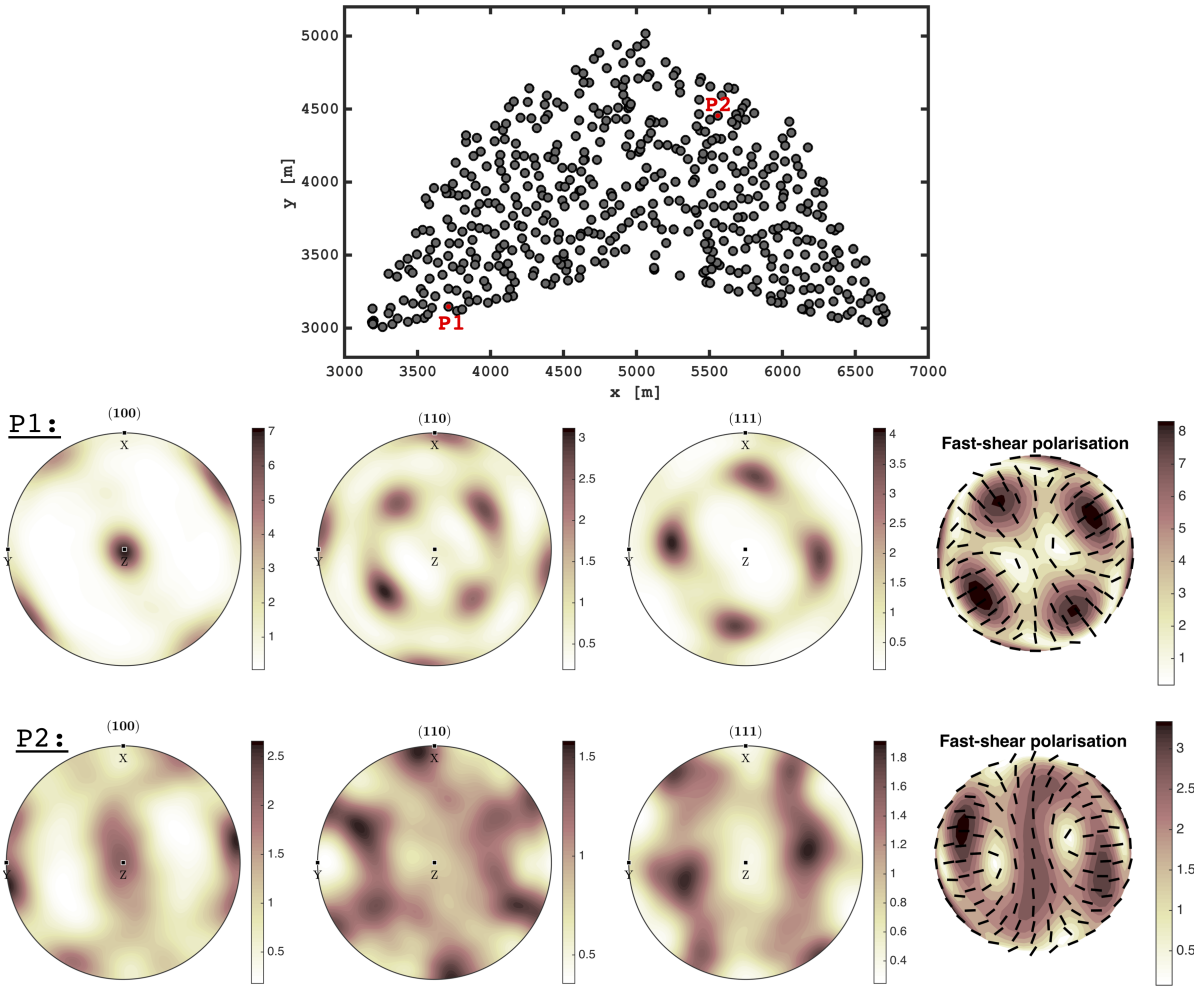

FIGURE 4.6. Deformation texture of two halite polcrystals deformed by their individual deformation path inside the diapir. The final position of the polycrystals are shown in the upper panel (P1 and P2). The pole figures show the lattice orientation of both polycrystals. Upper hemisphere equal area projections both polycrystals, together with the resulting S-wave anisotropy surface are shown. The units of the pole figures colour-scale are multiples of random distribution (MRD) (see the Appendix D). The pole figures are oriented such that the x-direction is to the North, the y-direction to the West and the z-direction is out of the plane. The textures of the three principle planes of a cubic crystal are displayed (projection planes are (100), (110), (111)). The polycrystal at position P2 has not been deformed extensively. The resulting texture is weak, and the resulting seismic anisotropy is comparably small (3.5% S-wave splitting). The polycrystal at point P1 is highly deformed. The texture is strong as consequently is the seismic anisotropy (8% S-wave splitting).

We assign calculated seismic anisotropy values to the model. For each traced particle, which represents one polycrystal, the effective elasticity tensors and their seismic anisotropy is calculated. The results are shown in Figure 4.7. Motivated by the observation in the last chapter, showing that salt anisotropy may be approximated by a VTI symmetry (which is a commonly assumed symmetry in seismic data processing) we show the Thomsen δ-parameter calculated for each effective elasticity tensor. The salt diapir stem is not shown here, as we are interested in seismic reflection from the base of the canopy. The δ-parameter is most negative at the highly strained areas inside the salt diapir, which is around the base of the canopy, consistent with the observations in the last chapter. Also shown is the universal-anisotropy index UA (*Ranganathan and Ostoja-Starzewski*, 2008a). The UA-index is valid for any elasticity matrix, and is not limited by symmetry assumptions. It is zero in the isotropic case and increases with increasing anisotropy. It takes into account all polarisation directions, and gives therefore a good representation of the overall seismic anisotropy. For a detailed description, see *Ranganathan and Ostoja-Starzewski* (2008a). The UA-index is highest at the base of the canopy, which is the most deformed part of the diapir, consistent with the observation of the δ-parameter. The model is a synthetic example, showing how much seismic anisotropy due to crystal plasticity can arise in a deformed salt diapir.

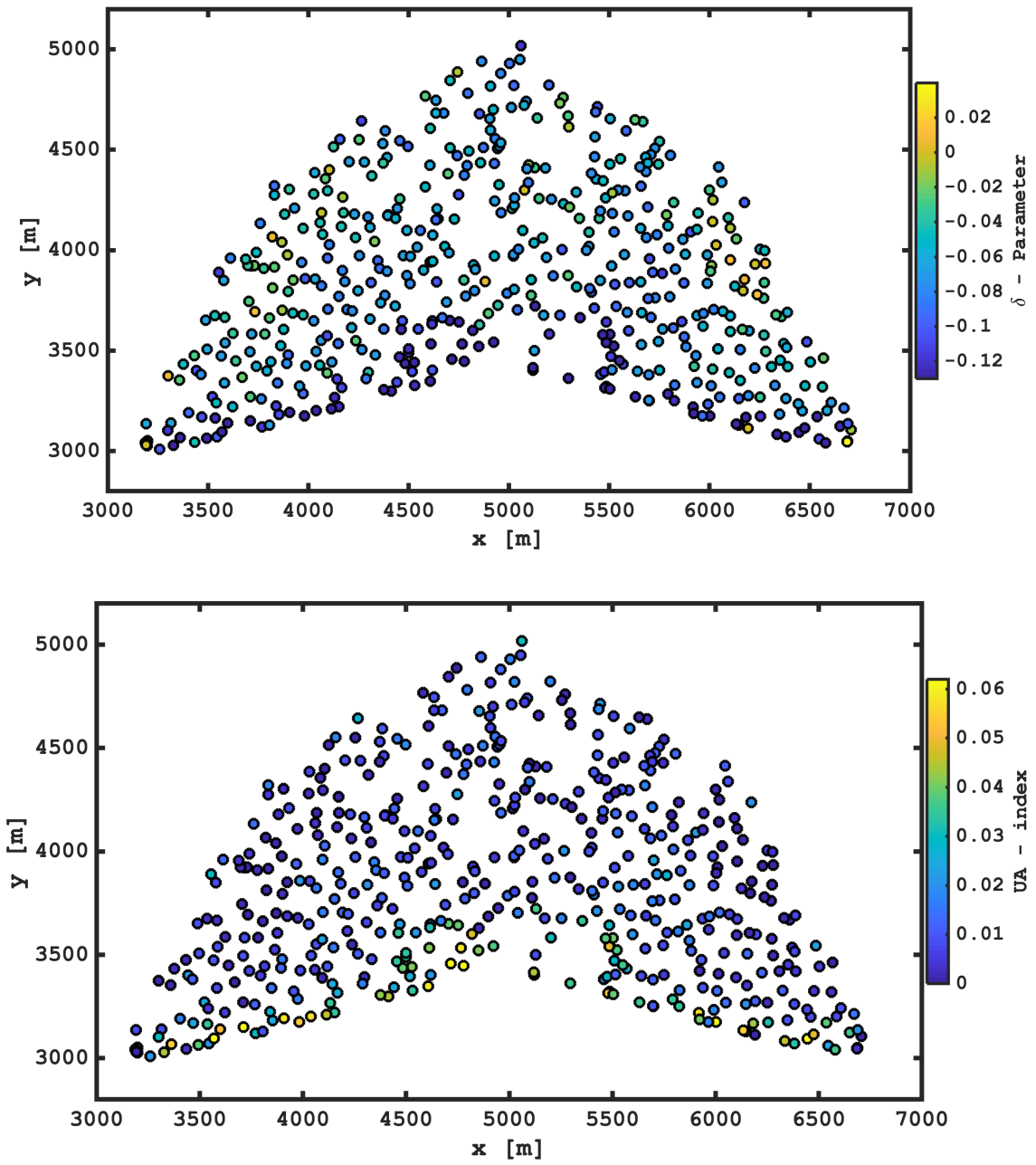

FIGURE 4.7. Seismic anisotropy arising inside the salt diapir due to lattice orientation by plastic deformation. Shown is the Thomsen δ-parameter for each effective elasticity constant. The anisotropy pattern is complicated, but it is possible to recognise parts which shows stronger seismic anisotropy. The base of the diapir head is generally higher in seismic anisotropy. The centre of the diapir appears rather undeformed and generally shows lower seismic anisotropy. The universal-anisotropy index UA (*Ranganathan and Ostoja-Starzewski*, 2008a), shown in the bottom panel, is also highest at the base, consistent with the Thomsen-parameter.

4.5 Implications and applications

Lattice preferred orientation of rock salt and the accompanied seismic anisotropy might have significant influence on, for example, reflection seismic imaging. We demonstrate this by building a synthetic seismic shot gather. The model imitates a simple 2D marine data acquisition set-up, typical for offshore exploration seismology. The synthetic data is created using full-wave form modelling. The simulation is performed using the modelling software Specfem2D (*Komatitsch and Tromp*, 2002a,b). Specfem2d is based on the spectral elements method (*Wang and Cai*, 2014) (SEM). It has been frequently used to simulate wave propagation. A summary is provided in the Appendix F.

The computational mesh is created with the open source software GMSH (*Geuzaine and Remacle*, 2009), a tool, written in C++ for 2D and 3D mesh generation, which can be used for numerical simulations. Once the mesh is generated it does not change dynamically in time and can be used throughout the simulation. When generating the mesh, the modelling domain is subdivided into non-overlapping elements. Classic spectral-element methods only support 2D/3D hexahedral unstructured mesh elements (*Chaljub et al.*, 2007).

4.5.1 Synthetic seismic gather

The generated seismic model is two dimensional and consists of a water layer at the top of the model and sediments surrounding a salt canopy. The geometry of the salt canopy is based on the salt diapir deformation model. To analyse reflections from the base of the salt body, a simpler model version is designed, where only the salt canopy is considered. The source is located at 20 m depth in the water, closely beneath the surface in the centre of the model (at x = 3000 m). We use a Ricker wavelet with a frequency of 20 Hz as the elastic source, similar to typical seismic marine source parameters.

In total 101 velocity receivers are used, which are located at the water surface. The maximum offset is 2500 m. The first receiver is located at x = 500 m and the last receiver at x = 5500 m, with a receiver spacing of 50 m. In total we analyse 3 s of wave-form propagation. For each model, we simulate waves polarised in the vertical (x-z) plane. We analyse two models. In the first one, the salt body is treated as isotropic. The isotropic velocity of the salt is based on the elasticity tensor of halite. The single halite elasticity tensor is decomposed in isotropic- and anisotropic components. The P- and S-wave velocities are then calculated, using the isotropic elasticity tensor. In the second, an anisotropic salt body is included. The velocities are based on the provided work flow applied to the geomechanical salt diapir deformation model. Each traced particle has a specific effective elasticity tensor. Every mesh element is assigned with the elasticity tensor of the closest traced particle. In both models the salt is assigned with a constant density of

$\rho_{Salt} = 2160\,kgm^{-3}$.

The waveform images are saved at specified time steps. Figure 4.8 shows the calculated wavefield after 0.84 s (upper panel), showing some identified phases. In general, the wavefield becomes complicated with ongoing time. Reflections from the bottom of the salt body are hard to identify in the wave field images, as the impedance contrasts permits most seismic energy to enter the salt base. . This is a common problem in imaging salt structures seismically (*Jones and Davison*, 2014). The synthetic seismograms are shown in the lower panel, together with the full-wave form difference between the isotropic and anisotropic model. The phases marked on the wave field plot are identified in the shot-gather. The phase reflected from the bottom of the canopy can be seen most clearly in the wave form difference plot. This reveals that seismic anisotropy effects the resulting traveltimes significantly. The largest difference appears on phases which travelled through the salt. However, phases reflected at the top of the salt are effected by the seismic anisotropy, as the reflection coefficient is affected. The geometry of the salt body effects the travel time curves, which are non-hyperbolic because of the shaped diapir head. While important, the effect of the salt geometry is not the focus of this study. This study investigates imaging distortion due to LPO and seismic anisotropy of the salt body.

To demonstrate how seismic anisotropy we compare seismic traveltimes between the isotropic- and an anisotropic model. At an offset of x = 4200 m the P-wave phase reflected at the bottom of the salt diapir is shown in Figure 4.9. The bottom reflected P-wave shows a travel-time difference of 15 ms between the isotropic and the anisotropic model. The amplitude is also affected. This simple model application shows that lattice preferred orientation of halite polycrystals can lead to significant seismic anisotropy (Figure 4.9).

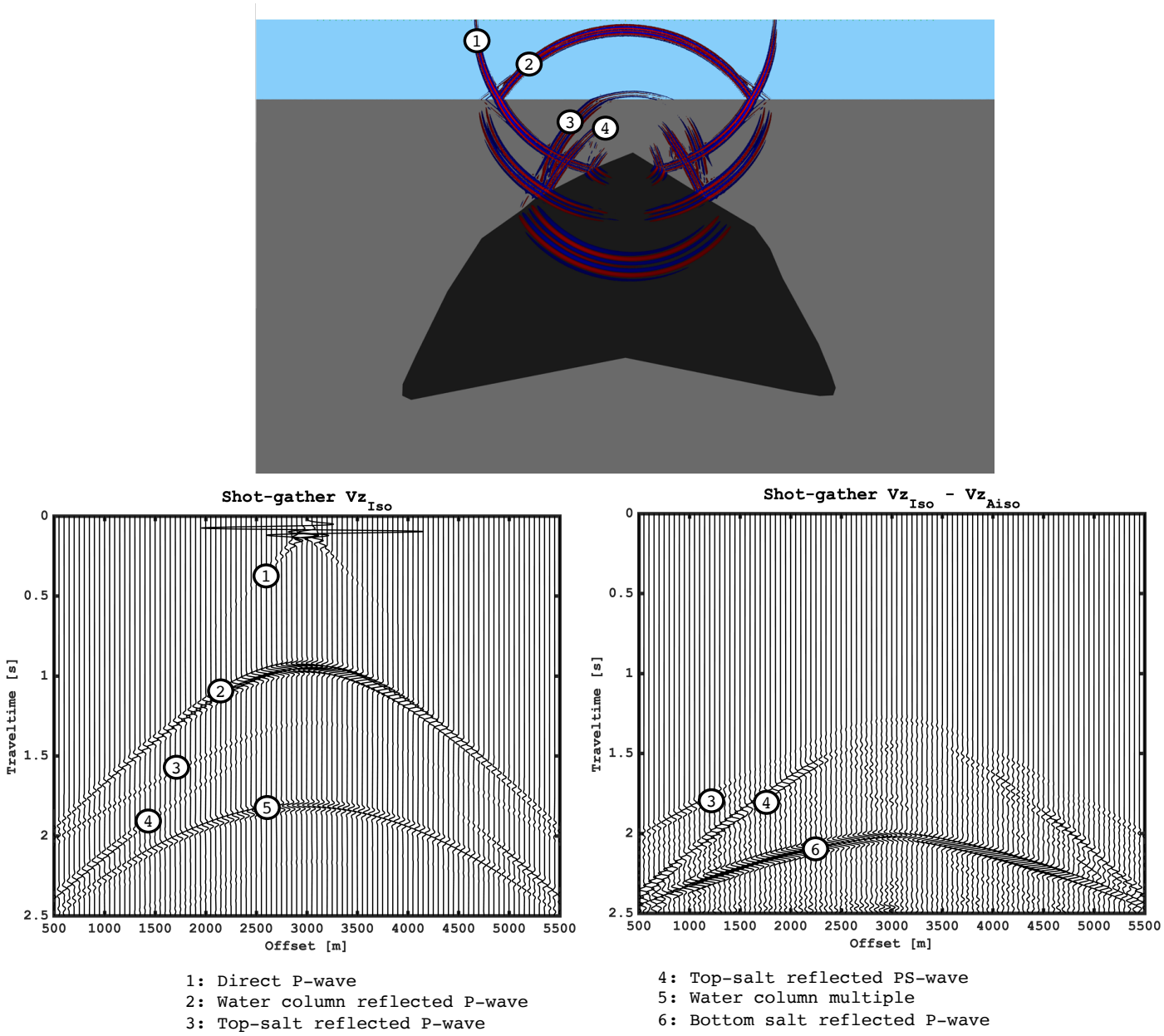

FIGURE 4.8. Simple seismic model mimics seismic offshore measurements. The amplitudes of vertical velocities after 0.84 s of travel time are shown in the upper panel. The synthetic seismograms for the 101 receivers, located at the water surface, are shown in the lower panel. The traces are scaled to make the reflections more apparent. Some reflections can be seen clearly, like the direct P-wave, the reflected P-wave from the top of the sedimentary layer as well as reflections from P-wave and P- to S- converted wave at the top of the salt diapir.

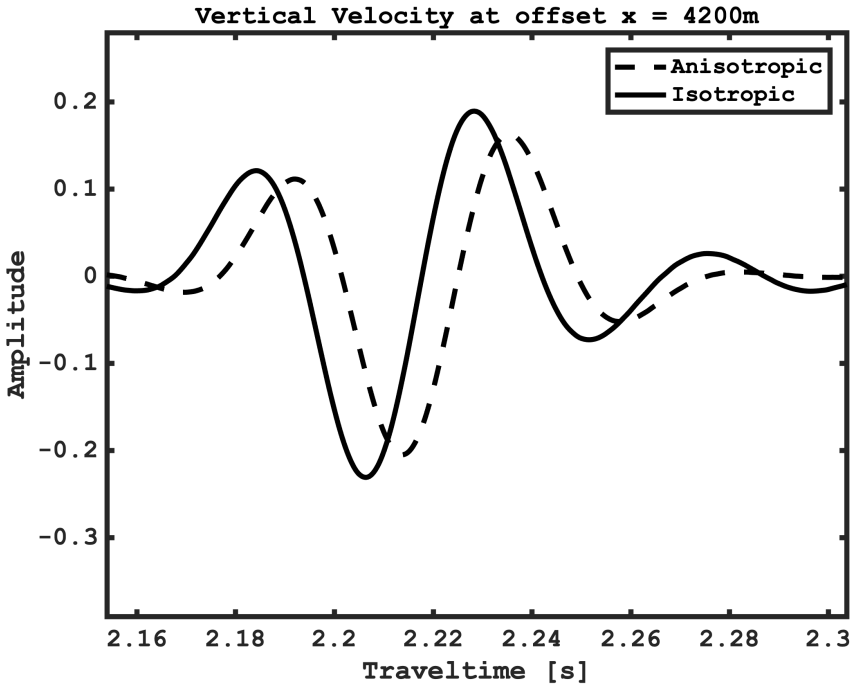

FIGURE 4.9. Vertical velocities at one single offset (x = 4200 m) of the anisotropic and isotropic model in comparison. Shown is the reflected PS-wave at the bottom of the salt layer.

4.6 Conclusions

We develop a numerical work flow to estimate LPO and seismic anisotropy in any rock salt deformation model. The work flow is based on the texture simulation model VPSC. VPSC predicts lattice orientation due to deformation crystal plasticity. The deformation is input as the velocity gradient in space direction of strain lines through the model in time. After the texture simulations, a full elasticity model of the salt is calculated by VRH averages of each polycrystal. Using the provided work flow provides an estimate about the expected lattice preferred orientation of the rock salt due to deformation plasticity and the accompanied seismic anisotropy.

We applied the work flow to a sample deformation model. The model resembles the evolution of a salt diapir. The diapir is not based on a specific salt diapir or region of the Earth, but includes general aspects of salt diapirism. This example is followed by a possible application of the calculated anisotropy. We create a seismic model, consistent of a water layer at the top of the model and a salt canopy being surrounded by isotropic sediment. The geometry of the salt body resembles the salt canopy from the geomechanical deformation model. We use Specfem2D to generate a synthetic common-shot gather. The synthetic gather mimics a typical offshore

seismic reflection measurement. The application shows that a travel time difference of about 15 ms is observed at the receivers at an offset of 4200 m, between a model treating the salt as isotropic and a model treating the salt as anisotropic. The full-wave form difference between the isotropic and anisotropic model reveals that anisotropy have a large effect on the seismic travel-times. Assuming salt isotropy is insufficient. Phases, reflected at the top are effected by seismic anisotropy as well. This potentially effects seismic imaging significantly.

The work shows a first step in estimating seismic anisotropy inside a deformed salt body and its seismic consequences, purely based on the deformation of the salt body. The work flow is simple and can be expanded, by, for example, using more sophisticated texture simulation techniques, which considers recrystallisation mechanisms. Also, possible anisotropy effects of areas around the salt are not considered here. The estimated seismic anisotropy and the work flow might be incorporated into traditional seismic processing schemes.

The example shows that high seismic anisotropy can be generated by deformation of salt bodies. In areas of high deformation, high seismic anisotropy is predicted, for example, at the bottom of the salt diapir head. Considering salt structures as seismically isotropic can lead to wrong subsurface images of salt structures.

CHAPTER 5

A DEFORMATION MODEL OF THE MAHOGANY SALT BODY – LPO AND SEISMIC ANISOTROPY

In this chapter, a forward geologic evolutionary model of the Mahogany salt body, located in the Gulf of Mexico is developed, simulating the evolution of a near surface salt diapir extruding into an advancing salt sheet in a compressional tectonic regime. Salt sheet geometry and size are based on the present geometry of the Mahogany salt body. The model properties are constrained with typical Gulf of Mexico properties, including material rheology, strain- or sedimentation rates. A methodology, established in Chapter 4, to model evolution of halite texture and associated seismic anisotropy, is applied to the geomechanical salt deformation model. A seismic model is created, considering salt anisotropy by deformation and crystalline LPO. Further, a synthetic vertical seismic profile (VSP) dataset is built, which acquisition imitates the VSP field data set from the Mahogany salt body, presented in Chapter 2. Shear wave splitting of SV- and SH polarised shear waves, travelling through the salt are compared with those from the VSP field data results. Delay times and fast-direction of the synthetic model data match the observed VSP field data well. We can explain the observed seismic anisotropy of the Mahogany salt body with lattice preferred orientation of the constituent halite polycrystals. This supports the hypothesis that deformation of salt structures can lead to significant seismic anisotropy and challenges the common assumptions of salt isotropy.

5.1 Introduction

When subject to large tectonic forces, salt deforms and flows on geological time scales. Under deformation, various salt structure evolve, including salt diapirs, domes and salt sheets. The observed salt structures vary significantly from region to region. Polycrystalline halite can exhibit LPO when deformed plastically (*Wenk et al.*, 1989; *Lebensohn and Tomé*, 1993; *Lebensohn et al.*, 2003; *Wenk et al.*, 2009), and thus, develop effective seismic anisotropic, as halite is anisotropic on single crystal scale (*Zong et al.*, 2014; *Vargas-Meleza et al.*, 2015; *Gebrande*, 1982). Seismic anisotropy describes the dependency of the seismic wave velocity on, for example, propagation and polarisation direction. Despite evidence that salt is seismically anisotropic (*Raymer et al.*, 2000a; *Zong et al.*, 2014; *Picard et al.*, 2018), it is treated in seismic processing considered as being seismically isotropic.

In Chapter 2 we demonstrated evidence that the Mahogany salt body is seismically anisotropic, by investigating shear wave splitting in data from a vertical seismic profile in a well drilled through the salt. We propose different scenarios to explain the observed seismic anisotropy, including LPO of halite. In subsequent chapters we created a numerical workflow, based on plasticity texture modelling, to link salt deformation with seismic anisotropy, and tested it on a complex salt diapir deformation model. Here, we present a further step and use the work-flow developed to explain the splitting results from Chapter 2. We develop a geomechanical deformation model of the Mahogany salt body and compare the estimated seismic anisotropy with those observed in seismic field data.

The salt deformation model of the Mahogany salt body is created and run using the geomechanical modelling software Elfen. The methodology described in Chapter 4 is then applied to calculate a model of halite alignment – and the associated seismic anisotropic – in the salt body. Using full wave form modelling we then generate a synthetic VSP seismic dataset. We compare SH- and SV-polarised shear waves travelling through the anisotropic synthetic salt model with shear wave splitting results from Chapter 2 and discuss whether this provides an explanation for the splitting we observed. Aligned halite crystals are tested as a hypothesis to explain the observed splitting results (section 5.3). After that we discuss and summarise the results in section 5.4.

5.2 Modelling the formation and evolution of the Mahogany salt body

The Mahogany salt body is located in the Northern Gulf of Mexico, where since it has been deposited, it was been deformed effectively as a salt sheet a salt sheet. Detailed reconstruction of the evolution of the Mahogany salt body is given in (*Rowan et al.*, 2001).

We simulate the geological evolution of a near-surface salt body into an advancing salt sheet, in a compressional tectonic regime in 2D, based on the deformation of the Mahogany salt body. Deformation is interposed with sedimentation of new material. The model is a plane-strain, forward finite-element model, with adaptive remeshing. The simulation and model building are done with the geomechanical modelling software Elfen, developed by the software company Rockfield Global. The computational framework of Elfen and the geomechanical governing equations used by Elfen were discussed in the previous chapter and a detailed description can be found in, for example, *Perić and Crook* (2004) or *Thornton and Crook* (2014).

The salt sheet geometry is based on the present geometry and size of the Mahogany salt body. Specifically, the dimensions are motivated by *Rowan et al.* (2001), who reconstructed the evolution of the Mahogany salt body. 2D- and 3D seismic data were used together with biostratigraphic constraints to reconstruct the evolutionary history of the Mahogany salt body. Cross sections from the restoration results along one seismic line are shown in Figure 5.1. We used the geometry to approximately constrain the size and evolution of the salt sheet.

Salt sheet structures are commonly observed in the whole Gulf of Mexico and also in other areas around the world, such as in the North Sea or in the Santos-Basin in Brazil (*Vendeville and Nilsen*, 1995; *Peel et al.*, 1995; *Rowan et al.*, 2003; *Hudec and Jackson*, 2007; *Jackson and Hudec*, 2017b). Therefore, this work is valuable not only for Mahogany and the Gulf of Mexico, but also for other areas, where typical deformation behaviour of salt sheets are observed. We limit the model to two dimensions, as the important deformation happens in 2D/2.5D. Moreover, the seismic data VSP-data set is effectively in 2D and does not cover differ azimuths. A 2D model improves the computational tractability.

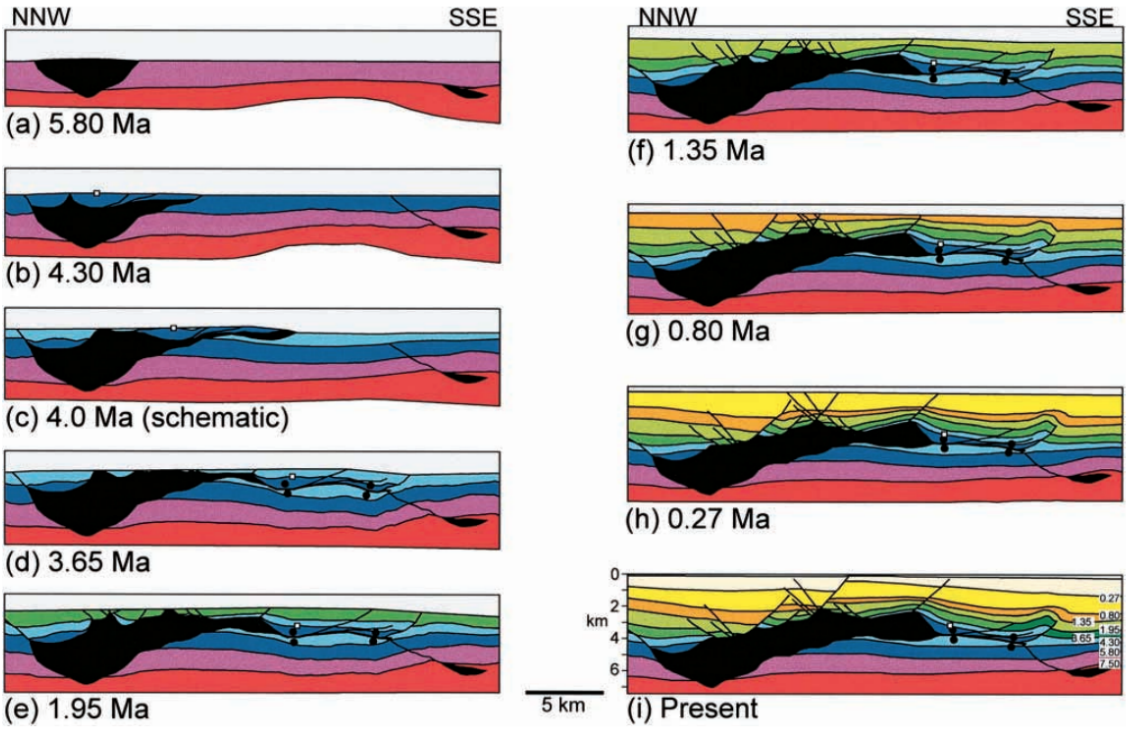

FIGURE 5.1. 2D-cross sections, taken from *Rowan et al.* (2001), showing the geological evolution of the Mahogany salt body in the northern Gulf of Mexico, based on seismic restoration and biostratigraphic constraints. Salt is shown in black, and pairs of dots indicate the frontal weld. The restoration in panel c is schematic because no horizon was interpreted for this time. The open square at the sea floor in panel b is tracked through to the present.

Our model consist of two materials, salt and sediments. The initial geometry is shown in Figure 5.2. The salt is initially trapezoidal, imitating a salt diapir. To the left- and right side, sediments are surrounding the salt. The initial extent of the model is 34 km × 4 km and rectangular in shape. The salt has an initial extension of about 5 km × 4 km. The salt represents a salt diapir which penetrated the upper sedimentary layers and reached the surface.

5.2.1 Applied deformation

Evaporite sediments undergo often large deformation. The applied tectonic stress is solely compression from the left side of the model, together with gravitational forces, as seen in Figure 5.2. The right side of the model is fixed.

The salt sheet spreads with a spreading rate of about 3 $mmyr^{-1}$, consistent with typical spreading rates of salt sheets, which are around 1-20 $mmyr^{-1}$, depending on the extrusion width and external

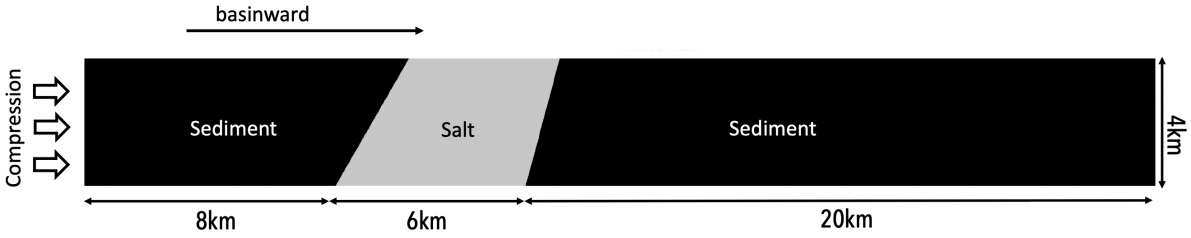

FIGURE 5.2. Initial geometry of the model (34 km × 4 km). The salt body imitates a salt diapir, which reached the surface. The applied deformation is compression from the left side of the model. The material is not allowed to move outside of the model domain at the right, left and bottom of the model, where we apply fixed boundary conditions. The salt is surrounded by sediments.

tectonic forces (*Warren*, 2016; *Jackson et al.*, 1994). At the end of the deformation, the model is shortened by 5.9 km in the x-direction. This corresponds to a shortening rate of about 1 $mmyr^{-1}$. The salt resist compaction and extrudes at the surface, triggered by compressional stress and gravitational forces.

5.2.2 Deposition

The compressive deformation is interspersed with simulated sedimentation events. The deposited material is assumed to be shale, as that is the main source-rock material seen in the Northern Gulf of Mexico (*Davis*, 2017), but could be also any other typical sediment. We implemented in total seven deposition events during the modelled time frame of 5.9 Myrs. Each deposition event adds 500 m of shale at the top of the domain. In total a 3.5 km shale layer is deposited over 5.9 Myrs, corresponding to 0.6 $mmyr^{-1}$. Sedimentation rates in of Mahogany salt body vary from 0.38 $mmyr^{-1}$ to 2.9 $mmyr^{-1}$ (*Rowan et al.*, 2001). The sediment layers are deposited with an angle in the dip direction, which mimics progradation sedimentation, where beds are deposited successively basinward. Sediment supply is larger than the accommodation. Progradation sedimentation is observed along the Northern coast of the Gulf of Mexico (*Galloway*, 2008). In Elfen various methods are available to implement deposition of new material. We use the aggregation method, which is best to mimic such progradation sedimentation. The aggregation method deposits layers in equal increments with an upper boundary until a specific horizon is reached. The top horizon for each of the seven depositional events is shown in Figure 5.3.

5.2.3 Model rheology

The rheology of the salt is represented by the Multimechanism Deformation (MD) constitutive model. The shale is modelled using the soft-rock SR3 constitutive model. Both are sophisticated

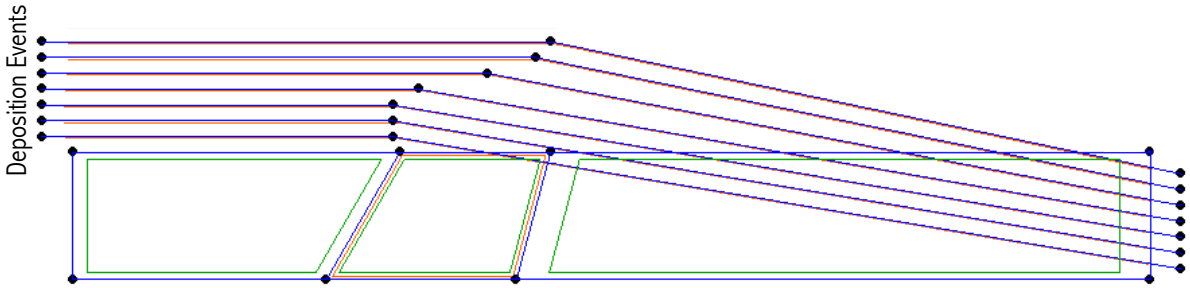

FIGURE 5.3. Horizons of each of the seven deposition events are shown. The material is deposited until the specific horizon is reached. The sediments are deposited with an angle towards the basin, which should mimic progradation sedimentation, observed in the Gulf of Mexico (*Galloway*, 2008). The seven deposition events happen at 1.5, 2, 2.5, 3.3, 4.1, 4.9 and 5.7 Myrs.

model rheologies, and have been used to model mechanical behaviour of salt and adjacent sediments (*Heidari et al.*, 2016). For a complete desription of the rheology models see Appendix E.

5.2.3.1 MD constitutive model

The formulation of the Multimechanism Deformation (MD) rheology model was first presented in *Munson and Dawson* (1979), and has been used extensively, to model creep behaviour of rock salt. It has been applied to various rock salt deposits around the world, for example to Brazilian salts (*Firme et al.*, 2015) or to salts from the Gulf coast (e.g. *Munson et al.* (2004); *Fredrich et al.* (2007)). It originated from the Waste Isolation Pilot Plant (WIPP). The WIPP is one of the most extensive studies on constitutive behaviour of rock salt, which included laboratory testing as well as constitutive model development (*Fredrich et al.*, 2007). From that the MD-model was developed and stands out as being of one of the most sophisticated models describing the creep constitutive behaviour of rock salt (*Firme et al.*, 2015).

5.2.3.2 SR3 constitutive model

The rheology of the sediments is modelled using the SR3 material model (*Crook et al.*, 2006). It is a constitutive model for sands and other sediments. A more detailed description can be found in the previous chapter, together with the model-parameter chosen. The SR3 model was applied to model geomechanical behaviour in, for example, *Heidari et al.* (2016), modelling a welding salt layer and the strain environment of adjacent sediments.

5.2.4 Evolution of the model

In total 5.9 Myrs of deformation are modelled. Snapshots, showing the development of the model in time can be seen in Figure 5.4. Geostatic initialisation is used to establish current-day stresses, where sediments are settled by gravitation, before the model domain is deformed by compressional stress, interspersed with sedimentation of new material.

0 - 1.8 Myrs

As the model domain is compressed, salt resists the compaction and flows upwards. The salt starts to spread at the surface with no-, or little sediments on top of the salt. The salt spreads basinward (right side of the model), preferentially favoured by the slightly shaped salt body. At 1.5 Myrs the first depositional event takes place, while compression continues. After the deposition, the left most part of the salt sheet is covered with sediments. The progradation sedimentation style further forces the salt basinward. Salt sheet advance is constrained by deposited sediments (Figure 5.4 b).

1.8 - 2.8 Myrs

As compression continues, more salt is pushed from the feeding salt diapir upwards to the surface. Salt is more buoyant and flows more easily than the shale. The advance of the salt sheet is similar to an extrusive advancing style, rafting along the surface with no sediments on top covering the salt (*Hudec and Jackson*, 2007; *Jackson and Hudec*, 2017b) (see Chapter 1 for salt sheet deformation styles). The salt can advance relatively freely from 1 Myrs to 2.5 Myrs and is relative rapid compared to the sedimentation rate (*Hudec et al.*, 2013; *Hudec and Jackson*, 2007). At 2.5 Myrs the third depositional event is implemented and half of the salt sheet is covered with sediments, with material deposited at both sides of the salt sheet (Figure 5.4 c).

2.8 - 4.7 Myrs

New deposited sediments are relatively weak, as they are not compacted by gravitation. When deposition becomes larger and sediments are constraining the sheet advance, the salt sheet is pushed upwards and the base of the salt is non-parallel to the bedding plane. More material is deposited in the front of the salt sheet (Figure 5.4 d-e). Deposition further buries the salt sheet. The base of the salt is oriented slightly towards the surface, ramping upwards.

4.7 - 5.9 Myrs

The advance becomes more difficult and the salt sheet thins towards the basin (a feature, which can be seen in the restoration study of *Rowan et al.* (2001) (Figure 5.1). The compression from the left side continues, which pushes almost all salt outside the salt body towards the surface. At

5.9 Myrs the deformation simulation ends (Figure 5.4 f). At the end of the deformation the salt has a longitudinal extension of about 15 km.

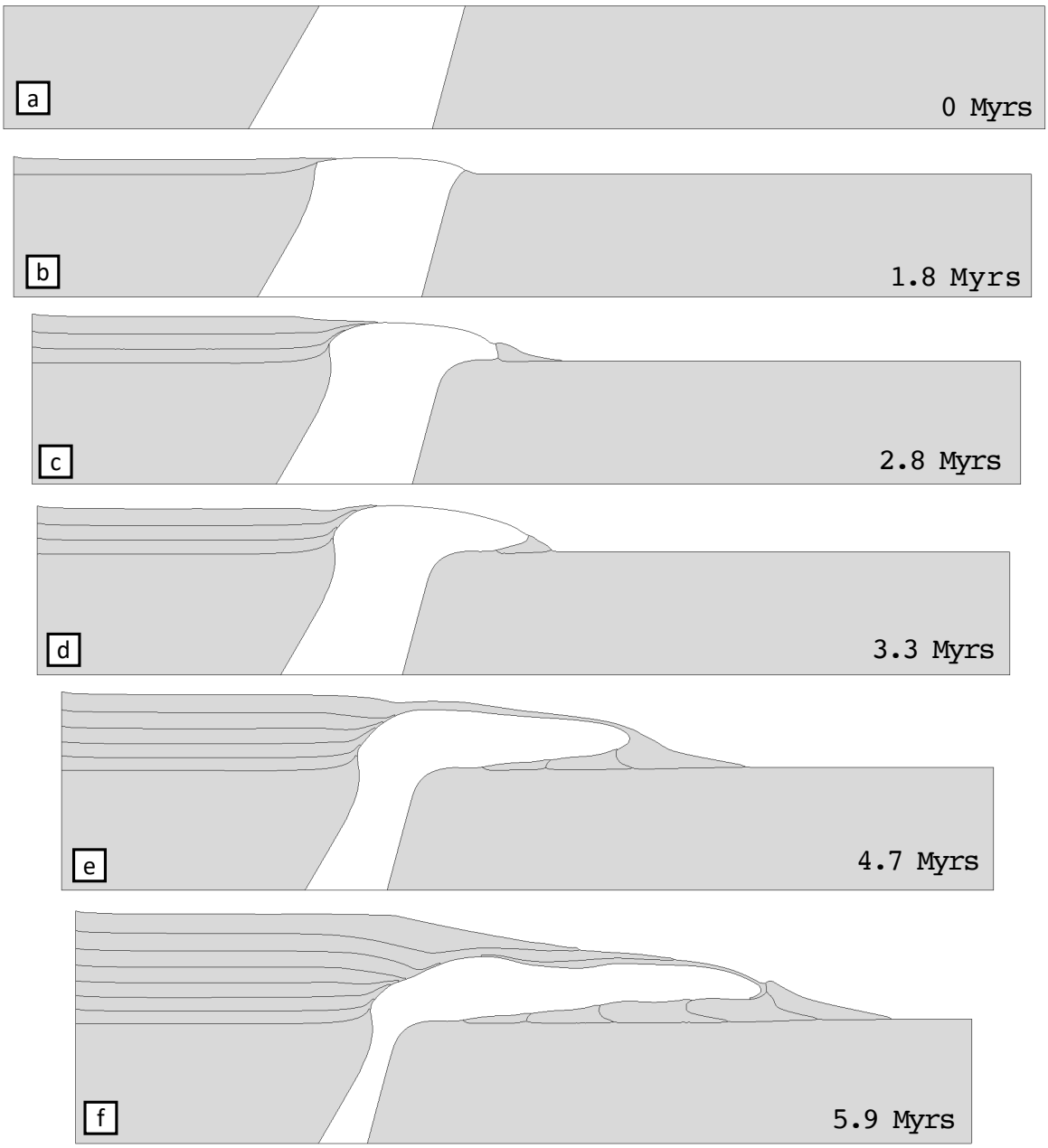

FIGURE 5.4. Elfen model simulating the transition from a near-surface salt body into an advancing salt sheet. The salt sheet geometry is based on the present size of the Mahogany salt sheet in the Gulf of Mexico, modelled for 5.9 Myrs. Panel (a) shows the initial geometry. Sediments are deposited and the salt sheet starts to extrude at the surface (panel b). At 2.8 Myrs sediments are deposited in the front of the salt sheet (c). The base of the salt ramps up, non-parallel to the bedding plane (d). This process continues with ongoing time and deposition (e). At 5.9 Myrs the salt sheet is thinned towards the basin and has an extension to about 15 km (f).

5.2.5 Calculation of elasticities

We apply the work-flow presented in Chapter 4 to the deformation model to calculate the LPO-induced seismic anisotropy. 512 passive tracer particle are followed through the model in time, where each particle represents a package of halite polycrystals, deformed individually. LPO-induced seismic anisotropy in the deformed salt sheet is the approximated by an VRH-average on the elastic constants (*Hill*, 1952).

Figure 5.5 shows the strain distribution inside the salt, separated into shear- and normal strain. Also shown are the results from the applied work-flow, calculating the LPO induced seismic anisotropy. The normal strain was calculated by only considering the normal strain components of the strain-rate tensor ($\dot{\varepsilon}_{xx}$ and $\dot{\varepsilon}_{yy}$) and adding the absolute values of the incremental strains in each time step ($|\dot{\varepsilon}_{yy}| + |\dot{\varepsilon}_{xx}|$). The shear strain was calculated accordingly ($|\dot{\varepsilon}_{xy}| + |\dot{\varepsilon}_{yx}|$). The anisotropy is displayed as the universal anisotropy index (*Ranganathan and Ostoja-Starzewski*, 2008a).

The salt sheet base is the most strained part of the model as it is sheared at the salt/shale boundary. In many salt sheets, the base is observed to be the most strained part (*Hudec et al.*, 2013; *Jackson and Hudec*, 2017a). The shear strain is higher than the normal strain. The left part of the salt sheet is generally higher in normal strain, and thus was deformed primarily by extension or compression. To the right side the salt sheet thins, and shear strain is dominant, especially at the bottom of the salt sheet, but also at the top. The anisotropy, however, shows a less clear pattern. The top of the salt sheet shows slightly higher anisotropy than the bottom of the salt sheet. This shows that less deformed areas can also show high seismic anisotropy. Areas at the bottom of the salt sheet show very high shear strain, but comparably low anisotropy. That is, because shear strain is less efficient in generating seismic anisotropy, compared to compression or extension. This also agrees with the results from Chapter 3, where pure compression and simple shear, and the resulting seismic anisotropy was analysed. The strains were, compared to here, considerably lower (2 and 5 for compression and simple shear, respectively). However, highly deformed areas at the bottom of the salt sheet also show generally high seismic anisotropy.

In Figure 5.6 we analyse the strain rate evolution of one particle, which is from the top of the salt sheet, which shows high seismic anisotropy, and comparably low strain. The other particle is taken from the bottom of the salt sheet, which underwent high shear strain, but has lower seismic anisotropy then the less deformed polycrystal. The less deformed particle show higher seismic anisotropy, as it has been deformed mainly by normal strain, while the other particle is deformed by shear. Compression, and extension, are, in comparison to simple shear, more effective in generating texture.

In comparison to the salt diapir model (shown in the previous chapter) the deformation pattern is less complex. The model domain in the Mahogany model was only compressed from the left side of the model, at a constant rate. Accordingly, strain areas can be more clearly separated into normal, and shear strain areas.

The strain rate in highly deformed areas is about 9×10^{-14} s^{-1}. Those values are in the range what is observed in the Gulf of Mexico and in other extruding salt sheets ($10^{-15} s^{-1}$ to $10^{-12} s^{-1}$, *Jackson and Talbot*, 1986; *Warren*, 2016; *Thigpen et al.*, 2019).

Figure 5.7 shows the plastic strain components of the strain-tensor inside the sediments surrounding the salt sheet. Shear strain is highest at the bottom salt/sediment boundary and normal strain is stronger at the top salt/sediment boundary with extensional features in x-direction ($\sigma_{xx} > 0$) and compressional features in y-direction ($\sigma_{yy} < 0$). This means that the sense of deformation is similar to the *Rowan et al.* (2001) deformation model. However, they identified normal faulting inside above the salt, which is not seen here.

To summarise, the model mimics the evolution of the Mahogany salt body. The properties of the model, including the salt rheology, geometry, deformation time, compression- and sedimentation rate are constrained with typical Gulf of Mexico and Mahogany properties.

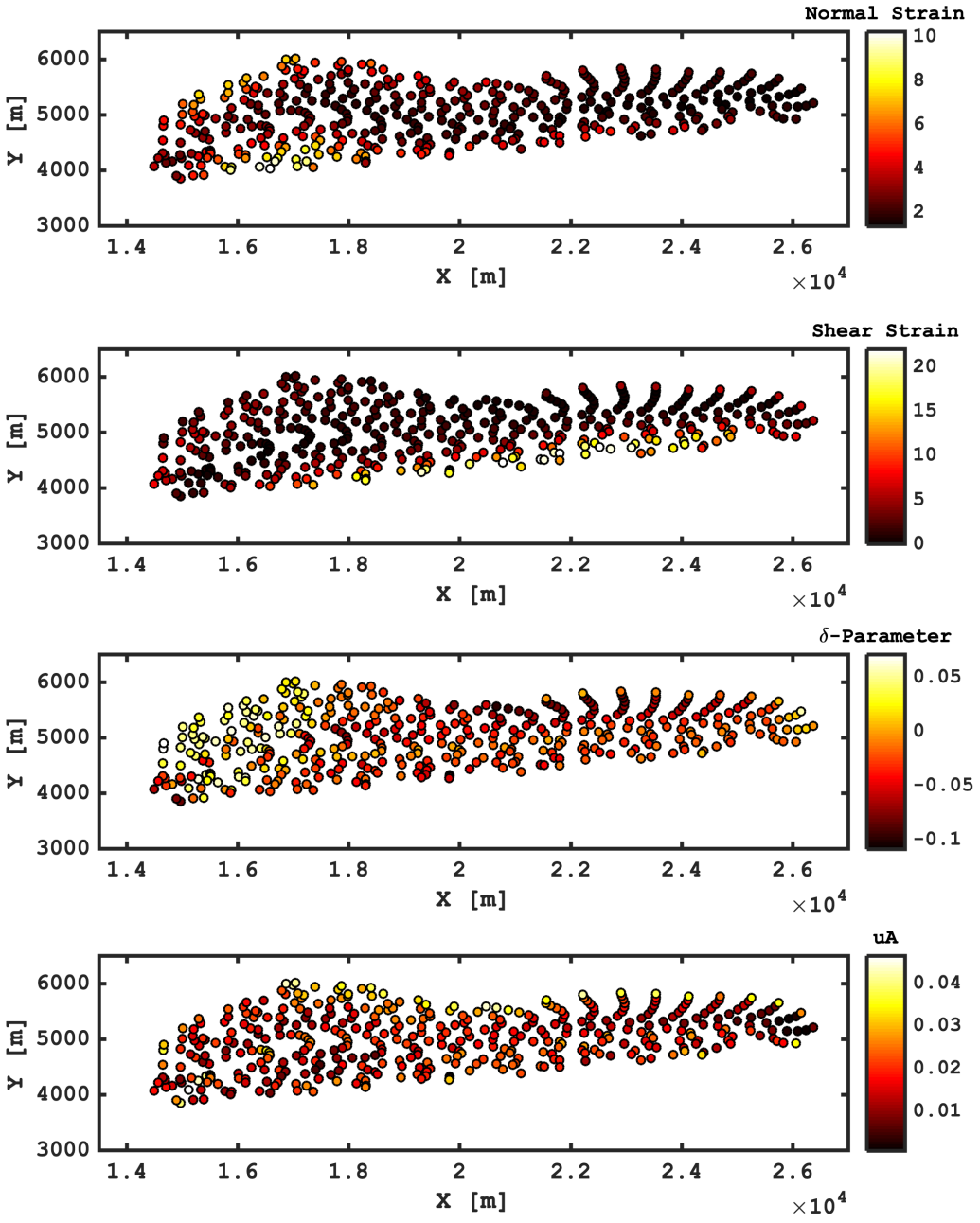

FIGURE 5.5. Strain and seismic anisotropy inside the Mahogany salt sheet model. Seismic anisotropy is given as the universal-anisotropy index (*Ranganathan and Ostoja-Starzewski*, 2008a) and as the Thomsen δ-parameter (*Thomsen*, 1986). The salt from the diapir is pushed at the surface and rafts along the base, where large strain accumulates. The salt sheet is thinned towards the basin. The bottom of the salt sheet is highly deformed, up to a shear strain of 20. Other areas are less deformed, as for example the centre of the salt sheet. The deformation history of the Mahogany salt body is complex with a highly heterogeneous deformation pattern.

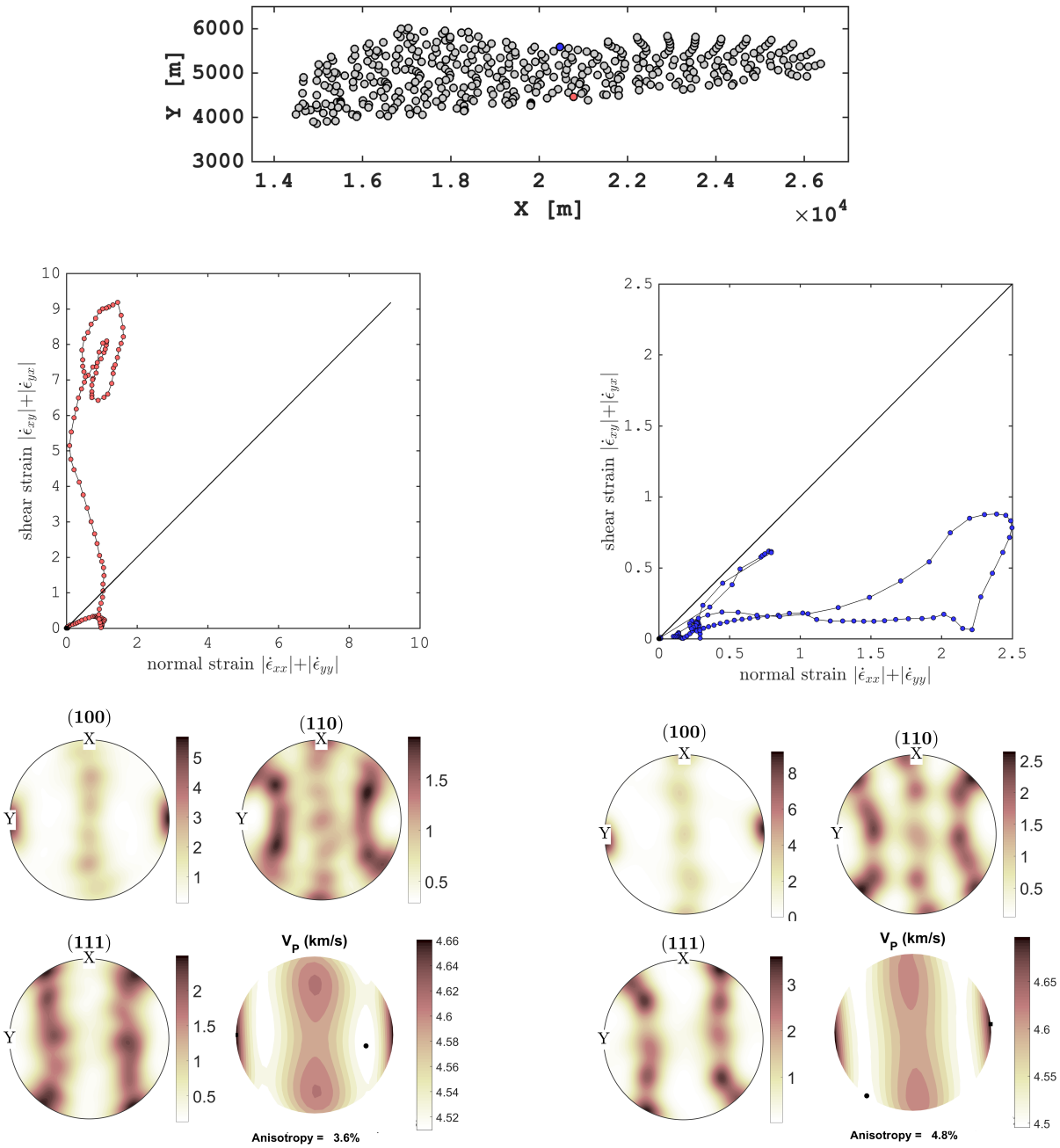

FIGURE 5.6. Strain-rate evolution of two particles, taken from the bottom and from the top of the salt sheet, respectively. The base of the salt sheet shows higher deformation and shear strain, while the top showed less deformation and primarily normal strain. Extension, and compression are more efficient in generating texture, which is why the base particle – although having a higher strain – results in lower seismic anisotropy (3.6% compared to 4.8%). The strain rate evolution is separated into absolute shear-, and normal strain. The blue, and red points were deformed by normal, and shear deformation, respectively. Also shown are textures of the two polycrystals, displayed as upper hemisphere, equal area pole figures.

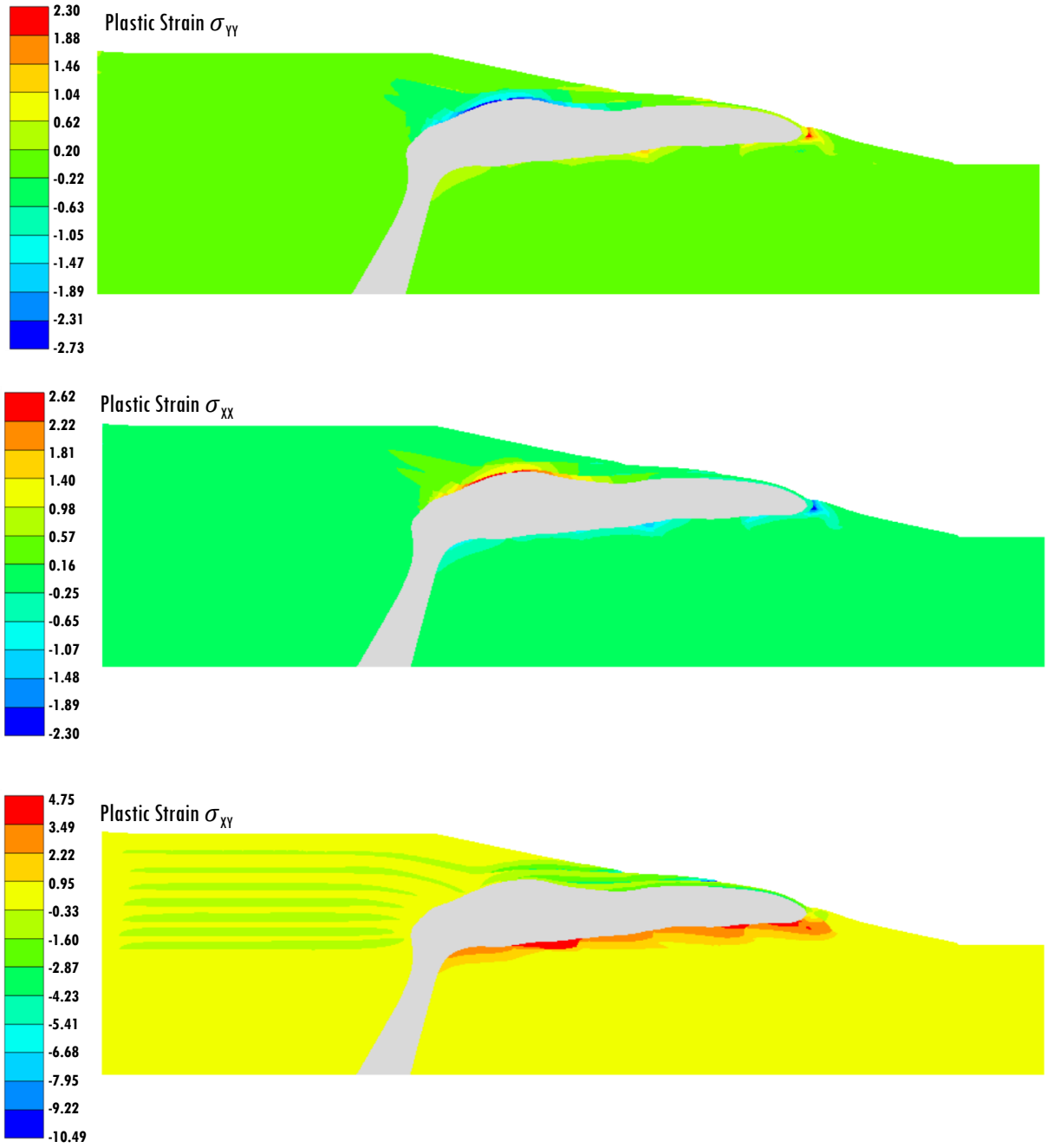

FIGURE 5.7. Shown is the plastic normal strain in y-direction σ_{yy}, in x-direction σ_{xx} and plastic shear strain σ_{xy} in the top, middle and bottom panel of the sediments, respectively. Plastic shear is highest at the bottom salt/sediment boundary. Plastic normal strain is pronounced at the top salt/sediment boundary with positive σ_{xx} and negative σ_{yy}, meaning extension in x-direction and compression in y-direction.

5.3 Predicting shear wave splitting with full wave form modelling

The workflow outlined above provides us with a complex model of the anisotropy of the Mahogany salt body. In order to compare it with the shear-wave splitting results presented in Chapter 2, we need to interrogate the model in a way which reproduces the appropriate seismic phases.

In order to do this, we simulate the propagation of seismic waves through the model. Wave propagation is simulated using Specfem2D (*Tromp et al.*, 2008), an open-source full wave form modelling software. Specfem2D is described in the Appendix F. Specfem2D uses the spectral elements method (e.g *Wang and Cai*, 2014) (SEM), solving the wave equation. It combines the properties from finite element method processing complicated mesh design and the accuracy of spectral methods (*Tromp et al.*, 2008; *Wang and Cai*, 2014; *Zheng et al.*, 2014). Spectral elements were successfully applied to modelling seismic waves (*Chaljub and Valette*, 2004; *Chaljub et al.*, 2007; *Liu et al.*, 2004). Specfem2D supports seismic anisotropy, where the velocity is implemented by defining the elasticity and density of the medium.

5.3.1 Model - setup

The mesh used for this calculation consists of about 85 000 mesh elements. The mesh was created by GMSH (*Geuzaine and Remacle*, 2009), which is an open-source meshing software. It can be used to generate meshes for finite- or spectral element analysis. We apply absorbing boundary conditions to all domain edges, avoiding reflections from the sides and top of the model. The mesh used is shown in Figure 5.8, where the two phases used in this model are shown in red (salt) and blue (shale). The simulation is run in 2D. This limits the computational costs and the complexity of the model. A future step in this work would be a full 3D analysis. That would require significantly more calculation time and a 3D deformation model of the Mahogany salt body.

The model geometry is similar to the field-data VSP setup, introduced in Chapter 2. The seismic source is close to the surface and has a far offset to the receivers. In the simulations, we assume the source to be a Ricker wavelet with a dominant frequency of 20 Hz, which lies within source frequency range conventionally used for seismic exploration (*Jones and Davison*, 2014). The receivers are located at the right-hand side of the model, which would correspond to the SSW-end (south southwest) of the Mahogany salt body in the VSP field data. As in the experimental data set, we use 48 receivers, vertically aligned on top of each other, at a spacing of 15m. Receiver 1 is at a depth of 4149 m and receiver 48 is at a depth of 4869 m. The first 11 receivers are within the salt and receiver 12-48 are beneath.

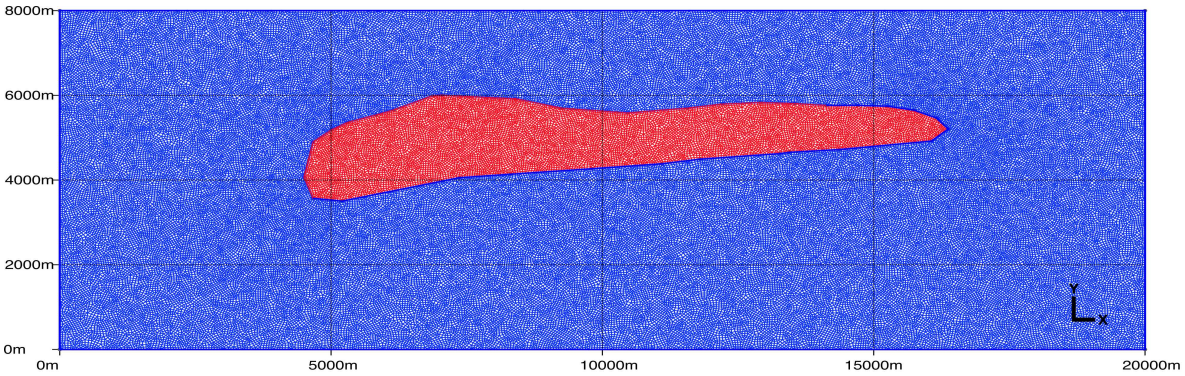

FIGURE 5.8. Element mesh created with GMSH. The model domain is 20km × 8km. The small mesh elements ensure stable results. The model is in 2D and consists of two material phases. We use absorbing boundary conditions for all sides of the model. The model geometry and the shape of the salt structure is based on the Mahogany deformation model. The salt mesh is shown in red and the shale in blue, respectively.

5.3.2 Model - elasticities

We assign each mesh element with elasticities and material densities. The sediment mesh elements have been assigned with the same isotropic velocity. We use a P-wave velocity of Vp_{Shale} = 2500 ms^{-1} and a shear velocity of Vs_{Shale} = 1600 ms^{-1}. The density of the shale is assumed to be ρ_{Shale} = 2.2 kgm^{-3}. The density of the salt is assumed to be constant throughout the salt body and has a value of ρ_{Salt} = 2160 kgm^{-3}.

The salt in the model is seismically anisotropic. The elasticities are calculated by the work flow described in the previous chapter. Based on the lattice orientation, an effective elastic constant, representing the elasticity of the entire polycrystal can be calculated (*Hill*, 1952). Thus, a full elasticity model of the salt is created. We assign each mesh element with an individual effective elasticity tensor (VRH-average), based on the closest traced particle to each mesh element.

5.3.3 Model - Solver

After the model is set up we run the forward simulation of wave-form propagation through the model. We use a constant time step of 0.02 ms over a total of 300 000 steps (i.e a duration 6 s of wave propagation is modelled). Those parameters gave us the best results in terms of computational cost and stability. In Specfem2D, the horizontal- and vertical plane of propagation are decoupled. We run two simulations, the first one for waves polarised in the xz-plane (horizontal plane): into the page looking at Figure 5.8 and 5.10. The wave propagation is in the xy plane.

The other simulation calculates seismic wave polarised in the xy-plane (vertical plane). The simulations are run on the University of Bristol computer cluster BlueCrystal. Each simulation uses 32 cores and takes about four hours.

5.3.4 Model - Waveforms

The wave field at different times is shown in Figure 5.9. The snapshots are after 0.8, 1.7 and 5 s. Most of the energy is reflected at the top of the salt body and does not propagate into the salt, thus amplitudes within the salt are relatively low. That is a common problem in sub-salt imaging, as it is difficult to see the reflected energy from the base of the salt structure (e.g *Jones and Davison*, 2014).

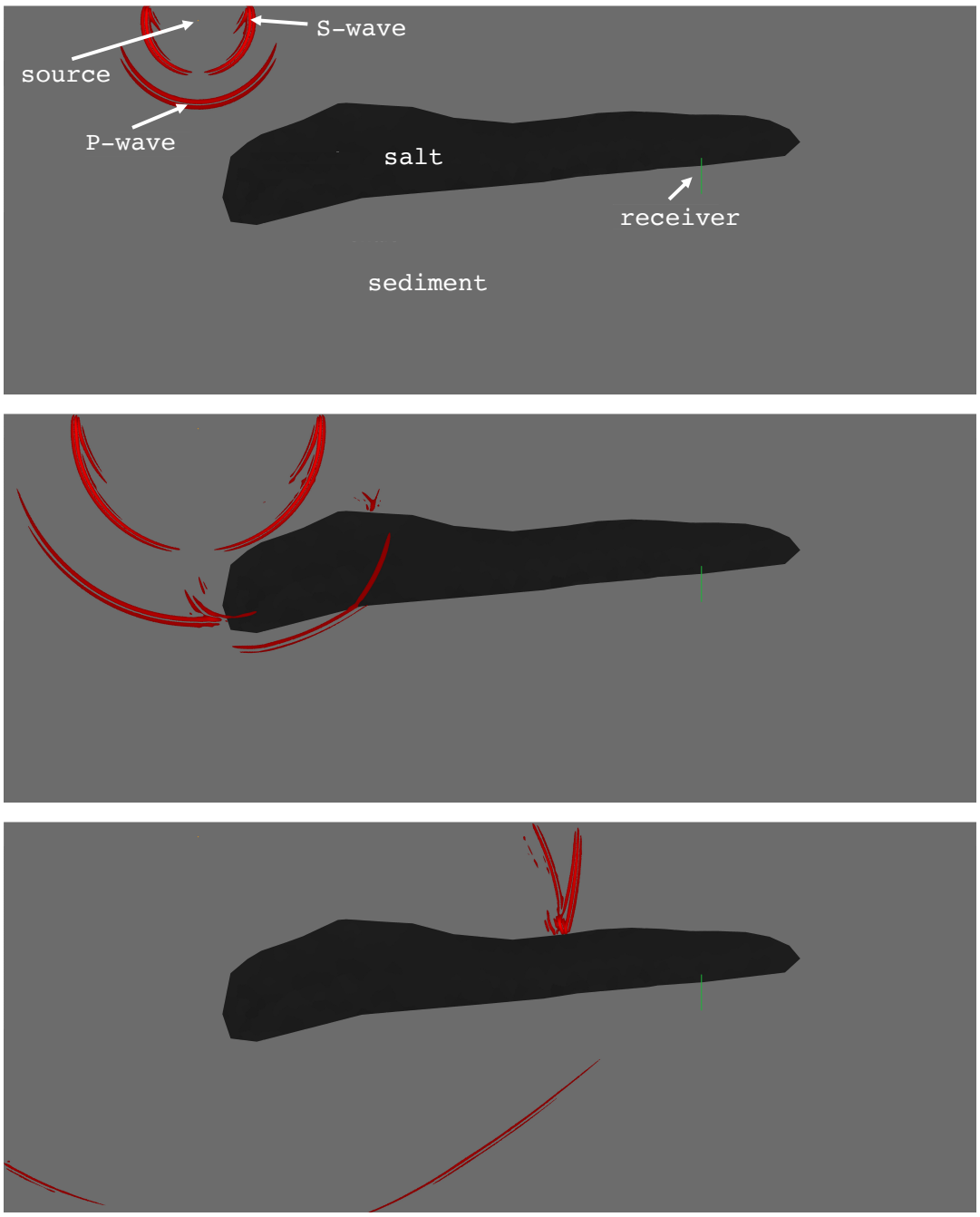

FIGURE 5.9. Wave propagation through the Mahogany model. The 48 receivers are shown in green and are located at the bottom right end of the salt body. The seismic waves are shown in red and display the displacement normalised to the highest amplitude in each time step. The source is at the left side of the model near the surface. The wave field is shown at 0.8 s, 1.7 s and 5 s. The P-wave and S-wave are marked in the first snapshot at 0.8 s. The model consists of two phases, the isotropic shale and the anisotropic salt. The model setup should mimics the VSP dataset from the Mahogany salt body (see Chapter 2).

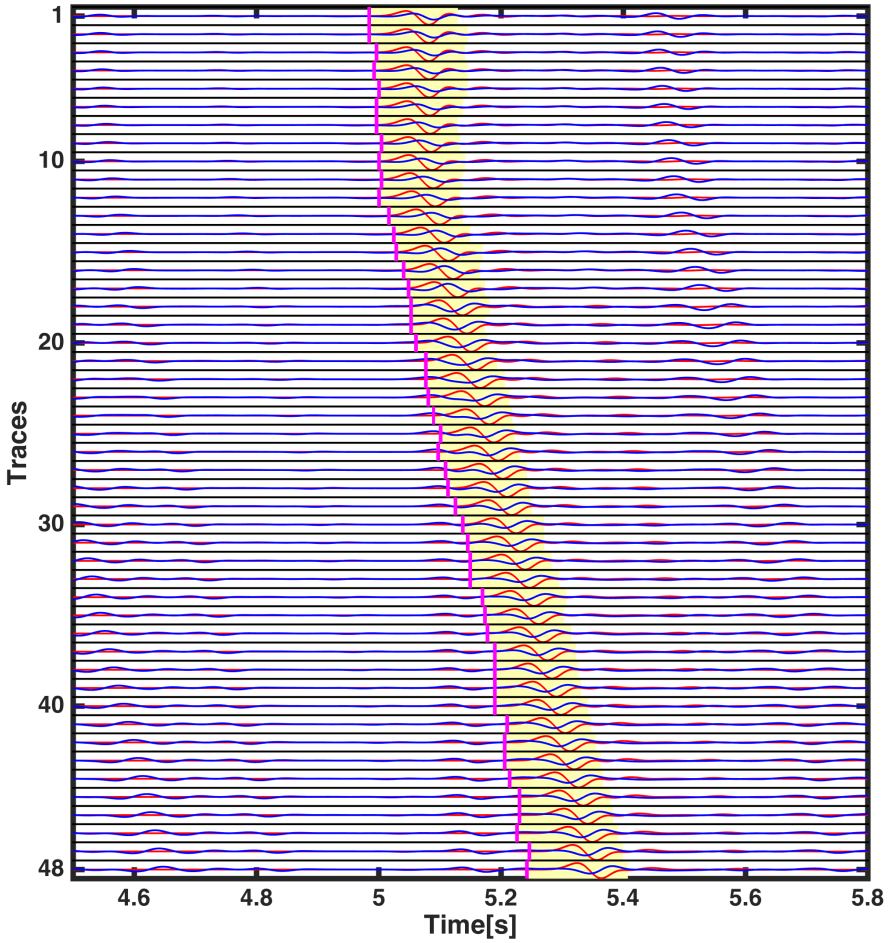

FIGURE 5.10. Synthetic seismograms generated by full wave-form modelling through the Mahogany salt model. The X- and Y-component are shown in red and blue, respectively, for each receiver. The X-component only contains SH-polarised energy, while the Y-component contains SV-polarised energy. The selected S-wave window for the shear wave splitting analysis is highlighted in yellow. This is the first S-wave arrival. The S- to P converted phase at the bottom of the salt body can be identified as well.

5.3.5 Synthetic VSP dataset - results

Calculating shear wave splitting parameters

The waveforms for the synthetic VSP are shown in Figure 5.10. The X- and Y- components are shown in red and blue, respectively. We use the first S-wave arrival (highlighted in the figure) and calculate shear wave splitting on this phase. The conversion from S to P at the bottom of the

salt can be identified as well.

Shear wave splitting measurements are performed with SHEBA (*Wuestefeld et al.*, 2010), which is built on the seismic analysis code platform (SAC) (e.g. *Helffrich et al.*, 2013). The splitting parameters are found by rotating the components into fast- and slow-direction, using the eigenvalue- and cross correlation method (e.g., *Teanby et al.* (2004)). In each measurement, the best splitting results are found from 100 shear wave splitting windows (see Appendix B for a complete description of the methodology).

In Specfem2D no wave conversion from P to SH is possible, because the P-SV and SH planes are decoupled. Therefore, we can not infer the fast direction from the shear-wave splitting measurements (They will always appear close to either horizontal or vertical, see Figure 5.14). We use SH-polarised and SV-polarised shear waves and compare the time delay between both components. Due to the anisotropy the SH- and SV polarised waves propagate with different velocities through the salt, which leads to a time delay at the recording receivers between both waves. These lag times can be compared to the VSP data-set results from Chapter 2. Figure 5.11 shows an example shear wave splitting result, recorded at receiver 37, including the corrected fast- and slow shear wave, the particle motion and the λ_2 error-surface.

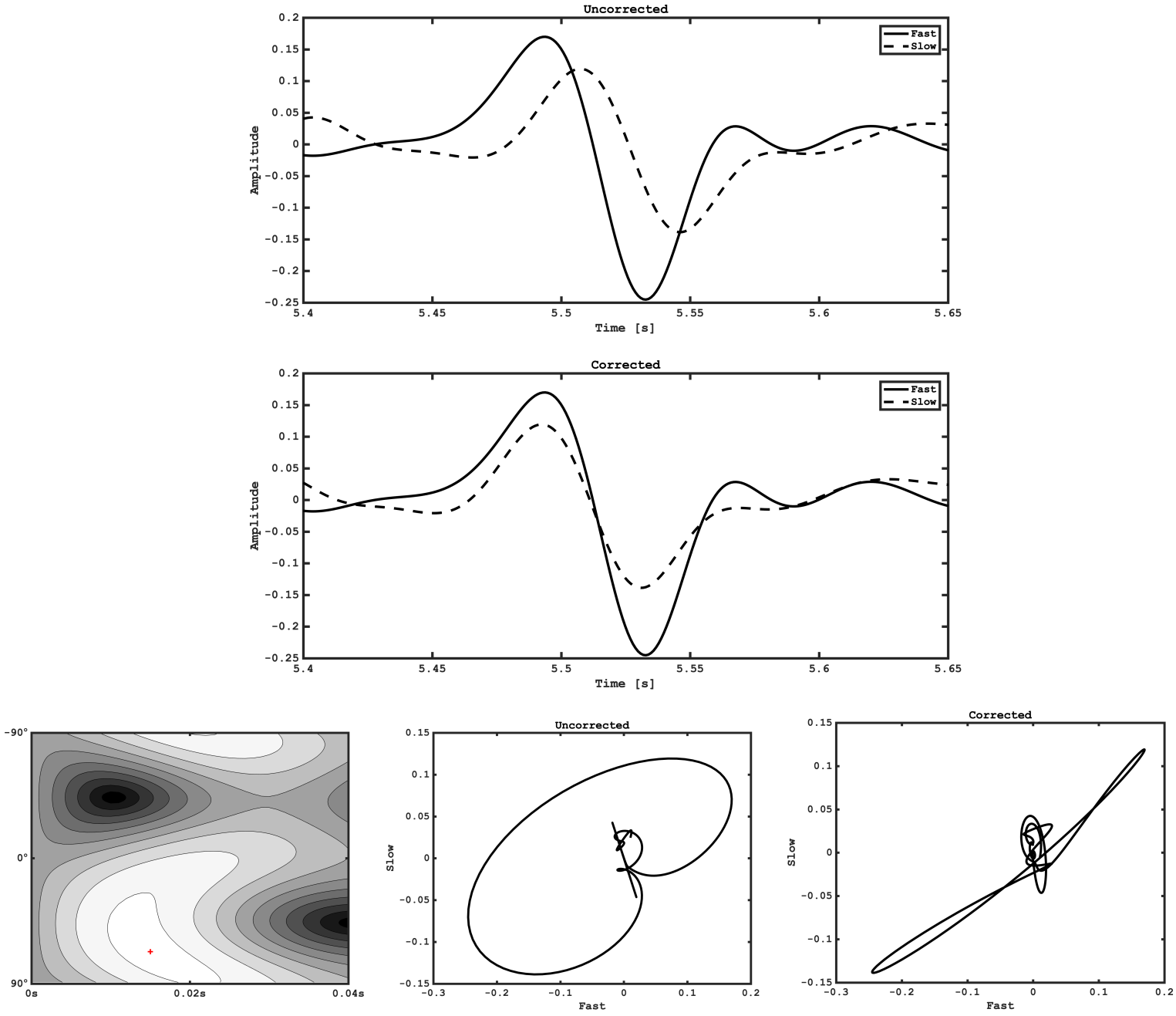

FIGURE 5.11. Synthetic shear wave splitting results recorded at receiver 37. Shown are the uncorrected and the corrected traces and the related particle motion. In the uncorrected case, the traces are separated by a time delay dt and the particle motion is elliptic. In the corrected case, the traces do not show a time delay and the particle motion is linear, because the splitting is removed, and energy is only polarised in one direction. The error-surface of the eigenvalue-method is shown; the fast direction is (within error)±90° (SH leading SV) as expected for the 2D model.

Comparison between the synthetic- and field VSP data

The comparison of delay times between the horizontally and vertically polarised shear waves with the splitting parameters from the VSP data set is shown in Figure 5.12. Delay times at each receiver are displayed for the VSP field dataset and for the synthetic VSP dataset, respectively.

We calculate the fast polarisation from the anisotropic salt model from each set of effective elastic constants, assuming a density of $\rho = 2.16 gcm^{-3}$, using the Christoffel equation (see Chapter 1). We assume an incidence angle of 30° (measured from horizontal to ray direction) and an azimuth of 0°. Fast shear-wave polarisations for the salt in the direction of propagation appropriate to the VSP data are shown in Figure 5.13. The fast orientation is nearly horizontal in the direction of the flow, together with the approximated ray path. Mostly the model part having a horizontal fast shear wave is sampled. Figure 5.14 shows the fast shear wave polarisation of the field data VSP (Chapter 2) in comparison with the horizontal prediction fast-wave prediction of the synthetic model.

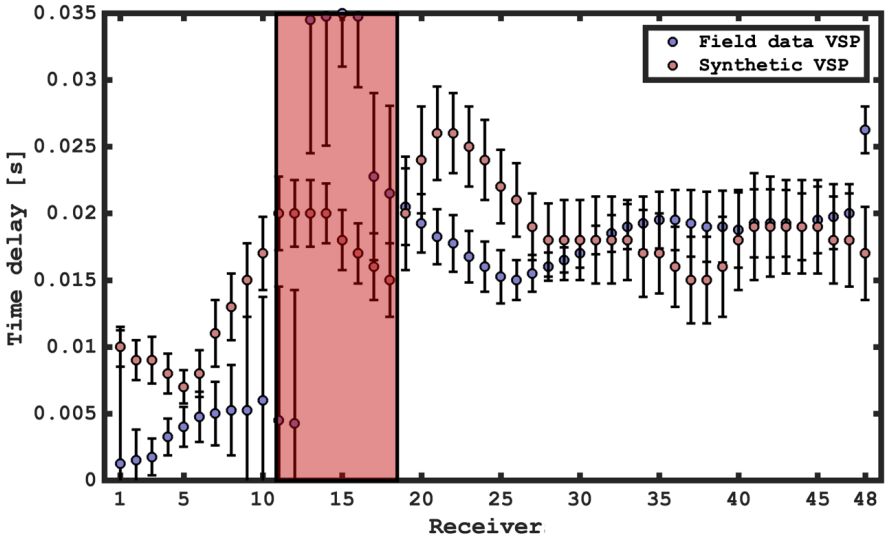

FIGURE 5.12. Comparison between the delay occurring in the synthetic data and the VSP field data (Chapter 2). Field data delay times are shown in blue, synthetics in red. In general these agree well, especially beyond 25 receiver, where both predict a delay time of about 20 ms. The region, in which we infer interference from the salt-sediment boundary is marked by the red bar.

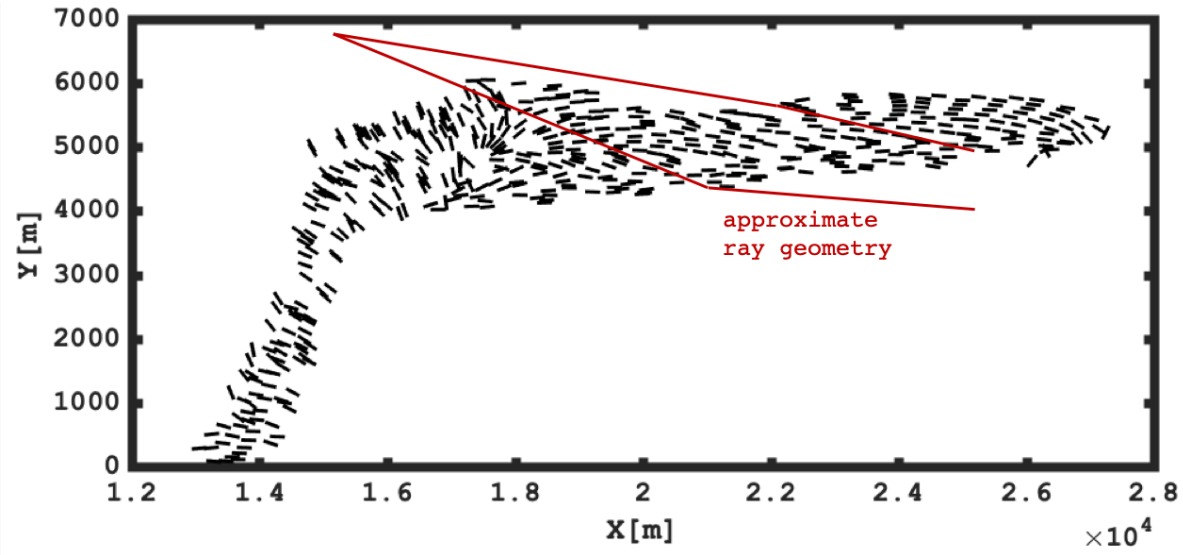

FIGURE 5.13. Fast direction at each particle position inside the model. The fast directions were calculated from each elasticity tenor for an azimuth of 0° and a incidence of 30°. The fast direction is horizontal throughout most of the model. Also shown is the approximate ray geometry, demonstrating that mostly the part with the horizontal fast shear-wave polarisation is sampled.

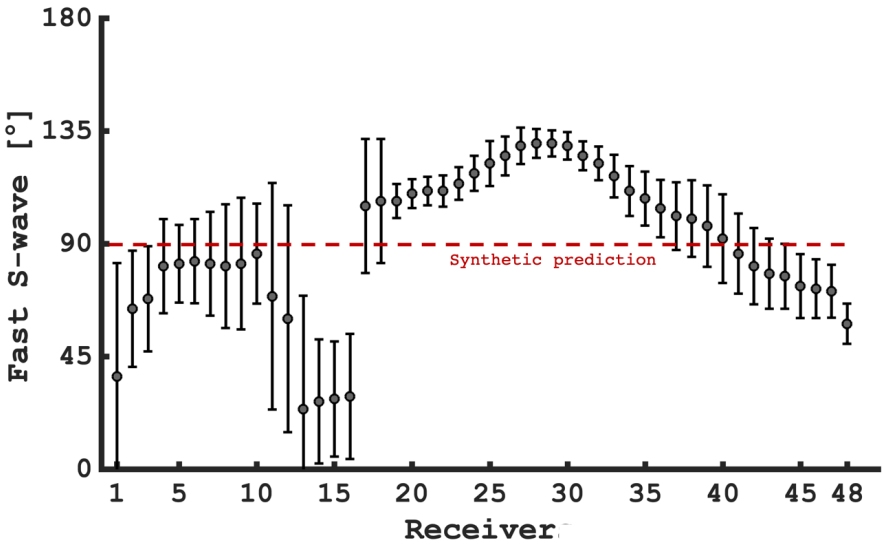

FIGURE 5.14. Fast shear orientation of the field-VSP data, reproduced from Chapter 2. The synthetic data prediction is a nearly 90° horizontal fast shear wave polarisation (dotted red line). Despite showing more complexity, the VSP-field data fast shear wave orientation generally agrees well with the synthetic prediction.

5.4 Discussion

VSP and the synthetic data show similar delay times and fits the data for most receivers (Figure 5.12). In the synthetic data, the delay time increases with increasing receiver depth in the salt up to receiver 11 at the salt/shale boundary. The same is seen in the VSP dataset, although the increase in time delay is more rapid in the synthetic dataset. Receiver 12 is at the salt/shale boundary, where wave conversions happen, as discussed in Chapter 2. For that reason, the results from receiver 12 to 23 might be compromised. After receiver 23 the delay time of the synthetic and VSP data show similar delay times. The delay time is about 20 ms. However, the receivers inside the salt fit the data less well than the receiver below the salt. The model predicts delay time which are slightly higher than in the data. This can be due to several reasons, such as the generally lower quality of the receivers inside the salt. Also, the model might reflect the anisotropy in the upper salt sheet not as well, which can be caused, for example, by the simplicity of the deformation model.

The general similarity in the results suggest that the workflow works well to predict anisotropy in salt structures and that the deformation induced LPO of halite can explain the splitting we observe associated with the Mahogany salt body. Despite more complexity in the real data, the fast shear-wave polarisation also shows a similar pattern, with SH leading SV.

The model predicts significant seismic anisotropy. Following the approach from Chapter 3, we can estimate the depth mismatch of a seismic reflector in a zero-offset measurement. Using $z_{dist} = z_{true} \cdot \sqrt{1+2\delta}$ (Chapter 3), the distorted reflector depth is related to the true reflected depth by the δ-Parameter (*Alkhalifah and Tsvankin*, 1995). In areas of high anisotropy the averaged δ~-0.6, which would correspond to a mismatch in reflector depth of 6.1%. This corresponds to in the centre region of the salt sheet, where the thickness is about 1.5 km to a misfit of ~91.5 m. This is a significant misfit.

However, this work is in the early stages and the suggested approach could off course be improved. Only dislocation plasticity is included in the VPSC modelling formulation, other recrystallisation mechanisms are not included. Grain boundary migration tends to weaken LPO (*Trimby et al.*, 2000). Grain boundary migration is observed in wet salts (*Urai and Spiers*, 2007). We discussed this effect in Chapter 3. To investigate further how valid this assumption is, comparisons to natural rock salt textures are a possible future direction. Texture modelling can be improved by including other deformation mechanisms, apart from dislocation plasticity. The model is a 2D deformation model, and a full 3D model could give additional insights. However, the seismic data here is essentially 2D as well, as no azimuthal coverage is available, which is why is this case, a 2D model is sufficient.

This study only investigates seismic anisotropy due to lattice preferred orientation. In future, the strain models we have derived could be used to parameterise shape preferred orientation model, modelling deformed inclusions or deformed halite crystals. Here, different inclusions could be tested, for example water inclusions, or sediment inclusions. Furthermore, mixed phases, such as anhydrite/halite mixtures, can be used to used instead of assuming only halite present in the rock salt. Anhydrite is highly anisotropic on crystal scale (e.g *Bass*, 1995) (see Chapter 2 for a simple model considering aligned anhydrite crystals). In the case of anhydrite being present, seismic anisotropy would be higher than in the modelled cases here. Future work could consider modelling deformation texture of anhydrite and/or mixed halite/anhydrite phases. Also, the anhydrite content could vary spatially, based on the final position of the traced particles. Anhydrite is unusually left as a caprock on top of the larger halite layer (e.g. *Jenyon*, 1986). In principle, VPSC is capable of modelling such scenarios, however, we did limit this study to halite, as we could not find well constrained single crystal properties of anhydrite (including slip systems and their strength as a function temperature). Other factors contributing to seismic anisotropy (for example layering) might improve the results.

5.5 Conclusions

5.5.1 Mahogany deformation model

We have created a forward-geomechanical model for the evolution of the Mahogany salt body in 2D. The model uses sophisticated salt- and sediment rheology models, which have previously been successfully applied to model the geomechanical behaviour of the salt and its surrounding sediments (for example in *Heidari et al.* (2016)). The salt rheology model is parameterised with well-constrained typical Gulf of Mexico parameters (*Fredrich et al.*, 2007). Other properties, such as strain rates and the sedimentation rates are well in the range of what is observed for salt deformation in the Gulf of Mexico and other areas around the world. The model is kept simple but captures realistic salt sheet deformation behaviour. The model shows characteristics which can also be applied to similar salt sheets structures in other parts of the world.

5.5.2 Synthetic- and field data VSP

The workflow presented in the previous chapter is applied to the Mahogany deformation model, predicting lattice orientation of the halite crystals and the accompanied seismic anisotropy. A full elasticity model is generated, which models seismic anisotropy induced by LPO.

We create a synthetic VSP-gather using the constructed seismic model. We use the full wave form modelling software Specfem2D to simulate seismic wave propagation through the model. We compare the SH- to SV delay times from the synthetic VSP-data to the shear wave splitting delay times from the field VSP field-data, presented in Chapter 2. The delay times are similar

and show consistent results around 20 ms. The fast directions (predominantly SH leading SV) predicted by the anisotropic model is also compatible with those observed in the VSP data. The results show that preferred orientation of halite crystals can explain the observed anisotropy and delay times measured on the VSP field data set.

This study has shown evidence that significant anisotropy can be observed in salt bodies, and that those observations can be explained by invoking deformation-induced texturing of halite. This places the assumption that salt bodies are isotopic on significantly unsafe ground.

CHAPTER 6

CONCLUSIONS

Salt is important and is used in various industrial applications. Many salt deposits around the world are associated to major hydrocarbon reserves (e.g., the Gulf of Mexico, the Persian Gulf or North Sea). Also, salt has properties which can be exploited for storing CO_2 or hazardous waste. Salt has a low density, high viscosity and is nearly impermeable. It is very deformable and has the ability to flow rather than to fracture. Although salt flows on geological time scales, it is in fact a crystalline solid. Therefore, it has the ability to form an anisotropic fabric, resulting from the alignment of crystals deformed over long time periods. As halite – the main mineral in evaporites – has a cubic crystal structure and is seismically anisotropic on single crystal scale, the alignment of crystals can lead to seismic anisotropy on scales relevant for seismic waves.

Despite these factors, seismic anisotropy in rock salt is generally poorly investigated, and broadly ignored in seismic processing. Just few studies consider anisotropy in rock salt environments. Therefore, there is a significant potential for improving seismic images in and around rock salt settings by incorporating anisotropy in seismic velocity models. Seismic anisotropy potentially has large impact on seismic traveltimes amplitudes, and ignoring such factors can lead to erroneous and distorted seismic images. These, if taken at face value, could lead to extremely costly mistakes in, for example, positioning of production wells.

This thesis presents a study of seismic anisotropy in rock salt. It combines evidence of anisotropy obtained from a seismic data with numerical modelling of salt anisotropy and its manifestation in seismic travel times and images. The study suggests that rock salt can exhibit high seismic anisotropy and particularly emphasises the role of lattice preferred orientation of constituent halite crystals in this. In this chapter I will highlight the main conclusions drawn in the thesis.

6.1 Key observations and main conclusions

Shear Wave splitting observations from the Mahogany salt body in the Gulf of Mexico

Chapter 2 motivates the thesis by presenting an investigation of a seismic data set from the Mahogany salt body in the Gulf of Mexico. It is a VSP in a vertical sub-salt well, with receivers in and beneath the salt body. We show clear evidence of shear wave splitting (a significant diagnostic for seismic anisotropy), in a natural rock salt settings. The key conclusions are:

- For the investigated acquisition and geometry, the Mahogany salt sheet in the Gulf of Mexico show clear signs of seismic anisotropy. Shear wave phases, converted at the top of the salt sheet show significant shear-wave splitting, while phases converted at the bottom of the salt sheet show much less. As well as producing the shear-wave splitting we measure, the inferred anisotropy may be strong enough to significantly distort seismic images.
- This study observed salt anisotropy in pure Gulf of Mexico rock salt. We have investigated various scenarios to explain the anisotropy in rock salt with simple forward modelling. We conclude that alignment of halite polycrystals is the most likely explanation of the observed splitting, though we cannot rule out a contribution from other factors including the presence of aligned water inclusions or other salt mineral phases. This motivates the investigations for the further chapters.

Numerical texture modelling of polycrystalline halite

Motivated by the shear wave splitting observations, we perform numerical texture modelling of polycrystalline halite and quantify the arising seismic anisotropy induced by deformation (Chapter 3,4 and 5). For that we first investigate the development of LPO and the associated seismic anisotropy for simple deformation geometries. This part of the study draws on previous literature to propose input parameters which are best to simulate LPO induced seismic anisotropy under natural deformation conditions. This is followed by investigating LPO and associated seismic anisotropy evolution in complex deformation regimes. We create a new numerical methodology to assess seismic anisotropy due to dislocation plasticity for complex salt deformation, and demonstrate its utility on a salt-diapir model. The work-flow is then applied to a realistic deformation model of the Mahogany salt body. The aim of this thesis part is to investigate halite alignment as a possible cause of the observed seismic anisotropy, and to predict numerically the expected seismic anisotropy in such a scenario. The main conclusions drawn of the second part of the thesis are:

- Rock salt deformed by dislocation plasticity develops high seismic anisotropy. This anisotropy, when deformed in several geometries prevalent in relevant environments, can be well approximated by VTI symmetry. Natural rock salt deposits experience extensive deformation

which, consequently, should manifest seismic anisotropy. Formations undergoing stronger deformation should show higher seismic anisotropy.

- Polycrystalline texture modelling can give good approximation to the resulting seismic anisotropy (judged by comparison with laboratory studies). The work-flow we present gives a quick estimation of seismic anisotropy expected for dislocation deformation.

- Realistic seismic elasticity models, based on our developed methodology to predict anisotropy associated with LPO, shows that a significant distortion of seismic images is expected. Shear wave splitting results, obtained in the first part of the thesis, are consistent with those from a synthetic VSP survey. This is strong evidence that polycrystalline alignment of halite crystals, and associated seismic anisotropy, is expected in salt settings which experienced high deformation, such as the Mahogany salt body.

6.2 Future directions

Texture modelling

The texture modelling in this study is performed with the visco-plastic self-consistent VPSC modelling approach. This neglects other deformation mechanisms apart from dislocation plasticity. In particular dynamic recrystallisation is expected to alter LPO in rock salt, and it has been shown that grain boundary migration weakens the LPO (*Trimby et al.*, 2000), which would in return result in lower seismic anisotropy. Possible future work could better quantify the LPO loss by grain boundary migration. So far, we are not aware of study which models the texture change by grain boundary migration in salt, though such models exist for, for example, olivine (e.g., D-REX, (*Kaminski et al.*, 2004)). Such an implementation would make the resulting texture simulations more realistic. A way to cope with grain boundary migration would be to reorient highly strained grains after each deformation step with a random orientation. This does not capture the physics but might lead to LPO which reflect grain boundary migration better. Such work could be done in future avenues.

We limit the texture modelling to halite. It is possible to include other minerals, such as clay or anhydrite into VPSC, same as mixed phases. This would require good understanding of the single crystal properties, most important active slip systems, their relative straight and stress exponents for estimated deformation temperature. For halite, these parameters are well constrained. For this and simplicity reasons, we limit only on halite. Future work could include incorporating such cases. Moreover, the clay/anhydrite content could be varied through the deformation model to better reflect the real geology. More comparisons to natural rock salt texture could also help to improve and constrain texture modelling

Seismic processing

Seismic anisotropy, observed in the shear wave splitting dataset, and the predictions by numerical models suggest significant seismic anisotropy may manifest in deformed rock salt. This would affect seismic images (for example, in the estimation of horizon depths) and should be accounted for in seismic processing. Thus far, this study does not intensively investigate how this seismic anisotropy might be accounted for in seismic processing schemes. For example, the δ Thomsen-parameter was predominantly negative for all investigated models (see Chapter 2 to 5), which is also in agreement with the few studies available, which investigated anisotropy in rock salt (*Raymer et al.*, 2000b; *Planchart*, 2014). This knowledge can be used in imaging rock salt, which went through high deformation. An important conclusion drawn is that salt anisotropy might be approximated by a VTI symmetry. More investigations of salt anisotropy are also necessary. Studies of measured salt anisotropy in further data-sets can be compared to our results.

Other methods of studying anisotropy can be applied to seismic data-sets of rock salt, such as non-hyperbolic moveout-analysis or AVOA-analysis. Such data-sets are, in principle, available and can be used for further investigation. Accompanied with numerical modelling this give insights into if, for example, further assumptions can be made regarding the anisotropy inside rock salt. Investigating various data sets would give more knowledge about the robustness of the proposed methodology to predict seismic anisotropy in rock salt.

Analysis of frequency dependent anisotropy could be performed to characterised the length-scale responsible for the anisotropy (*Al-Harrasi et al.*, 2011). The frequency dependency of SWS splitting parameters in layered anisotropic media were shown for example on global seismic phases (*Rümpker et al.*, 1999) or on multicomponent VSP data (*Maultzsch et al.*, 2003). This could distinguish if LPO or, for example, fluid inclusion were the reason for the observed splitting.

Deformation model

The main deformation model shown in this study is a relatively simple 2D salt sheet approximation of the Mahogany salt body. A more realistic model might give better approximation of the resulting salt anisotropy. Considering a 3D model can improve the complex anisotropy pattern inside a salt structure. In places where 3D seismic data coverage is available and 3D deformation is important, it is possible to consider such scenarios. Also, the mechanical properties of the model could be described more realistically. As deformation is increased and the rock experiences strain and the mechanical rock properties will change. This coupling could be included into the deformation model in future studies.

Wider implication

In this study we demonstrate a work-flow to estimate salt anisotropy by deformation and dislocation plasticity. If the work-flow gets improved by the effects discussed above, it might be possible to invert from seismic anisotropy back to the deformation a specific rock went through. By measuring the anisotropy, insights about the deformation history could be gained. Ideally, a full elasticity model of the observed salt body would be needed to perform the work-flow inversely.

The work-flow shown here was only applied to rocksalt, but could be applied to other rocks or minerals, such as ice. The deformation of ice glaciers might lead to seismic anisotropy. Also here, the work-flow can be inverted to gain information about the deformation.

This study is the first its kind that we are aware of to investigate salt anisotropy in that detail using both seismic data sets and sophisticated seismic modelling of such anisotropy. The study demonstrates the effect crystal plasticity on salt textures and salt anisotropy, and shows that it explains anisotropy measured in real data. This work thus challenges the common assumption of isotropy in the seismic imaging of natural salt bodies in particular, and in rock salt in general.

APPENDIX A

SALT TECTONICS

Over geological time scales salt flows and behaves like a fluid. It has low viscosity and is highly deformable. Salt is nearly incompressible, meaning it resists compaction and flows under tectonic forces. Salt has very often similar densities across a large depth range, showing its nearly incompressible characteristic (*Jenyon*, 1986; *Warren*, 2016).

Salt flow is triggered by externally applied forces (e.g., *Warren* (2016)). Those can be passive gravitational forces or active extensional- or compressional tectonic forces. The salt flow can be syndepositional or can occur long after salt was deposited (*Vendeville and Nilsen*, 1995; *Hudec and Jackson*, 2007; *Warren*, 2016; *Jackson and Hudec*, 2017b). Strain-rates of naturally deformed rock salt vary considerably, depending on, for example, water content and deformation style. For example, rising salt diapirs show vertical strain rates of 2×10^{-16} s^{-1} to 8×10^{-11} s^{-1} (*Jackson and Vendeville*, 1994). Salt flow forms various striking structures in the subsurface. The most significant ones are large salt diapirs and salt sheets.

A.1 Salt diapirism

Salt diapirs are evaporite structures which intrude vertically into surrounding rock strata, forming, for example, mushroom-shaped structures in the sub-surface (*Jenyon*, 1986). Salt diapirs often penetrate upper sedimentary layers and can rise towards the surface.

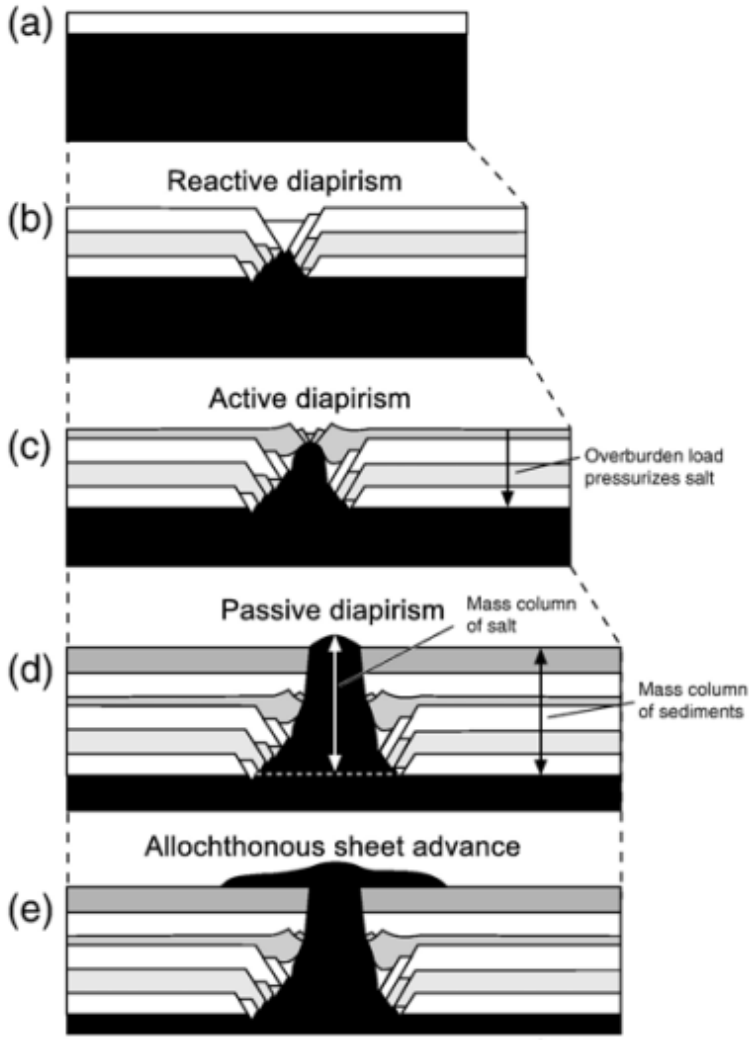

FIGURE A.1. Salt diapirism modified from *Hudec and Jackson* (2007). Three modes of diapir piercement exist. (b) Reactive diapirism describes processes where salt intrudes into, e.g., folds and faults, created by tectonic processes. In active diapirism (c) salt is deformed, resists compaction and eventually pierces the overlying sediments. In passive diapirism (d) salt flows without additional active tectonic stress. When the salt reaches the surfaces a salt sheet in formed (e). Allthonous deposits originated at a distance from its current position. A salt diapir does not necessarily evolve through all stages.

In fluid dynamics, three different models of diapirsm can be distinguished and are shown in Figure A.1. Active diapirsm describes the formation of salt structures where active tectonics support salt flow. For example, extensional forces thin and weaken the overburden and allows the salt to break through the sediments. In compressional tectonics the pressure inside the salt increases. Due to its incompressibility salt resists compaction and flows upwards.

Passive diapirism describes salt flow due to gravitational instability, occurring without exter-

nal tectonic forces. When sediments are deposited their density is initially lower than the salt density. Gravitational forces compact sediments and increase their density, while salt resists this compaction. If the density contrast becomes large enough, the salt begins to flow vertically.

Reactive diapirsm describes processes, where salt can not flow by passive diapirism. In those cases salt can still intrude into areas of low pressure. Such low pressure areas are, for example, folds and faults created by tectonics or other events (*Jenyon*, 1986; *Jackson and Talbot*, 1986; *Hudec and Jackson*, 2007; *Hudec et al.*, 2013; *Warren*, 2016; *Jackson and Hudec*, 2017a,b).

As shown in Figure A.1 a salt diapir evolves through different stages from reactive diapirism over active diapirism to passive diapirism, but does not necessarily go through all stages. However, salt diapirs deform by various mechanisms or a mix of all three described models. An example seismic section of two large salt diapirs from the East Central Graben in the North Sea is shown in Figure A.2.

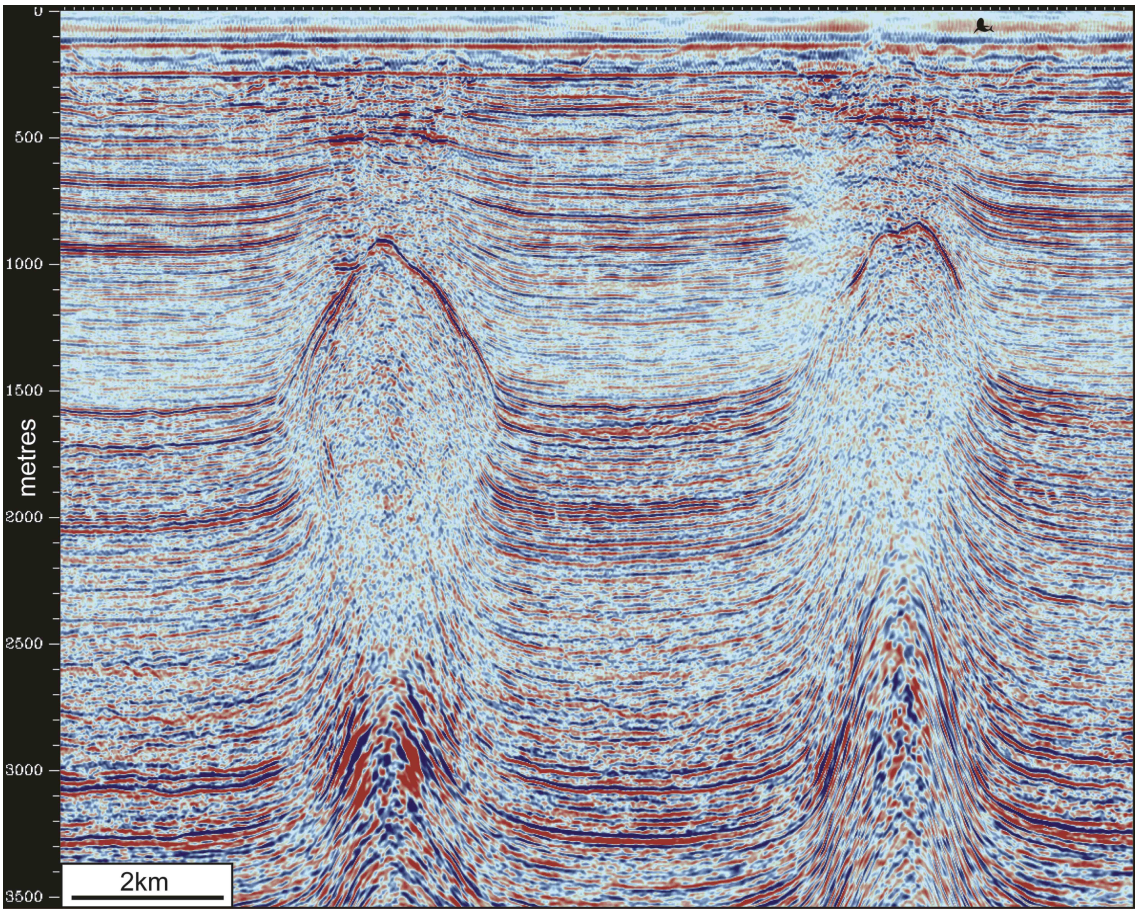

FIGURE A.2. Picture from (*Stewart*, 2007). Seismic depth migration showing two large salt diapirs from the East Central Graben in the North Sea. Vertical scale is approximately in metres.

A.2 Salt sheets

If salt is flowing vertically upwards, it can reach the surface. The up-flowing salt can spread laterally, due to gravitational- and tectonic forces. Such formations are called salt sheets. Salt sheets often occur after previous salt diapirism, which pushed the salt to the surface. Salt sheet structures are very common throughout many evaporite basins worldwide, including the Gulf of Mexico, the Santos basin or the Great Kavir basin in Iran (e.g., *Warren*, 2016).

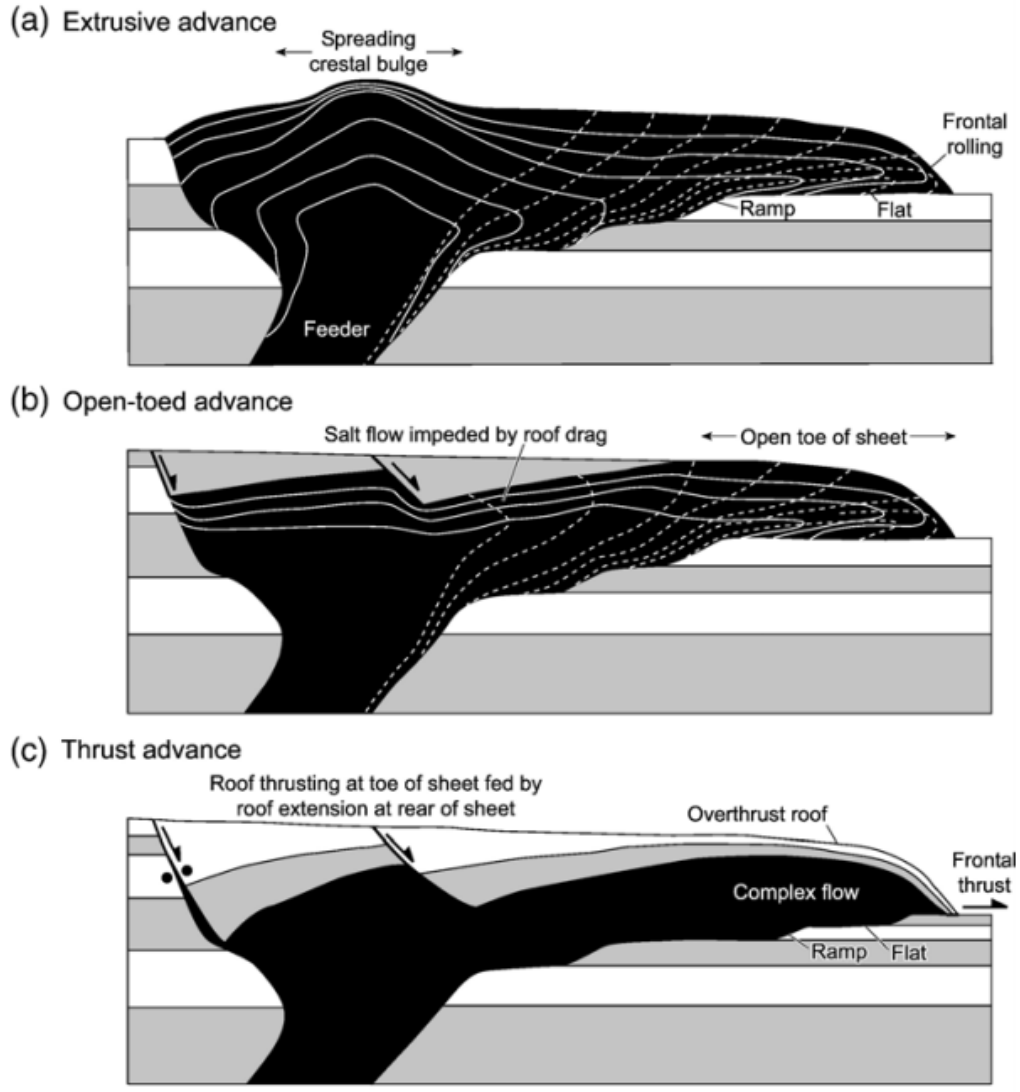

FIGURE A.3. Three main proposed salt sheet models modified from (*Hudec and Jackson*, 2007). They are (a) extrusive advance, (b) open-toed advance and (c) thrust advance. Salt sheets are fed by a source layer beneath them and tectonic forces push the salt near the surface. The advance of the salt sheet is dependent on the sheet advance rate and the sedimentation rate.

Salt sheet models have been constructed for various scenarios (*Hudec and Jackson*, 2007; *Hudec et al.*, 2013). They have in common that salt sheets raft along the surface with no- or little constraining sediments on top of the salt sheet. Salt sheet models can be divided into three main classes of models, which are: extrusive advance, open-toe advance and thrust-advance (*Hudec and Jackson*, 2007). A cartoon describing the three salt sheet models is shown in Figure A.3. The relative rates of the sheet advance (which depends on the tectonic forces) to the rate of sedimentation are important. If the sedimentation rate is zero then the salt sheet advances horizontally and parallel to the bedding plane. If the sedimentation is higher, but still low compared to the sheet advance rate, then the salt sheet climbs and ramps upwards with an angle towards the bedding plane. Commonly, salt sheets go through multiple stages and their advancing mechanisms changes over geological times (*Hudec and Jackson*, 2007).

Extrusive salt sheets spread at the surface from a passive salt feeder. The spreading rate is faster than the sedimentation rate (*Talbot and Jarvis*, 1984). Extrusive salt sheets advance without sediments on top or with sediments with negligible mechanical strength.

An open-toe advancing salt sheet is partly covered by sedimentation with a non-negligible mechanical strength, hampering the advance of the salt sheet. The salt sheet still advances, but is usually slower than the extrusive advancing salt sheet. It is called open-toe advance as often the "toe" of the salt sheet is uncovered, spreading along the surface.

Once completely buried the salt sheet may advance with sediments on top as a thrust if the driving forces are large enough to advance the salt sheet and the sediments (thrust-advance). Traction is exerted from the salt sheet to the over-thrusting roof (*Hudec et al.*, 2013; *Jackson and Hudec*, 2017b,a).

APPENDIX B

SHEAR WAVE SPLITTING

A crucial characteristic anisotropic media is shear wave splitting. Shear waves split into two different polarised waves, one slower than the other, when traversing anisotropic medium (*Savage*, 1999). This process is called shear wave splitting and is strong diagnostic of seismic anisotropy (*Crampin*, 1985). Figure B.1 shows a cartoon describing the shear wave splitting phenomena: an incoming wave, polarised in one direction split into two waves propagating with different seismic velocities and polarities, after entering an anisotropic medium. The faster propagating wave is called "fast shear wave" and the delayed one is called "slow shear wave". The delay time (δt) between the two polarised waves depends on the velocity difference of the fast and slow S-waves and on the distance the shear wave is travelling through the anisotropic medium. The polarisation angle depends on the projection of the symmetry axis of the medium onto a plane to the propagation direction. For example, a layered medium corresponds to a horizontally fast shear wave. Measuring its polarisation provide information about the kind of anisotropy or a possible symmetry axis of the medium (*Crampin*, 1985; *Savage*, 1999; *Wookey et al.*, 2005). Depending on the symmetry axis, either the horizontally polarised shear wave (SH) or the vertically polarised shear wave (SV) is faster. Measurement of shear wave splitting is an important tool to infer seismic anisotropy of a medium. It is used on different scales, from fractures to large scale anisotropy in the lower most mantle.

Shear wave splitting, and the associated splitting parameters can be observed in different ways. Shear wave splitting has an effect on the resulting particle motion. A particle motion diagram is a plot of the slow and fast wave component against each other around a specific phase, where splitting is observed. Analysing the particle motion diagram can further resolve splitting. Therefore, it can help to distinguish whether a shear wave travelled through an anisotropic medium or not. A unsplit shear wave manifest in linear particle motion is observed. This is

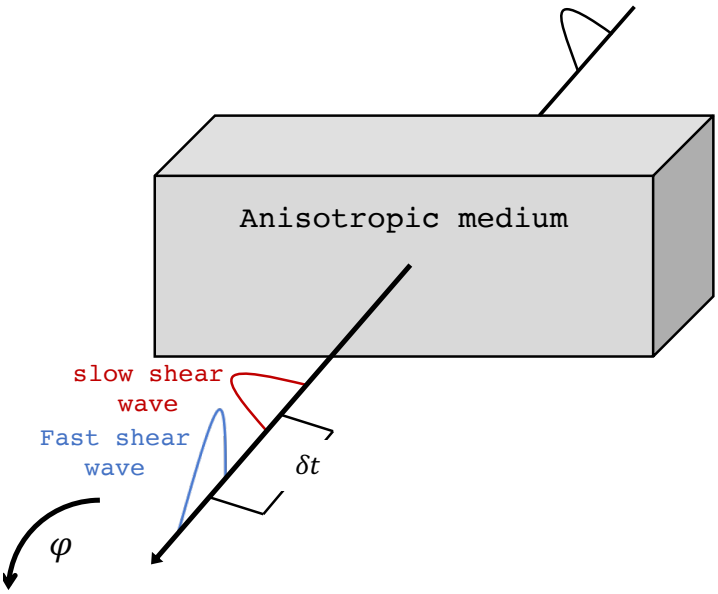

FIGURE B.1. When entering an anisotropic medium, shear waves split in two waves orthogonal polarised to each other. The polarisation direction of the fast shear wave is called ϕ throughout this work, the delay time between them is δt. ϕ and δt are called splitting parameters. By determining them it is possible to reveal anisotropic properties of the body. ϕ is the projection of the fast axis onto a plane perpendicular to the direction of wave propagation, and δt depends on the extent of the anisotropic layer and/or the degree of anisotropy.

sometimes referred as Null splitting (*Teanby et al.*, 2004). The fast and slow shear wave are recorded at the same time. If splitting is present the particle motion is elliptical often (e.g., *Vecsey et al.*, 2008), the two shear waves arrive separated in time. The shape of the particle motion is dependent on the relationship between the dominant period of the shear wave and the observed time shift (*Savage*, 1999).

Measuring shear wave splitting

The method to measure splitting parameters, used in this work, is based on the work of *Silver and Chan* (1991) and *Bowman and Ando* (1987). This technique works by finding splitting parameters which best removes splitting from the traces. If the correct splitting parameters are found the traces can be rotated into fast- and slow directions and the traces just remain with a delay time δt. In following, two complementary methods, the cross-correlation technique (*Bowman and Ando*, 1987) and the eigenvalue method (*Silver and Chan*, 1991) are presented. They are different approaches of determining the best splitting parameters for removing splitting. The properties of both methods are such that they can be used to estimate the "quality" (or credibility) of the shear wave splitting measurements (*Wuestefeld et al.*, 2010). They also provide a diagnos-

tic for identifying Null-measurements, where no splitting is observed. This can be the case if either no anisotropy is present, or if the initial polarisation of the shear wave is parallel or perpendicular to the fast direction of the medium (i.e., the fast or slow wave has an amplitude of zero).

During the correlation technique, the seismograms are rotated to different test polarisations. For each the cross correlation coefficient between the two components of motion is calculated. When rotated in fast- and slow axes, the waveforms are similar to each other. The highest cross correlation coefficient gives the fast-direction and consequently, the delay time. The cross-correlation technique searches for the best similarity of the traces by computing the cross-correlation coefficient of the seismic traces, rotated in different directions (*Ando et al.*, 1980; *Bowman and Ando*, 1987).

In the eigenvalue method a grid search over ϕ and δt is applied. The correct splitting parameters are those, which best linearise the particle motion. This is achieved by calculating for each pair of splitting parameters (ϕ and δt) the covariance matrix of the two components of the corrected seismogram (*Silver and Chan*, 1991). The best pair will have the lowest second eigenvalue (λ_2) of the covariance matrix. For the isotropic case (no splitting), the covariance matrix will have one non-zero eigenvalue λ_1, whereas there are two nonzero eigenvalues (λ_1 and λ_2) for the anisotropic splitting case (*Bowman and Ando*, 1987; *Silver and Chan*, 1991). The solution of the most singular singular eigenvalue matrix of the rotated and time shifted seismogram, based on λ_1 and λ_2 leads to the splitting parameters which best linearise the particle motion and best correct for the splitting effect (*Silver and Chan*, 1991; *Wuestefeld et al.*, 2010).

Quality measurement

The cross-correlation technique and the eigenvalue technique have complementary properties in a way that they can be used to identify null measurements and the quality of the shear wave splitting measurement (*Wuestefeld et al.*, 2010). The cross correlation- and eigenvalue method show significant differences for initial shear wave polarisations close to null directions (*Wuestefeld and Bokelmann*, 2007), but produce consistent splitting parameters away from the null direction. The cross correlation method will fail near null directions. While the time delay is correctly calculated to be zero for a shear wave polarisation in the null direction, the fast direction differ by $\pm 45^\circ$ from the expected solution of the fast shear wave. On the other hand, the eigenvalue method is unstable near nulls and fluctuates in the predicted delay time. The polarisation shows either $\pm 90^\circ$ or 0° away from the expected fast polarisation direction (*Wuestefeld and Bokelmann*, 2007).

As described in *Wuestefeld et al.* (2010), we can define a quality measure for ideal splitting

and ideal null results; dt_{EV}, ϕ_{EV}, dt_{XC} and ϕ_{XC} are splitting parameters predicted by the eigenvalue method and the cross correlation method, respectively. For an ideal null measurement the predicted delay time difference is $\delta = dt_{EV} - dt_{XC} = 0$ and the normalised difference in the predicted fast shear polarisations is $\sigma = \frac{\phi_{EV} - \phi_{XC}}{45} = 1$. That is, because the predicted fast shear wave polarisation in an ideal null case will differ by 45° for both methods. On the other hand, an ideal splitting case, both methods will predict the same delay time and fast shear wave polarisation, so $\delta = 1$ and $\sigma = 0$.

A quality factor Q can be defined, characterising the measurement. For each measured shear wave splitting, the distance d_{Null} to the ideal null ($\delta = 0$, $\sigma = 1$) and the distance d_{Good} to the ideal splitting event ($\delta = 1$, $\sigma = 0$) is calculated.

$$\mathrm{d_{Null}} = \sqrt{\delta^2 + (\sigma - 1)^2}\sqrt{2}, \tag{B.1}$$

$$\mathrm{d_{Null}} = \sqrt{(\delta - 1)^2 + \sigma^2}\sqrt{2}, \tag{B.2}$$

and the quality factor Q is then

$$Q = \begin{cases} -(1 - \mathrm{d_{Null}}) & \text{if } d_{Null} < d_{Good} \\ 1 - -d_{\mathrm{Good}} & \text{if } d_{Null} \geq d_{Good} \end{cases}. \tag{B.3}$$

With that we have an objective measure of confidence in each shear wave splitting event. If $Q \cong 1$, a clear splitting event is detected, if $Q \cong -1$ a clear Null measurement is detected and if $Q \cong 0$, no statement can be made.

B.1 Analysis windows selection

The results are, however, dependent on the selected time window on which the above analysis are preformed (*Teanby et al.*, 2004; *Vecsey et al.*, 2008). A method to select an optimum time window is essential for accurate splitting calculation. This work uses a time window selection method based on cluster analysis (*Teanby et al.*, 2004). The selected time window should provide stable and representative results. The window should be long enough to include the phase and several periods of the dominant frequency, while being short enough to exclude contamination from other phases (*Teanby et al.*, 2004). Time windows which are too small produce small and false error estimates (*Vecsey et al.*, 2008). To find the best window, shear wave splitting parameter are calculated for a range of windows (in this case we use 100 windows). Based on a cluster analysis, the "best" window is chosen (*Everitt et al.*, 2001; *Teanby et al.*, 2004). Every single measurement (so every ϕ; δt pair) is considered as a cluster by itself. Beginning with a number of clusters which is equal to the number of data points, all cluster distances to each other are calculated. The distance is defined as the normalised euclidean distance between the clusters centre. Thereafter,

the two nearest clusters are combined to one cluster, thus the number of clusters is reduced by one. This procedure is repeated until a critical number of clusters is reached, to make sure that significant different results end not in the same cluster. Finally, the optimum cluster based on the variance of the measurements and clusters is determined. From this cluster the window with the smallest error on ϕ and δt is chosen as the final window, which is then used for the splitting parameter calculation (*Everitt et al.*, 2001).

APPENDIX C

SHEAR WAVE SPLITTING RESULTS

Shown are the λ_2-error-surfaces of the VSP-field data set for the P- to S-wave conversion at the top of the salt body (Figure C.1 and C.2) and the base of the salt body (Figure C.3 and C.4). Also shown are the error-surfaces for the synthetic VSP shear-wave splitting (Figure C.5 and C.6).

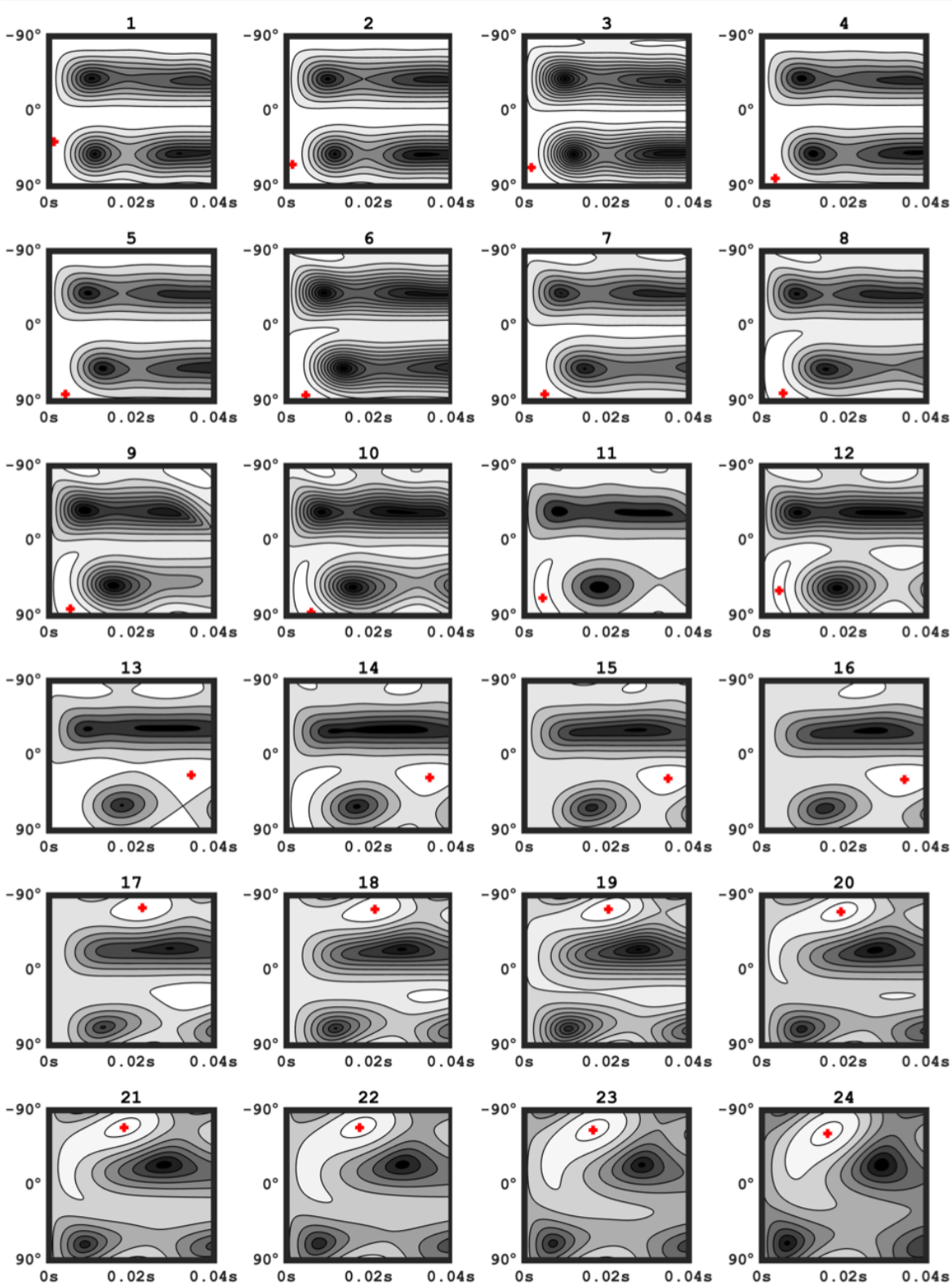

FIGURE C.1. Shear wave splitting λ_2 error surfaces from the VSP field-data set, presented in Chapter 2. Top P- to S conversion. Receiver 1-24.

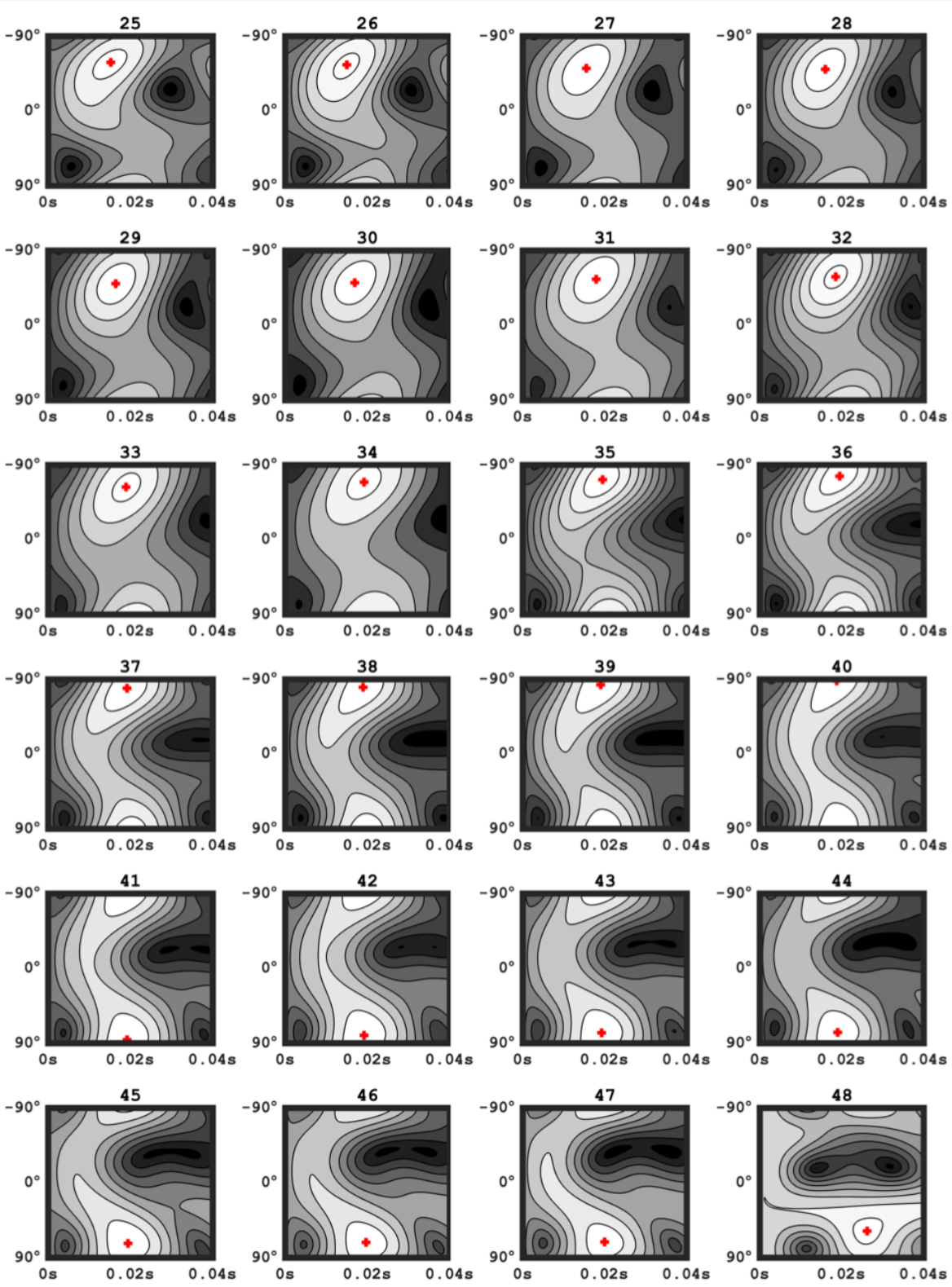

FIGURE C.2. Shear wave splitting λ_2 error surfaces from the VSP field-data set, presented in Chapter 2. Top P- to S conversion. Receiver 25-48.

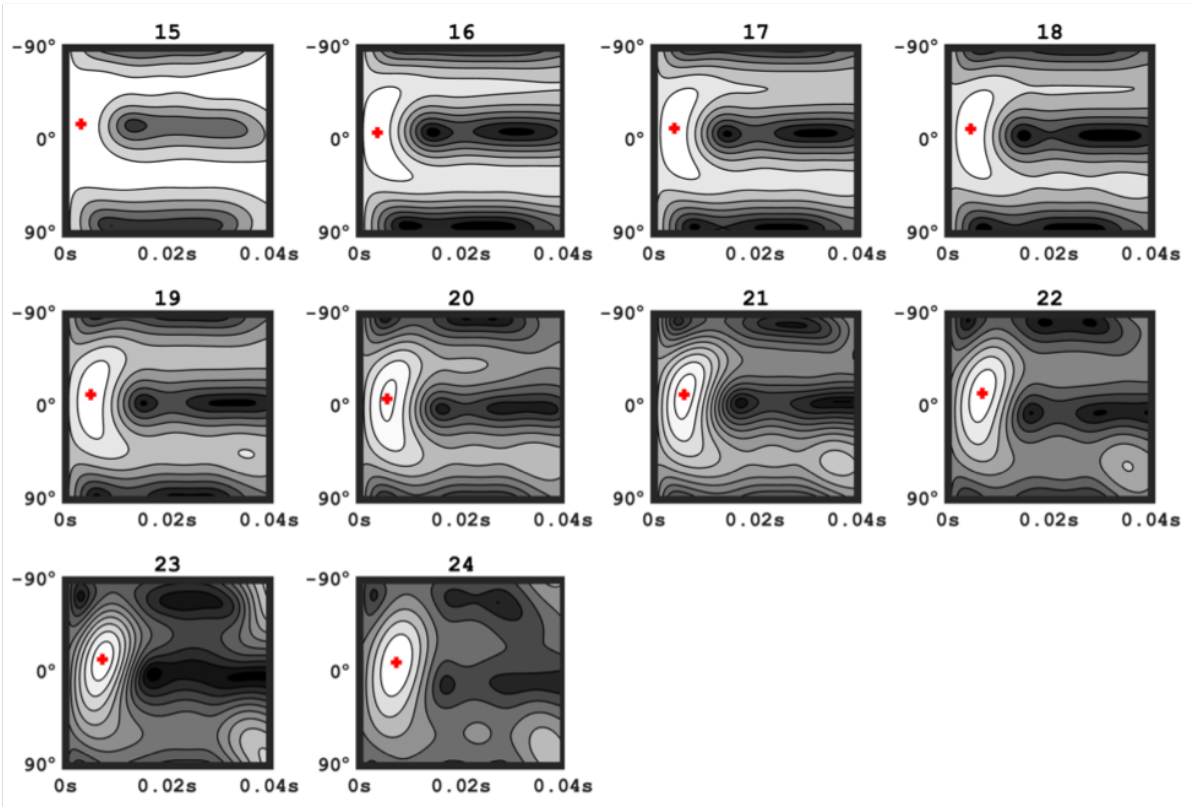

FIGURE C.3. Shear wave splitting λ_2 error surfaces from the VSP field-data set, presented in Chapter 2. Bottom P- to S conversion. Receiver 15-24.

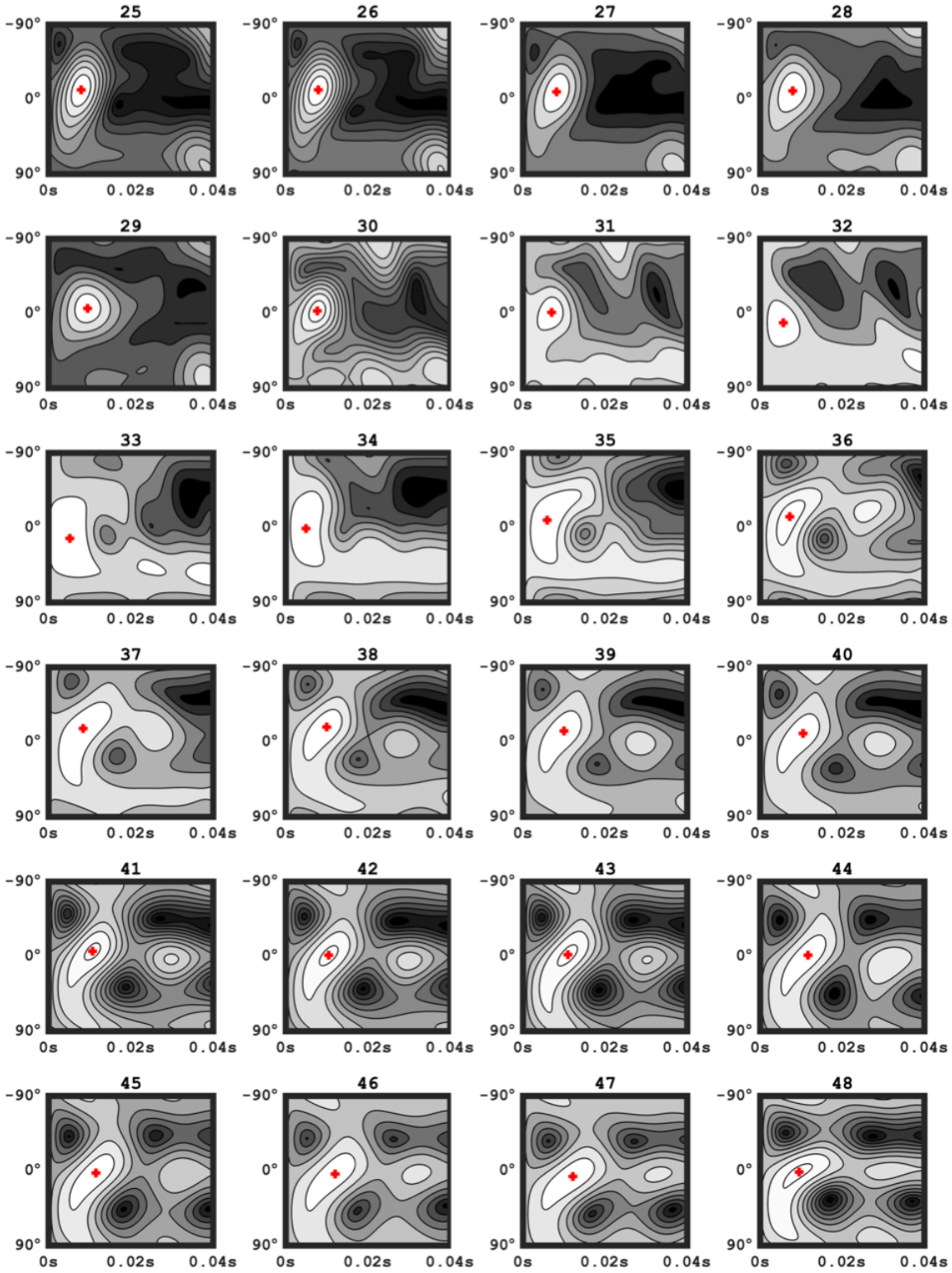

FIGURE C.4. Shear wave splitting λ_2 error surfaces from the VSP field-data set, presented in Chapter 2. Bottom P- to S conversion. Receiver 25-48.

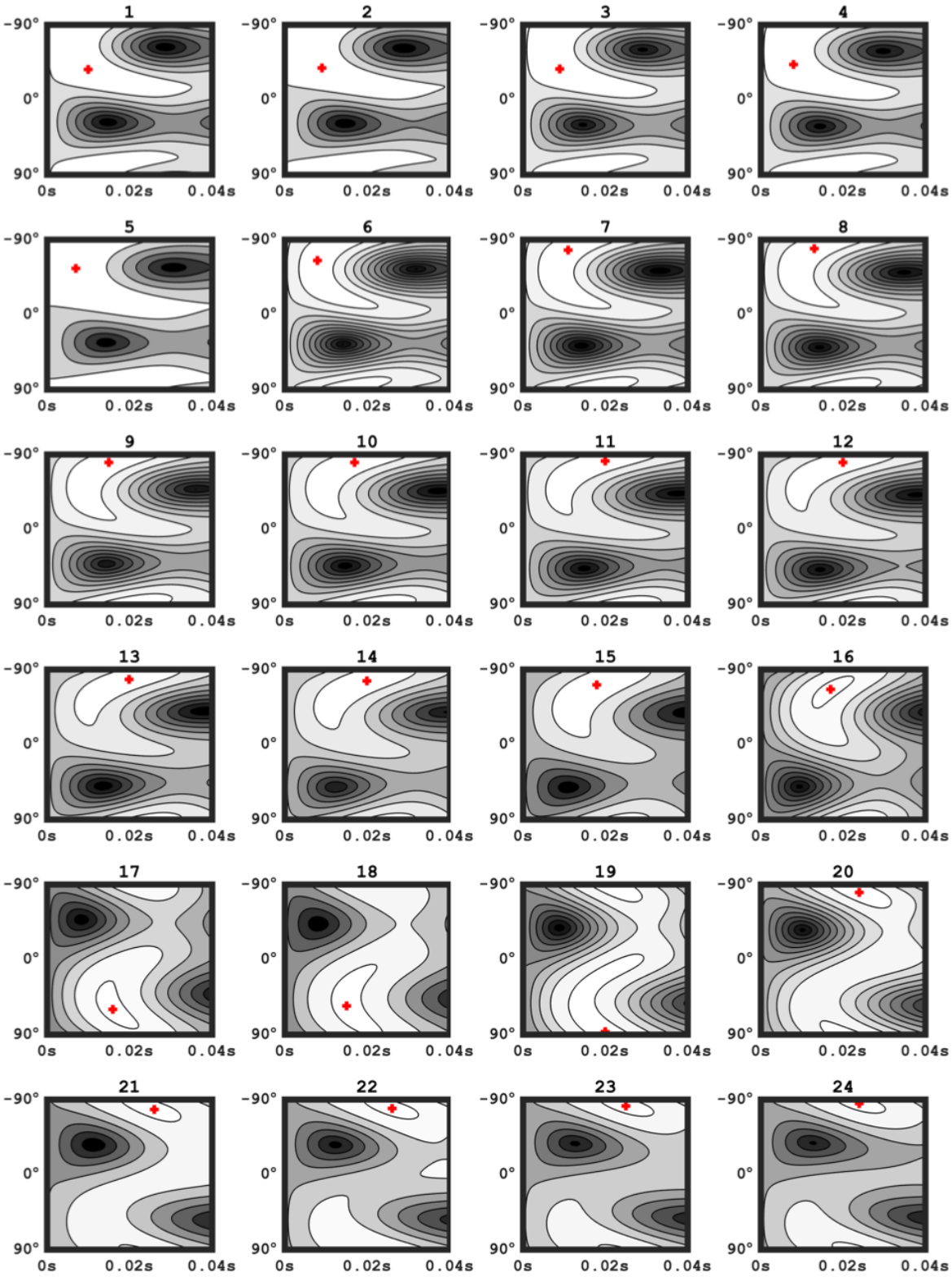

FIGURE C.5. Synthetic shear wave splitting λ_2 error surfaces, presented in Chapter 5. Receiver 1-24.

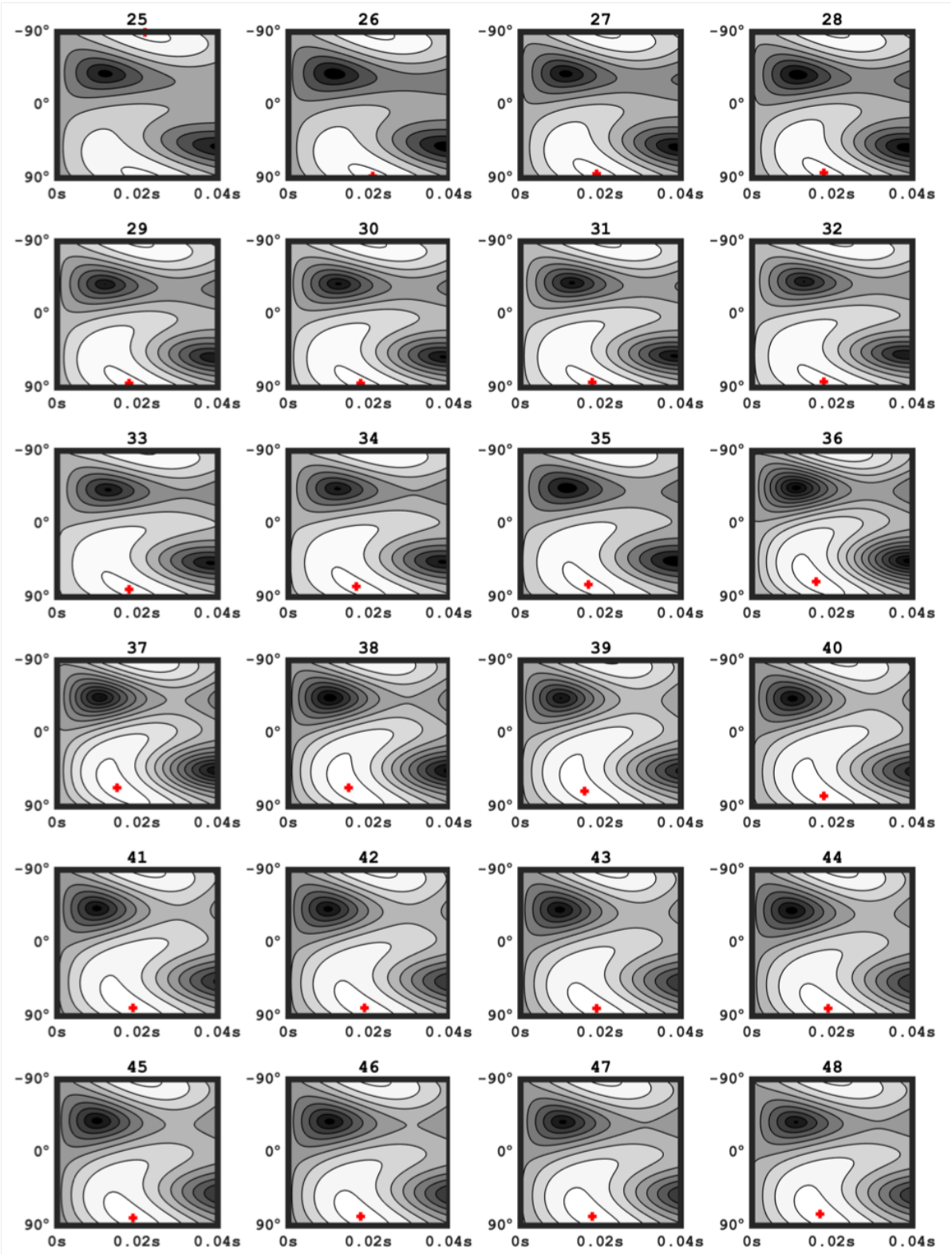

FIGURE C.6. Synthetic shear wave splitting λ_2 error surfaces, presented in Chapter 5. Receiver 25-48.

APPENDIX D

REPRESENTATION OF TEXTURE

The orientation of a crystal lattice can be represented by three angles, called Euler angles (φ, ϑ, ψ). Any orientation can be described by three rotations, which are given by the Euler angles, about the axes of a fixed coordinate system. A list of Euler angles represents the texture or lattice orientations of the polycrystal.

In crystallography there are conventions how to refer to planes and directions. When referring to a specific plane then round parentheses are used as a description (h,k,l). When referring to a set of symmetrically equivalent planes then curly parentheses are used {h,k,l}. For example for a crystal with cubic symmetry (such as haltite) the planes (100), (010), (001), ($\bar{1}$00), (0$\bar{1}$0), (00$\bar{1}$) are related to each other due to the crystal symmetry. The texture of polycrystalline halite is described by three set of planes {100}, {110} and {111}, shown in Figure D.1. Crystallographic directions are defined in the same way, where one specific direction is labelled with square brackets [hkl] and a number of crystallographic equivalent direction are labelled as <hkl>. Halite deformed through the slip systems {110}<110>, {100}<110>, and {111}<110>.

The texture of a polycrystal can be represented by a pole figure. Pole figures are graphical representations of orientations in space and are used to display the lattice orientations of polycrystals. The orientation of a plane in space can be defined by a vector normal to the plane-surface, called pole. To conveniently display 3D orientation in 2D, various projections exist. Equal area projection is often to represent texture, as it preserves the spherical area. Thus, a random distribution of crystal lattice orientations would lead to a uniform distribution of points in the projection area. This makes the equal area the favourably projection to represent texture. In contrast, stereographic projection of randomly oriented lattice orientation generates denser distributed points in the centre of the projection area.

A point P' is projected onto the visualisation plane as shown in Figure D.2. The direction from a centre C of a sphere, P is a point on the surface of the sphere and N is the North-pole of the sphere, assuming an upper hemisphere projection. The direction CP is projects to the point P' on a projection plane tangential to the sphere, such that the distance NP is the same as the distance NP'.

Any direction can be represented by an equal area projection. The pole figure shows all orientations of the each lattice for a specified pole and therefore for a specific crystallographic lattice plane. Texture is often represented by a orientation-distribution density plot (ODF). The strength of texture (i.e., the degree of alignment of the given crystallographic plane) is then given in multiples of a random distribution (MRD). An example pole figure displaying texture of a cubic

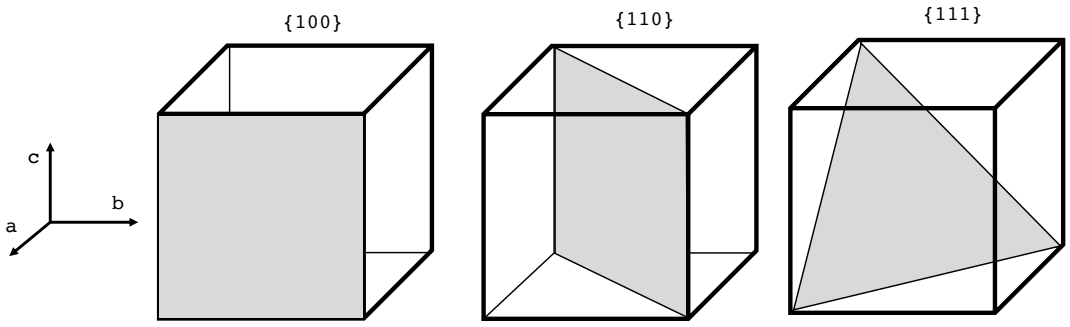

FIGURE D.1. Three crystal planes of a cubic crystal, {100}, {110} and {111}. These three planes are the planes to describe texture inside a halite polycrystal entirely. Other planes are symmetrical equivalent.

symmetry is shown in Figure D.3. Here, texture is displayed in ODF. The Figure is also displayed in this thesis in Chapter 4. It shows a deformed polycrystalline halite. The projection planes are (100), (110) and (111).

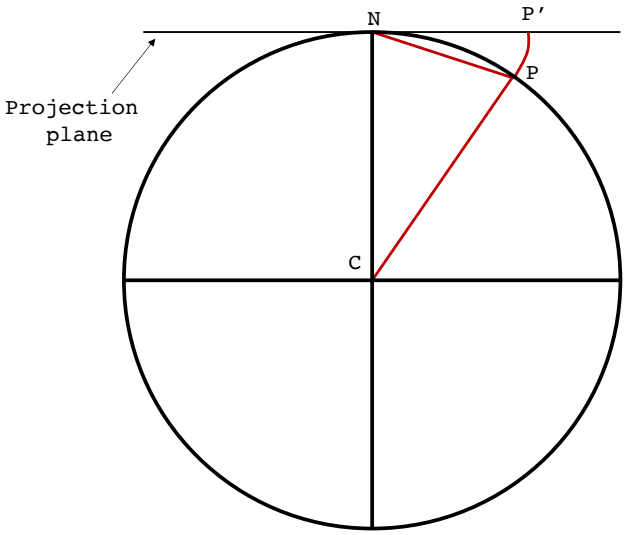

FIGURE D.2. Schematic summary of a equal area projection in a 2D view. In an equal area projection, any direction CP can be projected to a point P' on the projection plane tangential to the sphere at N, in a way that the distance NP' equals NP. This example is an upper hemisphere projection plot, if N is the North pole of the sphere. Equal area projection are often used for displaying texture and lattice orientations.

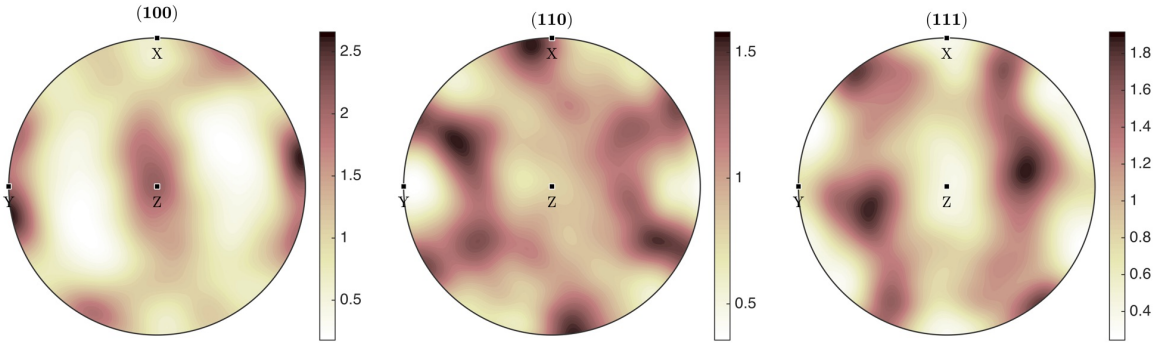

FIGURE D.3. Sample pole figure displaying texture. Pole figures are 2D representation of lattice preferred orientation in 3D space. Here, the projection planes are (100), (110) and (111).

APPENDIX E

MODEL RHEOLOGIES

The MD-constitutive model is used in this study to model salt deformation of the Mahogany salt deformation model in Chapter 5. The SR3 model is used to model sediment deformation in both model, the salt diapir model (Chapter 4) and the Mahogany salt sheet model (Chapter 5). Both are described here.

E.1 Multimechanism Deformation (MD) constitutive model

We follow *Munson and Dawson* (1979), *Munson et al.* (2004) and *Fredrich et al.* (2007) to describe the Multimechanism creep model. The MD-model is a mathematical formulation, describing the mechanical behaviour of various rock salts. Depending on stress/temperature is has been shown that different rock salt deformation mechanism are active, controlling the creep behaviour of rock salt (*Munson and Dawson*, 1979). The MD-model considers dislocations climb active at high temperatures and low stresses, dislocation slip at high stresses and a third undefined mechanism at low temperatures and low stresses, which is experimentally well characterised (*Fredrich et al.*, 2007). The steady state creep rates for the three mechanisms described are:

$$\dot{\varepsilon}_{s1} = A_1 e^{-Q_1/RT}\left(\frac{\sigma}{G}\right)^{n_1}, \tag{E.1}$$

$$\dot{\varepsilon}_{s2} = A_2 e^{-Q_2/RT}\left(\frac{\sigma}{G}\right)^{n_2}, \tag{E.2}$$

$$\dot{\varepsilon}_{s3} = H(\sigma-\sigma_0)\left(B_1 e^{\frac{-Q_1}{RT}} + B_2 e^{\frac{-Q_2}{RT}}\right)\sinh\left(\frac{q}{G}(\sigma-\sigma_0)\right). \tag{E.3}$$

The subscripts refer to the different mechanisms, where $\dot{\varepsilon}_{s_1}$ is the strain rate contributed by dislocation climb, $\dot{\varepsilon}_{s_2}$ by the undefined mechanism and $\dot{\varepsilon}_{s_3}$ by dislocation glide. $A_{1,2}$ and $B_{1,2}$ are

constant, Q is the activation energy, T is the absolute temperature. In both models, we assume a temperature gradient of 35 $\mathrm{Kkm^{-1}}$ and a surface temperature of 10 °C. G is the shear modulus, $n_{1,2}$ are stress exponents, q is a stress constant. The contribution of $\dot{\varepsilon}_{s3}$ is limited by a Heaviside function H with argument $\sigma - \sigma_0$, where σ_0 is a reference stress of this mechanism. The Heaviside function is equal to 1 if the argument is positive ($\sigma > \sigma_0$) and is zero if the argument is negative ($\sigma < \sigma_0$). R is the universal Gas constant and σ describes the equivalent stress, given in the Tresca Form:

$$\sigma = |\sigma_1 - \sigma_3|. \tag{E.4}$$

All the mechanisms act at the same time. The total steady state creep rate is therefore the sum over all steady state creep rates:

$$\dot{\varepsilon_s} = \dot{\varepsilon}_{s_1} + \dot{\varepsilon}_{s_2} + \dot{\varepsilon}_{s_3}. \tag{E.5}$$

A multiplier F relates the equivalent strain rate $\dot{\varepsilon}_{eq}$ to the steady state creep rate $\dot{\varepsilon}_s$:

$$\dot{\varepsilon}_{eq} = F\,\dot{\varepsilon}_s. \tag{E.6}$$

F is a function representing transient creep behaviour. It includes a work-hardening branch, an equilibrium branch, and a recovery branch:

$$F = \begin{cases} \exp\left(\Delta\left(1 - \frac{\zeta}{\varepsilon_t^*}\right)^2\right) & \text{if } \zeta < \varepsilon_t^* \\ 1 & \text{if } \zeta = \varepsilon_t^* \\ \exp\left(-\delta\left(1 - \frac{\zeta}{\varepsilon_t^*}\right)^2\right) & \text{if } \zeta > \varepsilon_t^* \end{cases}, \tag{E.7}$$

where Δ, is the work-hardening parameter and δ is the recovery parameter, ζ is the hardening variable and ε_t^* is the transient strain limit. The curvature is defined by Δ, or δ, depending weather the transient is work-hardening or recovering. The transient limit is defined by

$$\varepsilon_t^* = K_0 e^{cT}\left(\frac{\sigma}{G}\right)^m, \tag{E.8}$$

where K_0, c and m are constants. The evolution of the kinematic hardening parameter is given by

$$\dot{\zeta} = \left(F - 1\right)\dot{\varepsilon}_s, \tag{E.9}$$

which approaches zero when the steady-state condition is achieved.

The different model parameters need to be found by a fitting routine. *Fredrich et al.* (2007)

constrain the constitutive response of deepwater Gulf of Mexico salt diapirs from different regions. The expected constitutive behaviour of all rock salt samples lies within the range of well characterised Gulf of Mexico domal salts. The best estimates to the constitutive behaviour of Gulf of Mexico rock salts, according to *Fredrich et al.* (2007), are taken in this study and are shown in Table E.1. Those parameters are used to model the salt rheology in the Mahogany salt sheet model. Linear elastic parameters of the Gulf of Mexico salt assumed are a Youngs Modulus of $E = 31GPa$ and a poissons-ratio of $\nu = 0.4$, chosen according to *Heidari et al.* (2016).

G [GPa]	**A_1 [s^{-1}]**	**Q_1 [Kcal/mol]**	**n_1**	**B_1 [s^{-1}]**
12.4	5.954e22	25	5.5	4.321e6
A_2 [s^{-1}]	**Q_2 [Kcal/mol]**	**n_2**	**B_2 [s^{-1}]**	**σ_0 [MPa]**
6.869e12	10	5.0	2.154e-2	20.57
q	**R [cal/mol-deg]**	**m**	**K_0**	**c [T^{-1}]**
5.335e3	1.987	3	1.342e6	9.198e-3

TABLE E.1. MD model parameters used in the Mahogany salt body salt sheet model.

A creep strain curve can be separated into a steady state part, where the strain grows at a constant rate, and a transient part, where the strain rate decreases, representing work hardening. When the transient strain limit is reached, further strain accumulates only at the steady state creep rate. A typical creep curve is shown in Figure E.1.

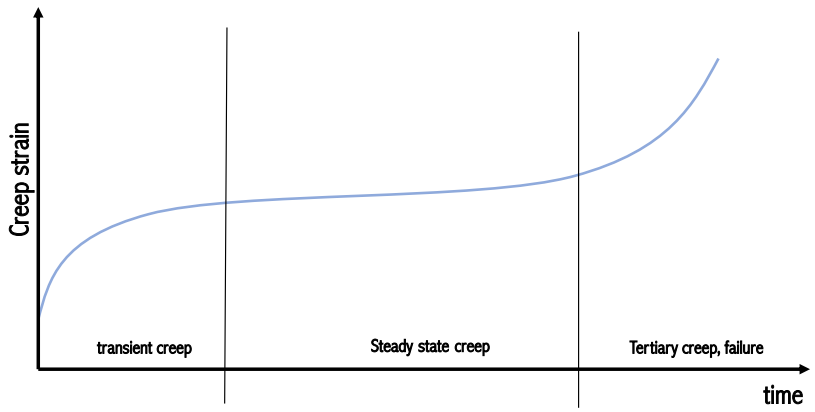

FIGURE E.1. Schematic and typical creep strain curve. The primary or transient creep is the work hardening branch. The strain/time slope decreases with time. At the transient limit, the curve is going over into the secondary creep. In the secondary creep or steady state branch the rate of straining is constant (recovery). After that failure happens and the strain rate accelerates quickly (tertiary creep).

E.2 SR3 constitutive model

The rheology of the sediments are modelled using the SR3 material model. The SR3 material model is a constitutive critical-state poroelastic-plastic material model, based on the "cam clay" material model concept (*Drucker and Prager*, 1952). The density of the sediment, assumed in both models is ρ_{Sediment}=2.4gcm^{-3}. A full description of the SR3-material model can be found in *Crook et al.* (2006). An important factor of this model is that takes into account material inelastic behaviour (*Wood*, 1990). In the elastic regimes the sediments deforms according to Hooke's Law. The boundaries of the elastic regime are defined by a smooth yield surface in p-q surface. The yield surface is defined as:

$$\phi(\sigma, \varepsilon_v^p) = g(\theta, p)q + (p - p_t)\tan\beta\Big(\frac{p - p_c}{p_t - p_c}\Big)^{\frac{1}{n}}, \tag{E.10}$$

where θ is the Lode angle, which can be considered as a measure of loading type (*Crook et al.*, 2006), p is the effective mean stress, q is the deviatoric stress, p_t is the tensile intercept, p_c is the compressive intersect, β and n are material constants defining the shape of the yield surface in $p-q$ plane and $g(\theta, p)$ is a function controlling the shape of the yield surface in the deviatoric plane. Figure E.2 shows a schematic illustration of the of the yield surface in $p-q$ space.

$$p_c = p_{c0}\exp\Big[\frac{v\varepsilon_v^p}{\lambda - \kappa}\Big], \tag{E.11}$$

$$p_t = p_{t0}\exp\Big[\frac{v(\varepsilon_v^p)_{max}}{\lambda - \kappa}\Big] \tag{E.12}$$

where v is the specific volume, and λ and κ are the slopes of the normal compression line and unloading-reloading lines; $(\varepsilon_v^p)_{max}$ is the maximum dilatational volumetric plastic strain. Inside the yield surface the deformation is plastic. The plastic strain rate is defined as:

$$\dot{\varepsilon}^p = \dot{\lambda}\frac{d\Psi}{d\sigma} \tag{E.13}$$

where Ψ is the plastic potential defined as:

$$\Psi(p, \varepsilon_v^p) = g(\theta, p)q + (p - p_t)\tan\psi\Big(\frac{p - p_c}{p_t - p_c}\Big)^{\frac{1}{n}} \tag{E.14}$$

where ψ is a material parameter and dilation angle, $\dot{\lambda}$ is a plastic multiplier. The deviatoric correction term $g(\theta, p)$ is defined as:

$$g(\theta, p) = \left[\frac{1}{1 - \beta^\pi(p)}\Big(1 + \beta^\pi(p)\frac{r^3}{q^3}\Big)\right]^{N^\pi}, \tag{E.15}$$

N^π is a material constant, and β^π is a function of p:

$$\beta^\pi(p) = \beta_0^\pi exp\Big(\beta_1^\pi p\frac{p_c}{p_c^0}\Big), \tag{E.16}$$

β_0^π and β_1^π are material constants, p_c^0 and p_c is the initial and current preconsolidation pressure.

The values used for in the SR3 material model are listed in Table E.2. Those values have been successfully used to model sediment rheology around rock salt in, e.g., *Heidari et al.* (2016).

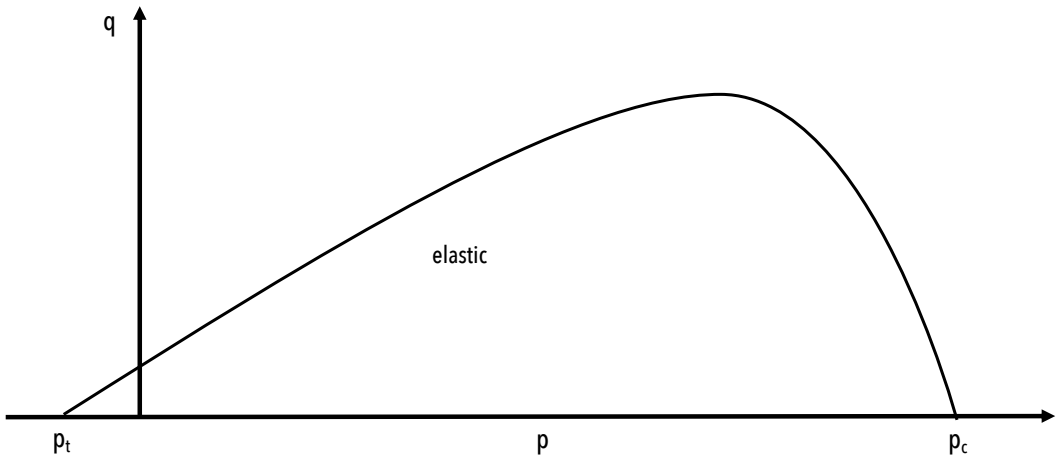

FIGURE E.2. Schematic illustration of the yield surface, showing the $p-q$ space. Inside the yield surface, the deformation is elastic. The yield surface defines the boundary to plastic deformation. The shape is defined by the equation shown in equation E.10.

E [MPa]	ν	$\mathbf{K_0}$ **[MPa]**	κ	$\mathbf{p_t^0}$ **[s^{-1}]**	$\mathbf{p_c^0}$ **[s^{-1}]**	
40	0.25	10	0.01	0.085	-1	
β[°]	ψ[°]	β_0	β_1 **[MPa^{-1}]**	α	**N**	**n**
60	51	0.6	0.725	0.25	1.3	0.38

TABLE E.2. SR3 modelling parameters used for the calculation, according to *Nygaard et al.* (2006) and *Rockfield Global* (2013).

APPENDIX F

SPECFEM2D - WAVE PROPAGATION USING SPECTRAL ELEMENTS

Chapter 4 and Chapter 5 use the Specfem2D as a tool to generate seismic wave propagation. In the past, wave propagation has been simulated by different numerical methods, from finite differences to finite elements and spectral-elements. Finite differences are the most frequently used method, due to their easy formulation and implementation, compared to other numerical methods. Finite differences estimate spatial- and time derivatives with differences of neighbouring grid points (*Levander*, 1988; *Graves*, 1996; *Ohminato and Chouet*, 1997). Also, other similar techniques, such as spectral methods, have been applied to solve the wave equation in smooth media (*Carcione*, 1994; *Komatitsch et al.*, 2005). In spectral methods, time domain quantities and differential equations are solved in the frequency domain, using Fourier-transformation. However, this method might fail or become numerically costly with complicated meshes including discontinuities (*Komatitsch and Vilotte*, 1998; *Komatitsch et al.*, 2005).

To address this problem, the finite element method has been used to calculate seismic wave propagation through media. The finite elements method is another numerical approach to solve differential equations and calculate wave propagation. The modelling domain is separated into elements, with different shapes, most commonly triangles or quadrangles (in 2D). This method allows greater flexibility to deal with complex surface topographies. Using finite elements, more complicated mesh designs can be implemented (*Tromp et al.*, 2008; *Peter et al.*, 2011). Traditionally low order polynomials are used to approximate the shape of each element, as this limits the computational costs (*Zheng et al.*, 2014). However, using low order polynomials might be insufficient in seismic wave propagation applications, as it can not capture larger wave oscillations across elements (*Zheng et al.*, 2014). The finite element method has been successfully used to approximate wave propagation (*Lysmer and Drake*, 1972; *Bao et al.*, 1998), but suffers from high computation cost and its complicated implementation, particular on parallel computers

(*Komatitsch et al.*, 2005).

In this study, wave propagation is approached by using the open source Fortran code Specfem2d (*Tromp et al.*, 2008). Specfem2d is based on the spectral elements method (*Wang and Cai*, 2014) (SEM). The spectral element method is a higher order finite element method. It combines the properties of the finite element method to deal with highly undulated topographies with the accuracy of spectral methods (*Tromp et al.*, 2008; *Wang and Cai*, 2014; *Zheng et al.*, 2014). Instead of using low order polynomials, spectral methods expands the solution by using trigonometric polynomials, exploiting that every continuous function can be displayed as a polynomial series. Spectral elements bring several advantages, e.g. it can be efficiently implemented in parallel simulations (*Komatitsch and Tromp*, 2002a,b; *Tromp et al.*, 2008; *Zheng et al.*, 2014). These properties have made the spectral element method to an important tool to analyse seismic wave propagation, and it has been successfully used in different studies, for example *Chaljub and Valette* (2004); *Liu et al.* (2004); *Chaljub et al.* (2007) and others. Formulations and mathematical descriptions of using spectral elements in seismology can be found in, for example, *Komatitsch and Vilotte* (1998); *Tromp et al.* (2008).

Specfem2d simulates acoustic, elastic, poro-elastic and acoustic wave propagation (*Komatitsch and Vilotte*, 1998) in isotropic and anisotropic media. The Specfem software package is freely available by the Computational Infrastructure for Geodynamics. Versions available range from 1d to 3d solutions on different scales from regional to global. Each Specfem2d simulation consists of three phases:

- Meshing/partitioning
  Defining the mesh and the computation geometry where the seismic wave equation is computed on. In this study, the mesh is defined by using the external meshing software GMSH (*Geuzaine and Remacle*, 2009).

- Building databases
  After the mesh design, Specfem assigns the velocity to each mesh element. In this case, the velocities are defined via the elasticity tensors and densities, estimated by the work flow. The geometry mesh designed before becomes a computational grid to solve the wave equation.

- Solver
  The last step is to solve the seismic wave equation on the computational grid. Synthetic seismograms are generated, based on the geometry and the source and receiver set up.

BIBLIOGRAPHY

Al-Harrasi, O., J.-M. Kendall, and M. Chapman (2011), Fracture characterization using frequency-dependent shear wave anisotropy analysis of microseismic data, *Geophysical Journal International*, *185*(2), 1059–1070.

Alkhalifah, T. (1997), Velocity analysis using nonhyperbolic moveout in transversely isotropic media, *Geophysics*, *62*(6), 1839–1854.

Alkhalifah, T., and I. Tsvankin (1995), Velocity analysis for transversely isotropic media, *Geophysics*, *60*(5), 1550–1566.

Alkhalifah, T., I. Tsvankin, K. Larner, and J. Toldi (1996), Velocity analysis and imaging in transversely isotropic media: Methodology and a case study, *The Leading Edge*, *15*(5), 371–378.

Allen, J., and C. Beaumont (2012), Impact of inconsistent density scaling on physical analogue models of continental margin scale salt tectonics, *Journal of Geophysical Research: Solid Earth*, *117*(B8).

Anderson, J., T. Alkhalifah, and I. Tsvankin (1996), Fowler dmo and time migration for transversely isotropic media, *Geophysics*, *61*(3), 835–845.

Ando, M., Y. Ishikawa, and H. Wada (1980), S-wave anisotropy in the upper mantle under a volcanic area in Japan, *Nature*, *286*(5768), 43.

Anthony, J. W., R. A. Bideaux, K. W. Bladh, and M. C. Nichols (1990), *Handbook of mineralogy*, vol. 1, Mineral Data Publ. Tucson.

Babuska, V., and M. Cara (1991), *Seismic anisotropy in the Earth*, vol. 10, Springer, Netherlands.

Backus, G. E. (1962), Long-wave elastic anisotropy produced by horizontal layering, *Journal of Geophysical Research*, *67*(11), 4427–4440.

Bailey, J., and P. B. Hirsch (1962), The recrystallisation process in some polycrystalline metals, *Proc. R. Soc. Lond. A*, *267*(1328), 11–30.

Baird, A. F., J. M. Kendall, Q. J. Fisher, and J. Budge (2017), The role of texture, cracks, and fractures in highly anisotropic shales, *Journal of Geophysical Research: Solid Earth*, *122*(12).

Bao, H., J. Bielak, O. Ghattas, L. F. Kallivokas, D. R. O'Hallaron, J. R. Shewchuk, and J. Xu (1998), Large-scale simulation of elastic wave propagation in heterogeneous media on parallel computers, *Computer methods in applied mechanics and engineering*, *152*(1-2), 85–102.

Bass, J. D. (1995), Elasticity of minerals, glasses, and melts, *Mineral physics & crystallography: a handbook of physical constants*, *2*, 45–63.

Beach, A. (1979), Pressure solution as a metamorphic process in deformed terrigenous sedimentary rocks, *Lithos*, *12*(1), 51–58.

Beaudoin, A., P. Dawson, K. Mathur, and U. Kocks (1995), A hybrid finite element formulation for polycrystal plasticity with consideration of macrostructural and microstructural linking, *International Journal of Plasticity*, *11*(5), 501–521.

Beyerlein, I., R. Lebensohn, and C. Tomé (2003), Modeling texture and microstructural evolution in the equal channel angular extrusion process, *Materials Science and Engineering: A*, *345*(1), 122 – 138.

Blackman, D. K., J. Kendall, et al. (2002a), Seismic anisotropy in the upper mantle 2. Predictions for current plate boundary flow models, *Geochemistry, Geophysics, Geosystems*, *3*(9).

Blackman, D. K., H.-R. Wenk, J. M. Kendall, et al. (2002b), Seismic anisotropy of the upper mantle 1. Factors that affect mineral texture and effective elastic properties, *Geochemistry, Geophysics, Geosystems*, *3*(9), 1–24.

Borchert, H., and R. O. Muir (1964), *Salt deposits: the origin, metamorphism and deformation of evaporites*, University series in geology, Van Nostrand.

Bourbié, T., O. Coussy, and B. Zinszner (1987), *Acoustics of Porous Media*, Institut français du pétrole publications, Gulf Publishing Company, Book Division.

Bowman, J. R., and M. Ando (1987), Shear-wave splitting in the upper-mantle wedge above the Tonga subduction zone, *Geophysical Journal of the Royal Astronomical Society*, *88*(1), 25–41.

Browaeys, J. T., and S. Chevrot (2004), Decomposition of the elastic tensor and geophysical applications, *Geophysical Journal International*, *159*(2), 667–678.

Camp, W. K. (1998), Geologic model and reservoir description of the deepwater "P Sand" at subsalt Mahogany field, Gulf of Mexico, in *Integration of geologic models for understanding risk in the Gulf of Mexico: papers from Hedberg Conference*.

Carcione, J. M. (1994), The wave equation in generalised coordinates, *Geophysics*, *59*(12), 1911–1919.

Carter, N., S. Horseman, J. Russell, and J. Handin (1993), Rheology of rocksalt, *Journal of Structural Geology*, *15*(9-10), 1257–1271.

Carter, N. L., and F. D. Hansen (1983), Creep of rocksalt, *Tectonophysics*, *92*(4), 275–333.

Carter, N. L., and H. C. Heard (1970), Temperature and rate dependent deformation of halite, *American Journal of Science*, *269*(3), 193–249.

Chaljub, E., and B. Valette (2004), Spectral element modelling of three-dimensional wave propagation in a self-gravitating Earth with an arbitrarily stratified outer core, *Geophysical Journal International*, *158*(1), 131–141.

Chaljub, E., D. Komatitsch, J.-P. Vilotte, Y. Capdeville, B. Valette, and G. Festa (2007), Spectral-element analysis in seismology, *Advances in Geophysics*, *48*, 365–419.

Chapman, N., and A. Hooper (2012), The disposal of radioactive wastes underground, *Proceedings of the Geologists' Association*, *123*(1), 46–63.

Christie, P., V. Hughes, and B. Kennett (1983), Velocity filtering of seismic reflection data, *First Break*, *1*(3), 9–24.

Close, F., R. D. McCavitt, B. Smith, et al. (2008), Deepwater Gulf of Mexico development challenges overview, in *SPE North Africa Technical Conference & Exhibition*, Society of Petroleum Engineers.

Crampin, S. (1985), Evaluation of anisotropy by shear-wave splitting, *Geophysics*, *50*(1), 142–152.

Crook, A., S. Willson, J. Yu, and D. Owen (2006), Predictive modelling of structure evolution in sandbox experiments, *Journal of Structural Geology*, *28*(5), 729–744.

Crotogino, F., K.-U. Mohmeyer, and R. Scharf (2001), Huntorf CAES: More than 20 Years of Successful Operation, *Solution Mining Research Institute (SMRI) Spring Meeting*, *45*.

Danas, K., and V. Deshpande (2013), Plane-strain discrete dislocation plasticity with climb-assisted glide motion of dislocations, *Modelling and Simulation in Materials Science and Engineering*, *21*(4).

Davis, R. A. (2017), *Sediments of the Gulf of Mexico*, pp. 165–215, Springer New York, New York.

Davison, I., I. Alsop, and D. Blundell (1996), Salt tectonics: some aspects of deformation mechanics, *Geological Society, London, Special Publications*, *100*(1), 1–10.

Di Leo, J., A. Walker, Z.-H. Li, J. Wookey, N. Ribe, J.-M. Kendall, and A. Tommasi (2014), Development of texture and seismic anisotropy during the onset of subduction, *Geochemistry, Geophysics, Geosystems*, *15*(1), 192–212.

Diegel, F. A., J. F. Karlo, D. C. Schuster, R. C. Shoup, and P. R. Tauvers (1995), Cenozoic Structural Evolution and Tectono-Stratigraphic Framework of the Northern Gulf Coast Continental Margin, in *Salt Tectonics: A Global Perspective*, American Association of Petroleum Geologists.

Dribus, J. R., M. P. Jackson, J. Kapoor, and M. F. Smith (2008), The prize beneath the salt, *Oilfield Review*, *15*, 4–17.

Drucker, D. C., and W. Prager (1952), Soil mechanics and plastic analysis or limit design, *Quarterly of applied mathematics*, *10*(2), 157–165.

Drury, M., and G. Pennock (2007), Subgrain rotation recrystallisation in minerals, in *Materials science forum*, vol. 550, pp. 95–104, Trans Tech Publ.

Drury, M. R., and J. L. Urai (1990), Deformation-related recrystallisation processes, *Tectonophysics*, *172*(3-4), 235–253.

Eshelby, J. D. (1957), The determination of the elastic field of an ellipsoidal inclusion, and related problems, *Proc. R. Soc. Lond. A*, *241*(1226), 376–396.

Everitt, B., S. Landau, and M. Leese (2001), *Cluster Analysis*, A Hodder Arnold Publication, Wiley.

Firme, P., D. Roehl, C. Romanel, E. Poiate Jr, and A. Costa (2015), Multi-mechanism deformation creep model applied to Brazilian salt rocks: PALP Firme D. Roehl, in *Mechanical Behaviour of Salt VIII*, pp. 351–358, CRC Press.

Folstad, P. G., and M. Schoenberg (1992), Low-frequency propagation through fine layering, in *SEG Technical Program Expanded Abstracts 1992*, pp. 1279–1281, Society of Exploration Geophysicists.

Fort, X., J.-P. Brun, and F. Chauvel (2004), Salt tectonics on the Angolan margin, synsedimentary deformation processes, *AAPG Bulletin*, *88*(11), 1523.

Franssen, R., and C. Spiers (1990), Deformation of polycrystalline salt in compression and in shear at 250–350 C^o, *Geological Society, London, Special Publications*, *54*(1), 201–213.

Franssen, R. C. (1994), The rheology of synthetic rocksalt in uniaxial compression, *Tectonophysics*, *233*(1), 1–40.

Fredrich, J., A. Fossum, and R. Hickman (2007), Mineralogy of deepwater Gulf of Mexico salt formations and implications for constitutive behaviour, *Journal of Petroleum Science and Engineering*, *57*(3-4), 354–374.

Galloway, W. E. (2008), Depositional evolution of the Gulf of Mexico sedimentary basin, *Sedimentary basins of the world*, *5*, 505–549.

Gebrande, H. (1982), Elastic wave velocities and constants of elasticity of rocks at room temperature and pressures up to 1 GPa, *Physical Properties of Rocks*, *1*, 35–99.

Gemmer, L., S. J. Ings, S. Medvedev, and C. Beaumont (2004), Salt tectonics driven by differential sediment loading: stability analysis and finite-element experiments, *Basin Research*, *16*(2), 199–218.

Gemmer, L., C. Beaumont, and S. J. Ings (2005), Dynamic modelling of passive margin salt tectonics: effects of water loading, sediment properties and sedimentation patterns, *Basin Research*, *17*(3), 383–402.

Geuzaine, C., and J.-F. Remacle (2009), Gmsh: A 3-D finite element mesh generator with built-in pre-and post-processing facilities, *International journal for numerical methods in engineering*, *79*(11), 1309–1331.

Gomez-Rivas, E., A. Griera, M.-G. Llorens, P. Bons, R. Lebensohn, and S. Piazolo (2017), Subgrain Rotation Recrystallization During Shearing: Insights From Full-Field Numerical Simulations of Halite Polycrystals, *Journal of Geophysical Research: Solid Earth*, *122*(11), 8810–8827.

Graves, R. W. (1996), Simulating seismic wave propagation in 3D elastic media using staggered-grid finite differences, *Bulletin of the Seismological Society of America*, *86*(4), 1091–1106.

Gurtin, M. (1982), *An Introduction to Continuum Mechanics*, Mathematics in Science and Engineering, Academic Press.

Hall, S. (2001), The development of large structures in the deepwater northern Gulf of Mexico, *Houston Geological Society Bulletin*.

Hall, S. A., and J.-M. Kendall (2003), Fracture characterization at Valhall: Application of P-wave amplitude variation with offset and azimuth (AVOA) analysis to a 3D ocean-bottom data setFracture Characterization Using P-Wave AVOA, *Geophysics*, *68*(4), 1150–1160.

Hall, S. A., J.-M. Kendall, and O. I. Barkved (2002), Fractured reservoir characterization using P-wave AVOA analysis of 3D OBC data, *The Leading Edge*, *21*(8), 777–781.

Harrison, H., D. Moore, and P. Hodgkins (2010), A geologic review of the Mahogany subsalt discovery: A well that proved a play (The Mahogany subsalt discovery: A unique hydrocarbon play, of shore Louisiana), in *AAPG Annual Conference & Exhibition*.

Heege, J. T., J. D. Bresser, and C. Spiers (2005), Rheological behaviour of synthetic rocksalt: the interplay between water, dynamic recrystallization and deformation mechanisms, *Journal of Structural Geology*, *27*(6), 948 – 963.

Heidari, M., M. A. Nikolinakou, M. R. Hudec, and P. B. Flemings (2016), Geomechanical analysis of a welding salt layer and its effects on adjacent sediments, *Tectonophysics*, *683*, 172–181.

Heidelbach, F., I. C. Stretton, and K. Kunze (2001), Texture development of polycrystalline anhydrite experimentally deformed in torsion, *International Journal of Earth Sciences*, *90*(1), 118–126.

Helffrich, G., J. Wookey, and I. Bastow (2013), *The seismic analysis code: A primer and user's guide*, Cambridge University Press, Cambridge.

Hess, H. (1964), Seismic anisotropy of the uppermost mantle under oceans, *Nature*, *203*(4945), 629.

Hildyard, R., D. Prior, E. Mariani, and D. Faulkner (2009a), Crystallographic preferred orientation (CPO) of gypsum measured by electron backscatter diffraction (EBSD), *Journal of microscopy*, *236*(3), 159–164.

Hildyard, R. C., D. J. Prior, D. R. Faulkner, and E. Mariani (2009b), Microstructural analysis of anhydrite rocks from the Triassic Evaporites, Umbria-Marche Apennines, Central Italy: An insight into deformation mechanisms and possible slip systems, *Journal of Structural Geology*, *31*(1), 92–103.

Hill, R. (1952), The elastic behaviour of a crystalline aggregate, *Proceedings of the Physical Society. Section A*, *65*(5), 349.

Holtzman, B. K., and J.-M. Kendall (2010), Organized melt, seismic anisotropy, and plate boundary lubrication, *Geochemistry, Geophysics, Geosystems*, *11*(12).

Hosford, W. F. (2010), *Mechanical behaviour of materials*, Cambridge University Press, Cambridge.

Hudec, M., M. Jackson, and F. Peel (2013), Influence of deep Louann structure on the evolution of the northern Gulf of Mexico, *AAPG Bulletin*, *97*, 1711–1735.

Hudec, M. R., and M. P. Jackson (2007), Terra infirma: Understanding salt tectonics, *Earth-Science Reviews*, *82*(1-2), 1–28.

Hudson, J. A. (1980), *The excitation and propagation of elastic waves*, Cambridge University Press, Cambridge.

Hudson, J. A. (1981), Wave speeds and attenuation of elastic waves in material containing cracks, *Geophysical Journal International*, *64*(1), 133–150.

Hutchinson, J. (1976), Bounds and self-consistent estimates for creep of polycrystalline materials, in *Proceedings of the Royal Society of London A: Mathematical, Physical and Engineering Sciences*, vol. 348, pp. 101–127, The Royal Society.

Ings, S., C. Beaumont, and L. Gemmer (2004), Numerical modelling of salt tectonics on passive continental margins: Preliminary assessment of the effects of sediment loading, buoyancy, margin tilt, and isostasy, in *Perkins Research Conference*, pp. 36–68.

Isaac, J. H., and D. C. Lawton (1999), Image mispositioning due to dipping TI media: A physical seismic modeling study, *Geophysics*, *64*(4), 1230–1238.

Isherwood, D. J. (1979), Fluid inclusions in salt: an annotated bibliography, *Tech. rep.*, California Univ., Livermore (USA). Lawrence Livermore Lab.

Jackson, M., and M. Hudec (2017a), *Salt Tectonics: Principles and Practice*, Cambridge University Press, Cambridge.

Jackson, M., and C. J. Talbot (1991), *A glossary of salt tectonics*, Bureau of Economic Geology, University of Texas at Austin, Texas.

Jackson, M., and B. Vendeville (1994), Regional extension as a geologic trigger for diapirism, *Geological society of America bulletin*, *106*(1), 57–73.

Jackson, M. P., and C. J. Talbot (1986), External shapes, strain rates, and dynamics of salt structures, *Geological Society of America Bulletin*, *97*(3), 305–323.

Jackson, M. P., B. C. Vendeville, and D. D. Schultz-Ela (1994), Structural dynamics of salt systems, *Annual Review of Earth and Planetary Sciences*, *22*(1), 93–117.

Jackson, M. P. A., and M. R. Hudec (2017b), *Salt Sheets and Salt Canopies*, pp. 119–154, Cambridge University Press, Cambridge.

Jaeken, J. W., and S. Cottenier (2016), Solving the Christoffel equation: Phase and group velocities, *Computer Physics Communications*, *207*, 445–451.

Jenyon, M. K. (1986), *Salt tectonics*, Springer, California.

Jones, I. F., and I. Davison (2014), Seismic imaging in and around salt bodies, *Interpretation*, *2*(4).

Kaminski, E., N. M. Ribe, and J. T. Browaeys (2004), D-Rex, a program for calculation of seismic anisotropy due to crystal lattice preferred orientation in the convective upper mantle, *Geophysical Journal International*, *158*(2), 744–752.

Karato, S.-i. (2012), *Deformation of earth materials: an introduction to the rheology of solid earth*, Cambridge University Press, Cambridge.

Kendall, J., and C. Thomson (1989), A comment on the form of the geometrical spreading equations, with some numerical examples of seismic ray tracing in inhomogeneous, anisotropic media, *Geophysical Journal International*, *99*(2), 401–413.

Kendall, J.-M., and P. G. Silver (1996), Constraints from seismic anisotropy on the nature of the lowermost mantle, *Nature*, *381*(6581), 409.

Kendall, R., and D. Raymer (1999), Processing and Interpretation of VSP Data to Determine Salt Anisotropy-Mahogany Field, Gulf of Mexico, in *61st EAGE Conference and Exhibition*.

Kendall, R. R., S. H. Gray, and G. E. Murphy (1998), Subsalt imaging using prestack depth migration of converted waves: Mahogany field, gulf of mexico, in *SEG Technical Program Expanded Abstracts 1998*, pp. 2052–2055, Society of Exploration Geophysicists.

Kennicutt Ii, M., T. McDonald, P. Comet, G. Denoux, and J. Brooks (1992), The origins of petroleum in the northern Gulf of Mexico, *Geochimica et Cosmochimica Acta*, *56*(3), 1259–1280.

Kern, H., and G. Braun (1973), Deformation und gefügeregelung von steinsalz im temperaturbereich 20–200 C^o, *Contributions to Mineralogy and Petrology*, *40*(2), 169–181.

Kern, H., and A. Richter (1985), Microstructures and textures in evaporites, in *Preferred Orientation in Deformed Metal and Rocks*, pp. 317–333, Elsevier.

Komatitsch, D., and J. Tromp (2002a), Spectral-element simulations of global seismic wave propagation-1. Validation, *Geophysical Journal International*, *149*(2), 390–412.

Komatitsch, D., and J. Tromp (2002b), Spectra–element simulations of global seismic wave propagation-2. Three-dimensional models, oceans, rotation and self-gravitation, *Geophysical Journal International*, *150*(1), 303–318.

Komatitsch, D., and J.-P. Vilotte (1998), The spectral element method: an efficient tool to simulate the seismic response of 2D and 3D geological structures, *Bulletin of the seismological society of America*, *88*(2), 368–392.

Komatitsch, D., S. Tsuboi, J. Tromp, A. Levander, and G. Nolet (2005), The spectral-element method in seismology, *geophysical monograph – American Geophysical Union*, *157*, 205.

Koyi, H. (1996), Salt flow by aggrading and prograding overburdens, *Geological Society, London, Special Publications*, *100*(1), 243–258.

Langer, M. (1993), Use of solution-mined caverns in salt for oil and gas storage and toxic waste disposal in Germany, *Engineering geology*, *35*(3-4), 183–190.

Lebensohn, R., and T. Leffers (1999), The rules for the lattice rotation accompanying slip as derived from a self-consistent model, *Texture, Stress, and Microstructure*, *31*(4), 217–230.

Lebensohn, R., and C. Tomé (1993), A self-consistent anisotropic approach for the simulation of plastic deformation and texture development of polycrystals: application to zirconium alloys, *Acta metallurgica et materialia*, *41*(9), 2611–2624.

Lebensohn, R. A., P. R. Dawson, H. M. Kern, and H.-R. Wenk (2003), Heterogeneous deformation and texture development in halite polycrystals: comparison of different modelling approaches and experimental data, *Tectonophysics*, *370*(1), 287–311.

Levander, A. R. (1988), Fourth-order finite-difference P-SV seismograms, *Geophysics*, *53*(11), 1425–1436.

Li, S.-Y., and J. L. Urai (2016), Rheology of rock salt for salt tectonics modeling, *Petroleum Science*, *13*(4), 712–724.

Liu, Q., J. Polet, D. Komatitsch, and J. Tromp (2004), Spectral-element moment tensor inversions for earthquakes in southern California, *Bulletin of the Seismological Society of America*, *94*(5), 1748–1761.

Lysmer, J., and L. A. Drake (1972), A finite element method for seismology, *Methods in computational physics*, *11*, 181–216.

Mainprice, D., G. Barruol, and W. B. Ismail (2000), The seismic anisotropy of the Earth's mantle: from single crystal to polycrystal, *Earth's Deep Interior: Mineral physics and tomography from the atomic to the global scale*, pp. 237–264.

Maultzsch, S., M. Chapman, E. Liu, and X. Y. Li (2003), Modelling frequency-dependent seismic anisotropy in fluid-saturated rock with aligned fractures: implication of fracture size estimation from anisotropic measurements, *Geophysical Prospecting*, *51*(5), 381–392.

Miralles, L., M. Sans, S. Gali, and P. Santanach (2001), 3-D rock salt fabrics in a shear zone (Súria Anticline, South-Pyrenees), *Journal of Structural Geology*, *23*(4), 675–691.

Molinari, A., G. Canova, and S. Ahzi (1987), A self consistent approach of the large deformation polycrystal viscoplasticity, *Acta Metallurgica*, *35*(12), 2983–2994.

Muehlberger, W. R., and P. S. Clabaugh (1968), Internal Structure and Petrofabrics of Gulf Coast Salt Domes, in *Diapirism and Diapirs: a symposium*, American Association of Petroleum Geologists.

Müller, W., S. Schmid, and U. Briegel (1981), Deformation experiments on anhydrite rocks of different grain sizes: rheology and microfabric, *Tectonophysics*, *78*(1-4), 527–543.

Munson, B. R., T. H. Okiishi, W. W. Huebsch, and A. P. Rothmayer (2013), *Fluid mechanics*, Wiley, Singapore.

Munson, D. E., and P. Dawson (1979), Constitutive model for the low temperature creep of salt (with application to WIPP), *Tech. rep.*, Sandia Laboratories, United States.

Munson, D. E., et al. (2004), MD constitutive model parameters defined for gulf coast salt domes and structures, in *Gulf Rocks 2004, the 6th North America Rock Mechanics Symposium (NARMS)*, American Rock Mechanics Association.

Nygaard, R., M. Gutierrez, R. K. Bratli, and K. Hoeg (2006), Brittle - ductile transition, shear failure and leakage in shales and mudrocks, *Marine and Petroleum Geology*, *23*, 201–212.

Ohminato, T., and B. A. Chouet (1997), A free-surface boundary condition for including 3D topography in the finite-difference method, *Bulletin of the Seismological Society of America*, *87*(2), 494–515.

Passchier, C. W., and R. A. Trouw (2005), *Microtectonics*, vol. 1, Springer, Berlin.

Peel, F. J., C. J. Travis, and J. R. Hossack (1995), Genetic Structural Provinces and Salt Tectonics of the Cenozoic Offshore U.S. Gulf of Mexico: A Preliminary Analysis, in *Salt Tectonics: A Global Perspective*, American Association of Petroleum Geologists.

Peraire, J., M. Vahdati, K. Morgan, and O. C. Zienkiewicz (1987), Adaptive remeshing for compressible flow computations, *Journal of computational physics*, *72*(2), 449–466.

Perić, D., and A. Crook (2004), Computational strategies for predictive geology with reference to salt tectonics, *Computer Methods in Applied Mechanics and Engineering*, *193*(48-51), 5195–5222.

Peter, D., D. Komatitsch, Y. Luo, R. Martin, N. Le Goff, E. Casarotti, P. Le Loher, F. Magnoni, Q. Liu, C. Blitz, et al. (2011), Forward and adjoint simulations of seismic wave propagation on fully unstructured hexahedral meshes, *Geophysical Journal International*, *186*(2), 721–739.

Picard, D., A. Dimanov, and J. Raphanel (2018), Plastic behavior of halite single-crystals at different temperatures and strain rates: New insights from in-situ experiments and full field measures, *Materials Science and Engineering: A*, *732*, 284–297.

Pindell, J. L., and L. Kennan (2009), Tectonic evolution of the Gulf of Mexico, Caribbean and northern South America in the mantle reference frame: an update, *Geological Society, London, Special Publications*, *328*(1), 1–55.

Planchart, C. (2014), Estimation of salt anisotropy using zero offset, walkaway and walkaround VSP data from the Red Sea, Saudi Arabia: A case study, in *SEG Technical Program Expanded Abstracts*, pp. 389–393, Society of Exploration Geophysicists.

Princeton University and University of Marseille - Specfem2d User Manual (2015), *Specfem2d User Manual*, Princeton University and University of Marseille, 7.0.0 ed.

Putnis, A. (1992), *An introduction to mineral sciences*, Cambridge University Press, Cambridge.

Ranganathan, S. I., and M. Ostoja-Starzewski (2008a), Universal elastic anisotropy index, *Physical Review Letters*, *101*(5), 055,504.

Ranganathan, S. I., and M. Ostoja-Starzewski (2008b), Universal Elastic Anisotropy Index, *Physical Review Letters*, *101*(055504), doi:10.1103.

Raymer, D., J. Kendall, D. Pedlar, R. Kendall, M. Mueller, and G. Beaudoin (2000a), The significance of salt anisotropy in seismic imaging, in *SEG Technical Program Expanded Abstracts 2000*, pp. 562–565, Society of Exploration Geophysicists.

Raymer, D. G., A. Tommasi, and J.-M. Kendall (2000b), Predicting the seismic implications of salt anisotropy using numerical simulations of halite deformation, *Geophysics*, *65*(4), 1272–1280.

Rockfield Global (2013), ELFEN Forward Modelling Manual.

Rockfield Global (2014), Formation of a Salt Diapir with Sedimentation, Advanced Example: APSX019.

Roedder, E. (1984), The fluids in salt, *American Mineralogist*, *69*(5-6), 413–439.

Rose, K. (2015), Gulf of Mexico Geology and Petroleum System: Overview and Literature Review in Support of Risk and Resource Assessments.

Rösler, J., H. Harders, and M. Bäker (2007), *Mechanical behaviour of engineering materials: metals, ceramics, polymers, and composites*, Springer, Berlin.

Rowan, M. G. (1995), Structural Styles and Evolution of Allochthonous Salt, Central Louisiana Outer Shelf and Upper Slope, in *Salt Tectonics: A Global Perspective*, American Association of Petroleum Geologists.

Rowan, M. G., R. A. Ratliff, B. D. Trudgill, and J. B. Duarte (2001), Emplacement and evolution of the Mahogany salt body, central Louisiana outer shelf, northern Gulf of Mexico, *AAPG bulletin*, *85*(6), 947–969.

Rowan, M. G., T. F. Lawton, K. A. Giles, and R. A. Ratliff (2003), Near-salt deformation in La Popa basin, Mexico, and the northern Gulf of Mexico: A general model for passive diapirism, *AAPG bulletin*, *87*(5), 733–756.

Rümpker, G., A. Tommasi, and J.-M. Kendall (1999), Numerical simulations of depth-dependent anisotropy and frequency-dependent wave propagation effects, *Journal of Geophysical Research: Solid Earth*, *104*(B10), 23,141–23,153.

Sachs, G. (1929), Zur Ableitung einer Fliessbedingung, in *Mitteilungen der deutschen Materialprüfungsanstalten*, pp. 94–97, Springer.

Salvador, A. (1991), Origin and development of the Gulf of Mexico basin, *The gulf of Mexico basin*, pp. 389–444.

Savage, M. (1999), Seismic anisotropy and mantle deformation: what have we learned from shear wave splitting?, *Reviews of Geophysics*, *37*(1), 65–106.

Schléder, Z., J. L. Urai, S. Nollet, and C. Hilgers (2008), Solution-precipitation creep and fluid flow in halite: a case study of Zechstein (Z1) rocksalt from Neuhof salt mine (Germany), *International Journal of Earth Sciences*, *97*(5), 1045–1056.

Schwerdtner, W. (1968), Intragranular gliding in domal salt, *Tectonophysics*, *5*(5), 353–380.

Sena, A. G., and M. N. Toksöz (1993), Kirchhoff migration and velocity analysis for converted and nonconverted waves in anisotropic media, *Geophysics*, *58*(2), 265–276.

Shearer, P. M. (2019), *Introduction to seismology*, Cambridge university press.

Sheriff, R. E. (1974), *Encyclopedic dictionary of exploration geophysics*, Society of Exploration Geophysicists.

Sheriff, R. E., and L. P. Geldart (1995), *Exploration seismology*, Cambridge University Press, Cambridge.

Silver, P. G., and W. W. Chan (1991), Shear wave splitting and subcontinental mantle deformation, *Journal of Geophysical Research: Solid Earth*, *96*(B10), 16,429–16,454.

Skrotzki, W., and P. Haasen (1981), Hardening mechanisms of ionic crystals on {110} and {100} slip planes, *Le Journal de Physique Colloques*, *42*(C3), C3–119.

Skrotzki, W., and P. Welch (1983), Development of texture and microstructure in extruded ionic polycrystalline aggregates, *Tectonophysics*, *99*(1), 47–61.

Skrotzki, W., K. Helming, H. Brokmeier, H. Dornbusch, and P. Welch (1995), Textures in pure shear deformed rock salt, *Textures and Microstructures*, *24*, 133–133.

Smith, E. C., A. F. Baird, J. M. Kendall, C. Martín, R. S. White, A. M. Brisbourne, and A. M. Smith (2017), Ice fabric in an Antarctic ice stream interpreted from seismic anisotropy, *Geophysical Research Letters*, *44*(8), 3710–3718.

Spiers, C., and N. Carter (1998), Microphysics of rocksalt flow in nature, *Proceedings of the 4th Conference,Trans Tech. Publ. Ser. on Rock and Soil Mech*, *22*(1), 115–128.

Spiers, C., P. Schutjens, R. Brzesowsky, C. Peach, J. Liezenberg, and H. Zwart (1990), Experimental determination of constitutive parameters governing creep of rocksalt by pressure solution, *Geological Society, London, Special Publications*, *54*(1), 215–227.

Stewart, S. (2007), Salt tectonics in the North Sea Basin: a structural style template for seismic interpreters, *Special Publication-Geological Society of London*, *272*, 361.

Stovas, A., M. Landrø, and P. Avseth (2006), AVO attribute inversion for finely layered reservoirs, *Geophysics*, *71*(3), C25–C36.

Talbot, C., and M. Jackson (1987), Internal kinematics of salt diapirs, *AAPG Bulletin*, *71*(9), 1068–1093.

Talbot, C., and R. Jarvis (1984), Age, budget and dynamics of an active salt extrusion in Iran, *Journal of Structural Geology*, *6*(5), 521–533.

Tandon, G. P., and G. J. Weng (1984), The effect of aspect ratio of inclusions on the elastic properties of unidirectionally aligned composites, *Polymer composites*, *5*(4), 327–333.

Taylor, G. (1938), Plastic strain in metals, *Inst. Metals (62) pp*, pp. 307–324.

Teanby, N., J.-M. Kendall, and M. Van der Baan (2004), Automation of shear-wave splitting measurements using cluster analysis, *Bulletin of the Seismological Society of America*, *94*(2), 453–463.

Ter Heege, J., J. De Bresser, and C. Spiers (2005), Dynamic recrystallisation of wet synthetic polycrystalline halite: dependence of grain size distribution on flow stress, temperature and strain, *Tectonophysics*, *396*(1-2), 35–57.

Thiemeyer, N., G. Zulauf, M. Mertineit, J. Linckens, M. Pusch, and J. Hammer (2016), Microfabrics and 3D grain shape of Gorleben rock salt: Constraints on deformation mechanisms and paleodifferential stress, *Tectonophysics*, *676*, 1–19.

Thigpen, J. R., D. Roberts, J. K. Snow, C. D. Walker, and A. Bere (2019), Integrating kinematic restoration and forward finite element simulations to constrain the evolution of salt diapirism and overburden deformation in evaporite basins, *Journal of Structural Geology*, *118*, 68–86.

Thomsen, L. (1986), Weak elastic anisotropy, *Geophysics*, *51*(10), 1954–1966.

Thornton, D., and A. Crook (2014), Predictive modeling of the evolution of fault structure: 3-D modeling and coupled geomechanical/flow simulation, *Rock mechanics and rock engineering*, *47*(5), 1533–1549.

Tomé, C., and R. Lebensohn (2009), Manual for code visco-plastic self-consistent (VPSC).

Tomé, C., R. Lebensohn, and U. Kocks (1991), A model for texture development dominated by deformation twinning: application to zirconium alloys, *Acta Metallurgica et Materialia*, *39*(11), 2667–2680.

Tommasi, A., D. Mainprice, G. Canova, and Y. Chastel (2000), Viscoplastic self-consistent and equilibrium-based modeling of olivine lattice preferred orientations: Implications for the upper mantle seismic anisotropy, *Journal of Geophysical Research: Solid Earth*, *105*(B4), 7893–7908.

Trimby, P. W., M. R. Drury, and C. J. Spiers (2000), Recognising the crystallographic signature of recrystallisation processes in deformed rocks: a study of experimentally deformed rocksalt, *Journal of Structural Geology*, *22*(11-12), 1609–1620.

Tromp, J., D. Komattisch, and Q. Liu (2008), Spectral-element and adjoint methods in seismology, *Communications in Computational Physics*, *3*(1), 1–32.

Tsvankin, I., J. Gaiser, V. Grechka, M. Van Der Baan, and L. Thomsen (2010), Seismic anisotropy in exploration and reservoir characterization: An overview, *Geophysics*, *75*(5), 75A15–75A29.

Urai, J. (1987), Deformation Mechanisms Operating in Naturally Deformed Halite Rocks as Deduced from Microstructural Investigation, *Geol. Mijnbouw*, *66*, 165–176.

Urai, J., and C. Spiers (2007), The effect of grain boundary water on deformation mechanisms and rheology of rocksalt during long-term deformation, in *Proc. 6th Conf. Mech. Beh. of Salt*, pp. 149–158.

Urai, J., W. Means, and G. Lister (1986a), Dynamic recrystallisation of minerals, *Mineral and rock deformation: laboratory studies*, *36*, 161–199.

Urai, J., C. J. Spiers, H. J. Zwart, and G. S. Lister (1986b), Weakening of rock salt by water during long-term creep, *Nature*, *324*(6097), 554.

Urai, J., Z. Schleder, C. Spiers, and P. Kukla (2008), Flow and transport properties of salt rocks, *Dynamics of complex intracontinental basins: The central European basin system*, pp. 277–290.

US Energy Information Administration (2016), U.S. Gulf of Mexico crude oil production to continue at record highs through 2019.

US Energy Information Administration (2019), S Energy Information Administration crude oil production grew 17% in 2018, surpassing the previous record in 1970.

Van Keken, P., C. Spiers, A. Van den Berg, and E. Muyzert (1993), The effective viscosity of rocksalt: implementation of steady-state creep laws in numerical models of salt diapirism, *Tectonophysics*, *225*(4), 457–476.

Vargas-Meleza, L., D. Healy, G. I. Alsop, and N. E. Timms (2015), Exploring the relative contribution of mineralogy and CPO to the seismic velocity anisotropy of evaporites, *Journal of Structural Geology*, *70*, 39–55.

Vecsey, L., J. Plomerová, and V. Babuška (2008), Shear-wave splitting measurements‚ÄîProblems and solutions, *Tectonophysics*, *462*(1-4), 178–196.

Vendeville, B. C., and K. T. Nilsen (1995), Episodic growth of salt diapirs driven by horizontal shortening, in *Salt, Sediment, and Hydrocarbons. SEPM Gulf Coast Section 16th Annual Research Foundation Conference*, vol. 285, p. 295.

Walker, A., A. Forte, J. Wookey, A. Nowacki, and J.-M. Kendall (2011), Elastic anisotropy of D" predicted from global models of mantle flow, *Geochemistry, Geophysics, Geosystems*, *12*(10).

Walker, A. M., and J. Wookey (2012), MSAT - A new toolkit for the analysis of elastic and seismic anisotropy, *Computers and Geosciences*, *4*, 81–90.

Wang, X., and M. Cai (2014), Wave propagation simulation in underground mines by Specfem2D, in *Proceedings of the Seventh International Conference on Deep and High Stress Mining*, pp. 723–738, Australian Centre for Geomechanics.

Wardlaw, N., and W. Schwerdtner (1966), Halite-anhydrite seasonal layers in the middle Devonian Prairie evaporite formation, Saskatchewan, Canada, *Geological Society of America Bulletin*, *77*(4), 331–342.

Warren, J. (1989), *Evaporite Sedimentology*, Old Tappan, NJ (USA); Prentice Hall Inc.

Warren, J. K. (2006), *Evaporites: sediments, resources and hydrocarbons*, Springer, Berlin.

Warren, J. K. (2016), Flowing Salt: Halokinesis, in *Evaporites*, pp. 491–612, Springer, Switzerland.

Weimer, P., M. G. Rowan, B. C. McBride, and R. Kligfield (1998), Evaluating the petroleum systems of the northern deep Gulf of Mexico through integrated basin analysis: An overview, *AAPG bulletin*, *82*(5), 865–877.

Wenk, H., and P. Van Houtte (2004), Texture and anisotropy, *Reports on Progress in Physics*, *67*(8), 1367.

Wenk, H., G. Canova, A. Molinari, and H. Mecking (1989), Texture development in halite: comparison of Taylor model and self-consistent theory, *Acta metallurgica*, *37*(7), 2017–2029.

Wenk, H.-R. (1999), A voyage through the deformed earth with the self-consistent model, *Modelling and Simulation in Materials Science and Engineering*, *7*(5), 699.

Wenk, H.-R., G. Canova, Y. Brechet, and L. Flandin (1997), A deformation-based model for recrystallisation of anisotropic materials, *Acta Materialia*, *45*(8), 3283–3296.

Wenk, H.-R., M. Armann, L. Burlini, K. Kunze, and M. Bortolotti (2009), Large strain shearing of halite: Experimental and theoretical evidence for dynamic texture changes, *Earth and Planetary Science Letters*, *280*(1), 205–210.

Wilhelm, O., and M. Ewing (1972), Geology and History of the Gulf of Mexico, *GSA Bulletin*, *83*(3), 575.

Wood, D. M. (1990), *Soil behaviour and critical state soil mechanics*, Cambridge university press, Cambridge.

Wookey, J. (2003), Modelling and Interpreting Seismograms for 3D Earth Structure: A Study of Mid-Mantle Anisotropy, Ph.D. thesis, School of Earth Sciences, University of Leeds.

Wookey, J., J.-M. Kendall, and G. Rümpker (2005), Lowermost mantle anisotropy beneath the north Pacific from differential S-ScS splitting, *Geophysical Journal International*, *161*(3), 829–838.

Wuestefeld, A., and G. Bokelmann (2007), Null detection in shear-wave splitting measurements, *Bulletin of the Seismological Society of America*, *97*(4), 1204–1211.

Wuestefeld, A., O. Al-Harrasi, J. P. Verdon, J. Wookey, and J.-M. Kendall (2010), A strategy for automated analysis of passive microseismic data to image seismic anisotropy and fracture characteristics, *Geophysical Prospecting*, *58*(5), 755–773.

Yan, F., D.-h. Han, Q. Yao, and H. Li (2014), Seismic velocities of halite salt: Anisotropy, dispersion, temperature, and stress effects, in *SEG Technical Program Expanded Abstracts 2014*, pp. 2783–2787, Society of Exploration Geophysicists.

Yan, F., D.-h. Han, Q. Yao, and X.-L. Chen (2016), Seismic velocities of halite salt: Anisotropy, heterogeneity, dispersion, temperature, and pressure effects, *Geophysics*, *81*(4), D293–D301.

Zheng, L., Q. Zhao, B. Milkereit, G. Grasselli, and Q. Liu (2014), Spectral-element simulations of elastic wave propagation in exploration and geotechnical applications, *Earthquake Science*, *27*(2), 179–187.

Zong, J., R. Stewart, and N. Dyaur (2014), Salt anisotropy: Ultrasonic lab experiments and traveltime ramifications, *SEG Technical Program Expanded Abstracts 2014*, pp. 383–388.

Zong, J., R. R. Stewart, N. Dyaur, and M. T. Myers (2015), Elastic properties of rock salt: Lab measurements and well log analysis in the Gulf of Mexico, in *SEG Technical Program Expanded Abstracts 2015*, pp. 3095–3099, Society of Exploration Geophysicists.

Zong, J., R. R. Stewart, N. Dyaur, and M. T. Myers (2017), Elastic properties of rock salt: Laboratory measurements and Gulf of Mexico well-log analysis, *Geophysics*, *82*(5), D303–D317.